Modeling and simulation of transport during acupuncture

Yannick Deleuze




ÉCOLE DOCTORALE SCIENCES MATHÉMATIQUES DE PARIS CENTRE
UNIVERSITÉ PIERRE ET MARIE CURIE

DEPARTMENT OF ENGINEERING SCIENCE AND OCEAN ENGINEERING
COLLEGE OF ENGINEERING
NATIONAL TAIWAN UNIVERSITY

DOCTORAL DISSERTATION

Modeling and simulation of transport during acupuncture

By : **Yannick DELEUZE**

Advisors : **Marc THIRIET**, M.D., Ph.D. and **Tony W. H. SHEU**, Ph.D.

Submitted in partial fulfillment of the requirement for
the degree of Doctor of Philosophy
specialized in Engineering Science
at National Taiwan University
and
the degree of Doctor of science,
specialized in Applied Mathematics
at University Pierre and Marie Curie

Reviewers :

HUANG Huaxiong	*York University*
MAURY Bertrand	*Université Paris-Sud*

Defended publicly on the 22/09/2015 in Taipei in front of a Committee composed of :

THIRIET Marc	*UPMC*	*Advisor*
SHEU Tony W.H	*NTU*	*Advisor*
PIRONNEAU Olivier	*UPMC*	*Examiner*
MAURY Bertrand	*Université Paris-Sud*	*Reviewer*
LIN Jaung-Geng	*China Medical University*	*Examiner*
TSAI Wu-Ting	*NTU*	*Examiner*
CHU Yeh-Shiu	*National Yang-Ming University*	*Examiner*
PERTHAME Benoit	*UPMC*	*Examiner*

Laboratoire Jacques-Louis Lions
Université Pierre et Marie Curie
Boîte courrier 187
75252 Paris Cedex 05 France

École Doctorale de Sciences Mathématiques de Paris Centre (ED 386)
Université Pierre et Marie Curie
Boîte courrier 290
4, Place Jussieu
75252 Paris Cedex 05
France

Scientific Computing and Cardiovascular Simulation Laboratory
Department of Engineering Science and Ocean Engineering
National Taiwan University
No. 1, Sec. 4, Roosevelt Rd., Daan District, Taipei City 106
Taiwan

À mes parents, mon frère, et ma femme

"Ceux qui vivent, ce sont ceux qui luttent."
Victor Hugo

Acknowledgements

I am heartily thankful to my supervisors, Tony Sheu and Marc Thiriet, for allowing me to work on this exciting subject and giving me the opportunity to be part of this international project. Their enthusiasm, encouragement, understanding, guidance, and support have made this work a thoughtful and rewarding journey.

I owe my deepest gratitude to Huaxiong Huang and Bertrand Maury to have accepted to read and review my thesis. I would like to thank Olivier Pironneau, Bertrand Maury, Benoit Perthame, Jaung-Geng Lin, Wu-Ting Tsai, and Yeh-Shiu Chu to have accepted to be part of my dissertation Committee.

I thank the UPMC for the funding of my doctoral studies. I thank the FSMP, the CASTS, the "Bureau de Représentation de Taipei en France", and the Department of Engineering Science and Ocean Engineering for the several partial fundings during my master and doctoral studies.

My work has been made possible thanks to the efforts and scientific excellency of the researchers and professors in the LJLL, SCCS, and CASTS that generously shared their time and ideas. A special thanks to Nadine Foucart, Salima Lounici, Danielle Boulic, Liliane Ruprecht, Christian David, Khashayar Dadras, and Antoine Le Hyaric for their help both in France and during my stay in Taiwan. Thanks also to Ms Huang and Ms Wang for the precious help and counsels during my stay in the NTU.

I would like to thank the teachers who led me to the world of research through their inspirational teaching. I would like to cite in particular Yvon Maday, Jean-Pierre Françoise, Pascal Frey, Frédéric Hecht, Albert Goldbeter, Alessandra Carbone, David Holcman, and Olivier Pironneau. I also would like to show my gratitude to Benoit Perthame who has introduced me to the world of interactions between mathematics and biology. I would also like to thank Benoit for his collaboration and proofreading for parts of the work presented in chapter 4 and his precious advices during our encounters both in France and Taiwan.

Thanks to Frédéric Hecht for generously sharing his time and ideas with the use of the software FreeFem++.

I also would like to thank Hiroshi Suito for inviting me to share my work in Japan. I really enjoyed the rewarding experience. During the several conferences and events along my doctoral studies, I met remarkable researchers that had the kindness to interact with me and whose work have inspired me. I would like to cite, among others, Norikazu Saito,

Olivier Pironneau, Pascal Frey, Kenji Takizawa, Bertrand Maury.

The dual degree project between France and Taiwan has been made possible with the great help of the International Relations Department in UPMC and the Office of International Affairs in NTU. I would like to thank in particular Patricia Zizzo for her help and advices during the elaboration of the project.

I don't forget the students and post-doctors of UPMC and NTU with who I had friendly, helpful, and productive discussions: Juliette, 承佑, 育瑋, 聖宗, Lise-Marie, Nicole, Charles, Vincent, Mamadou, Pierre, Marie, Paul, Jean-Paul, Grégoire, Claire, Maxim, Céline, 仕超, 燿宇, 向成, 豫潔, 林樂, 日陽, 聖鋒, 禹鑫, 哲安, 嘉敏, 倫語.

I'm very grateful for the unconditional support of my wife Camille, my parents, my brother, and family during the completion of the project.

And finally, thanks to my all my friends and especially to Guillaume, Thibault, Thibault, Sébastien, and the Orry team for their friendship during all these years.

Abstract

The objective of this thesis is to comprehend the complexity of the underlying basis of acupuncture. Acupuncture needling is investigated in order to establish a multiscale model that takes into account the complexity of biology but is mathematically simple enough to run simulations.

Acupuncture is one of the oldest practices in the history of medicine and is the core of Traditional Chinese Medicine. Once needles are inserted in the right locations, called acupoints, they are manipulated via manual needling, such as lifting and thrusting or rotating, to stimulate the acupoint. The same acupoints can also be stimulated by other techniques such as moxibustion, acupressure, electroacupuncture, and more recently, laser acupuncture. Growing public interest for acupuncture treatments has led the scientific community to investigate the underlying physiological basis of acupuncture. The physiological reactions of acupuncture needling lead to therapeutic effects which can be explained by a series of interactions between the skin and the nervous, the endocrine, and the immune systems.

In the present work, the thrusting and lifting of an acupuncture needle inserted in subcutaneous connective tissue is modeled. This loose connective tissue is composed of cells and an extracellular matrix of collagen and elastic fibers embedded in gel made of glycoproteins and proteoglycans. A porous media model is used to run simulations and compute the pressure and shear stress affecting the organization of fibers and of isolated cells in their matrix. The predicted pressure and shear stress show that the implantation of a needle can produce local mechanical stimulation in its environment.

A mathematical model was conceived to take into account cell signaling. There is ample evidence that needle manipulation in acupuncture can cause degranulation of mastocytes directly through a physical stress to occur. Activated mastocytes rapidly release granules containing chemical mediators. These chemical mediators play a key role recruiting mastocytes in their environment and are known to affect the excitability of nerve endings as well as local microcirculation permeability and size for the appropriate transfer of long-term acting endocrine signals. The process is sustained by the recruitment of mastocytes through chemotaxis.

The mathematical model of the mastocyte response to acupuncture needling relies on the macroscopic description of chemotaxis. Its simplest form describes the evolution of the density of mastocytes and the concentration of a chemoattractant emitted only

by mastocytes when activated by the mechanical stress induced by needle manipulation. Blow-up of the solution in finite time is proven to occur for large initial data concentrated around the acupoint in a simplified model. A numerical study infers the theoretical results and the observed blow-up is interpreted as a self-sustained response of stimulation and recruitment of mastocytes at the acupoint.

Keywords : acupuncture; mastocyte; chemotaxis ; fluid-structure interaction; fluid-fibrous porous medium interaction ; chemotaxis-fluid model; numerical simulation ; finite element method; FreeFem++

Résumé

L'objectif de cette thèse est d'appréhender la complexité des mécanismes biologiques de l'acupuncture afin de construire un modèle mathématique multi-échelle. Ce modèle est étudié théoriquement et numériquement.

L'acupuncture est une des plus vielles pratiques de l'histoire de la médecine et une partie intégrante de la médecine traditionnelle chinoise. Dans sa pratique la plus classique, une ou plusieurs aiguilles sont placées à des endroits spécifiques, nommés points d'acupuncture. L'aiguille est ensuite manipulée en utilisant des mouvements de rotation et de translation de façon à stimuler le point d'acupuncture. Ces mêmes points peuvent être stimulés par d'autres techniques telles que la moxibustion, l'acupression, l'électro-acupuncture et l'acupuncture par laser.

L'intérêt croissant pour l'acupuncture a incité la communauté scientifique à s'intéresser aux bases physiologiques de l'acupuncture. Les effets cliniques de l'acupuncture pourraient être le résultat d'effet de cascades de réactions produites par les interactions entre l'hypoderme et les systèmes nerveux, endocrinien et immunitaire.

Le travail présenté s'articule sur la modélisation de l'insertion d'une aiguille dans le tissu conjonctif de l'hypoderme. Ce tissu conjonctif lâche est composé de cellules et d'une matrice extracellulaire. Cette dernière est constituée principalement d'un maillage de fibres de collagène et d'élastine stabilisées ainsi que d'un fluide formé de protéoglycanes et de glycoprotéines. Les mastocytes sont des cellules du système immunitaire présentes dans l'hypoderme. Ces dernières contiennent dans leur cytoplasme de très nombreuses granulations contenant des médiateurs vaso-actifs et neuro-actifs ainsi que des attractants chimiques. Ces attractants jouent un rôle important pour le recrutement de mastocytes. Les médiateurs neuro-actifs sont impliqués dans l'excitabilité des terminaisons nerveuses pour permettre l'émission de potentiels d'action transmis jusqu'au système nerveux central. Les médiateurs vaso-actifs augmentent notamment la perméabilité vasculaire et la microcirculation pour permettre une production, à long terme, de signaux endocriniens. Activés par un signal externe, les mastocytes dégranulent et libèrent les médiateurs de manière très rapide.

Un modèle d'écoulement en milieu poreux du liquide interstitiel de l'hypoderme a permis d'étudier numériquement les composantes de contrainte qui agissent sur les récepteurs à la surface des cellules du tissu et notamment des mastocytes. La pression et le cisaillement calculés renforcent l'hypothèse selon laquelle que l'insertion de l'aiguille

peut produire une stimulation mécanique suffisante pour activer les mastocytes proches du point d'acupuncture.

Un modèle mathématique de la réponse chimiotactique des mastocytes à une contrainte physique créée par le traitement d'acupuncture est développé. Ce modèle prend en compte les mécanismes de signalisation cellulaire. La contrainte physique induit la libération rapide et continue, grâce au recrutement chimotactique de mastocytes, d'attractants et de médiateurs chimiques. Le modèle est basé sur le modèle de chimiotaxie de type Keller-Segel. Il décrit l'évolution de la densité de mastocytes et de la concentration des médiateurs chimiques libérés par les mastocytes après avoir été activés. Dans sa version la plus simplifiée, la solution du système d'équation aux dérivées partielles devient singulière en un temps fini pour des conditions initiales suffisamment grandes et concentrées autour du point acupuncture. Dans ces conditions, l'explosion en temps fini de la solution résulte de l'agrégation des cellules et pourrait mesurer l'efficacité de la manipulation de l'aiguille sur le point d'acupuncture. L'étude numérique confirme les résultats théoriques. La stimulation en dehors d'un point d'acupuncture n'est que légèrement amplifiée. Selon le modèle proposé, la présence d'un nombre important de mastocytes au point d'acupuncture est impérative pour qu'une réponse appropriée soit observée.

Mots clés : acupuncture; chimiotaxie; mastocyte; intéraction fluide-structure; intéraction fluide-milieu poreux fibreux; modèle de chimiotaxie-fluide; simulation numérique; méthode des éléments finis; FreeFem++

Contents

Introduction **23**

0.1 Acupuncture 23

0.1.1 History of acupuncture 24

0.1.2 Traditional theory behind acupuncture 25

0.2 Underlying acupuncture mechanisms 28

0.3 Contribution of this thesis 30

1 Literature survey of acupuncture study **33**

1.1 Introduction 34

1.1.1 Subcutaneous connective tissue 34

1.1.2 Mastocytes 35

1.2 Underlying acupuncture mechanisms 36

1.2.1 Stimulation of acupoints 36

1.2.2 Biochemical signaling at acupoints 41

1.3 Modeling in acupuncture 43

1.3.1 Electroosmotic meridian model 43

1.3.2 Interstitial flow in acupuncture 44

1.3.3 Mastocyte dynamics of degranulation 45

1.4 Concluding remarks 46

2 FreeFem++ **48**

2.1 Introduction 49

2.2 FreeFem++ and its interpreted language 49

2.2.1 The syntax 49

2.2.2 Meshing tools and mesh exemples 50

2.2.3 Finite element method 59

2.3 Solving problems in FreeFem++ . . . 63
2.3.1 Evolution problem . . . 63
2.3.2 Incompressible Navier-Stokes equation . . . 65
2.3.3 Moving domain problem in computational fluid dynamics . . . 68
2.4 Concluding remarks . . . 75

3 Modeling and simulation of local physical stress field during needling 76
3.1 Introduction . . . 78
3.2 Biological medium . . . 78
3.3 Mathematical modeling . . . 79
3.4 Computational model . . . 80
3.4.1 Scaling and setting for numerical simulations . . . 80
3.4.2 Numerical methods . . . 81
3.5 Results and discussion . . . 83
3.5.1 Effect of needle motion on the interstitial flow . . . 83
3.5.2 Effects of fractional fluid volume and Darcy number on the interstitial flow . . . 84
3.5.3 Shear stress and pressure distributions along the cell membrane . 88
3.6 Concluding remarks . . . 91

4 Mastocyte response to acupuncture 94
4.1 Introduction . . . 96
4.2 Mathematical model of mastocyte response to acupuncture treatment . . . 98
4.3 Blow-up and existence conditions in the Keller-Segel system . . . 100
4.4 Blow-up condition in a simplified system with mass conservation . . . 104
4.5 Blow-up condition in the case of a sole state for mastocytes . . . 108
4.6 Existence condition in the case of a sole state for mastocytes . . . 112
4.7 Scaling and numerical method . . . 113
4.7.1 Scaling . . . 113
4.7.2 Finite element method . . . 114
4.8 Computational model . . . 121
4.8.1 Acupoints . . . 121
4.8.2 Stress function Φ . . . 122
4.9 Numerical results . . . 124

4.10 Concluding remarks 124

5 Chemotaxis–diffusion–convection coupling system 127

5.1 Introduction 128
5.2 Mathematical model 131
5.3 Computational model 133
5.3.1 Scaling and setting for numerical simulations 133
5.3.2 Numerical methods 134
5.3.3 Code validation for the coupled Navier-Stokes and Keller-Segel equations 135
5.4 Numerical results and discussion 136
5.4.1 Descending plumes 136
5.4.2 Stabilizing effect of chemotaxis 141
5.4.3 Distribution and number of plumes and initial conditions 144
5.4.4 Comparison with other buoyancy-driven convections 151
5.5 Concluding remarks 155

Conclusion and future work 156

Bibliography 157

List of Figures

1 Foundation in traditional Chinese medicine: A *qì*-blood-tissue fluid triple coupling circulation system 26
2 Meridians and acupuncture points in traditional Chinese medicine 27
3 Correspondence between the meridians, *zàng-fǔ* organs and the *yīn* and the *yáng* in traditional Chinese medicine 28
4 Meridian compartment model 30

1.1 Locoregional activation of mastocytes 40
1.2 Chemical messengers released by mastocytes upon stimulation 42

2.1 Uniform square mesh and rectangle mesh 51
2.2 Mesh representing a plum blossom of the Taiwan national flower 52
2.3 Meshes of Taiwan generated from an image 54
2.4 3d mesh of Taiwan generated from an image 55
2.5 Mesh generated with the truncation tool 56
2.6 Mesh of two collated rectangles 56
2.7 Mesh adaptation with the *splitmesh* function 57
2.8 Mesh adaptation with the *adaptmesh* function 58
2.9 Mesh manipulation with the *movemesh* function 59
2.10 Solution of the Poisson's equation on a Taiwan shaped mesh 63
2.11 Mesh and numerical solutions of the heat equation 65
2.12 Numerical simulation of flow in idealized 2D aneurysm model, stenosis model, bifurcation model, and bended tube model 69
2.13 Moving meshes in FreeFem++ 73
2.14 Numerical simulation of flow accelerated from rest by an oscillating circular cylinder 73
2.15 Comparison of the predicted and referenced solutions at $t = \frac{9}{2}T$ 74

2.16 Comparison of the computed and referenced solutions at $t = \frac{55}{12}T$ 74
2.17 Comparison of the computed and referenced solutions at $t = \frac{59}{12}T$ 75

3.1 Schematic of the computational domain 80
3.2 Illustration of the prescribed needle position and the corresponding generated meshes 82
3.3 The simulated velocity magnitude resulting from the needle motion in interstitial fluid 85
3.4 The simulated pressure profiles resulting from the needle motion in interstitial fluid 86
3.5 The simulated pressure profiles at different vertical locations 87
3.6 The simulated mean shear stress on the cell surface 88
3.7 The simulated pressure profiles resulting from the motion of a needle in interstitial fluid at acupoint 89
3.8 The α_f profiles given at the acupoint, close to the acupoint, and far from the acupoint 90
3.9 The simulated velocity and pressure profiles with an interstitial cell 92
3.10 Evolution of the pressure and the shear stress distributions along the cell surface 93

4.1 Stress function Φ in 1D 100
4.2 Convergence rates for the $\mathbb{P}_1$-$\mathbb{P}_2$ finite elements 118
4.3 Convergence rates for the $\mathbb{P}_2$-$\mathbb{P}_2$ finite elements 119
4.4 Convergence rates for the $\mathbb{P}_2$-$\mathbb{P}_3$ finite elements 119
4.5 Influence of the chemotactic sensitivity parameter S with a mesh size $\Delta x = 1/16$ 120
4.6 Influence of the chemotactic sensitivity parameter S with a mesh size $\Delta x = 1/64$ 120
4.7 Influence of the chemotactic sensitivity parameter S with a mesh size $\Delta x = 1/256$ 121
4.8 Gaussian spatial distribution of mastocytes in a bounded domain 123
4.9 Stress function Φ defined as a bump function 123
4.10 Needling at acupoint and non-acupoint 124
4.11 Needling outside an acupoint 125
4.12 Granulated mastocyte density dynamics 125

5.1 Boundary conditions for the the chemotaxis–diffusion–convection system 132

5.2 The computed rates of convergence for the coupled set of Navier-Stokes and Keller-Segel equations 137
5.3 Examples of convection cells for the chemotaxis–diffusion–convection, Rayleigh-Bénard convection, and double diffusive convection 138
5.4 Time evolution of the cell density 139
5.5 Time evolution of the cell density number at the surface 140
5.6 The stable and unstable regions of the dimensionless chemotaxis–diffusion–convection coupling system 143
5.7 Numerical results for the cell density with respect to the deterministic initial conditions 144
5.8 Numerical results for the cell density with respect to the deterministic initial conditions 145
5.9 Numerical results for the cell density with respect to the deterministic initial conditions 145
5.10 Numerical results for the cell density with respect to the deterministic initial conditions 146
5.11 Numerical results for the cell density with respect to the deterministic initial conditions 147
5.12 Numerical results for the cell density with respect to the deterministic initial conditions 147
5.13 Numerical results for the cell density with respect to the deterministic initial conditions 148
5.14 Numerical results for the cell density with respect to the deterministic initial conditions 148
5.15 Initial random condition and the corresponding numerical results for the cell density 149
5.16 Growth rate of plume amplitude 151
5.17 Numerical solution of the double diffusive system 153
5.18 Numerical solution of the Rayleigh-Bénard system 153

List of Tables

1.1 Scales and sizes in the hypodermis 35
1.2 Cells of the subcutaneous loose connective tissue 35
1.3 Vasoactive mediators 37
1.4 Neuroactive mediators 37
1.5 Autocrine mediators 38

3.1 Nomenclature and parameter dimensions 77

4.1 Nomenclature and parameter dimensions 95
4.2 Repartition of the mass in a Gaussian distribution in the full domain . . . 122

5.1 Nomenclature and parameter dimensions 129
5.2 Representative dimensionless numbers involved in the double diffusive convection, chemotaxis–diffusion–convection, and Rayleigh-Bénard convection 130
5.3 Phenomenological analysis based on time scales of the three competitive mechanisms: chemotaxis, diffusion, and convection of bacteria 142
5.4 The predicted number of plumes, wavenumber and wavelength for $\ell = 2$. 149
5.5 The predicted number of plumes, wavenumber and wavelength for $\ell = 3$. 150
5.6 The predicted number of plumes, wavenumber and wavelength for $\ell = 4$. 150
5.7 The predicted number of plumes, wavenumber and wavelength for $\ell = 5$. 150
5.8 The predicted growth rate of the plume amplitudes for two simulations subject to the random initial condition 152
5.9 Recapitulative of the physical mechanisms involved in the double diffusive convection, chemotaxis–diffusion–convection, and the Rayleigh-Bénard convection 154

List of FreeFem++ Scripts

2.1 Exemples of variable types, function declarations, and operators 49
2.2 Script to build a mesh of square domain plotted in figure 2.1. 50
2.3 Script to build the mesh of a rectangle domain plotted in figure 2.1. 51
2.4 Script to build the mesh plotted in figure 2.2. 52
2.5 Script to build 2d and 3d meshes from an image 52
2.6 Script to build a truncated mesh. An exemple is plotted in figure 2.5. . . . 54
2.7 Script to add two meshes to form a single mesh 55
2.8 Script to split mesh triangles with *splitmesh*. 57
2.9 Script to adapt a mesh with the function *adaptmesh*. 57
2.10 Mesh manipulation with the *movemesh* function 59
2.11 Declaration of finite element spaces. 60
2.12 Declaration of finite element functions in the space V_h. 60
2.13 Solving the Poisson's equation in 2d with the keyword *solve*. 61
2.14 Solving the Poisson's equation in 2d with the keyword *problem*. 62
2.15 Solving the Poisson's equation in 2d with the keyword *varf*. 62
2.16 Solving the heat equation in FreeFem++ 64
2.17 Solving the incompressible Navier-Stokes equations 67
2.18 Solving the incompressible Navier-Stokes equations in a moving domain with the ALE method 72

Notations

References
A number in brackets, example (1.2), refers to the equation (2) of chapter 1. The numbers in square brackets like [1] indicate a reference in the bibliography. Figures and parts of figures use numerals and labels enclosed in parentheses, respectively. For exemple, figure 4.12 refers to the figure 12 of chapter 4 and figure 5.3 (a) refers to subfigure (a) of figure 3 of chapter 5. Tables and scripts use numerals, for exemple table 3.1 refers to table 1 of chapter 3 and script 2.16 refers to script 16 of chapter 2.

Differential operators
The classical grad, div, and laplacian operators are denoted respectively as

$$\nabla c, \quad \nabla \cdot u, \quad \nabla^2 u.$$

Geometry of the domains
The domain of a PDE is in general denoted by Ω, which is a bounded open set in $\mathbb{R}^d$ ($d = 2, 3$), it's volume element by dx and its boundary by $\partial\Omega$ or Γ. The domain is sufficiently regular to define an outward normal unit vector $\mathbf{n}(x)$ for almost all x of the boundary $\partial\Omega$. Domains with corners are also admitted. $|\Omega|$ denotes the area of Ω.

Function spaces
$\mathcal{C}^0(\Omega)$ is the space of continuous functions on Ω

$L^1(\Omega)$ is the space of integrable functions on Ω.

$L^1_+(\Omega)$ is the space of nonnegative integrable functions on Ω.

$L^2(\Omega)$ is the space of square integrable functions on Ω.

$H^1(\Omega)$ is the Sobolev space of order 1.

$H^1_0(\Omega)$ is the space of $H^1(\Omega)$ functions with zero trace on $\partial\Omega$.

Introduction

Contents

0.1 Acupuncture 23

0.1.1 History of acupuncture 24

0.1.2 Traditional theory behind acupuncture 25

0.2 Underlying acupuncture mechanisms 28

0.3 Contribution of this thesis 30

This thesis aims at modeling and simulating transport processes of physical and chemical signals during acupuncture. It is divided into five chapters, grouped into three parts. Each chapter contains an introduction to the topic which will be examined and provides relevant references.

The two main objectives of this work are (i) to understand the biomechanics of acupuncture needling; more specifically, understand how the pressure and stress field affect the network of fibers and cells of subcutaneous tissues during the manipulation of an acupuncture needle; and (ii) to understand the response of mastocytes and the transmission of information to the vascular and nervous systems.

0.1 Acupuncture

Although an extensive portrayal of thousands of years of acupuncture theory and practice is beyond the scope of this thesis, a brief description is useful for the discussion of modeling and simulation in acupuncture. For more details, readers can refer to Cheng [2] for example.

0.1.1 History of acupuncture

This section is the fruit of an exchange with Dr Gilles Cury, general secretary of the "Association Française d'Acupuncture[1]" (`http://acupuncture-france.com/`. Accessed January 26, 2015.).

Acupuncture and moxibustion are two age-old medical techniques of Traditional Chinese medicine. Their names come from the Chinese words "*zhen jiu*" meaning needle and moxibustion, respectively. The name acupuncture takes its form from the Latin words "*acus*", meaning needle, and "*puncture*". Acupuncture is in fact a therapeutic practice based on inserting needles into the skin at acupoints. The name moxibustion is formed from the word "*moxa*" and "*combustion*". Moxibustion is a therapeutic practice of burning moxa sticks next to the skin to stimulate acupoints.

Acupuncture and moxibustion practices date back more than 3000 years. Acupuncture has been practiced in Asia for at least 2500 years. In China, written texts and graphics related to acupuncture and moxibustion date back over 2000 years [3]. The foundation of acupuncture lays in Taoist principles. The "*Huáng Dì Nèi Jīng*" (黃帝內經), translated "The Yellow Emperor's Classic of Medicine", one of the first known documentations of Chinese medicine, has been accepted as one of the fundamental doctrinal sources of Chinese medicine.

Traditional Chinese medicine was brought to Europe, notably to France, at the end of the 17th century. The Jesuits, among which the Belgian Philippe Couplet, were the first to provide documents in French about Chinese medicine. In 1805, the manual "De l'acupuncture", written by Dr. Félix Vicq d'Azir, was published in France. Afterwards, experimentation started, especially by doctors Louis Berlioz and Jules Cloquet. There was a growing interest in acupuncture at the end of the 19th century. During this period, enthusiasm for China reached the arts and sciences because of its mysteries and wonders.

It was not until recent years that acupuncture gained wider attention in America and Europe. In France, acupuncture really began in the 1930's with George Soulié-de-Morant, the French consul in Kunming, China. Upon his return to France in 1929, thanks to his knowledge of the Chinese language, he published, together with Dr. Ferreyrolles, an article entitled "l'acupuncture en Chine vingt siècles avant JC et réfléxothérapie moderne" in the journal "l'homéopathie française". Later, in 1934, he published "L'acupuncture chinoise", a work of several volumes achieved in the 1950's, that served for the teaching of acupuncturists in France. The museum "Musée de la médecine traditionelle chinoise en occident" directed by professor Ting Hor in Kunming, in the Yunnan province of China, is dedicated to George Soulié-de-Morant for his great role in introducing acupuncture in the West. In 1971, Reston Reston [4], a journalist covering President Nixon's trip to China, developed appendicitis and wrote a long article that drew attention in the United States on how acupuncture treatments helped relieve his pain.

[1] French Association of Acupuncture.

The popularity of acupuncture practices has now attracted mainstream medical attention and acupuncture has become the subject of scientific investigation [5]. Today in France, the number of acupuncturists is estimated at 2000. Although a diploma of capacity in acupuncture is required to practice (3 years after being qualified as Medical Doctor), the acupuncture specialty has not been recognized yet. Only four universities in Paris, Nantes, Strasbourg and Montpellier-Nîmes provide the diploma in acupuncture. In obstetrics, an inter-university degree is open to obstetricians and midwives.

Acupuncture treatments are reimbursed by the French medical care system within strict provisions. Accreditation of France (La Haute Autorité de Santé) has limited acupuncture treatments to alternative treatments to chemotherapy, analgesic treatment, treatment for depression and anxiety, and treatment for alcohol and tobacco withdrawal. However, acupuncture can treat a wider range of symptoms.

Several research projects dedicated to acupuncture are currently being carried out in France and acupuncture is increasingly recognized by professionals and administration. Acupuncture and moxibustion practices were recognized in 2010 by UNESCO and inscribed on the Representative List of the Intangible Cultural Heritage of Humanity. They have also been endorsed by the American National Institutes of Health, the National Health Service of the United Kingdom and the World Health Organization. Today, Taiwan remains one of the most important places for the practice of traditional acupuncture.

0.1.2 Traditional theory behind acupuncture

The foundation of Chinese acupuncture has a basis in Taoist principles. In acupuncture, the internal organs are assumed to be interconnected with one another by a system of complex channels called “meridians”. The meridians are pathways in which the vital energy *qì* (chinese: 氣) flows throughout the body. The flow of *qì* regulates bodily health and reflects illness. Acupuncture needling is used to treat and prevent many diseases. In fact, all symptoms can be treated with acupuncture. Hair-thin needles are used to stimulate specific points on the body, acupoints (chinese: *xuè*, 穴), in order to balance *yīn* (chinese: 陰) and *yáng* (chinese: 陽) by removing blocks in the flow of *qì* [2]. During the needle insertion and manipulation process, *dé qì* (chinese: 得氣) sensation is experienced when the needle has been placed at a proper location.

> *"* Yáng *and* yīn *are 2 fundamental opposing, complementary, and interdependent forces found in all things in the universe, with traces of one in the other, that support each other and can transform into one another. Nothing in the universe is completely* yīn *or* yáng*; everything is a mixture of the two. In particular,* yáng *may be considered as mental activity in its strength aspect,* yīn *mental activity in its imaginative aspect; in other words,* yáng *constructs, yīn instructs, or conversely.* Yīn *is related to static and hypoactive phenomena,* yáng *to dynamic and hyperactive processes, or conversely. "* [6]

Qì, blood, and body fluids are the fundamental substances which maintain the normal vital activities of the body. *Qì* refers to both the essential substances of the human body and the functional activities of the organs and tissues. All the vital activities of the body are explained by the change and movement of *qì*. Blood circulates throughout the organs, the skin, muscles, tendons and bones. Blood nourishes and moistens various tissues and organs from the inside. Body fluid is the collective term for all the normal fluids of the body : saliva, gastric juice, tears, sweat, urine. Body fluids nourish various parts of the body. Together they are the material foundation for the physiological functions of the *zàng-fǔ* (chinese: 臟腑) organs, tissues and meridians. Their close and complex relationships manifest in physiology and are important in determining the treatment [2].

> *"When the liver receives blood, it gives rise to vision ; when the feet receive blood, they are capable of walking ; when the palms receive blood, they are capable of holding ; and when the fingers receive blood, they are capable of grasping."* [2]

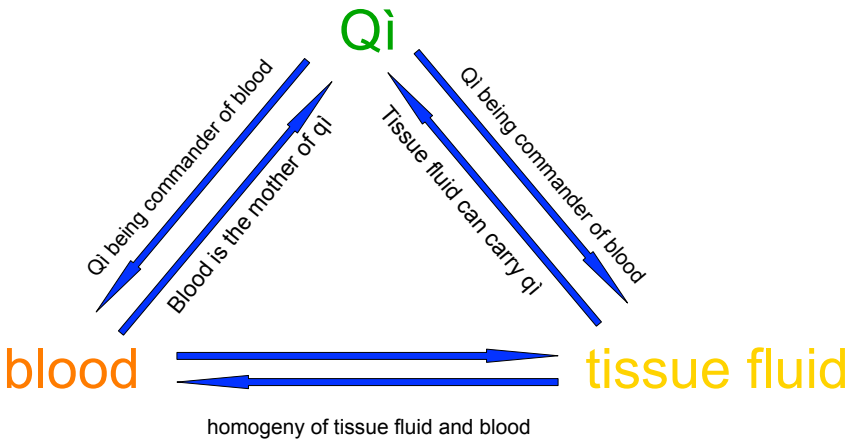

Figure 1: Foundation in traditional Chinese medicine: A *qì*-blood-tissue fluid triple coupling circulation system.

The meridians (chinese: *jīng*, 經) and collaterals (chinese: *luò*, 絡) are pathways along which the *qì* and blood flow (see figure 2). They are connected to the *zàng-fǔ* organs internally and extend over the body externally, thereby forming a network and linking tissues and organs into a whole [2]. Acupoints are distributed mostly along the major meridians and collaterals. There are around 400 acupoints scattered throughout the body. Each acupoint is either related to a *zàng* or a *fǔ* organ (see figure 3).

The system of *zàng* organs includes the Heart, the Lung, the Spleen, the Liver and the Kidney. They manufacture and store essential substances, *qì*, blood, and body fluid

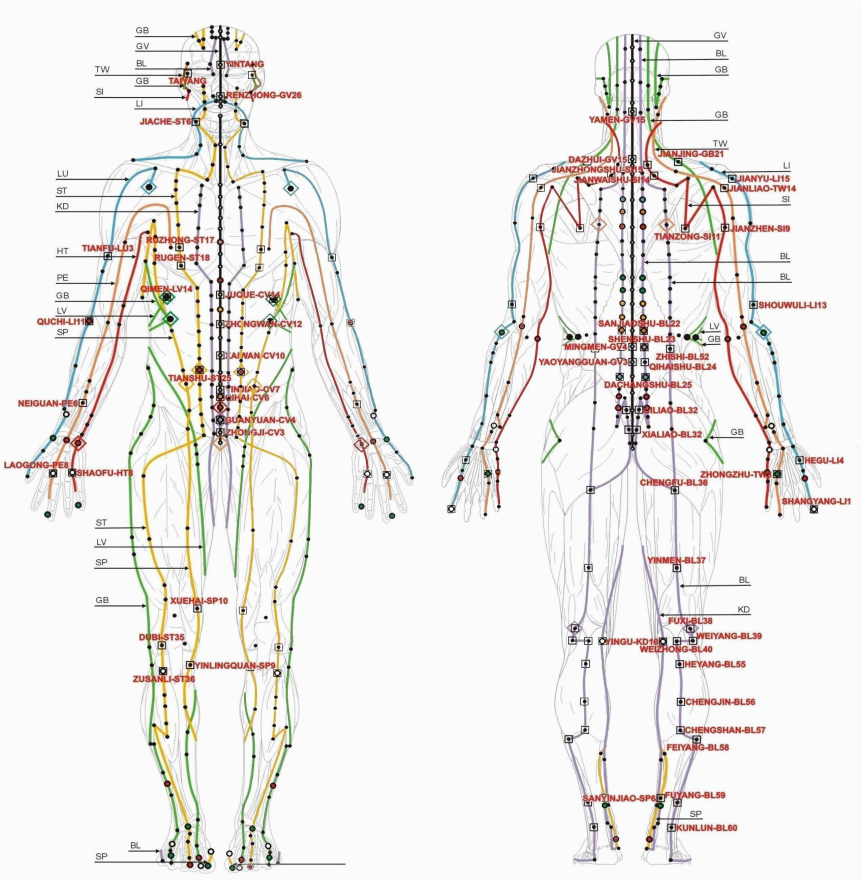

Figure 2: Meridians and acupuncture points in traditional Chinese medicine. / (Image modified from KVDP, 2010. Chinese meridians. Licensed under public domain via Wikimedia Commons. `https://commons.wikimedia.org/wiki/File:Chinese_meridians.JPG`)

[2]. The system of *fŭ* organs includes the Gall Bladder, the Stomach, the Small Intestine, the Bladder and the Triple Heater. They receive and digest food ; transmit and excrete wastes [2]. The *zàng-fŭ* are not equivalent to the anatomical organs and their names are capitalized in the text.

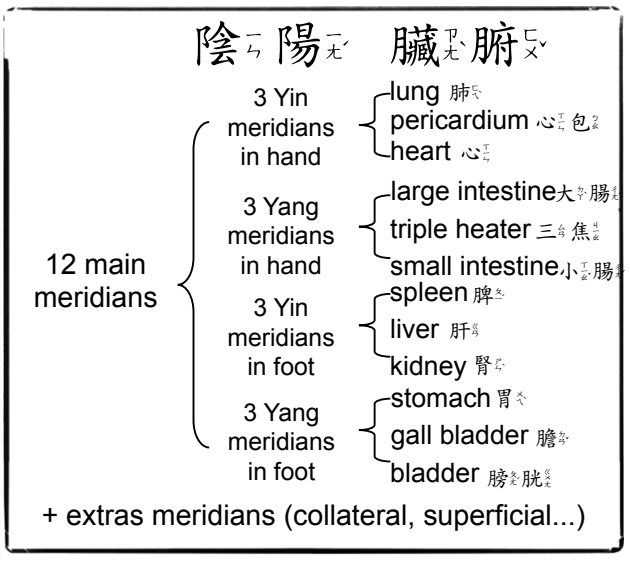

Figure 3: Correspondence between the meridians, *zàng-fǔ* organs and the *yīn* and the *yáng* in traditional Chinese medicine.

0.2 Underlying acupuncture mechanisms

Acupuncture is a minimally invasive procedure. It involves a penetration of the skin with hair thin needles to stimulate acupoints in order to restore the balance and flow of *qì* through meridians. There is a great demand for explanations regarding the basic concepts such as *qì*, meridians, and acupuncture points. The absence of scientific background of the acupuncture biochemical mechanisms has motivated us to carry out modeling and numerical simulation of both macroscopic and microscopic aspects of the acupuncture process.

The anatomical and physiological natures of acupoints and meridians are not yet well understood [7]. Still, the effects of acupuncture can be explained by interactions among the nervous, circulatory, endocrine, and immune systems. Recent investigations have shown evidence that meridians and acupuncture points are correlated with subcutaneous loose connective tissue [8]. The subcutaneous connective tissue is composed of cells embedded in the extracellular matrix mainly constituted by collagen and elastic fibers in a gel of glycoproteins and proteoglycans. Mastocytes play a major role in acupuncture. They are scattered throughout tissue, yet their density is higher near acupoints [9].

The insertion of thin needles into the skin is the most common technique. The needles are then manually manipulated at acupoints. Acupoints are located near bones, aponeuroses [2], muscles, and tendons that contain neural units with somatosensory receptors.

[2] An aponeurosis is a sheet of pearly white fibrous tissue which takes the place of a tendon in sheet-like muscles having a wide area of attachment.

Acupoints are characterized to have a large density of mastocytes. This pool of mastocytes resides close to neurovascular bundles, in regions where capillaries, lymphatic vessels, and nervous structures abound. Other features of acupoints include larger skin electrical conductance and higher ionic concentrations [10].

During acupuncture needling, mechanical stimuli result from the local deformation of the connective tissue imposed by a sequence of needle motions. This stress field is sensed by the local population of mastocytes that react by degranulation. Other cells, such as neurons, macrophages, fibroblasts, and lymphocytes can contribute to the emission of local and endocrine signals.

Nerve endings are stimulated and can release substances that further activate mastocytes. A self-sustained process is created via the recruitment of circulating mastocytes and excitation of regional pools of mastocytes. This traditional Chinese medicine procedure relies on signaling aimed at triggering mastocyte chemotaxis and sending messages via released molecules. Released molecules include vaso- and neuroactive messengers, the latter targeting the central nervous system via both nervous transmission and blood convection. Targeted nervous regions then respond by regulating the behavior of peripheral organs.

Taxis refers to the collective motion of cells or an organism in response to an attractant gradient. The nature of the attractant stimulus can be of chemical (chemotaxis), physical (baro-, electro-, magneto-, phono-, photo-, and thermotaxis), or mechanical (hapto- and rheotaxis) origins. Chemotaxis refers to cell movement primed by an external chemical signal that can either be emitted by the same population of cells or created by an external source [11].

In this scenario, a meridian can be assumed to be a neurovascular signaling tract. A compartmental model can then be designed (see figure 4). Compartment 1 is related to the signal transmission of external stimuli via mechano-, electro-, thermo, phototransduction. Compartment 2 is the acupoint region with three components: (1) mastocytes, (2) blood and lymph vessels, and (3) nerves. Chemoattractants increase the mastocyte population by recruiting the nearby mastocytes; autocrine signals intensify a self-sustained response. Compartment 3 is related to signal transmission to the central nervous system, either very rapidly via nervous impulses, or delayed via messenger convection through the blood circulation. A feedforward loop associated with elevated cardiac function enables an increased blood flow for a relevant material transport. Compartment 4 deals with signal processing with a quick and late response corresponding to a fast and delayed input. Compartment 4 represents outputs sent from the central nervous system and the body's response.

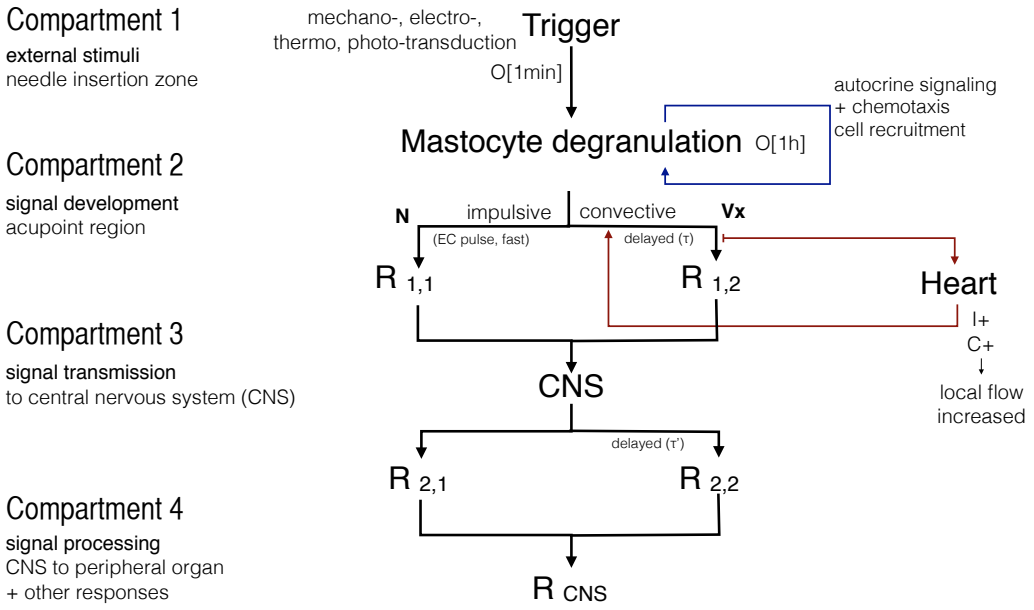

Figure 4: Meridian compartment model

0.3 Contribution of this thesis

This thesis makes contributions to the fields of mathematical modeling in medicine and life sciences.

In chapter 1, the mechanism of acupuncture is introduced. This first chapter is purely bibliographical and describes the physiological basis of acupuncture as well as the current research in acupuncture. During a traditional acupuncture treatment, a needle is inserted into the skin and the tip of the needle reaches the subcuteaneous tissue, namely, the hypodermis. Cells of the immune system such as mastocytes are stressed by the needle manipulation. In turn, chemical messengers, released by the mastocytes, participate in the biochemical response of acupuncture. Nerve messengers stimulate nerve endings to send quick information to the central nervous system. Endocrine messengers produce a slower response targeting the heart and the brain. Chemoattractants play an important role to sustain and strengthen the process by recruiting neighboring mastocytes.

Chapter 2 introduces the finite element software FreeFem++ used in this work. FreeFem++ is a finite element software with an interpreted language used to solve partial differential equations using the finite element method. Construction and manipulation of the mesh of the geometry, discretization of the weak form, and visualization of the solutions are done within a single framework.

Chapter 3 contains a biomechanical model of the interaction of an acupuncture needle with the interstitial fluid of the hypodermis. Acupuncture can be assumed to be based on

the chemical response of mastocytes and other cells at acupoints to the sensed mechanical stresses caused by the needle motion.

The extracellular matrix forms a fibrous media in which interstitial fluid can flow. The interstitial fluid flow is modeled as a Brinkman's flow in a fibrous media deformed by a moving needle. The model equations are solved with an arbitrary Lagrangian–Eulerian (ALE) finite element scheme. The numerical results reinforce the hypothesis that the mechanical stimuli are localized and acute at the acupoint. The change in the fluid pressure and shear stress field can be sensed by local pools of mastocytes and activate a mechanotransduction process.

Chapter 4 presents a novel mathematical model of the chemotactic response of mastocytes to the physical stress. Mastocytes are presumed to play a major role in acupuncture. The physical stress field, described in chapter 3, is sensed by the local population of mastocytes which in turn degranulate. A self-sustained process is created via recruitment of the circulating mastocytes and excitation of regional pools of mastocytes.

Emphasis is put into the model of mastocyte response to acupuncture needling and is based on the Keller-Segel model for chemotaxis. The effect of physical stress is assumed to be a forcing term in the model. The mathematical analysis focuses on the simple leading situation dominated by the granulated mastocytes and the chemoattractant. This reduced model is of the nonlinear degenerate parabolic type. It is shown that the solution is positive and that it blows up in the sense that a weighted L1 norm does not stay positive if the forcing term times the initial condition is large. The blow-up is interpreted as a hyper reactivity at the acupoint where a large quantity of mastocytes are present. Conversely if the forcing term times the initial condition is not large, the solution to the coupled nonlinear partial differential equations exists. In this case, the action of acupuncture is considered ineffective. The theoretical results serve as a validation of numerical experiments. Numerical simulations show that when the needle is positioned in the periphery of the acupoint or outside it, the response is too weak. The acupoint must contain a highly concentrated population of mastocytes to get a proper initial response. Permanent signaling is provided by chemotaxis and continuous recruitment of mastocytes.

Chapter 5 describes the coupling of chemotaxis and fluid flow. Although, this chapter does not directly focus on acupuncture but gives insight into the interaction between the chemotaxis of cells with an incompressible fluid when the external force is gravity. The chemotaxis–diffusion–convection coupling system is presented in the particular case of suspensions of swimming microorganisms which are denser than the fluid in which they are immersed in. The system describes a form of buoyant convection in which the fluid develops convection cells and plume patterns. The numerical results indicate that the chemotaxis can stabilize the overall chemotaxis/fluid system when the chemotaxis head and sensitivity is large.

In addition, a comparison of the differential system of chemotaxis–diffusion–convection, double diffusive convection, and Rayleigh-Bénard convection is established. A set of evidences shows that even if the physical mechanisms are different, the dimensionless

systems are strongly related to each other.

As a conclusion, some directions for future research are pointed out.

Chapter 1

Literature survey of acupuncture study

Contents

1.1 Introduction 34

1.1.1 Subcutaneous connective tissue 34

1.1.2 Mastocytes 35

1.2 Underlying acupuncture mechanisms 36

1.2.1 Stimulation of acupoints 36

1.2.2 Biochemical signaling at acupoints 41

1.3 Modeling in acupuncture 43

1.3.1 Electroosmotic meridian model 43

1.3.2 Interstitial flow in acupuncture 44

1.3.3 Mastocyte dynamics of degranulation 45

1.4 Concluding remarks 46

Abstract

The aim of this chapter is to provide the fundamental basis for the modeling and simulation presented in this study. The content of this chapter is purely bibliographical and summarizes the physiology of tissues involved in acupuncture, details of current research in acupuncture, and previous mathematical models in acupuncture.

1.1 Introduction

This section provides the physiological basis of the different components involved in the mechanism of acupuncture.

1.1.1 Subcutaneous connective tissue

The skin consists of three layers of tissue known as the epidermis, dermis, and hypodermis. The hypodermis is the subcutaneous connective tissue that provides (1) structural and mechanical support, (2) transport of nutrients, metabolites and waste between the blood and tissues, (3) storage of energy, (4) immunological defense. For a complete description of the extracellular matrix one can refer to [12, 13]. The hypodermis is a loose connective tissue that lies above skeletal muscles and forms a continuous body-wide network including subcutaneous and interstitial connective tissues surrounding all muscles, organs, nerves, blood vessels, and lymphatic system [14]. Like other types of connective tissues, the loose connective tissue is made of scattered cells immersed in the extracellular matrix and contains an abundant ground substance and relatively sparse fibers.

The extracellular matrix is a key participant in mechanotransduction[1], or mechanisms allowing cells to perceive and interpret mechanical forces. The extracellular matrix skeleton is made of collagen and elastin fibers. Collagen fibers ensure progressive resistance to deformation and, hence, have low extensibility [15]. The collagen molecules are crosslinked to form the collagen fibers. Collagen fibers of type III and I are mainly found in the connective tissues [12]. Type I is a tensile fiber, usually forming wavy bundles, which does not ramify and is associated with the resistance and rupture of the connective tissue [12, 16]. Elastic fibers, thinner than collagen fibers, enable strain and tissue resilience, the energy being reinstated upon stress removal [15]. The tissue is structured in multiple layers of thin collagen sheets loosely interconnected by elastin fibers to limit distension and prevent tearing [17].

The ground substance is a non-cellular component occupying the space between cells and fibers. The ground substance consists of water, proteoglycans, glycoproteins, and other macromolecules, thereby forming a viscous hydrated gel that can stabilize fiber network or can undergo fluidization under stress [18]. Proteoglycans control the level of hydration of connective tissues, and thus partially determine the physical properties of connective tissues [12]. The aqueous phase of the ground substance is the essential medium between cells and bloods through which all nutrients and wastes must pass [19].

The connective tissue has three scales of heterogeneity :

- mesoscopic scale (0.01 to 1 mm) : dividing the connective tissue into different compartments

[1] Mechanotransduction refers to the various mechanisms by which cells convert mechanical stimuli into biochemical activity.

- microscopic scale (1 to 10 μm) : description of each compartment (collagen, elastin,...)
- nanoscopic scale (< 1 μm) : cellular structure

The size and scale of each component of the extracellular matrix are listed in table 1.1.

	diameter	references
epidermis	10 - 100 μm	[20]
dermis	1000 - 3000 μm	[20]
hypodermis	1000 - 10000 μm	[20]
collagen fiber (type I)	1 - 20 μm	[12, 16, 20]
elastin fiber	0.1 - 1 μm	[12, 16, 20]
Mastocyte	2 - 12 μm	[21]
acupuncture needle	100 - 300 μm	

Table 1.1: Scales and sizes in the hypodermis

1.1.2 Mastocytes

1.1.2.1 Loose connective tissue cells

Cell types of connective tissue include both resident cells (e.g., fibroblasts, mastocytes, and macrophages) and immigrant cells (e.g., monocytes, lymphocytes, and granulocytes) (see table 1.1.2.1). Fibroblasts, which are matrix-secreting cells, account for 70-80% of the cells [22]. The wandering cells of connective tissue are involved mainly in immune defense and inflammation. Macrophages are large phagocytic cells found in stationary form in the tissues or as mobile cells that are found especially at sites of infection. Mastocytes are found in numbers in connective tissue. They contain granules storing chemical mediators. Mastocytes are able to release their granule contents within minutes for intra-, auto-, juxta-, paracrine signaling and to resynthesize their content.

Resident cells	Immigrant cells
Fibroblasts	Lymphocytes
Fibrocytes	Granulocytes
Adipocytes	Monocytes
Macrophages	Mastocytes
Mastocytes	Macrophages

Table 1.2: Cells of the subcutaneous loose connective tissue

1.1.2.2 Mastocytes

Mastocytes of the connective tissue are believed to play an important role in acupuncture [9]. Mastocytes are tissue-resident sentinels of the immune system. In particular, they are found in tissues close to the external environment [23]. Mastocytes are well known for their role in the inflammatory process where they accumulate at the site of inflammation in response to a chemical mediator [24]. However, they also appear to have a protective role [25]. Mastocytes contain granules storing inflammatory mediators, including histamine, serotonin, and chemotactic factors, in particular for eosinophils and neutrophils [12]. Mastocytes are scattered throughout the connective tissues of the body especially neurovascular bundles.

1.1.2.3 Released chemical mediators from mastocytes

Mastocytes contain granules storing chemical mediators. They release the content of their granules into the surrounding tissues by exocytosis[2] within minutes.

The cytoplasmic granules include stimulants that aim at triggering action potential to nearby nerve endings, that can lead for example to liberate opioids and analgesic in the brain [27] (see table 1.4). Some stimulants increase the blood vessel lumen as well as its permeability and increase blood flow rate after reaching the heart [28, 29] (see table 1.3). Mastocytes also release chemoattractants that participate in cell recruiting (see table 1.5).

1.2 Underlying acupuncture mechanisms

This section describes the underlying basis of acupuncture needling involving signal transduction through the connective tissues together with the immune system, the endocrine system and the nervous system to explain how the signals are transported from acupoints to close and distant tissues and organs of the body.

1.2.1 Stimulation of acupoints

Whatever the technique chosen to stimulate the acupoint, physical stimuli are sent to the subcutaneous connective tissue. In turn, mastocytes rapidly release vesicles containing chemical mediators that participate in biochemical responses that induce the acupuncture effects.

[2] process by which the contents of a cell vesicle are released to the exterior through fusion of the vesicle membrane with the cell membrane [26].

Table 1.3: Vasoactive mediators

Effect	Mediators
Vasodilation	Histamine [30]
	Histamine + NO [31]
	Serotonin [32]
	Substance-P + NO [32]
	CGPR [33]
	$LktC_4$, $LktD_4$, $LktE_4$ [12]
	PGE_2 [34, 35]
Vascular permeability	$LktB_4$, $LktC_4$, $LktD_4$ [12]
Vasoconstriction	Serotonin [32]
	TXA_2 [12, 36]
Anticoagulant	Heparin [12]
Positive chronotropy	CGRP [37]
	PGE_2 [34, 35]
Positive inotropy	CGRP + NO [38, 39, 39]
	PGE_2 [34, 35]

Table 1.4: Neuroactive mediators

Nerve ending stimulation	Histamine [23]
	PGD_2
	LktC

Table 1.5: Autocrine mediators

Chemotaxis for mastocytes	IL [40] TNFα [41] Tryptase [42] NGF [43]
Mastocyte degranulation and secretion	Substance-P [44] CGRP [45]

1.2.1.1 Acupoints

At the present moment, the anatomy and physiology of acupoints are not clearly defined but recent studies have revealed some of their specific properties. Acupoints are mainly located in the loose connective tissue not far from bones, aponeuroses, muscles, and/or tendons and close to dense neurovascular bundles [46]. Acupoints differentiate from nonacupoint locations by displaying high density of mastocytes [9], high density of capillaries [47], high collagen concentration [48], high skin electrical conductance [49, 50] and high ionic concentrations (K^+, Ca^{2+}, Fe^{2+}, Mn^{2+}, Zn^{2+}, PO_4^{3-}). Free nerve endings, cutaneous receptors, sarcous sensory receptors (muscle spindles and tendon organs), and their afferent fibers, as well as somatic efferent fibers innervating muscles, small nerve bundles, and plexi are observed in acupoints [51].

1.2.1.2 Needle and collagen fiber deformation

The needle is inserted in the hypodermis. After a short term of needle manipulation, the needle is retained about 20 minutes with possible restimulation at the acupoint. When the desired effect has been achieved, the needle is removed from the acupoint.

The mechanical signal induced by the needle manipulation causes the collagen fibers to wrap around the needle body [8]. When the needle is coupled to tissues, needle manipulation engenders the deformation of the extracellular matrix. The reorganization of the extracellular matrix affects the interstitial pressure and flow producing mechanical stimuli that are perceived by the mechanosensitive proteins on the surface of cells [52]. Mastocytes react to the mechanical stimulus and calcium signaling. There is ample evidence that activation and degranulation of mastocytes are increased with shear stress [53] and heating during moxibustion as well [54]. Mathematical models have been established for the dynamics of mastocyte degranulation with calcium signaling induced by laser irradiation [55] and induced by shear stress [53]. *Dé qì* sensation could be a response to the

wrapping of connective tissues around the needle body [52].

1.2.1.3 Extracellular matrix and mastocyte interaction

Mastocytes are scattered throughout the connective tissues of the body especially beneath the skin near blood and lymphatic vessels and within nerves. Experimentation showed that needle manipulation in acupuncture causes degranulation of mastocytes to occur [9, 48]. In particular, inhibition of mastocyte degranulation annihilates the analgesic effect of acupuncture [9].

There is an evidence that the shear and pressure stresses from the winding of connective tissues with the needle are transmitted to the extracellular matrix of the subcutaneous connective tissue and lead to the excitation of receptors on the mastocyte membrane [48]. In turn, there are several signaling pathways associated with a rapid entry of calcium (Ca^{2+}) waves in the mastocyte cytosol leading to mastocyte degranulation. The mastocytes release, within minutes after activation, numerous chemoattractants, neural stimulants, and endocrine mediators that are diffused in the tissue and interplay with blood vessels and nerve endings, thereby causing a cascade of biological effects and resulting in the alteration of systems, tissues and organs (see figure 1.1).

1.2.1.4 Other acupuncture treatments

The same acupoint can be stimulated by acupressure, moxibustion, electroacupunture and, more recently, by laser acupuncture. Acupressure, or needleless acupuncture, stimulates the acupoints by applying finger pressure near these points that in turn creates a local mechanical stress. Electroacupuncture (or percutaneous electrical nerve stimulation) [56] creates a local electrical field by applying a small electric current between a pair of acupuncture needles at acupoints. Laser acupuncture [57] is an optical method used to stimulate acupoints with laser irradiation. Laser acupuncture does not seem to work via physical processes such as excitation with an electromagnetic wave and heating. Laser acupuncture seems to trigger phototransduction pathways. Moxibustion is a popular alternative therapy that involves burning a mugwort stick (or moxa candle) and moving it back and forth above a short meridian segment centered at a given acupoint. To reduce the risk of burns, indirect moxibustion using both needles and ignited moxa is currently more popular. This practice involves inserting a needle into an acupoint. The tip of the needle is then ignited to supply heat flux to the acupoint and surrounding area. To sum up, mastocytes can be activated by a mechanical stress field (mechanotransduction), heating (thermotransduction), electrical field (electrotransduction), or an electromagnetic wave (phototransduction).

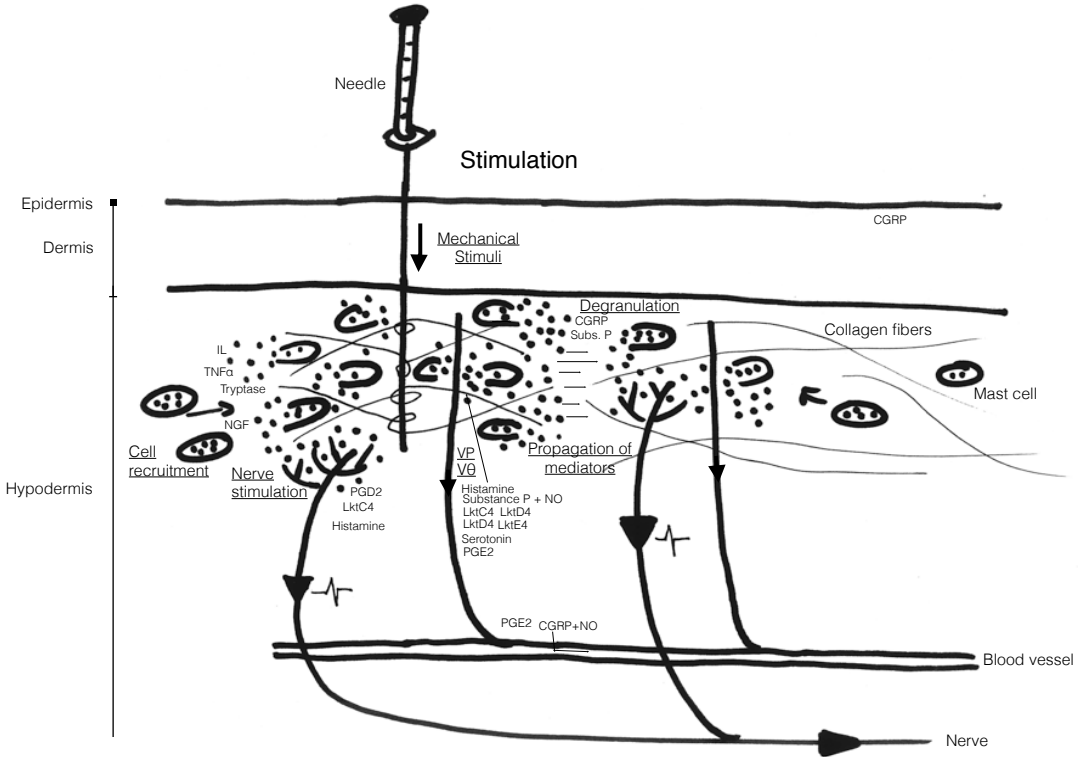

Figure 1.1: Locoregional activation of mastocytes. Acupuncture needling sends mechanical stimuli capable of activating mastocytes in acupoints, causing their degranulation via mechanotransduction.

1.2.2 Biochemical signaling at acupoints

In response to external stimuli, mastocytes rapidly release vesicles containing chemical mediators (see tables 1.3, 1.4, and 1.5). These chemical messengers can be grouped intp three major groups: nerve messengers, endocrine messengers and chemoattractants (see figure 1.2).

1.2.2.1 Nerve messengers

The release of a nerve messengers immediately (O[s- mn]) affects the excitability of the nerve endings triggering fast short-lived action potentials [6]. Secretion of neuropeptides, like substance-P and CGRP, released from mastocytes could stimulate nerve endings sending neural signals from the acupoint site along the respective fibers to the given local regions of the central nervous system. This process is responsible for hyperemia and regulates the secretion of neurotransmitters (substance-P) and analgesic substances such as endocannabinoids, enkephalins, endomorphins, dynorphins [27, 58]. Nerve endings release substance-P that further activates mastocytes and triggers the production of nitric oxide. Nitric oxide levels decrease in the central nervous system and increase in the plasma and organs [58]. This interaction corresponds to an impulsive (fast) response to acupuncture.

1.2.2.2 Endocrine messengers

The release of endocrine messengers and vasoactive mediators participates in the increase of blood vessel lumen size (vasodilation) and wall permeability as well as cardiac function, thus increasing the local blood flow and enhancing the exchanges of chemical mediators to the brain [28, 29]. NO together with other chemicals mediators is known to affect the local blood circulation increasing the blood flow [59]. Some of the vasoactive mediators have a positive chronotropic effect on the heart rate and inotropic effect on the heart contractions that can maintain blood pressure. Vasoactive mediators, like leukotrienes, increase blood vessel permeability allowing the flow of chemical mediators or cells to the blood. These chemical signals are transported in the blood throughout the central nervous system, tissues and organs. They are however preferentially conveyed to the previously activated and highly perfused region of the central nervous system. Neurons from this region can then receive sets of action potentials for a long period of time and respond by regulating the behavior of the appropriate peripheral organs. This interaction corresponds to a delayed (slow) response to acupuncture.

1.2.2.3 Chemoattractants

The effective action time of chemical mediators is short due to the presence of degrading enzymes. For this reason, a high and continuous secretion of messengers is ensured

by mastocyte recruitment through chemotaxis. Following chemotaxis, newly arrived mastocytes at acupoints experience a degranulation triggered by the stress field. The arrival of new mastocyte pools from nearby capillaries and regional mastocyte populations ensures a continuous flux of activators. Simultaneously, the already degranulated mastocytes at acupoints resynthesize chemical messengers. The regeneration of granules is slow (O[mn- h]). The resulting self-sustained process enhances the exchange of messengers with nerve endings, enables the local elevation of vascular permeability for the increase of cardiac output, and enhances vasodilation associated with a resulting increase in blood flow. It also supports endocrine signaling to the central nervous system and especially neurons situated in a brain region characterized by hyperemia. This process corresponds to a permanent response to acupuncture.

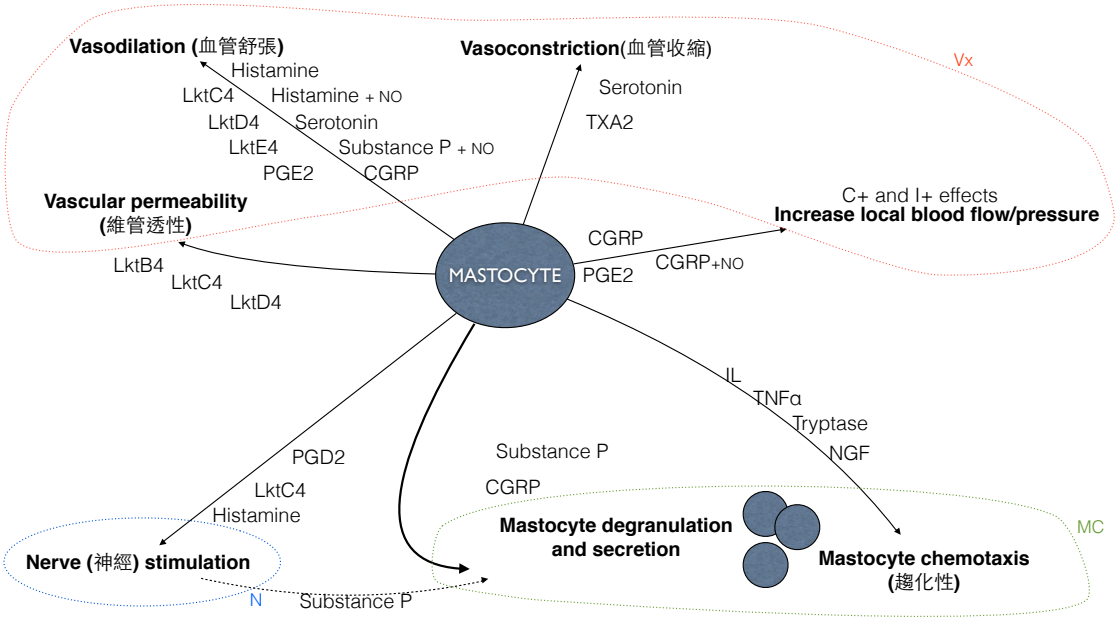

Figure 1.2: Chemical messengers released by mastocytes upon stimulation can be grouped into three major groups: nerve messengers (N), endocrine messengers (Vx) and chemoattractants (MC).

In summary, the classical method of acupuncture relies on the following set of events: (1) generation of a local stress field caused by the needle manipulation; (2) mechanotransduction of sensed local tension into chemical signals, i.e., increase in cytosolic Ca^{2+} concentration, granule exocytosis, and substance release; (3) triggering of action potentials (early, quick response) by nerve stimulants bound to cognate receptors on local nerve terminals and activation of the target brain region that is associated with a local functional hyperemia (local increase in blood flow due to nervous activity); (4) chemotaxis of neighboring mastocytes and degranulation of newly arrived mastocytes at acupoints that enables a sustained process, degranulation being effective only near the needle, where the

mechanical stress is large enough; (5) local elevation of vascular permeability and vasodilation, induced by released compounds, together with increased local blood flow, induced by targeted cardiotonic messengers, enhanced endocrine signaling, i.e., delayed, permanent stimulation of the target brain region, as endocrine messengers are preferentially distributed in active brain regions.

1.3 Modeling in acupuncture

While acupuncture and moxibustion have been safely used for centuries, the reason why moxibustion can strengthen the flow of blood, stimulate the flow of *qì*, and maintain health remains barely understood by scientists. Model development, analysis and numerical simulation in acupuncture and moxibustion can be studied from the macroscopic and microscopic viewpoints.

1.3.1 Electroosmotic meridian model

As does acupuncture via mechanotransduction, that is activation by the stretch of mechanosensitive ion channels at the mastocyte surface, moxibustion may trigger opening of a thermosensitive ion channel. A previous study of the transfer of heat from burning moxa in an indirect moxibustion setting describes the construction of the electroosmotic meridian model for the modeling of a *qì*-blood interaction [60–64]. The electroosmotic model reads

$$\frac{\partial \underline{u}}{\partial t} + \underline{u} \cdot \nabla \underline{u} + \nabla p - \nu \nabla^2 \underline{u} = \underline{f} \tag{1.1}$$

The electroosmotic force $\underline{f}$ on the right hand side of the momentum equation (1.1) for the fluid flow velocity is as follows

$$\underline{f} = \frac{\epsilon}{\rho \lambda_D^2} \psi \nabla (\varphi + \psi) \tag{1.2}$$

This distinguished driving force stems from the fact that tissue fluid near acupoints is full of ions with the permittivity ϵ. In the presence of an externally applied electric field φ or the electric potential between the patient and acupuncture practitioner, zeta potential ϕ will be formed within the electric double layer of thickness λ_D, thereby resulting in the total electrical potential $\varphi + \psi$. Hydrodynamic equation (1.1) will be solved subject to the divergence free constraint equation

$$\nabla \cdot \underline{u} = 0. \tag{1.3}$$

Flow equations used in the continuous porous capillaries with the porosity ϵ and the permeability κ are as follows

$$\frac{\partial}{\partial t}(\epsilon \rho \underline{u}) + \nabla \cdot (\epsilon \rho \underline{u}\underline{u}) = -\epsilon \nabla p + \nabla \cdot (\epsilon \underline{\underline{\tau}}) - \frac{\epsilon^2 \mu}{\kappa} \underline{u} - \frac{\epsilon^3 \, \mathrm{C_F} \, \rho}{\kappa^{1/2}} |\underline{u}| \underline{u}, \tag{1.4}$$

$$\frac{\partial}{\partial t}(\epsilon\rho) + \nabla \cdot (\epsilon\rho\underline{u}) = 0. \tag{1.5}$$

In the above, ρ is the fluid density, μ the dynamic viscosity, $\underline{\underline{\tau}}$ the shear stress tensor and $\mathrm{C_F}$ the drag factor.

Equations (1.1 - 1.5) have been solved in the three-dimensional meridian model schematically shown in [62] by finite volume method. The results detailed in [60, 62] have revealed (1) if the blood is weak, then the *qì* is weak as well; (2) if *qì* is blocked, then the blood is in stasis (or if *qì* is flowing, then blood is flowing as well).

1.3.2 Interstitial flow in acupuncture

Interstitial flow plays important roles in the biological functions of tissues. Shear stress induced by fluid flow can trigger mechanotransduction pathways leading to cell activities such as degranulation of mastocytes. The fluid flows in the interstitial space (collagen-elastin matrix) between blood and lymphatic capillaries and carries nutrients, wastes, and proteins. The flow is driven by the difference in hydrostatic and osmotic pressures between the capillaries and the interstitial space [65]. The interstitial fluid is composed of water, ions, and other small molecules partially coming from the plasma. It interacts with the ground substance, containing proteoglycans and other macromolecules networks, to form a gel-like medium [12].

The interstitial tissue is considered as a fluid-filled porous medium. Low speed flow through rigid porous media is described by the Darcy law:

$$\boldsymbol{\nabla} p_f = -\frac{\mu}{\mathcal{P}}\bar{\mathbf{u}}, \tag{1.6}$$

where $-\frac{\mu}{\mathcal{P}}\bar{\mathbf{u}}$ denotes the Darcy drag, μ the dynamic viscosity of the fluid, $\mathcal{P}$ the Darcy permeability, $\bar{u}$ the averaged velocity, p_f the pressure, and α_f the fluid volume fraction. This volume fraction corresponds to the effective porosity of the medium.

The incompressible Brinkman equations [66], which permit the computation of flow profile around a solid body in porous media, take the following form:

$$-\mu\nabla^2\bar{\mathbf{u}} + \boldsymbol{\nabla} p_f = -\frac{\mu}{\mathcal{P}}\bar{\mathbf{u}} \qquad \text{in } \Omega, \tag{1.7}$$

$$\boldsymbol{\nabla} \cdot \bar{\mathbf{u}} = 0 \qquad \text{in } \Omega. \tag{1.8}$$

Brinkman equations (1.7-1.8) and the Darcy equation (1.6) constitute a continuum model for the current simulation of microscopic flow in porous media.

In the context of acupuncture, the interstitial flow has been modeled by the Brinkman equations to investigate the effects of shear stress on interstitial cells [67, 68]. A numerical study of the effect of shear stress induced by interstitial fluid flow on the interstitial cells was carried in 2D [67] and 3D [68]. Computed shear stress is shown to be large enough to activate cell functions. Simulations show that the interstitial fluid flow varies with capillary size and density, capillary permeability, blood pressure, interstitial pressure, and interstitial porosity.

1.3.3 Mastocyte dynamics of degranulation

Mastocytes are one of the key components of the physiological response in acupuncture treatment. Mastocytes can be activated by fluid shear stress generated, for example, by the needle manipulation in connective tissues. Chemical mediators are released via mechanotransduction process that mainly relies on calcium entry in the mastocyte cytosol. This calcium entry enables exocytosis of granules containing chemoattractants, nerve messengers and cardiovascular messengers. The concentration of cytosolic calcium entry can be computed under the applied shear stress. Wiesner et al. [69] developed a mathematical model to reproduce the change in mastocyte cytosolic Ca^{2+} concentration under fluid shear stress in the interstitial flow. The Ca^{2+} dynamics model reads as

$$\begin{aligned}
\frac{dc_c}{dt} &= \frac{S_0}{V_0}\frac{D}{d}\frac{f_e W(\tau)}{kTN}\frac{c_c - c_0\,\mathrm{e}^{\frac{f_e W(\tau)}{kTN}}}{1-\mathrm{e}^{\frac{f_e W(\tau)}{kTN}}}\frac{1}{1+\alpha\mathrm{e}^{-\frac{f_e W(\tau)}{kTN}}} + (k_1+\frac{k_2 c_c^4}{K_d^4+c_c^4})(c_e-c_c) - \frac{V_p c_c^2}{K_p^2+c_c^2} - k_3 c,\\
\frac{dc_e}{dt} &= -\beta(k_1+\frac{k_2 c_c^4}{K_d^4+c_c^4})(c_e-c_c) + \frac{\beta V_p c_c^2}{K_p^2+c_c^2},
\end{aligned} \tag{1.9}$$

where c_c is the cytosolic Ca^{2+} concentration and c_e is the endoplasmic reticulum Ca^{2+} concentration. τ denotes the external applied shear stress and $W(\tau)$ is the strain energy density that corresponds to the function of applied shear stress. The first term of the first equation in (1.9) describes the flux of Ca^{2+} entering the cytoplasm. The second term describes the flux of Ca^{2+} stored in the endoplasmic reticulum. The third term depicts the flux of Ca^{2+} leaving the cytoplasm. The fourth term describes the Na^+ and Ca^{2+} regulation. Both model (1.9) and observations [53] confirmed that mastocyte cytosolic Ca^{2+} concentration increases with shear stress.

In turn, a mathematical model can be used to compute the dynamics of mastocyte degranulation provided that the concentration c_c of cytosolic Ca^{2+} is known [55]. The degranulation dynamics model reads

$$\begin{aligned}
\frac{dP_1}{dt} &= k_4(P_1 0 - P(t)))c_c(t) - k(5)P_1(t),\\
\frac{dP_2}{dt} &= \frac{k_6 P_1(t)(1-P_2(t))}{K_1+1-P_2(t)} - \frac{V_S P_2(t)}{K_2+P_2(t)},\\
\frac{dP_3}{dt} &= -k_7 P_3(t) + k_8 P_2(t),
\end{aligned} \tag{1.10}$$

where the first equation describes the evolution of the activated protein kinase C concentration, the second equation describes the evolution of phosphorylated synaptosomal-associated protein 23 (SNAP23) concentration, and the third equation depicts the degranulation rate.

Both model (1.10) and observations [53] show that the mastocyte degranulation rate increases with the increase of cytosolic Ca^{2+} concentration, that corresponds to a higher

level of shear stress, until it reaches a steady state value. Yao et al. [70] linked the imbalance of the *qì* in traditional Chinese medicine to the imbalance of the nutrients and waste exchanges between blood and interstitial fluid.

1.4 Concluding remarks

From a mathematical modeling point of view, the remaining problems arise :

(1) How can the physical stress that serves as stimuli during acupuncture needling be studied?

During moxibustion therapy, a local temperature field is developed by directly or indirectly applying a burning moxa stick on the skin at acupoints. The temperature contours have been predicted in the case of direct moxibustion and needle moxibustion therapy [63]. The computed temperature decreases rapidly away from the heating point.

During acupuncture needling, does the mechanical stress field created by the insertion of a needle behave in the same way ? Shear stress and interstitial pressure are the two main physical parameters needed to measure the mechanical stress field developed by the motions of the needle. Mastocytes are considered as one of the primary actors in acupuncture therapy. Degranulation of mastocytes can occur under high shear stress induced by interstitial flow. In the interstitial fluid models, such as (1.7), studied in [67, 68], shear stress on mastocytes varies with interstitial pressure. The interstitial pressure is considered as a boundary condition and is thus essential to predict the flow. In the mastocyte degranulation dynamic model (1.10), studied in [53], shear stress on mastocytes is considered as a parameter.

One of the main purposes of chapter 3 is to give a positive answer to the previous question and provide some tools to predict numerically the shear stress on mastocytes and pressure of the interstitial flow by extending the studies of the Brinkman model with a moving needle.

(2) How can the response of mastocytes to external physical stimuli be modeled?

The models of mastocyte degranulation dynamics [53] and more recently mastocyte-nerve interaction [71] have been studied. These models strengthen the idea raised by experimentation that mastocytes could play a primary role at the acupoint. The models give a clearer insight on the mechanisms of mechanotransduction and degranulation processes induced by acupuncture and the interaction of released nerve stimulants with nerve endings. However, it is not clear how the observed abundance of mastocytes at acupoint could be a factor in the effects of acupuncture. More generally, to our knowledge, the evolution of the spatial distribution of mastocytes in response to physical stimuli has yet to be studied. Recent experiments [72] have been designed to exhibit the temporal and spatial dynamics of mastocytes, blood

vessels and nerves in stimulated acupoints by comparing the initial and final states of the components at the acupoint.

The main purpose of chapter 4 is to give a first model of the spatial evolution of mastocytes in response to physical stimuli. The model integrates magnitude and the spatial range of physical stimuli to which the mastocytes respond by releasing chemoattractants, nerve stimulants, and endocrine stimulants. The transport equation of mastocyte density is derived from the random (brownian) diffusion of the mastocytes with a bias directed by the released chemoattractant concentration. In that way, the model can describe the dynamics of mastocytes and make it easier to understand the role of the abundance of mastocytes near acupoints. The model reveals that mastocyte chemotactic recruitment plays a key role in the long lasting physiological effects of acupuncture.

Chapter 2

FreeFem++

Contents

2.1 Introduction 49

2.2 FreeFem++ and its interpreted language 49

2.2.1 The syntax 49

2.2.2 Meshing tools and mesh exemples 50

2.2.3 Finite element method 59

2.3 Solving problems in FreeFem++ 63

2.3.1 Evolution problem 63

2.3.2 Incompressible Navier-Stokes equation 65

2.3.3 Moving domain problem in computational fluid dynamics . . . 68

2.4 Concluding remarks 75

Abstract

The second chapter of this study is designed to briefly introduce the software FreeFem++ developed by Hecht [1]. It includes details on the tools needed to solve the differential system presented in this thesis within the finite element method. Parts of this chapter are from courses and presentations given within the FreeFem++ Activity Group of the Taiwan Society of Industrial and Applied Mathematics (TWSIAM Activity Group : FreeFem++. `http://homepage.ntu.edu.tw/~twhsheu/twsiamff++/freefem.html`. Accessed January 26, 2015.). A full documentation of FreeFem++ can be found on the FreeFem++ website (`http://www.freefem.org/ff++/`. Accessed January 26, 2015.).

2.1 Introduction

FreeFem++ is an open source partial differential equation solver developed by Frédéric Hecht, in collaboration with Olivier Pironneau, Jacques Morice, Antoine Le Hyaric and Kohji Ohtsuka, in the Laboratory Jacques-Louis Lions (LJLL) of University Pierre et Marie Curie (Paris, France). FreeFem++ runs on Unix, Windows and MacOS platforms. FreeFem++ allows its users to solve problems which admit a weak formulation. Users can write their own algorithms in FreeFem++ scripts to solve 2D and 3D PDEs and visualize their results within the software. Freefem++ includes the following modules: triangular finite element spaces, including discontinuous FE spaces; automatic mesh generator; mesh adaptation; fast linear solvers; MPI (Message Passing Interface) tools for parallel computing.

2.2 FreeFem++ and its interpreted language

2.2.1 The syntax

FreeFem++ language is an interpreted language based on the C++ object oriented programming language. FreeFem++ script instructions are executed directly by the FreeFem++ software. FreeFem++ syntax embeds the C++ syntax. For instance, the syntax for the loops `for` and `while` or the conditional statements `if`/`else` is the same as C++ with the use of the brackets `{ }` to define blocks. As in C++, the user can declare and define types of variables. FreeFem++ basic types `real`, `int`, and `bool` correspond in C++ to `double`, `long`, and `bool`, respectively. The declared variables can be manipulated with most of the usual C++ operators. A special feature of the FreeFem++ language is that some variable types, such as the mesh type `mesh`, the finite element space type `fespace`, or the variational formulation type `varf`, are relevant to the finite element method. Examples of types used in FreeFem++ are given in script 2.1.

```
1  x,y,z   // Cartesian coordinates
2  N.x, N.y, N.z  //Normal vector components
3  int k = 10; // integer
4  real a=2.5; // real
5  bool b=(a<3.); /boolean
6  real [int] array(k); // array of k real elements
7  array[][5]; //6th value of the array
8  mesh Th; //2d mesh
9  mesh3 Th3 //3d mesh
10 fespace Vh(Th,P1); //finite element space
11 Vh u=x; //finite element function
12 Vh3<complex> uc = x+ 1.i *y; //complex finite element function
```

```
13 fespace Xh(Th,[P2,P2,P1]);
14 Xh [u1,u2,p]; // a vectorial finite element function or array
15 u[]; //the array associated to FE function u
16 u(1.,0.1,3.); //value of u at point (1.,0.1,3.)
17 u[].max; // max of the array u
18 u[].min; // max of the array u
19 u[].sum; //sum of all elements of u
20 u[].l1; // l1 norm of u
21 u[].l2; // l2 norm of u
22 u[].linfty; // l.infinity norm of u
23 macro div(u,v) (dx(u)+dy(v))// macro
24 macro Grad(u) [dx(u),dy(u)]// macro
25 func f=cos(x)+sin(y); //function depending of the spatial coordinates
26 func real f(int i, real a){real r=i+a; return r;} // function
       declaration
27 varf a([u1,u2,p],[v1,v2,q])= int2d(...) + on(..); //variational
       formulation
28 matrix A = a(Vh,Vh,solver=UMFPACK); //stifness matrix of the problem
29 real[int] b=a(0,V3h); // right hand side
30 u[] =A^-1*b; // solving u = A^{-1}b
```

Script 2.1: Exemples of variable types, function declarations, and operators

2.2.2 Meshing tools and mesh exemples

The initial step, as in all finite element method numerical simulations, is to discretize a geometry Ω into the associate mesh, that is in FreeFem++ a triangulation $\mathcal{T}_h$. Two-dimensional and three-dimensional meshes can be generated directly using the FreeFem++ built-in tools. FreeFem++ can also import and export mesh files that are in the FreeFem++ required format. The tools `savemesh` and `readmesh` are used to save or load, respectively, a mesh file ".msh". Third-party software such as Gmsh [73] or TetGen [74] can be used together with FreeFem++.

2.2.2.1 Uniform square mesh

A square mesh can be defined with the built-in function `square`. It allows the user to triangulate a square domain and generate the mesh from a set of boundary points. The code in script 2.2 can be written to build a mesh of square domain. The keyword `plot` is used to plot the mesh (see figure 2.1). In the same way, the code in script 2.3 can be written to build a mesh of rectangle domain plotted in figure 2.1.

```
1 int nn=10; //number of points on each border
2 mesh Th = square (nn,nn);
```

```
plot(Th);
```

Script 2.2: Script to build a mesh of square domain plotted in figure 2.1.

```
int nn=10;
real x0=0, x1=10;
real y0=0, y1=5;
mesh Th=square(nn,2*nn,[x0+(x1-x0)*x,y0+(y1-y0)*y]);
plot(Th);
```

Script 2.3: Script to build the mesh of a rectangle domain plotted in figure 2.1.

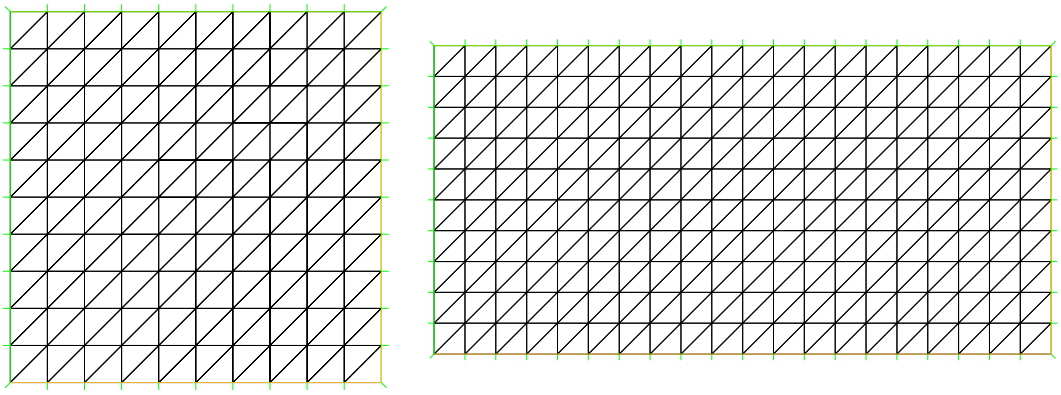

Figure 2.1: Uniform square mesh and rectangle mesh generated by the scripts 2.2 and 2.3, respectively

2.2.2.2 Analytic description of a domain

The geometry can also be defined by an analytic description of boundaries by pieces from which the mesh is automatically generated. Each piece of boundary is described by its parametric equation and is declared with the `border` type. The keyword `label` labels one curve or a group of curves of the boundary. The `label` type can be either an integer or a name. The mesh is then generated by calling the tool `buildmesh` that will automatically generate the Delaunay triangulation from a set of boundary points (see script 2.4). An example of generated mesh is shown in figure 2.2.

Note that the orientation of the curve is important in order for the domain to be defined on the correct side of the curve. In the `buildmesh` command, a number of vertices must be provided each piece of boundary. These numbers are positive or negative. The change of sign changes the orientation of the curve. It should also be noted that the boundaries can only intersect at their end points.

```
border b1(t=0,2*pi/5.)
        {x=(6*cos(t)-cos(6*t));y=(6*sin(t)-sin(6*t));label= 1;}
border b2(t=2*pi/5.,4*pi/5.)
        {x=(6*cos(t)-cos(6*t));y=(6*sin(t)-sin(6*t));label= 1;}
border b3(t=4*pi/5.,6*pi/5.)
        {x=(6*cos(t)-cos(6*t));y=(6*sin(t)-sin(6*t));label= 1;}
border b4(t=6*pi/5.,8*pi/5.)
        {x=(6*cos(t)-cos(6*t));y=(6*sin(t)-sin(6*t));label= 1;}
border b5(t=8*pi/5.,10*pi/5.)
        {x=(6*cos(t)-cos(6*t));y=(6*sin(t)-sin(6*t));label= 1;}
int np=25; //mesh resolution
mesh Th=buildmesh(b1(np)+b1(np)+b1(np)+b1(np)+b1(np));
plot(Th);
savemesh(Th,"meshfile.msh");
```

Script 2.4: Script to build the mesh plotted in figure 2.2.

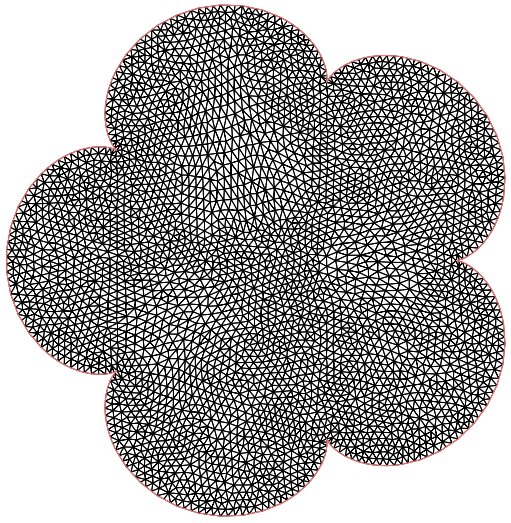

Figure 2.2: Mesh generated by the script in 2.4 representing a plum blossom of the Taiwan national flower

2.2.2.3 Mesh construction from an image

FreeFem++ embeds tools that allow the generation of meshes from a given image. The code in script 2.5 illustrates the capability to generate a two-dimensional mesh of Taiwan and a three-dimensional mesh of the elevation of Taiwan (see figures 2.3 and 2.4).

```
1  //Code adapted from F. Hecht - FreeFem++ - LJLL - UPMC
2  load "msh3"
3  load "medit"
4  load "ppm2rnm"
5  load "isoline"
6
7  string taiwan="Taiwan.pgm";
8  string taiwanelevation="Taiwanelevation.pgm";
9
10 real AreaTaiwan =  35883.; // Km^2
11 real hsize= 5;
12 real[int,int] Curves(3,1);
13 int[int] be(1);
14 int nc;// nb of curve
15
16   real[int,int] ff1(taiwan); // read image and set to an rectangle array
17   real[int,int] ffe(taiwanelevation);
18
19   int nx = ff1.n, ny=ff1.m; // build a Cartesian mesh with the origin at the right
       place.
20   mesh Th=square(nx-1,ny-1,[(nx-1)*(x),(ny-1)*(1-y)]);
21   fespace Vh(Th,P1);
22   Vh f1; f1[]=ff1; // transforme array in finite element function.
23   Vh fe; fe=0; fe[]=ffe; fe=1-fe;
24
25   nc=isoline(Th,f1,iso=0.25,close=1,Curves,beginend=be,smoothing
       =.1,ratio=0.5); // longest
       isoline
26   int ic0=be(0), ic1=be(1)-1;
27   int NC= Curves(2,ic1)/hsize;
28   real xl = Curves(0,ic0:ic1).max-5;
29   real yl = Curves(1,ic0:ic1).min+5;
30   border G(t=0,1){P=Curve(Curves,ic0,ic1,t); label=1+(x>xl)*2+(y
       <yl);}
31   mesh Sh=buildmesh(G(-NC));
32
33   fespace Wh(Sh,P1);
34   Wh deep = fe; // define the elevation on the new mesh
35
36   real scale = sqrt(AreaTaiwan/Th.area);
37   Sh=movemesh(Sh,[x*scale,y*scale]); // resize the mesh to have the correct
       scale
38   Wh temp; temp[]=deep[]; deep=0; deep[]=temp[];
39   plot(Sh,wait=0);
40   savemesh(Sh,"Taiwan2D.mesh");
41
```

```
42  deep = deep*20/abs(deep[].max);
43  plot(deep,wait=1);
44  int nn=30;
45  real maxdeep = deep[].max;
46  int[int] rup=[0,200], rdown=[0,100],rmid(17*2);
47  for(int i=0;i<rmid.n;++i) rmid[i]=1+i/2;
48  mesh3 Th3=buildlayers(Sh,nn, //3d mesh with layers
49  coef= deep/maxdeep, zbound=[0,deep], labelmid=rmid,
50  reffaceup = rup, reffacelow = rdown);
51  medit("Th3",Th3); //plot in medit
52  savemesh(Th3,"Taiwan3D.mesh");
```

Script 2.5: Script to build 2d and 3d meshes from an image

The keyword `load` is used to include an external library such as `msh3` to handle three-dimensional meshes and `medit` to visualize 3d meshes and results in the software MEDIT [75]. FreeFem++ natively includes three-dimensional visualization but MEDIT has advanced visualization tools.

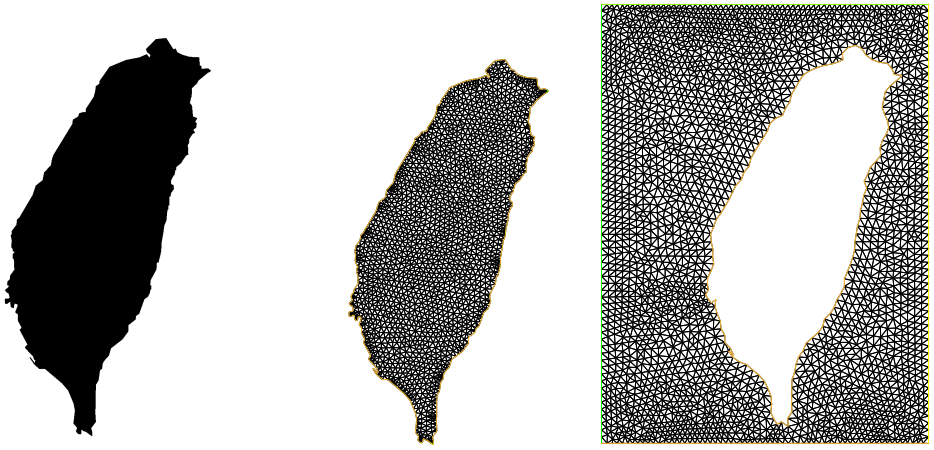

Figure 2.3: Meshes of Taiwan generated from the image on the left

2.2.2.4 Mesh manipulation

Truncating and adding meshes Another way to build meshes is to use the built-in truncation tool or the addition operator. To truncate a mesh, i.e. to remove triangles from the mesh, one can use the function `trunc`. The code in script 2.6 gives an exemple of the use of the function `trunc`. The resulting mesh is plotted in figure 2.5.

```
1  mesh Th=square(nn,ly/lx*nn,[x0+(x1-x0)*x,y0+(y1-y0)*y]);
```

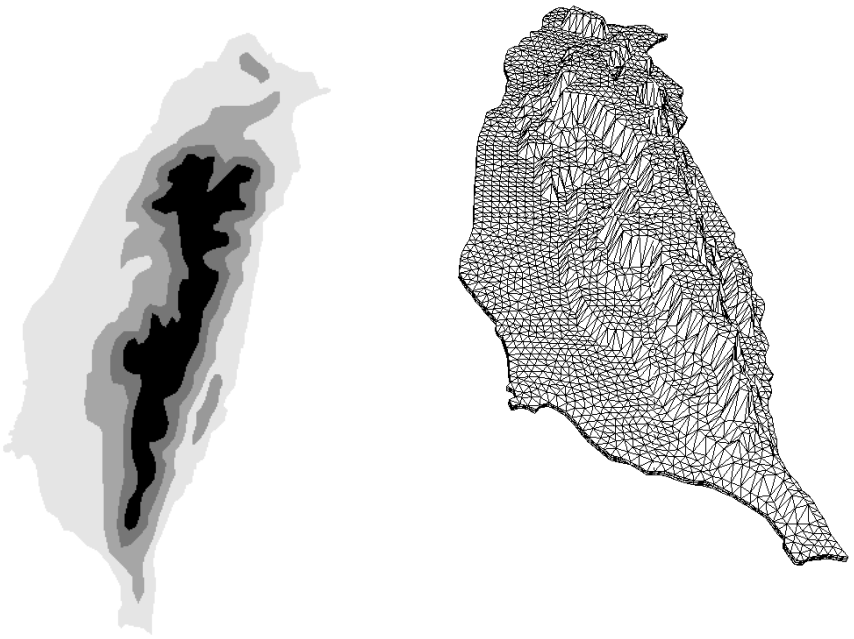

Figure 2.4: 3d mesh of Taiwan generated from the elevation map on the left

```
2 mesh Th1=trunc(Th,(max(abs(x),abs(y))>=1),label=5); //new mesh and
    label number of new boundary
```

Script 2.6: Script to build a truncated mesh. An exemple is plotted in figure 2.5.

To add or collate two meshes together, one can simply use the + operator. Note that to collate two meshes, the vertices on the adjoining boundary must correspond (see figure 2.10).

```
1 mesh Th=Th1+Th2;
2 plot(Th);
```

Script 2.7: Script to add two meshes to form a single mesh

Mesh adaptation A basic tool that can be used for mesh adaptation is the function `splitmesh`. This function divides each triangle by the value at the center of the triangle of a spatial function. The `splitmesh` function can be used to divide some or all triangles in a mesh. In fact, one can use a characteristic function to divide only the triangles in the support of the characteristic function. An example of the use of the previous function is given in script 2.8. The resulting is shown in figure 2.7.

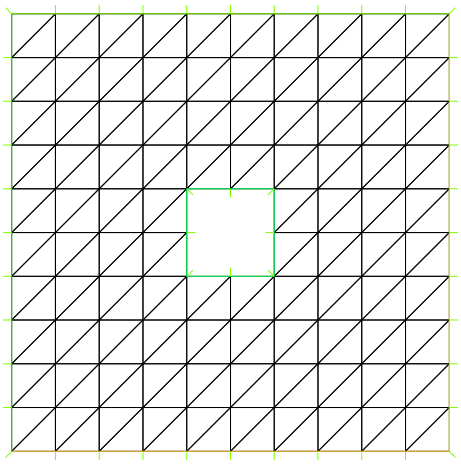

Figure 2.5: Mesh generated with the truncation tool

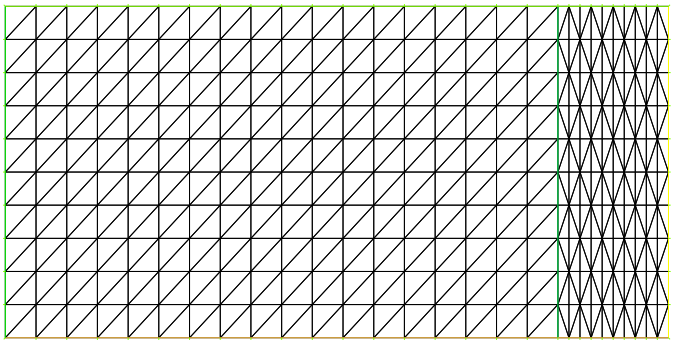

Figure 2.6: Mesh of two collated rectangles

```
border b(t=0,4.*pi){x=-.5*cos(t)+cos(-0.5*t)+1.5;y=-sin(-0.5*t);
    label=1;}
mesh Th=buildmesh(b(50));
plot(Th,wait=1,ps="nosplitmesh.eps");

mesh Sh=splitmesh(Th,1+x*x);  //split in int(1+x*x) triangles
plot(Sh,wait=1,ps="splitmesh.eps"); // see figure 2.7 (middle)

mesh Qh=splitmesh(Th,5);  // all triangles are split in 5
plot(Qh,wait=1,ps="splitallmesh.eps"); //see figure 2.7 (right)
```

Script 2.8: Script to split mesh triangles with *splitmesh*.

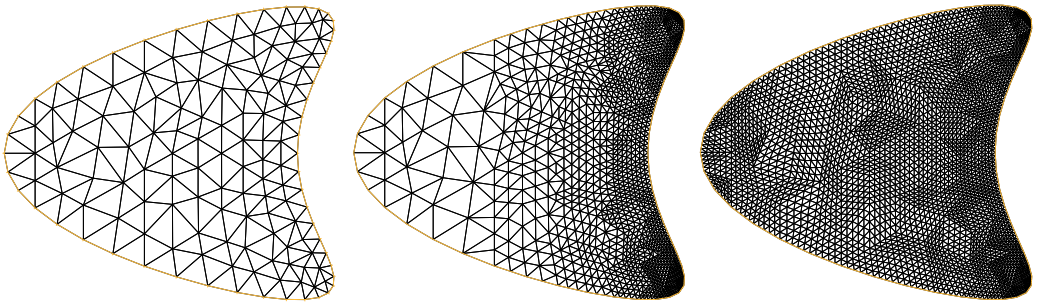

Figure 2.7: Mesh adaptation with the *splitmesh* function. Initial mesh (left), mesh with triangles split in $1+x*x$ triangles (middle), and mesh with all triangle split in 5 triangles (right).

The best tool for mesh adaptation is the `adaptmesh` function. This tool is based on a variable metric/Delaunay automatic meshing algorithm. Mesh adaptation is very useful to generate a finer mesh where the solution of a problem varies sharply. It is also very useful to make the mesh coarser in given regions where the solution varies very slowly in order to reduce computational cost. The generated mesh can be adapted to a function or finite element function. The function `adaptmesh` takes various arguments, including the required precision `err`, the minimum `hmin` or maximum `hmax` edge size of the triangles, or the maximum number of vertices `nbvx`. See the full documentation for the other arguments. Mesh adaptation can be performed following the example given in script 2.9 and illustrated in figure 2.8.

```
border b(t=0,4.*pi){x=-.5*cos(t)+cos(-0.5*t)+1.5;y=-sin(-0.5*t);
    label=1;}
mesh Th=buildmesh(b(70));
```

```
3  fespace Vh(Th,P1);
4  func f= 10*exp(-50*square(x-1)/-50*square(y)); //
       f = 10 * e^(-50*(x-1)^2+y^2)
5  Vh u=f; //u is the projection of f to Vh
6  Vh u0;
7  plot(Th,u,wait=1,ps="adaptmesh0.eps");
8  for(int it=0; it<5; ++it) {
9          Th = adaptmesh(Th,u,err=1.e-3); //mesh adaptation
10         u=f;
11         plot(Th,u,wait=1,ps="adaptmesh.eps"); //see figure 2.8.
12 }
```

Script 2.9: Script to adapt a mesh with the function *adaptmesh*.

Note that the command `adaptmesh` does not destroy the old mesh and all finite element functions using the old mesh remain unchanged. In the script 2.9, the command `u=f` redefines the variable `u` on the new mesh and, as a result, destroys the old mesh because `u` was the only variable defined on it.

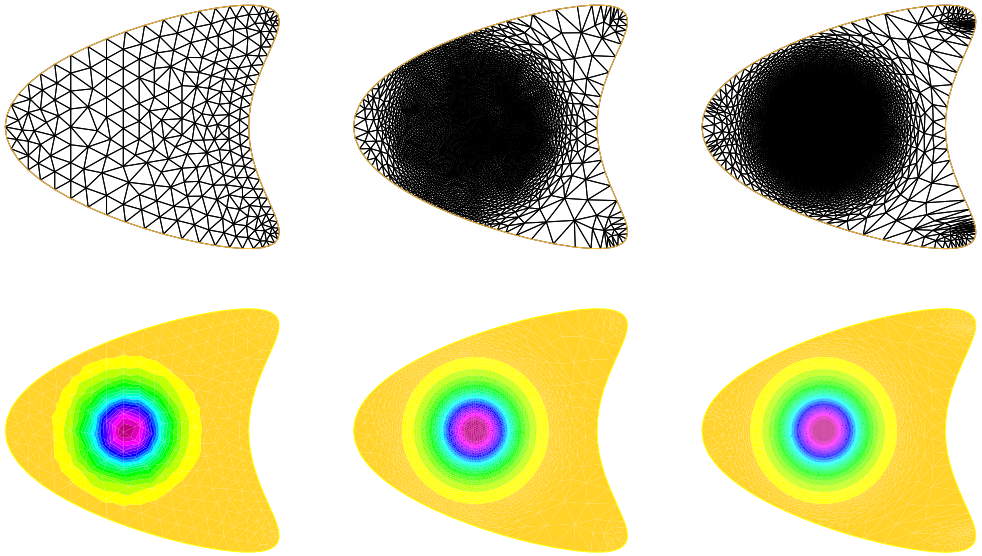

Figure 2.8: Mesh adaptation with the *adaptmesh* function. Initial mesh (left), mesh adapted after one iteration (middle), and mesh adapted after five iterations (right).

Movemesh Meshes can be translated, rotated and deformed by the function `movemesh`. This tool is very useful to follow the deformation due to displacement or to deal with moving boundary problems. If $\mathcal{T}_h$ is the triangulation and $\mathbf{d}$ the displacement vector, then the displaced mesh can be obtained with the script 2.10 and illustrated in figure 2.9.

```
1 border b(t=0,4.*pi){x=-.5*cos(t)+cos(-0.5*t)+1.5;y=-sin(-0.5*t);
    label=1;}
2 mesh Th=buildmesh(b(60));
3 plot(Th,wait=1,ps="movemesh0.eps");
4
5 Th = movemesh(Th,[y,-x]); //rotation
6 plot(Th,wait=1,ps="movemeshrotation.eps");
7
8 Th = movemesh(Th,[x+cos(x),y]); //deformation
9 plot(Th,wait=1,ps="movemeshdeformation.eps");
```

Script 2.10: Mesh manipulation with the *movemesh* function

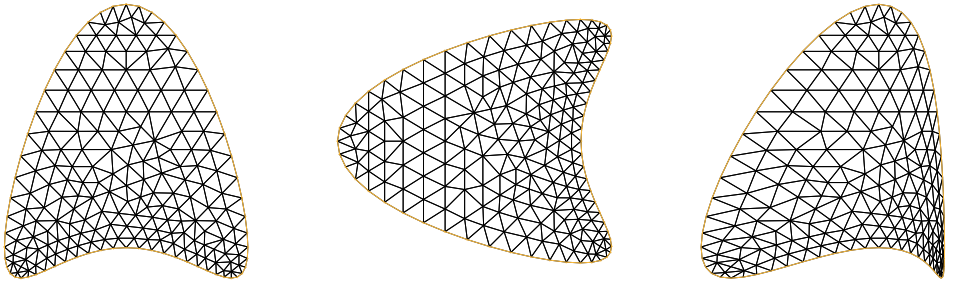

Figure 2.9: Mesh manipulation with the *movemesh* function. Initial mesh (left), mesh rotation of π rad (middle), and mesh deformation with a displacement of $\cos(x)$ in the x-direction (right).

2.2.3 Finite element method

2.2.3.1 Finite element space

In FreeFem++, the problems must be expressed in their weak form. The weak formulation consists of multiplying the equation by a test function and integrating it over the fluid volume Ω. Then time discretization needs to be chosen and the final finite element formulation can be expressed as: find $w \in V_w(\Omega)$ such that

$$a(w,\varphi) - l(\varphi) = 0 \qquad \forall \varphi \in V_\varphi(\Omega). \tag{2.1}$$

Neumann boundary conditions can be directly implemented into the weak formulation without introducing any derivation error. FreeFem++ uses a penalty method to impose Dirichlet boundary conditions.

FreeFem++ handles a large variety of classical finite elements such as Lagrangian finite elements ($\mathbb{P}_0$,$\mathbb{P}_1$,$\mathbb{P}_2$,$\mathbb{P}_3$,$\mathbb{P}_4$), bubble elements ($\mathbb{P}_{1b}$,$\mathbb{P}_{2b}$), discontinuous $\mathbb{P}_1$ finite elements, and Raviart-Thomas elements. The reader can refer to the FreeFem++ online documentation for the full list of finite elements already implemented in FreeFem++. FreeFem++ is not limited to such a list and the user can add its own finite elements in a C++ extension file.

Let V_h be a space embedded in the continuous space $H^1(\Omega)$. The $\mathbb{P}_1$ finite element discretization of V_h on a triangulation $\mathcal{T}_h$ of Ω correspond to the the space of continuous piecewise polynomial of degree one defined as follows

$$V_h = \left\{ w_h \in H^1(\Omega), w_h \in \mathcal{C}^0(\Omega), w_{h|_K} \in P^1(K), \forall K \in \mathcal{T}_h \right\}. \tag{2.2}$$

The type `fespace` serves to define the discrete finite element space for the unknowns and test functions. The declaration of a finite element space on any mesh $\mathcal{T}_h$ can be written as follows.

```
1 fespace Vh(Th,P1);          // scalar space
2 fespace Wh(Th,[P2,P2,P1]);  // vectorial space
```

Script 2.11: Declaration of finite element spaces.

The trial function u and test function v can then be declared in the finite element space V_h accordingly.

```
1 Vh u,v;  // unknown and test function
2 Vh w = cos(x);
3 Wh [u,v,p] = [y*(1.-y), 0., 2./Re*(1.-x)];
```

Script 2.12: Declaration of finite element functions in the space V_h.

2.2.3.2 Weak formulation

To solve partial differential equations, FreeFem++ allows users to define the problems in their weak forms to be treated by the finite element method. A problem is defined using the keywords `solve`, `problem` or `varf`, whether the user desires an immediate resolution, a resolution by calling the solver, or a manual resolution by constructing the linear system associated to the discretized problem, respectively.

It is possible to solve linear problems, non linear problems and evolution problems. Nevertheless, FreeFem++ is an elliptic solver and it is the users' responsibility to provide their own algorithms to solve time dependent and nonlinear problems. In any case, the problem comes down to the resolution of a linear system.

The Poisson's equation illustrates the use of the keywords `solve`, `problem` or `varf` by showing a great similarity of the FreeFem++ script and the weak formulation of the problem. Consider the following Poisson problem. Given a piecewise continuous function f, find $u \in \mathcal{C}^2$, such that $-\nabla^2 u = f$ in Ω and $u = 0$ in $\partial\Omega$. If $f \in L^2(\Omega)$, multiplication by a test function of compact support in Ω and integration by part of the previous equation yields the weak formulation: find $u \in H_0^1(\Omega)$ such that

$$\forall v \in H_0^1(\Omega), \int_\Omega \nabla u \cdot \nabla v - \int_\Omega f v = 0. \tag{2.3}$$

Then, discretization of the problem relies on the choice a triangulation $\mathcal{T}_h$ and a finite element space that corresponds to a vectorial space V_h on $\mathbb{R}$ of dimension N such that $V_h \subset H_0^1(\Omega)$. Let φ_i, $0 \leq i \leq N-1$, the basis function of V_h, the problem (2.3) can be rewritten as: find $u_h \in V_h$ such that

$$\forall i \in [0, N-1], \int_{\mathcal{T}_h} \nabla u_h \cdot \nabla \varphi_i - \int_\Omega f \varphi_i = 0. \tag{2.4}$$

$u_h \in V_h$ can be written in the finite element basis $u_h = \sum_{j=0}^{N-1} u_j \varphi_j$. The problem (2.4) corresponds to the following linear system: find u_j, $0 \leq j \leq N-1$ such that

$$\forall i \in [0, N-1], \sum_{j=0}^{N-1} u_j \int_{\mathcal{T}_h} \nabla \varphi_j \cdot \nabla \varphi_i - \int_\Omega f \varphi_i = 0. \tag{2.5}$$

Let $A = (\int_{\mathcal{T}_h} \nabla \varphi_j \cdot \nabla \varphi_i)_{0 \leq i,j \leq N-1}$, $U = (u_j)_{0 \leq j \leq N-1}$, and $F = \left(\int_\Omega f \varphi_i\right)_{0 \leq i \leq N-1}$, the linear system (2.5) is equivalent to a matrix equation of the form $AU = F$.

FreeFem++ uses a penalty method to treat the Dirichlet boundary condition that preserves the symmetry of the system. Instead of replacing the lines of the matrix A corresponding to indices belonging to $\partial\Omega$ with zeros, diagonal elements A_{ii}, where the suffix i belongs to the border $\partial\Omega$, are replaced by a very large value `tgv`. If the Dirichlet condition is not homogeneous, the right hand side is modified such that F_i, when i belongs to $\partial\Omega$, equals `tgv` multiplied by the value on the border.

To solve the linear system $AU = F$ associated with the discretized problem, FreeFem++ provides many direct and iterative solvers such as the conjugate gradient, GMRES, the multifrontal solver UMFPACK, and the parallel solver MUMPS. In dimension two, the problem can be solved with the following script.

```
1 mesh Th = readmesh("taiwan.msh"); //mesh
2 fespace Vh(Th,P2); // P2 FE space
3 Vh u,v; // unkown and test function.
4 func f=1; // right hand side function
5 func g=0; // boundary condition function
6 solve Poisson(u,v, solver=UMFPACK) //declare and solve immediately the
    problem
```

```
7           = int2d(Th)( dx(u)*dx(v) + dy(u)*dy(v)) //bilinear form ∫_{T_h} ∇u · ∇v
8           - int2d(Th)( f*v)                       // linear form ∫_{T_h} fv
9           + on(1,u=g) ;                           // boundary condition u = 0
10 plot(u,ps="Poisson.eps",value=1, fill=1); // export an eps image
```

Script 2.13: Solving the Poisson's equation in 2d with the keyword *solve*.

```
1  mesh Th = readmesh("taiwan.msh"); //mesh
2  fespace Vh(Th,P2); // P2 FE space
3  Vh u,v; // unkown and test function.
4  func f=1; // right hand side function
5  func g=0; // boundary condition function
6  problem Poisson(u,v, solver=UMFPACK)   //declare de problem
7           = int2d(Th)( dx(u)*dx(v) + dy(u)*dy(v)) //bilinear form ∫_{T_h} ∇u · ∇v
8           - int2d(Th)( f*v)                       // linear form ∫_{T_h} fv
9           + on(1,u=g) ;                           // boundary condition u = 0
10 Poisson; //solve the problem
11 plot(u,ps="Poisson.eps",value=1, fill=1); // export an eps image
```

Script 2.14: Solving the Poisson's equation in 2d with the keyword *problem*.

```
1  mesh Th = readmesh("taiwan.msh"); //mesh
2  fespace Vh(Th,P2); // P2 FE space
3  Vh u,v; // unkown and test function.
4  func f=1; // right hand side function
5  func g=0; // boundary condition function
6  varf a(u,v)   //bilinear form
7           = int2d(Th)( dx(u)*dx(v) + dy(u)*dy(v)) // ∫_{T_h} ∇u · ∇v
8           + on(1,u=g) ;                           // boundary condition u = 0
9  matrix A=a(Vh,Vh,solver=UMFPACK); //constructing the stiffness matrix
10 varf l(unused,v)   //linear form
11          = int2d(Th)( f*v)                       // ∫_{T_h} fv
12          + on(1,unused=g) ;                      // boundary condition u = 0
13 Vh F; F[] = l(0,Vh); // constructing the RHS vector
14 u[]=A^-1*F[]; //solve the problem
15 plot(u,ps="Poisson.eps",value=1, fill=1); // export an eps image
```

Script 2.15: Solving the Poisson's equation in 2d with the keyword *varf*.

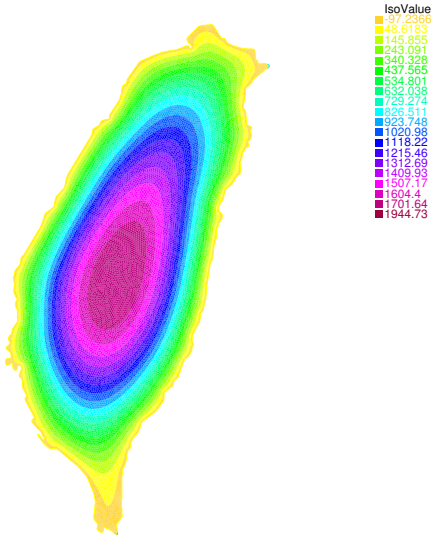

Figure 2.10: Solution of the Poisson's equation on a Taiwan shaped mesh obtained from the scripts 2.13, 2.14, and 2.15

2.3 Solving problems in FreeFem++

2.3.1 Evolution problem

To solve an evolution problem, the user should reduce it to a stationary problem using , for example, a finite difference scheme for the discretization in time. In the context of finite element method, the space-time finite element method adopts the weak formulation written over the space-time domain of a problem [76–79]. At each step, the integration of equations is performed over a space-time element.

The heat equation needs few lines of code in FreeFem++ to be solved and illustrates some tools needed to solve an evolution problem. A general form of the reaction-diffusion problem is: find a function $u \in \mathcal{C}([0,T])$, for $T > 0$, such that

$$\begin{aligned} \frac{\partial u}{\partial t} - \mathcal{D}\nabla^2 u &= f && \text{in }]0,T] \times \Omega, \\ u &= g_D && \text{on }]0,T] \times \Gamma_D, \\ \nabla u \cdot \mathbf{n} &= g_N && \text{on }]0,T] \times \Gamma_N, \\ u(0,x) &= u_0(x) && \text{in } \Omega. \end{aligned} \tag{2.6}$$

$u_0 \in L^2$ is the initial condition to the problem, f the reaction term, $\mathbf{n}$ the normal and g the value of Dirichlet boundary condition. For any $g \in H^{1/2}(\Gamma_D)$, let $V_g = \{v \in H^1(\Omega), v = g \text{ on } \Gamma_D\}$. The weak formulation of (2.6) is: find $u \in L^2\left(]0,T[, V_{g_D}\right) \cap \mathcal{C}\left([0,T], L^2(\Omega)\right)$

such that, $\forall t \in]0, T[$,

$$\forall v \in V_0, \int_\Omega \frac{\partial u}{\partial t} v + \int_\Omega \mathcal{D}\nabla u \cdot \nabla v - \int_{\Gamma_N} \mathcal{D}\nabla u \cdot \mathbf{n} v = \int_\Omega f v, \qquad u(0, x) = u_0(x). \tag{2.7}$$

As a first step, consider a time-discretization of the equation, let say the implicit Euler scheme. The equation (2.7), in its semi-discrete form, reads, find $u^{n+1} \in V_{g_D}$ such that

$$\forall v \in V_0, \int_\Omega \frac{u^{n+1} - u^n}{\Delta t} v + \int_\Omega \mathcal{D}\nabla u^{n+1} \cdot \nabla v - \int_{\Gamma_N} \mathcal{D}\nabla u^{n+1} \cdot \mathbf{n} v = \int_\Omega f v, \quad \forall n \in \mathbb{N}. \tag{2.8}$$

Let $V_{h,g}$ be the finite element approximation of the space V_g on the triangulation $\mathcal{T}_h$. The weak formulation sets into a finite dimensional linear system: find $u^{n+1} \in V_{h,g_D}$ such that

$$\forall v \in V_{h,0}, \int_{\mathcal{T}_h} \frac{u^{n+1} - u^n}{\Delta t} v + \int_{\mathcal{T}_h} \mathcal{D}\nabla u^{n+1} \cdot \nabla v - \int_{\Gamma_N^h} \mathcal{D} g_N v = \int_{\mathcal{T}_h} f v, \quad \forall n \in \mathbb{N}. \tag{2.9}$$

In the following script 2.16, the keyword `problem` introduced in section 2.2.3.2 allows to write the problem in a form very similar to the formulation (2.9).

```
1  int GammaD=10, GammaN=20; //labels for the boundary
2  border boutside(t=0,2*pi){x=cos(t);y=sin(t);label= GammaN;}
3  border binside(t=-.5,.5){x=t;y=-0.5+0.5*t^2;label= GammaD;}
4  mesh Th=buildmesh(boutside(150)+ binside(150/(2*pi))); //esh
5
6  int it; //time loop iterator
7  int M=6; //time iterations
8  real dt=0.5; //time step
9  real D=.1; //thermal conductivity
10 real gD = 10; //initial and Dirichlet boundary condition
11 real gN=1; //Neumann boundary condition
12
13 fespace Vh(Th,P2); // finite element space
14 Vh u,u0,v; //unknown, function to store the data from previous step, and test function
15 problem heat(u,v,init=it) // when init ≠ 0, the stiffness matrix is not reconstructed
16          = int2d(Th)(u*v/dt)
17          + int2d(Th)(D*(dx(u)*dx(v)+dy(u)*dy(v)))
18          + int1d(Th,GammaN)(D*gN*v)
19          - int2d(Th)(u0*v/dt)
20          + on(GammaD,u=gD);
```

```
21
22 u = gD; //initialization
23 for(it=0;it<M; it++) {
24             u0=u; //update from previous step time
25             heat; //solve the linear system a the next time step
26             plot(u,nbiso=40,fill=1,ps="solution"+it+".eps");
27 }
```

Script 2.16: Solving the heat equation in FreeFem++

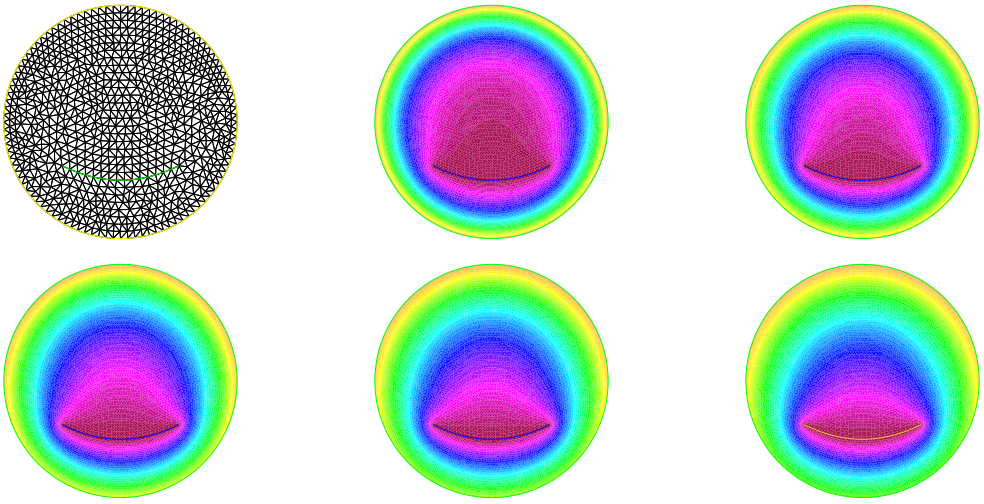

Figure 2.11: Mesh and numerical solutions of the heat equation (2.9) at the five first time steps computed with the FreeFem++ script 2.16

2.3.2 Incompressible Navier-Stokes equation

The incompressible Navier-Stokes system consists of the following equations

$$\begin{aligned} \frac{\partial \mathbf{u}}{\partial t} + \mathbf{u}\cdot\nabla\mathbf{u} - \nu\nabla^2\mathbf{u} + \nabla p = \mathbf{f} \quad &\text{in } \Omega, \\ \nabla\cdot\mathbf{u} = 0 \quad &\text{in } \Omega, \end{aligned} \tag{2.10}$$

for the primitive variables $\mathbf{u}$ and p.

The incompressible Navier-Stokes equations (2.10) are solved using the characteristics/Galerkin method [80] for the space discretization together with the Euler implicit scheme for the time discretization. This is implemented using an interpolation operator for the term $\frac{\partial}{\partial t} + (\mathbf{a}\cdot\nabla)$

$$\frac{u^{n+1}(\mathbf{x}) - u^n \circ \mathbf{X}^n}{\Delta t} = f^n(\mathbf{x}). \tag{2.11}$$

$\mathbf{X}^n$ is an approximation of the solution at time $t = n\,\Delta t$ of the ordinary differential equation

$$\begin{aligned} \frac{\mathbf{X}(t)}{dt} &= \mathbf{a}^n(\mathbf{X}(t)), \\ \mathbf{X}((n+1)\,\Delta t) &= x. \end{aligned} \tag{2.12}$$

The term $u^n \circ \mathbf{X}^n$ is approximated by $u^n \circ \mathbf{X}^n \approx u^n(\mathbf{x} - \mathbf{a}^n(x)\,\Delta t)$ and computed by the interpolation operator $\texttt{convect}(\mathbf{a}^n, -\Delta t, u^n)$.

The Navier-Stokes equations can be approximated by the pseudo-compressible approximation

$$\begin{aligned} \frac{\partial \mathbf{u}}{\partial t} + \mathbf{u}\cdot\nabla\mathbf{u} - \nu\nabla^2\mathbf{u} + \nabla p = \mathbf{f} \quad &\text{in } \Omega, \\ \nabla\cdot\mathbf{u} + \varepsilon p = 0 \quad &\text{in } \Omega, \end{aligned} \tag{2.13}$$

where ε is a small parameter. The formulation (2.13) follows the so called artificial compressibility method introduced by Chorin [81] and Témam [82]. The pseudo compressibility term is not only important to get the V-ellipticity property of the bilinear form in the semi-discretized system (2.33-**??**), but also serves as a stabilization term in the numerical scheme. The time discretization of (2.13) yields

$$\begin{aligned} \frac{\mathbf{u}^{n+1} - \mathbf{u}^n \circ \mathbf{X}^n}{\Delta t} - \nu\nabla^2\mathbf{u}^{n+1} + \nabla p^{n+1} = \mathbf{f}^{n+1} \quad &\text{in } \Omega \\ \nabla\cdot\mathbf{u}^{n+1} + \varepsilon p^{n+1} = 0 \quad &\text{in } \Omega, \end{aligned} \tag{2.14}$$

where $\mathbf{u}^n \circ \mathbf{X}^n$ is approximated by $\mathbf{u}^n \circ \mathbf{X}^n \approx \mathbf{u}^n(\mathbf{x} - \mathbf{u}^n(\mathbf{x}))\,\Delta t)$. Let us consider the product space

$$V = \left\{(\mathbf{w}, q) \in [H^1(\Omega)]^2 \times L^2(\Omega), \mathbf{w} = 0 \text{ on } \Gamma\right\} \tag{2.15}$$

Considering the boundary condition (2.21), the weak formulation of (2.13) is as follows: find $(\mathbf{u}^{n+1}, p^{n+1}) \in V$ such that

$$\begin{aligned} \int_\Omega \left(\frac{\mathbf{u}^{n+1} - \mathbf{u}^n \circ \mathbf{X}^n}{\Delta t}\right)\cdot\mathbf{v}^{n+1} + \nu\int_\Omega \nabla\mathbf{u}^{n+1}\cdot\nabla\mathbf{v} - \int_\Omega p^{n+1}\nabla\cdot\mathbf{v} = \int_\Omega f\mathbf{v}, \\ \int_\Omega q\nabla\cdot\mathbf{u}^{n+1} + \varepsilon\int_\Omega p^{n+1}q = 0, \end{aligned} \tag{2.16}$$

for all $(\mathbf{v}, q) \in V$.

Under the given temporal discretization, the semi-discretized system (2.33) is now regarded as the Stokes equations. As $\varepsilon \to 0$, the solution of (2.33) tends to the solution of the problem: find $(\mathbf{u}'^{n+1}, p'^{n+1}) \in V$ such that

$$\begin{aligned} \int_\Omega \left(\frac{\mathbf{u}'^{n+1} - \mathbf{u}'^n \circ \mathbf{X}^n}{\Delta t}\right)\cdot\mathbf{v}^{n+1} + \nu\int_\Omega \nabla\mathbf{u}'^{n+1}\cdot\nabla\mathbf{v} - \int_\Omega p'^{n+1}\nabla\cdot\mathbf{v} = \int_\Omega f\mathbf{v}, \\ \int_\Omega q\nabla\cdot\mathbf{u}'^{n+1} = 0, \end{aligned} \tag{2.17}$$

for all $(\mathbf{v}, q) \in V$, and it has been proven that [83]

$$||\mathbf{u}'^{n+1} - \mathbf{u}^{n+1}||_{[H_0^1]^2} + ||p'^{n+1} - p^{n+1}||_{L^2} < C\,\varepsilon, \tag{2.18}$$

where C is a constant independent of ε. In this study, we choose $\varepsilon = 10^{-10}$. Taylor-Hood $\mathbb{P}_2$–$\mathbb{P}_1$ elements are adopted to satisfy the LBB (Ladyžhenskaya - Babuška - Brezzi) stability condition [84–87]. The continuous linear basis function ($\mathbb{P}_1$) and the continuous quadratic functions ($\mathbb{P}_2$) are assigned in FreeFem++.

The incompressible Navier-Stokes equations (2.10) are solved subject to the boundary conditions

$$\mathbf{u} = 0 \qquad \text{on } \Gamma, \tag{2.19}$$

$$\mathbf{u} = f \qquad \text{on } \Gamma_0 \tag{2.20}$$

$$-p\mathbf{n} + \nu\nabla u \cdot \mathbf{n} = 0 \qquad \text{on } \Gamma_1, \tag{2.21}$$

the initial condition

$$\mathbf{u}_{|_{t=0}} = \mathbf{u}_0 \qquad \text{in } \Omega, \tag{2.22}$$

and subject to the divergence-free initial condition

$$\nabla \cdot \mathbf{u}_0(\mathbf{x}, t) = 0. \tag{2.23}$$

The linear system at each time step is given in FreeFem++ script 2.17.

```
1  mesh Th=readmesh("tube.msh");
2  int it=0;
3  real nu=1./200.;
4  real dt=0.1;
5  real alpha=1/dt;
6  func f=4*y*(1-y); // inlet boundary condition
7  fespace Xh(Th,P2);
8  fespace Mh(Th,P1);
9  Xh u2,v2;
10 Xh up1,up2;
11 Xh u1,v1;
12 Mh p,q;
13 // Navier-Stokes equations
14 problem NS ([u1,u2,p],[v1,v2,q],solver=UMFPACK, init=it)
15         = int2d(Th)(
16               alpha*( u1*v1 + u2*v2)
17           + nu * ( dx(u1)*dx(v1) + dy(u1)*dy(v1)
18           +  dx(u2)*dx(v2) + dy(u2)*dy(v2) )
19           - p*q*(0.00000001)
```

```
            - p*dx(v1)- p*dy(v2)
            - dx(u1)*q- dy(u2)*q
           )
           + int2d(Th) ( -alpha*convect([up1,up2],-dt,up1)*v1 -
              alpha*convect([up1,up2],-dt,up2)*v2 )
           + on(1,u1=f,u2=0)
           + on(2,4,u1=0,u2=0)
;
//initialization: Stokes flow
solve Stokes ([u1,u2,p],[v1,v2,q],solver=UMFPACK)
           = int2d(Th)(
              nu* ( dx(u1)*dx(v1) + dy(u1)*dy(v1)
            +  dx(u2)*dx(v2) + dy(u2)*dy(v2) )
            - p*q*(0.00000001)
            - p*dx(v1)- p*dy(v2)
            - dx(u1)*q- dy(u2)*q
           )
           + on(1,u1=f,u2=0)
           + on(2,4,u1=0,u2=0)
;
for (it=0;it<=80;it++){  //time loop
           up1=u1;up2=u2;
           NS;
           plot(coef=0.2,cmm="p, [u1,u2]",p, [u1,u2], wait=0);
};
```

Script 2.17: Solving the incompressible Navier-Stokes equations

2.3.3 Moving domain problem in computational fluid dynamics

Different methods exist to predict flows in moving domains with the finite element method. Fixed mesh methods use a single mesh covering the domain occupied by the fluid and the domain where there is no fluid to compute the flow. The immersed boundary approach [88] relies on the description of a solid phase by adding a force vector to the governing equations. A similar approach, known as the fictitious domain method, is based on the use of Lagrange multipliers to enforce kinematic condition on the solid phase [89–91] or alternatively based on a penalty method [92]. Both methods track the solid phase with a characteristic function or a level set function. These methods can be adapted to track moving bodies in fluid. The latest methods have been implemented with FreeFem++ [93].

Moving mesh methods use meshes following the domain occupied by the fluid. The mesh is then given exactly at the boundary. The ALE framework is mathematically rigorous to describe transport phenomena in time. However, it raises some implementation

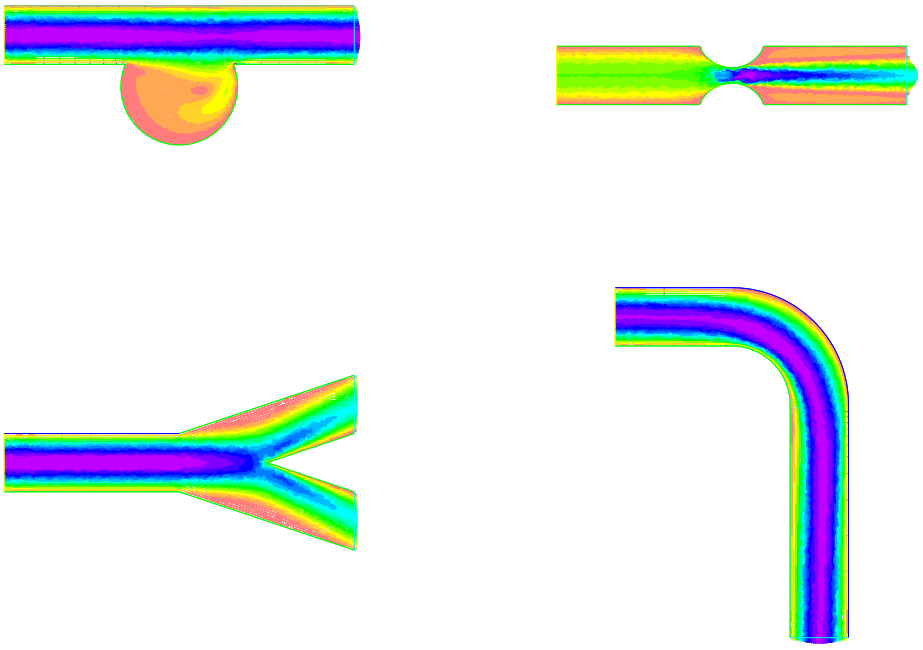

Figure 2.12: Numerical simulation of flow in idealized 2D aneurysm model, stenosis model, bifurcation model, and bended tube model. Velocity vectors are computed with the FreeFem++ script 2.17.

questions on the interface tracking with time discretization. Implementation of the ALE method can be done in FreeFem++. The ALE method of characteristics [92] applied to the mesh moving scheme can be implemented to improve stability properties of the mesh moving scheme. The space-time finite element method is also well-suited to track the moving domain [76, 77]. The space-time finite element method can be implemented in FreeFem++ in 1D and 2D using an extra variable such as the time variable.

Moving mesh methods use meshes following the domain occupied by the fluid. The mesh is then exactly given at the boundary. The ALE framework is mathematically rigorous to describe transport phenomena in time and allows some freedom in the description of the mesh motion. However, it raises some implementation questions on the interface tracking with time discretization. Implementation of the ALE method can be done in FreeFem++. The ALE method of characteristics [94] applied to the mesh moving scheme can be implemented to improve stability properties of the mesh moving scheme. The space-time finite element method is also well suited to track the moving domain [78, 79]. The space-time finite element method can be implemented in FreeFem++ in 1D and 2D using and extra variable as the time variable.

A straightforward implementation of the ALE approach is briefly described below. The implementation in FreeFem++ follows the method given by Decoene A. and Maury B. [95]. For a detailed description of the ALE approach, the reader can refer to [96]. Let $\Omega(t)$ be a domain at each time t with regular boundary $\partial\Omega(t)$. In the Eulerian representation, the fluid is described by

$$\mathbf{u}(\mathbf{x},t) \text{ and } p(\mathbf{x},t), \forall \mathbf{x} \in \Omega(t). \tag{2.24}$$

To follow a moving domain, one can define the ALE map as

$$\tilde{\mathcal{A}} : \tilde{\omega} \times \mathbb{R}^+ \to \mathbb{R}^2 \quad (\tilde{\mathbf{x}},t) \to \tilde{\mathcal{A}}(\tilde{\mathbf{x}},t) := \tilde{\mathcal{A}}_t, \tag{2.25}$$

such that $\omega(t) = \tilde{\mathcal{A}}(\tilde{\omega},t)$, where $\tilde{\omega}$ is the reference computational domain. Given an ALE field $\tilde{q} : \tilde{\omega} \times \mathbb{R}^+ \to \mathbb{R}$, its Eulerian description is given by

$$\forall \mathbf{x} \in \Omega(t), q(\mathbf{x},t) = \tilde{q}(\tilde{\mathcal{A}}_t^{-1}(\mathbf{x}),t) \tag{2.26}$$

In this framework, the computational domain velocity (ALE velocity or grid velocity) is defined as

$$\tilde{\mathbf{a}}(\tilde{\mathbf{x}},t) = \frac{\partial \tilde{\mathcal{A}}}{\partial t}(\tilde{\mathbf{x}},t), \quad \forall \tilde{\mathbf{x}} \in \tilde{\omega}, \tag{2.27}$$

so that

$$\mathbf{a}(\mathbf{x},t) = \tilde{\mathbf{a}}(\tilde{\mathcal{A}}_t^{-1},t). \tag{2.28}$$

The ALE time-derivative is defined as

$$\left.\frac{\partial q}{\partial t}\right|_{\tilde{\mathcal{A}}} = \frac{\mathrm{d}}{\mathrm{d}t} q(\tilde{\mathcal{A}}(\tilde{\mathbf{x}},t),t), \tag{2.29}$$

and the following identity holds

$$\left.\frac{\partial q}{\partial t}\right|_{\tilde{\mathcal{A}}} = (\mathbf{a}.\nabla)q + \frac{\partial q}{\partial t}. \tag{2.30}$$

A general method used to construct the mapping, or equivalently the domain velocity $\mathbf{a}$, consists of solving the the following Laplace equation its boundary condition

$$\begin{aligned} -\nabla^2\mathbf{a} &= 0, \\ \mathbf{a}_{|\partial\Omega} &= \mathbf{f}, \end{aligned} \tag{2.31}$$

where $\mathbf{f}$ is the velocity of the boundary.

A better model for dealing with a computationally more challenging large deformation case can be given by

$$\begin{aligned} -\nabla^2\mathbf{a} + \nabla p &= 0, \\ \nabla \cdot \mathbf{a} &= 0, \\ \mathbf{a}_{|\partial\Omega} &= \mathbf{f}. \end{aligned} \tag{2.32}$$

Let the interaction of an oscillating circular cylinder with a fluid at rest be considered. The problem is to find the velocity vector field $\mathbf{u}$ and the pressure p of a flow satisfying the incompressible Navier-Stokes (2.13) in the domain $\Omega = [-l, l] \times [-h, h]$ with no-slip boundary conditions. no-slip boundary conditions on the cylinder and traction-free boundary condition on the outside border.

In the ALE framework, the weak formulation of the incompressible Navier-Stokes is as follows: find $(\mathbf{u}^{n+1}, p^{n+1}) \in V$ such that

$$\begin{aligned} \int_\Omega \left(\frac{\mathbf{u}^{n+1} - \mathbf{u}^n \circ \mathbf{X}^n}{\Delta t}\right) \cdot \mathbf{v}^{n+1} + \nu \int_\Omega \nabla\mathbf{u}^{n+1} \cdot \nabla\mathbf{v} - \int_\Omega p^{n+1} \nabla \cdot \mathbf{v} &= \int_\Omega f\mathbf{v}, \\ \int_\Omega q \nabla \cdot \mathbf{u}^{n+1} + \varepsilon \int_\Omega p^{n+1} q &= 0, \end{aligned} \tag{2.33}$$

for all $(\mathbf{v}, q) \in V$, where $\mathbf{u}^n \circ \mathbf{X}^n$ is approximated by

$$\mathbf{u}^n \circ \mathbf{X}^n \approx \mathbf{u}^n(\mathbf{x} - (\mathbf{u}^n(\mathbf{x}) - \mathbf{a}^n(\mathbf{x}))\,\Delta t) \approx \texttt{convect}(\mathbf{u}^n - \mathbf{a}^n, -dt, \mathbf{u}^n). \tag{2.34}$$

The horizontal velocity of the cylinder of diameter D is given by $u_c(t) = -U\,\cos(2\pi\,f\,t)$, where $U = 2\pi\,A\,f$. At each time step, the mesh is moved with the command `movemesh` according to the displacement $\mathbf{a}\,\Delta t$, where $\mathbf{a}$ is the solution of (2.31) (see figure 2.13). As soon as the mesh is moved, the computed $\mathbf{a}^n$ and $\mathbf{u}^n$, that are defined in the previous mesh, are then pushed to the new mesh without interpolation following the scheme proposed in [95]. The solution can be computed with the FreeFem++ script 2.18.

```
int n=20,nc=80, M=100;
real Re=100, KC=5., U=1, D=1, R=D/2., A=KC*D/(2*pi), F=U/KC/D;
real L=50*D, H=30*D;
real x0=(-1./2./pi)*sin(2*pi*0),y0=0, nu=1./Re, T=1, dt=T/M;
border b1(t=-L,L){x=t;y=-H;label=1;}
border b2(t=-H,H){x=L;y=t;label=1;}
border b3(t=L,-L){x=t;y=H;label=1;}
border b4(t=H,-H){x=-L;y=t;label=1;}
border c(t=0,2*pi){x=x0+R*cos(t);y=y0+R*sin(t);label=3;}
mesh Th=buildmesh(b1(n)+b2(n*H/L)+b3(n)+b4(n*H/L)+c(-nc));
fespace Vh(Th,P2);
Vh u=0,uu, v=0,vv, uold, vold;
Vh a1,a2,w,s,f1=0,f2=0;
real[int] tmp(u[].n);
fespace Ph(Th,P1);
Ph p=0,pp;
int m=0;
problem MeshVelocity([a1,a2],[w,s], init=m) //Lapalce eq : mesh velocity
                = int2d(Th)(dx(a1)*dx(w)+dy(a1)*dy(w)+dx(a2)*dx(
                    s)+dy(a2)*dy(s))
                        +on(1,2,a1=0,a2=0)
                        +on(3,a1=f1,a2=f2);
problem aleNS([u,v,p],[uu,vv,pp],init=m) //ALE Navier-Stokes eq.
        = int2d(Th)((u*uu+v*vv)/dt
    + nu*(dx(u)*dx(uu)+dy(u)*dy(uu)+dx(v)*dx(vv)+dy(v)*dy(vv))
    - (dx(u)+dy(v))*pp
    + (dx(p)*uu+dy(p)*vv)
    - 1e-5*p*pp)
        -int2d(Th)((convect([uold-a1,vold-a2],-dt,uold)*uu
                + convect([uold-a1,vold-a2],-dt,vold)*vv)/dt)
        +on(3,u=a1,v=a2);
for(m=0;m<M;m++){
        f1=-U*cos(2*pi*F*m*dt);
        f2=0.;
        aleNS; //compute (u,p)
        MeshVelocity; //compute the mesh velocity
        Th = movemesh(Th,[x+dt*a1,y+dt*a2]); //move the mesh
        tmp=u[]; uold=0; uold[]=tmp ; // push to the new mesh
        tmp=v[]; vold=0; vold[]=tmp ; // push to the new mesh
        tmp=a1[]; a1=0; a1[]=tmp ; // push to the new mesh
        tmp=a2[]; a2=0; a2[]=tmp ; // push to the new mesh
        plot(coef=0.1,[u,v],value=1,wait=0); }
```

Script 2.18: Solving the incompressible Navier-Stokes equations in a moving domain with the ALE method

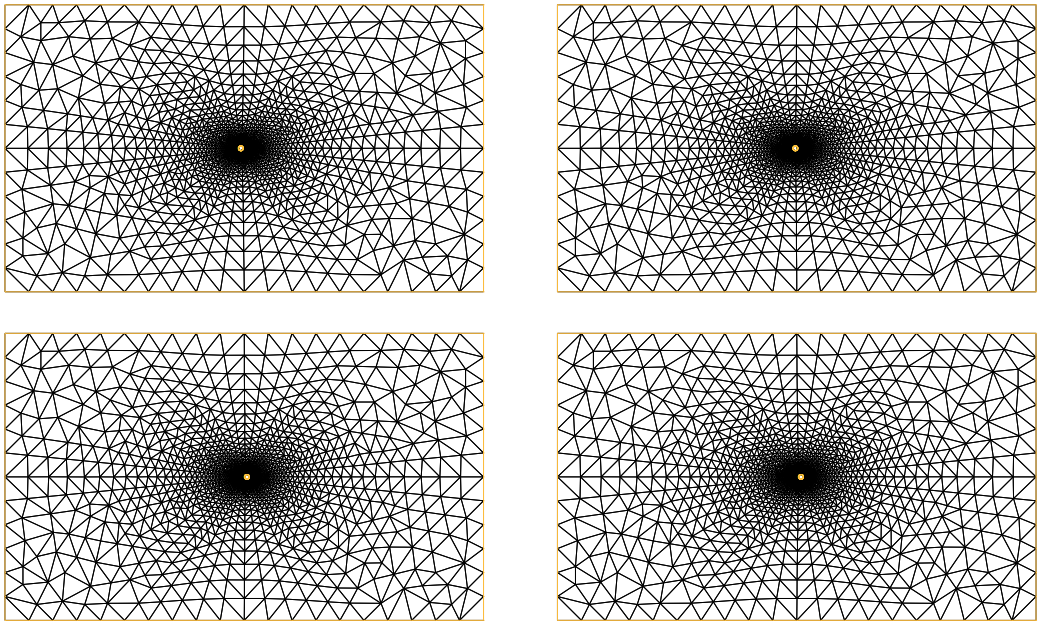

Figure 2.13: Moving meshes in FreeFem++

In figure 2.14, numerical simulation of flow is shown for $\mathrm{Re} = 100$ and $\frac{U}{Df} = 5$, where $U = 1$, $D = 1$, $T := 1/f = 5$, and $A = 5/2\pi$. In figures 2.15, 2.3.3, and 2.17, good comparison between the computed solution, solution from [97], and experimental data from [98] is shown at at three different times corresponding to the three phases $2\pi ft = \pi$, $7\pi/6$, and $11\pi/6$.

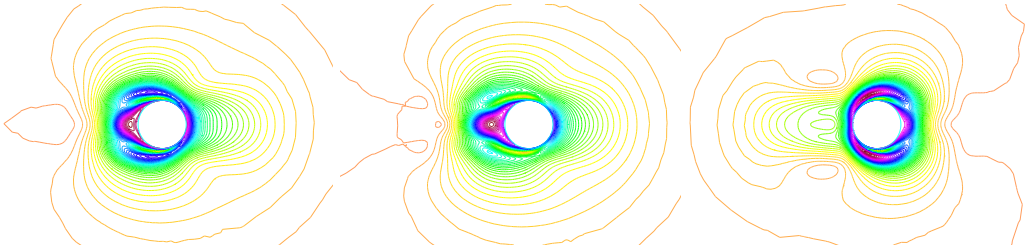

Figure 2.14: Numerical simulation of flow accelerated from rest by an oscillating circular cylinder. Velocity magnitude is at $t = \frac{9}{2}T$ (left), $t = \frac{55}{12}T$ (middle), and $t = \frac{59}{12}T$ (right).

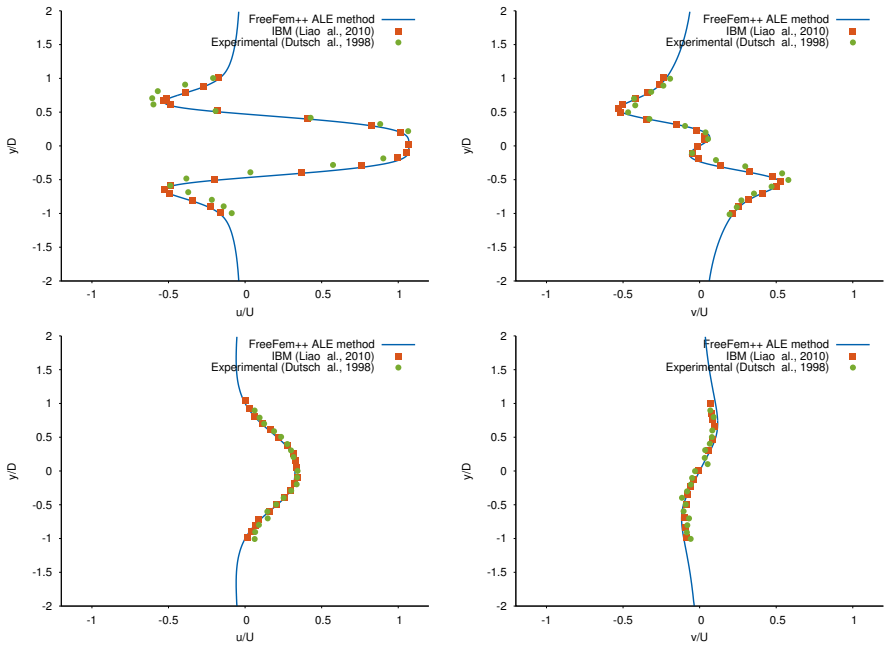

Figure 2.15: Comparison of the computed and referenced solutions along the line $x = -0.6 * D$ (top) and $x = 1.2 * D$ (bottom) for the values of $\mathbf{u} = (u, v)$ at $t = \frac{9}{2}T$.

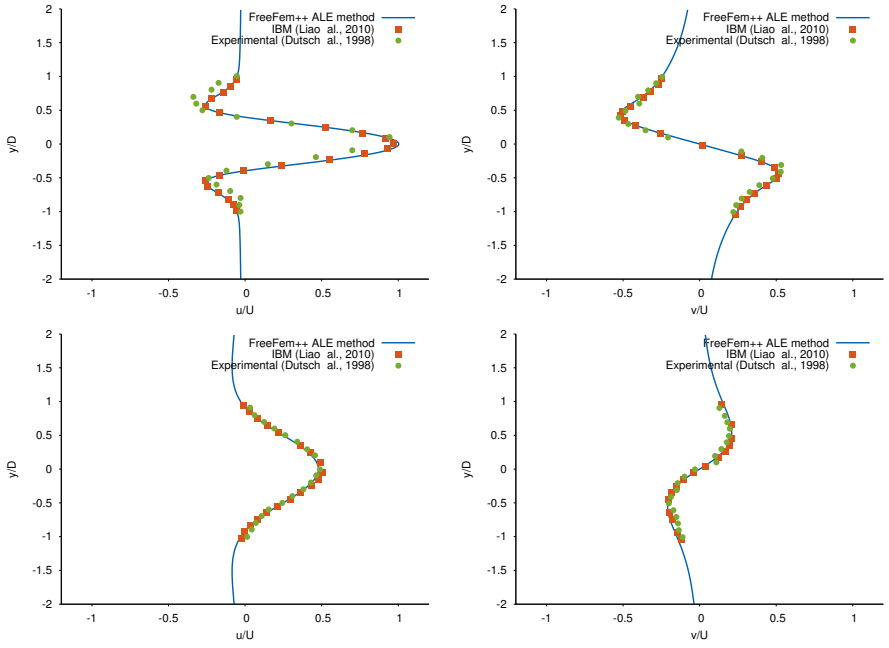

Figure 2.16: Comparison of the computed and referenced solutions along the line $x = -0.6 * D$ (top) and $x = 1.2 * D$ (bottom) for the values of $\mathbf{u} = (u, v)$ at $t = \frac{55}{12}T$.

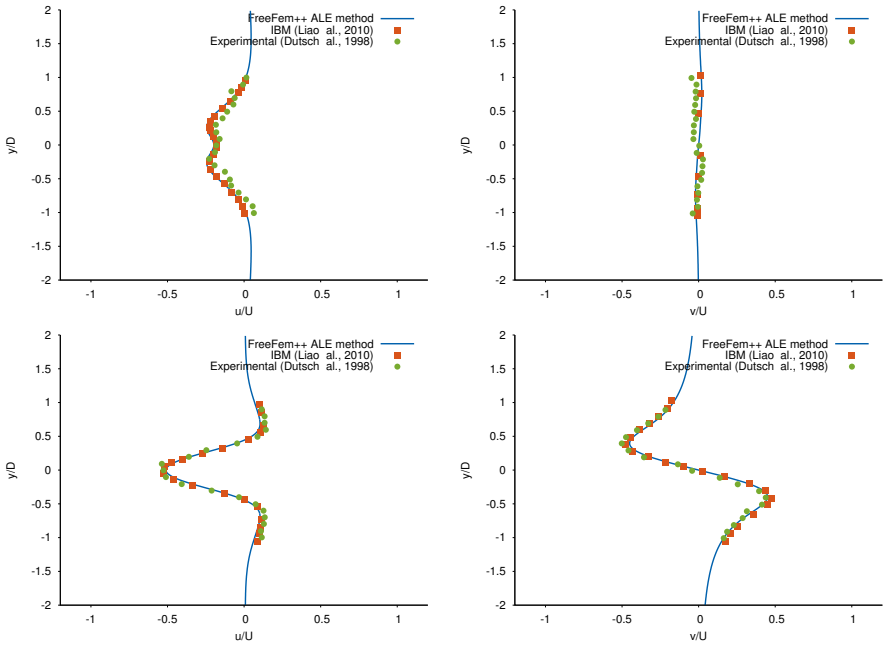

Figure 2.17: Comparison of the computed and referenced solutions along the line $x = -0.6 * D$ (top) and $x = 1.2 * D$ (bottom) for the values of $\mathbf{u} = (u, v)$ at $t = \frac{59}{12}T$.

2.4 Concluding remarks

FreeFem++ makes it easy to generate and manipulate meshes for the resolution of partial differential equations in two and three dimensions. Simple functions presented in this chapter allow the user to perform challenging tasks on a triangulation. External tools and software can be linked with FreeFem++ to deal with more complex tasks especially in three dimensions.

FreeFem++'s major task consists in assembling automatically the stiffness matrix and the right hand side associated with the discretized problem within the framework of the finite element method. Furthermore, FreeFem++ possesses a large panel of linear solvers.

There is no systematic tool to treat evolution and nonlinear problems. Special treatments need to be provided by the user to work within the FreeFem++ framework. This gives a certain advantage in making it possible for to user to work efficiently on a given problem. In the specific case of convection problems, FreeFem++ makes it possible to use the method of the characteristics directly.

Finally, while all the tasks presented in this chapter are sequential, they can be parallelized by calling different processes simultaneously.

Chapter 3

Modeling and simulation of local physical stress field during needling

Contents

3.1 Introduction 78
3.2 Biological medium 78
3.3 Mathematical modeling 79
3.4 Computational model 80
3.4.1 Scaling and setting for numerical simulations 80
3.4.2 Numerical methods 81
3.5 Results and discussion 83
3.5.1 Effect of needle motion on the interstitial flow 83
3.5.2 Effects of fractional fluid volume and Darcy number on the interstitial flow 84
3.5.3 Shear stress and pressure distributions along the cell membrane 88
3.6 Concluding remarks 91

The work presented in this chapter has association with the following publication.

- Y. Deleuze, M. Thiriet, T.W.H. Sheu. "Modeling and simulation of local physical stress on the mastocytes created by the needle manipulation during acupuncture" (forthcoming).

Parameter	Definition	Dimension
Da	Darcy number	
d	cell center/needle tip distance along the x-axis	m
$f_{d,s}$	fiber diameter and spacing	m
L	characteristic length	m
$\mathbf{n}$	unit outward normal vector	
$\mathcal{P}$	Darcy permeability	m^2
p_f	pressure	$\mathrm{kg.\,m^{-1}.\,s^{-2}}$
Re	Rayleigh number	
t	time	s
$\bar{\mathbf{u}}$	averaged velocity vector	$\mathrm{m^{-3}.\,s^{-1}}$
$\mathbf{u}_f$	fluid velocity	$\mathrm{m.\,s^{-1}}$
$\mathbf{v}_{\mathrm{needle}}$	needle velocity	$\mathrm{m.\,s^{-1}}$
V	characteristic velocity	$\mathrm{m.\,s^{-1}}$
$\mathbf{x} = (x, y)$	coordinate axes	
Greek symbols		
α_f	fluid volume fraction	
μ	dynamic viscosity	$\mathrm{kg.\,m^{-1}.\,s^{-1}}$
ρ	fluid density	$\mathrm{kg.\,m^{-3}}$
θ	angle	rad

Table 3.1: Nomenclature and parameter dimensions

Abstract

In this chapter, the effects of an needle, inserted in the subcutaneous tissue, on the interstitial flow is studied. One of the goals is to describe the physical stress affecting cells during acupuncture treatments. A Brinkman model is considered to describe the flow through a fibrous medium. Numerical studies in FreeFem++ are performed to illustrate the acute interstitial pressure developed by the implanted needle that triggers the physiological reactions of acupuncture.

3.1 Introduction

The initiation of the effects of acupuncture is due to the local stress generation. The insertion and manipulation of an acupuncture needle cause the deformation of the interstitial tissue to occur and in turn makes the corresponding change in interstitial flow. The local stress field is sensed by mastocytes and the sensory transduction is immediately followed by Ca^{++} entry and subsequently granule exocytosis. After a short period of needle manipulation, the needle remains in the skin until the desired effects have been obtained. This stimulation can thus lead to a cascade of biochemical reactions that drive acupuncture effects.

In the present chapter, focus is given to the effects of interstitial fluid flow during implantation of an acupuncture needle until the tip has reached the desired location within the hypodermis. The objective of this work is to give a description of the physical stress produced by the interstitial fluid and affecting the network of fibers and cells in the tissue.

3.2 Biological medium

The interstitial fluid contains water, ions and other small molecules. Such a fluid is like plasma without macromolecules. It interacts with the ground substance to form a gel-like medium.

A model taking into account individual fibers and cell adhesion complexes is already a falsification of reality. Moreover, it is very costly from the computational sense. When considering an organized homogeneous matrix of fibers, computation of such a model shows the microscopic fluctuations of the fluid shear stress at the protein level [99].

On a microscopic scale, the interstitial tissue is composed of fluid and solid fibers, thereby clearly forming two phases. Homogenized two-phase media coupling with a Newtonian fluid and an elastic matrix have been considered to model soft tissue [100]. This well-posed model exhibits both the fluid and the viscoelastic property of the fluid.

The interstitial tissue can be modeled as a porous medium. Darcy's law approximates fibers of the media as a continuum and allows us to compute the actual microscopic flow phenomena that occurs in the fibrous media. The phenomenological model cannot give information on unneeded microscopic events but the Darcy equation can describe macroscale flow patterns in porous media.

The Brinkman equation is an extension of the Darcy equation. Introduction of a second order derivative in the Darcy equation allows the application of no-slip boundary conditions. The Brinkman equation can thus describe the flow field around solid bodies such as the embedded cells in extracellular matrix but the fibrous medium itself is still treated as a continuum.

The interstitial tissue can also be modeled by a poroviscoelastic material [18, 101–

104]. The interstitial fluid, cells, and the extracellular matrix are viewed to constitute a two-phase system consisting of a solid and a fluid phase, each of which is regarded as a continuum. Biot's equations for the linear theory of poroelasticity are derived from the equations of linear elasticity for the solid matrix, the Navier–Stokes equations for an incompressible viscous fluid flow, and Darcy's law (1.6) for the flow of a fluid through fibrous matrix.

Interstitial flow and deformed matrix fibers can exert stress directly at the cell surface. This stress can be sensed by membrane molecules. Mastocytes, among other cells, can respond to fluidic stimuli caused by the fluid shear stress [105]. In this chapter, the transient convective Brinkman equations are applied to simulate the interstitial flow in a porous medium deformed by a moving needle.

3.3 Mathematical modeling

In this work, the interstitial tissue is considered as a fluid-filled porous medium. Because the study focuses on the moving needle effects on the interstitial fluid, convective terms should not be neglected. The Reynolds number and the Darcy number are normally small. As a result, the nonlinear drag such as the Forchheimer law [106] can be neglected. The fluid motion is considered to be governed by the incompressible convective Brinkman equations for a fluid-filled porous material. The derivation of the governing equations was given in [107–109] in the context of heat transfer in porous media. The set of equations reads as follows

$$\begin{aligned} \frac{\rho}{\alpha_f}\left(\frac{\partial \bar{\mathbf{u}}}{\partial t} + \bar{\mathbf{u}}\cdot\boldsymbol{\nabla}\left(\frac{\bar{\mathbf{u}}}{\alpha_f}\right)\right) - \mu\nabla^2\bar{\mathbf{u}} + \frac{1}{\alpha_f}\boldsymbol{\nabla}(\alpha_f p_f) &= -\frac{\mu}{\mathcal{P}}\bar{\mathbf{u}} \quad \text{in } \Omega, \\ \boldsymbol{\nabla}\cdot\bar{\mathbf{u}} &= 0 \qquad\quad \text{in } \Omega, \end{aligned} \tag{3.1}$$

where $-\frac{\mu}{\mathcal{P}}\bar{\mathbf{u}}$ denotes the Darcy drag, μ the fluid dynamic viscosity, ρ the fluid density, $\mathcal{P}$ the Darcy permeability, $\bar{\mathbf{u}}$ the averaged velocity and p_f the pressure. The averaged velocity is defined as

$$\bar{\mathbf{u}} = \alpha_f \mathbf{u}_f, \tag{3.2}$$

where $\mathbf{u}_f$ is the fluid velocity and

$$\alpha_f = \frac{\text{fluid volume}}{\text{total volume}} \tag{3.3}$$

is the fluid volume fraction. This volume fraction corresponds to the effective porosity of the medium. The fluid fractional volume α_f is taken as a space-dependent parameter to model the distinguished properties of an acupoint.

The system (3.1), subject to the initial conditions given below, is solved in the domain Ω

$$\bar{\mathbf{u}}(\mathbf{x}, 0) = \bar{\mathbf{u}}_0(\mathbf{x}). \tag{3.4}$$

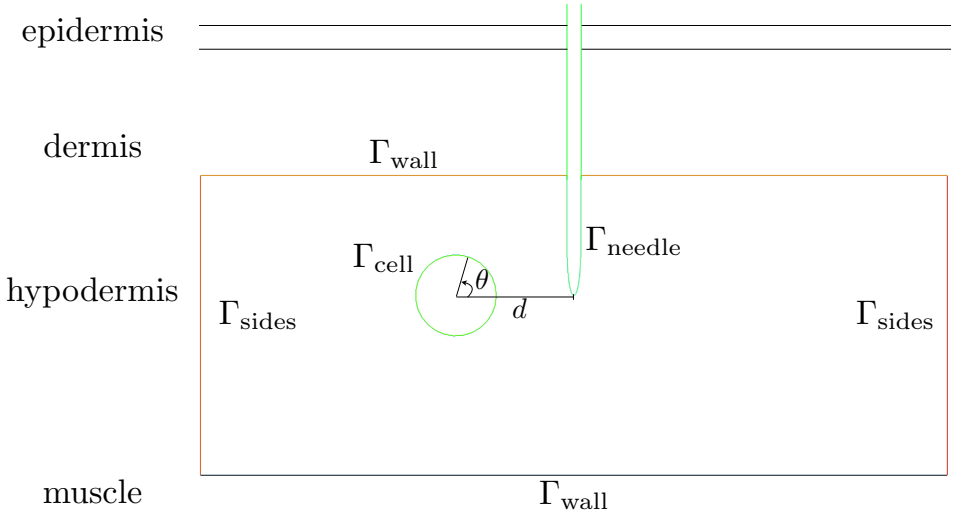

Figure 3.1: Schematic of the computational domain Ω. The cell is mapped to the trigonometric unit circle where θ, in radian, is the angle. d is the distance along the x-axis between the cell center and the needle tip.

The domain boundary (figure 3.1) can be decomposed into the needle boundary denoted by Γ_{needle}, an impervious boundary (wall) denoted by Γ_{wall}, and the open boundary on the sides denoted by Γ_{sides}.

On the top and bottom of the domain Ω, the boundary condition on Γ_{wall} is prescribed as

$$\bar{\mathbf{u}} = 0. \tag{3.5}$$

On the needle boundary Γ_{needle}, the boundary condition is imposed as

$$\bar{\mathbf{u}} = \mathbf{v}_{\text{needle}}. \tag{3.6}$$

On both sides of the domain Ω, the traction-free boundary condition is prescribed on Γ_{sides} as

$$-\mu \boldsymbol{\nabla} \bar{\mathbf{u}} \cdot \mathbf{n} + p_f \mathbf{n} = 0. \tag{3.7}$$

3.4 Computational model

3.4.1 Scaling and setting for numerical simulations

L denotes the characteristic length that is the needle width and V is the characteristic velocity set to be the needle maximum velocity. Rescaling the variables leads to

$$\mathbf{x}' = \frac{\mathbf{x}}{\mathsf{L}}, \quad t' = \frac{t}{(\mathsf{L}/\mathsf{V})}, \quad p' = \frac{p_f}{(\rho V^2)}, \quad \mathbf{u}' = \frac{\bar{\mathbf{u}}}{\mathsf{V}}. \tag{3.8}$$

In the resulting dimensionless form, after removing the prime in the rescaled variables, the dimensionless incompressible convective Brinkman equations read as

$$\frac{1}{\alpha_f}\frac{\partial \mathbf{u}}{\partial t} + \frac{1}{\alpha_f}\mathbf{u}\cdot\boldsymbol{\nabla}\left(\frac{\mathbf{u}}{\alpha_f}\right) - \frac{1}{\mathrm{Re}}\nabla^2\mathbf{u} + \frac{1}{\alpha_f}\boldsymbol{\nabla}(\alpha_f p) = -\frac{1}{\mathrm{Da}\,\mathrm{Re}}\mathbf{u}, \tag{3.9}$$

$$\boldsymbol{\nabla}\cdot\mathbf{u} = 0. \tag{3.10}$$

where Re is the Reynolds number and Da is the Darcy number. The two dimensionless parameters are defined as

$$\mathrm{Re} = \tfrac{\rho \mathsf{L}\mathsf{V}}{\mu}, \quad \mathrm{Da} = \tfrac{\mathcal{P}}{\mathsf{L}^2}. \tag{3.11}$$

In considering the above dimensionless governing equations, the boundary condition on the domain boundary is prescribed as

$$\mathbf{u} = 0 \qquad \text{on } \Gamma_{wall}, \tag{3.12}$$

$$\mathbf{u} = \mathbf{v} \qquad \text{on } \Gamma_{needle}, \tag{3.13}$$

$$-\frac{1}{\mathrm{Re}}\boldsymbol{\nabla}\mathbf{u}\cdot\mathbf{n} + p\mathbf{n} = 0 \qquad \text{on } \Gamma_{sides}. \tag{3.14}$$

3.4.2 Numerical methods

The governing equations in section 5.3.1 are solved using the finite element software FreeFem++ [1]. This code programs discrete equations derived from the finite element weak formulation of the problem presented in section 3.4.2.2 using a characteristic/-Galerkin model to stabilize the convection terms.

3.4.2.1 ALE implementation on moving meshes

In the present section, the ALE framework in FreeFem++, described in section 2.3.3, is employed to compute the flow in the moving domain. In the current problem setting, the motion of needle is prescribed with respect to time. The boundary of the domain is thus known exactly at each time step so that an area preserving mesh can be precisely generated.

In the ALE framework, subject to a prescribed needle motion (see figure 3.4.2.1), the equations (3.9-3.10) become

$$\left.\frac{\partial(\mathbf{u}/\alpha_f)}{\partial t}\right|_{\tilde{\mathcal{A}}} + \left(\left(\frac{\mathbf{u}}{\alpha_f} - \mathbf{a}\right)\cdot\boldsymbol{\nabla}\right)\frac{\mathbf{u}}{\alpha_f} - \frac{1}{\mathrm{Re}}\nabla^2\mathbf{u} + \frac{1}{\alpha_f}\boldsymbol{\nabla}(\alpha_f p) = -\frac{\mathbf{u}}{\mathrm{Da}\,\mathrm{Re}}, \tag{3.15}$$

$$\boldsymbol{\nabla}\cdot\mathbf{u} = 0,$$

in $\Omega(t)$. The solutions $\mathbf{u}$ and p are sought subject to the initial (3.4) and boundary conditions (3.5-3.7) described in section 5.3.1.

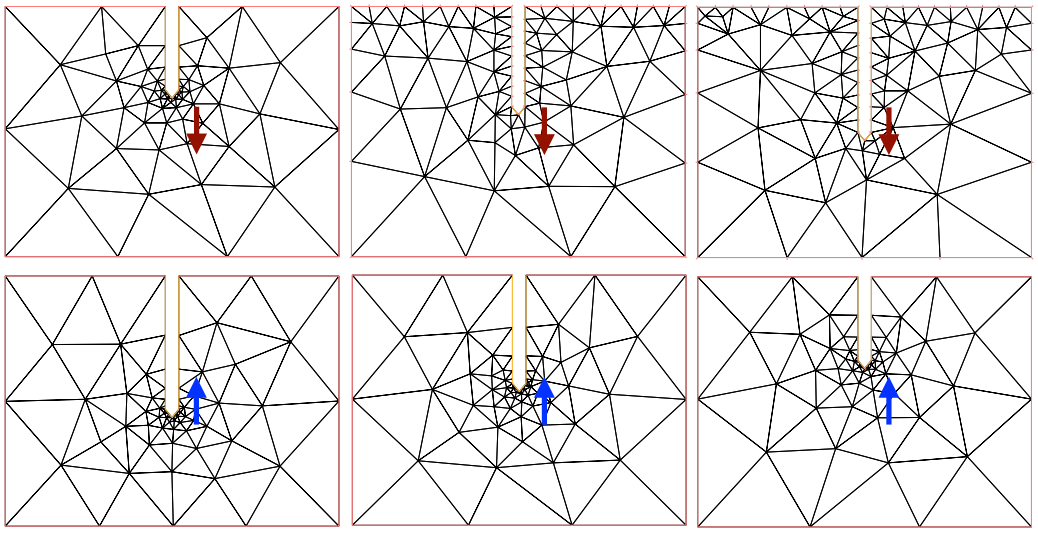

Figure 3.2: Illustration of the prescribed needle position and the corresponding generated meshes. At each time step, the new mesh is generated with the FreeFem++ *movemesh* command.

3.4.2.2 Finite element discretization

To solve for the convective Brinkman equations and to fix the pressure constant part, the convective Brinkman equations with the pseudo compressibility approximation are investigated. The equations read as follows

$$\left.\frac{\partial(\mathbf{u}/\alpha_f)}{\partial t}\right|_{\tilde{\mathcal{A}}} + \left(\left(\frac{\mathbf{u}}{\alpha_f}-\mathbf{a}\right)\cdot\boldsymbol{\nabla}\right)\frac{\mathbf{u}}{\alpha_f} - \frac{1}{\mathrm{Re}}\nabla^2\mathbf{u} + \frac{1}{\alpha_f}\boldsymbol{\nabla}(\alpha_f p) = -\frac{\mathbf{u}}{\mathrm{Da}\,\mathrm{Re}}, \qquad \boldsymbol{\nabla}\cdot\mathbf{u} + \varepsilon p = 0, \tag{3.16}$$

in $\Omega(t)$, where ε is a small parameter. The formulation consisting of (3.16) follows the so-called artificial compressibility method introduced in [81] and [82].

The convective Brinkman equations are approximated with the method of characteristics for the nonlinear convection term and a Galerkin method for the rest of the spatial derivative terms. The time discretization of (3.16) gives

$$\frac{1}{\Delta t}\left(\frac{\mathbf{u}^{n+1}}{\alpha_f} - \left(\frac{\mathbf{u}^n}{\alpha_f}\right)\circ\mathbf{X}^n\right) - \frac{1}{\mathrm{Re}}\nabla^2\mathbf{u}^{n+1} + \frac{1}{\alpha_f}\boldsymbol{\nabla}(\alpha_f p^{n+1}) = -\frac{\mathbf{u}^{n+1}}{\mathrm{Da}\,\mathrm{Re}}, \qquad \boldsymbol{\nabla}\cdot\mathbf{u}^{n+1} + \varepsilon p^{n+1} = 0, \tag{3.17}$$

in Ω^{n+1}. Note that $\mathbf{X}^n$ is approximated by $\mathbf{X}^n \approx \mathbf{x} - \left(\frac{\mathbf{u}^n}{\alpha_f} - \mathbf{a}^n\right)(\mathbf{x})\,\Delta t$. For all $\varphi \in$

$H^{1/2}(\Gamma_{\text{needle}})$, let us introduce the product space

$$V_\varphi = \left\{(\mathbf{w}, q) \in [H^1(\Omega)]^2 \times L^2(\Omega), \mathbf{w} = \varphi \text{ on } \Gamma_{\text{needle}}, \mathbf{w} = 0 \text{ on } \Gamma_{\text{wall}}\right\}. \tag{3.18}$$

Let

$$(a, b) = \int_{\Omega^{n+1}} ab \, \mathrm{d}\mathbf{x}. \tag{3.19}$$

The weak formulation sets into a finite dimensional linear system: find $(\mathbf{u}^{n+1}, p^{n+1}) \in V_g$ such that

$$\begin{aligned} \frac{1}{\Delta t}\left(\frac{\mathbf{u}^{n+1}}{\alpha_f} - \left(\frac{\mathbf{u}^n}{\alpha_f}\right) \circ \mathbf{X}^n, \mathbf{w}\right) + \frac{1}{\mathrm{Re}}\left(\frac{1}{\alpha_f}\boldsymbol{\nabla}\mathbf{u}^{n+1}, \boldsymbol{\nabla}\mathbf{w}\right) \\ - \left(\alpha_f \, p^{n+1}, \boldsymbol{\nabla} \cdot \left(\frac{\mathbf{w}}{\alpha_f}\right)\right) + \frac{1}{\mathrm{Da}\,\mathrm{Re}}\left(\mathbf{u}^{n+1}, \mathbf{w}\right) = 0, \\ \left(\boldsymbol{\nabla} \cdot \mathbf{u}^{n+1}, q\right) + \varepsilon\left(p^{n+1}, q\right) = 0, \end{aligned} \tag{3.20}$$

for all $(\mathbf{w}, q) \in V_0$.

The Taylor-Hood $\mathbb{P}_2$–$\mathbb{P}_1$ elements are adopted to ensure satisfaction of the LBB stability condition [84–87]. Note that temporal accuracy order of the presented characteristic/Galerkin method is one. Meshes are generated within FreeFem++ so that calculation of the solution is independent of the mesh. Mesh adaptation is performed prior to simulations so as to enhance mesh quality around the needle and the cell.

3.5 Results and discussion

3.5.1 Effect of needle motion on the interstitial flow

In this study, the needling direction is perpendicular to the skin surface. In practice, the needling direction can be oblique to the skin surface. The simulation results show that the insertion of an acupuncture needle can influence interstitial fluid flow. Indeed, under a stress field glycoproteins undergo fluidization. The computed velocity field shows that the magnitude of the velocity is higher in regions close to the needle tip (figure 3.3) and can vanish quickly at a location away from the needle due to repolymerization of glycoprotein constituents.

Furthermore, when the needle reaches its maximum speed, the interstitial pressure gradient becomes higher at a location close to the needle tip (figure 3.4). The changes in the interstitial fluid flow and the high pressure gradient can affect the activities of the mastocyte pools near the stimulated area. Local mastocyte pools can be activated in regions close to the acupoint and remain granulated outside this region of triggered mechanical stress. Degranulation is effective only where the mechanical stress is high

enough. Results of the numerical simulation in figures 3.5 and 3.6 show how the pressure and shear stress, respectively, evolve according to the distance from the needle. Both shear stress and pressure are larger near the needle and diminish quickly at a location away from the needle.

3.5.2 Effects of fractional fluid volume and Darcy number on the interstitial flow

In this section, the focus is on to the effects of the variation of the fractional fluid volume α_f, defined in (3.3), and the Darcy number Da, defined in (3.11), on the incompressible convective Brinkman equations (3.9) subject to the needle motion. The fractional fluid volume α_f and the Darcy permeability $\mathcal{P}$ are chosen to model the fibrous tissue matrix. It is noted that the fractional fluid volume and the permeability alone cannot fully describe the microscopic behavior of the fiber matrix. In soft tissues, the permeability of the tissue P varies with the fluid volume fraction α_f [65]. Amongst the laws for the permeability of the tissue reported in [110], the Karman-Kozeny relation given in [111] is adopted. The Karman-Kozeny equation relates the permeability $\mathcal{P}$ to the fractional fluid volume α_f and the extracellular matrix fiber properties. With a simplified and structured network of cylindrically parallel and perpendicular fibers, the Karman-Kozeny function [65] is a decreasing function of α_f. The Karman-Kozeny function reads as follows

$$\mathcal{P} = \frac{\alpha_f \, f_r^2}{f_k} \tag{3.21}$$

where $f_r = (f_s^2 - f_d^2)/4f_d$ and $f_k = (2/3)k_+ + (1/3)k_-$. Note that f_d and f_s correspond to the fiber diameter and the fiber spacing, respectively.

$$k_+ = 2\alpha_f^3/(1-\alpha_f)\left[\ln(1/(1-\alpha_f)) - (1-(1-\alpha_f)^2)/(1+(1-\alpha_f)^2)\right]$$

and

$$k_- = 2\alpha_f^3/(1-\alpha_f)\left[2\,\ln(1/(1-\alpha_f)) - 3 + 4(1-\alpha_f) - (1-\alpha_f)^2\right]$$

model the resistance to a flow perpendicular and parallel to the fibers, respectively.

The flow through interstitium is computed according to the data given in [110]. The simulation results shown in figure 3.7 suggest that the effects of the needle on the interstitial pressure are more effective in a tissue richer in fibers. A slight change of the fluid fraction volume results in a substantial change in the pressure field. In particular, acupoints are located in regions close to neurovascular bundles, in which fibrous matrix, capillaries, lymphatic vessels, nervous structures, and cells abound. It is therefore reasonable to make the assumption that the fractional fluid volume α_f is lower at the acupoint loci. Thus, higher interstitial pressure is expected at the acupoint.

If parameters α_f and $\mathcal{P}$ are space dependent, the assumption that they decrease locally reaching their minimum precisely at the acupoint can be made. According to the α_f and

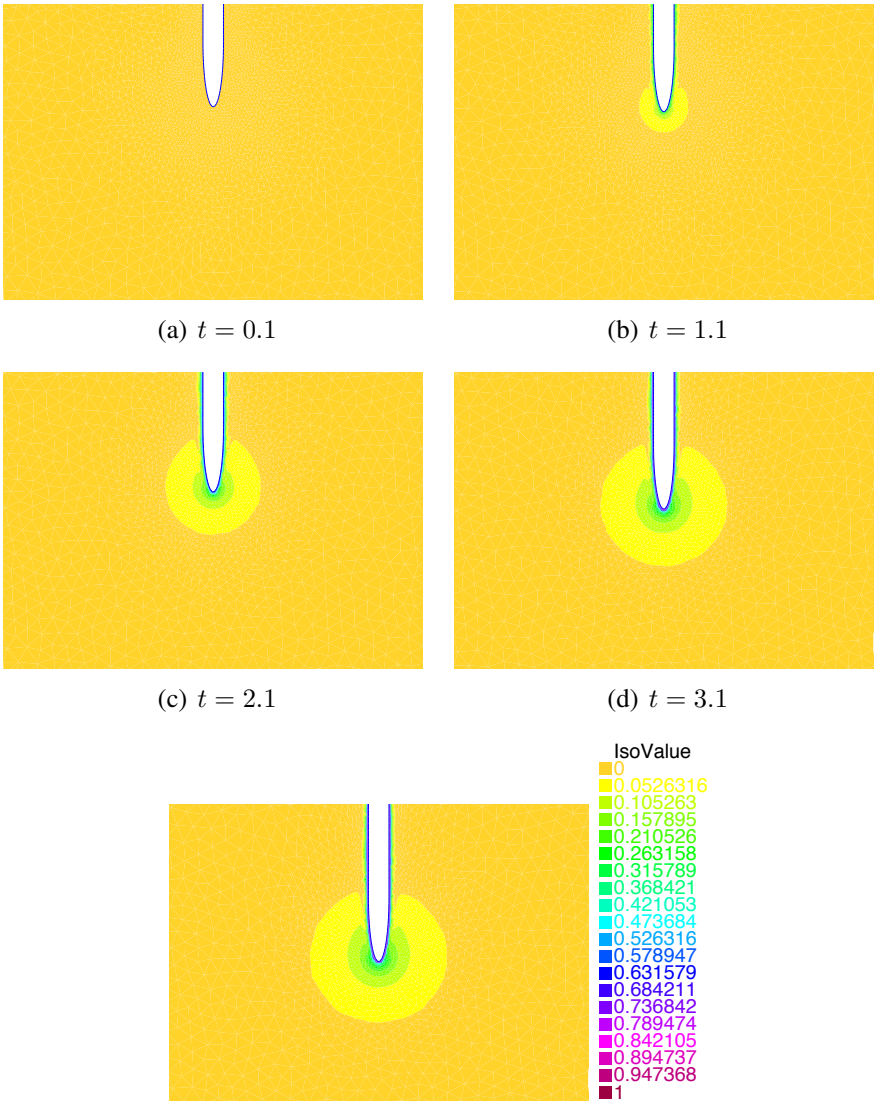

(a) $t = 0.1$ (b) $t = 1.1$

(c) $t = 2.1$ (d) $t = 3.1$

(e) $t = 4.1$

Figure 3.3: The simulated velocity magnitude $|\mathbf{u}|$ resulting from the needle motion in interstitial fluid given at different times.

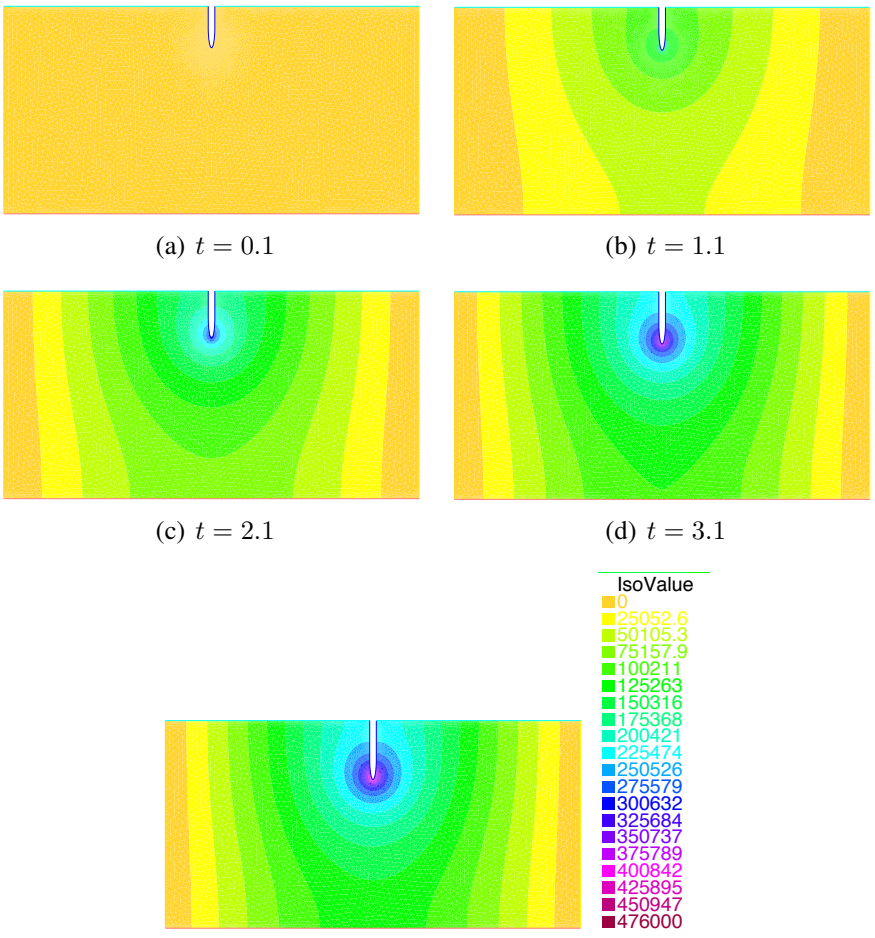

(a) $t = 0.1$ (b) $t = 1.1$

(c) $t = 2.1$ (d) $t = 3.1$

(e) $t = 4.1$

Figure 3.4: The simulated pressure profiles resulting from the needle motion in interstitial fluid.

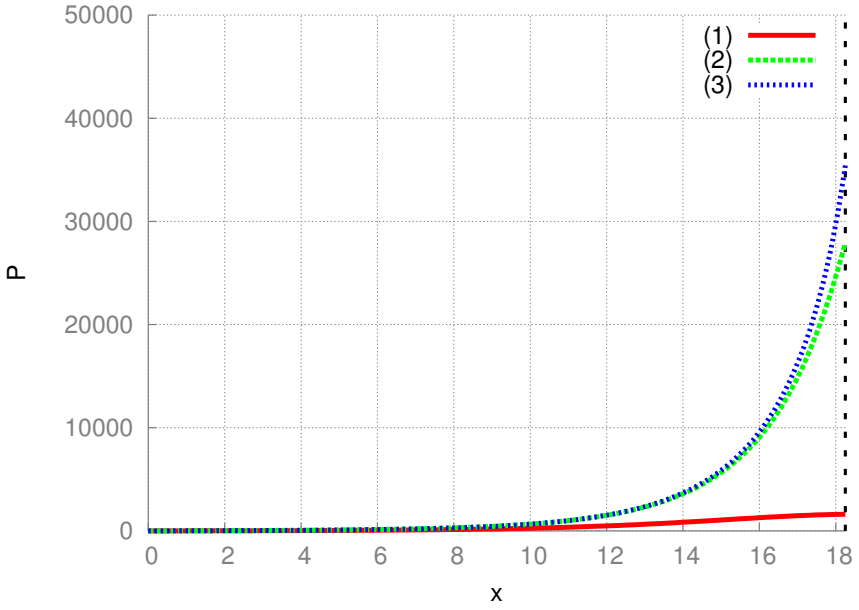

(a) Convective Brinkman result: $\mathrm{Re} = 0.208$, $\mathrm{Da} = 3.48 \times 10^{-05}$, $\alpha_f = 0.6$.

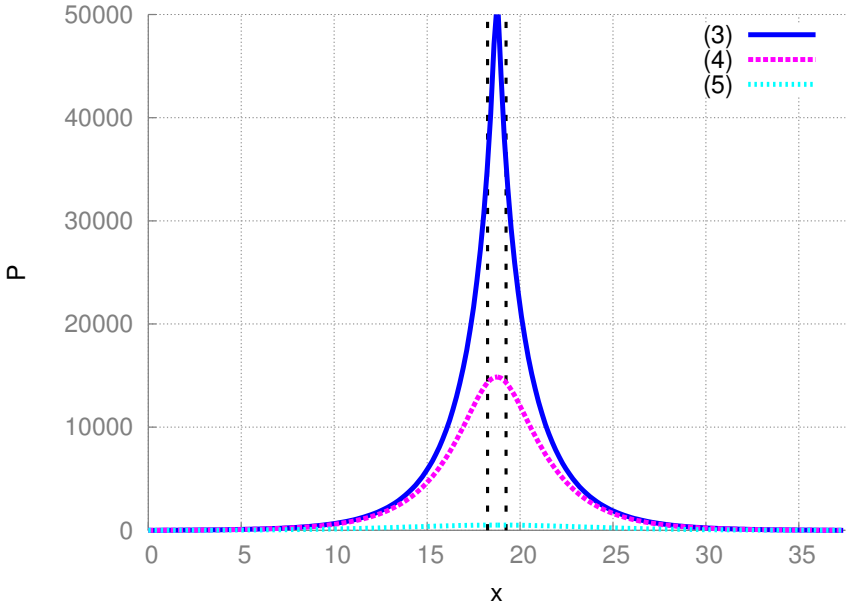

(b) Convective Brinkman result: $\mathrm{Re} = 0.208$, $\mathrm{Da} = 3.48 \times 10^{-05}$, $\alpha_f = 0.6$.

Figure 3.5: The simulated pressure profiles p at different vertical locations: (1) at half the height of the needle, (2) the middle of the needle tip, (3) the needle tip, at (4) half the height of the needle tip under the needle, and (5) half the height between the needle tip and the bottom wall. The lines in dots show the x-position of the needle.

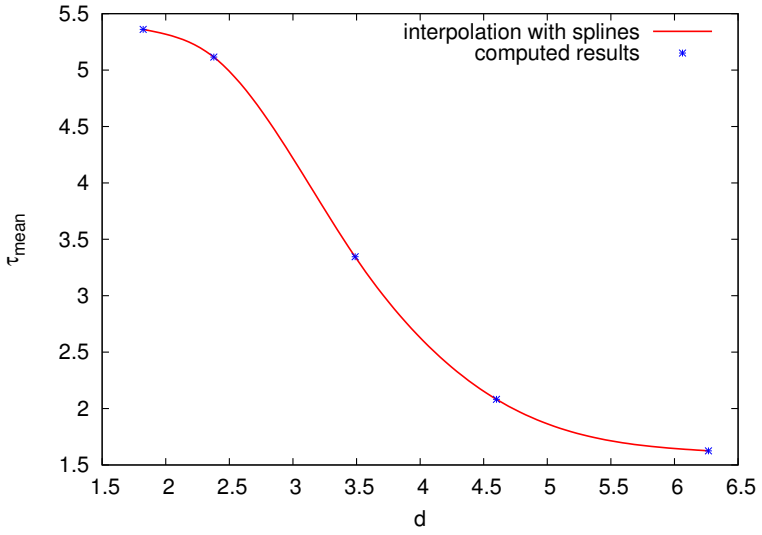

Figure 3.6: The simulated mean shear stress τ_{mean} on the cell surface with respect to the distance d measured from the needle (see figure 3.1). A higher shear stress is expected to be observed at a location close to the needle.

$\mathcal{P}$ distributions on the one hand and to the needle position with respect to the location of the peak density of fibers (see figures 3.8(a), 3.8(b), and 3.8(c)) on the other hand, the effects of the needle on the interstitial flow are greater when the needle is inserted exactly where α_f reaches its minimum (see figure 3.8(d)). These simulation results reveal that a proper location of the insertion of the needle is relevant to this model for interstitial fluid.

The results show that the particularity of acupoints seems to procure a more suitable mechanical environment for the cells. A denser distribution of cells, neurovascular components, and concentration produce a high resistance to flow within the interstitium. High interstitial fluid pressure is only achieved close to the needle.

3.5.3 Shear stress and pressure distributions along the cell membrane

In this section, focus is on the effects of fluidic stimuli on an interstitial cell. Simulations are carried out by considering no-slip boundary condition prescribed at the cell surface. Figure 3.9 shows the velocity magnitude and the pressure contours with a cell added closely to the needle.

Figure 3.10 shows the distribution of the shear stress and the pressure along the cell surface. The cell is mapped to the trigonometric unit circle, where θ denotes the angle in radian. The pressure on the cell surface is higher at a point closest to the needle tip ($\theta \in [\frac{\pi}{2}, \frac{3\pi}{2}]$), whereas the shear stress can be higher on the side furthest from the needle ($\theta \in [-\frac{3\pi}{2}, \frac{\pi}{2}]$). The interstitial flow induced by needle motion leads to a phase shift

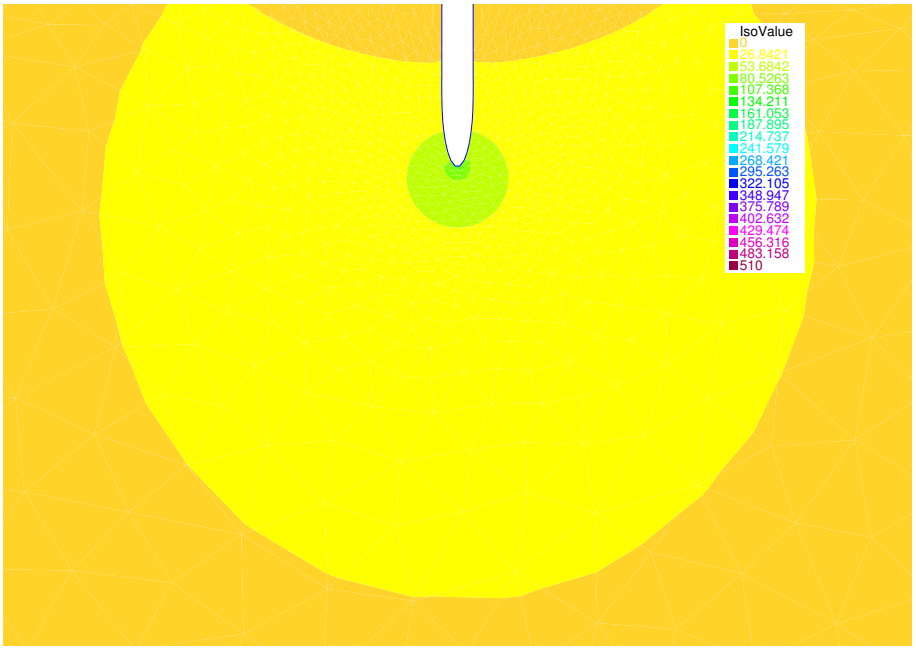

(a) $\alpha_f = 0.7$, Da $= 0.321$, Re $= 0.103$

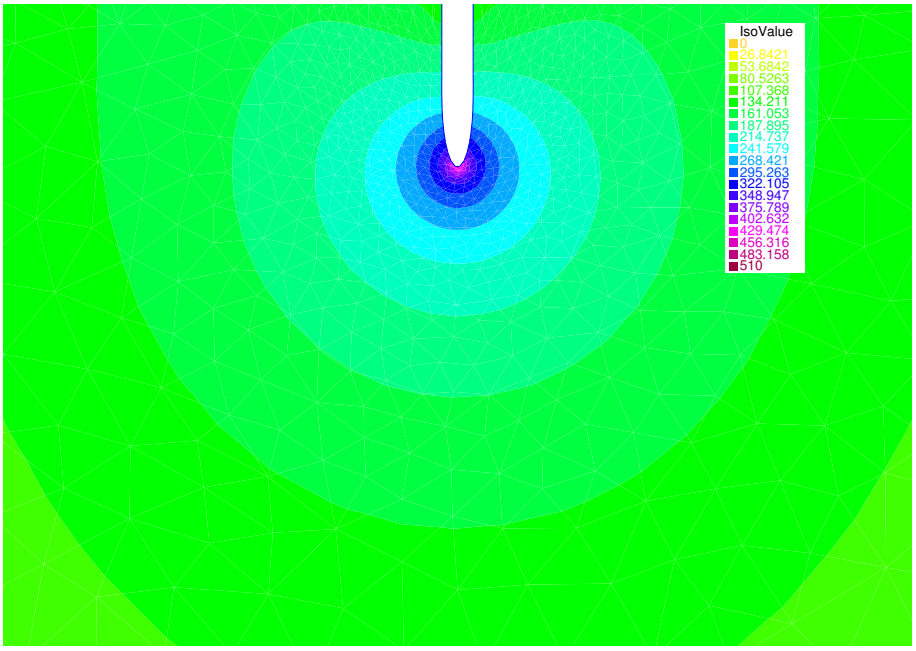

(b) $\alpha_f = 0.6$ Da $= 0.040$, Re $= 0.103$

Figure 3.7: The simulated pressure profiles resulting from the motion of a needle in interstitial fluid at acupoint (right) and at a non-acupoint (left). High interstitial pressure is only expected to occur at acupoint.

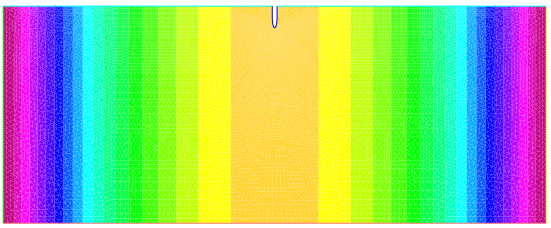

(a) α_f distribution with needle at acupoint.

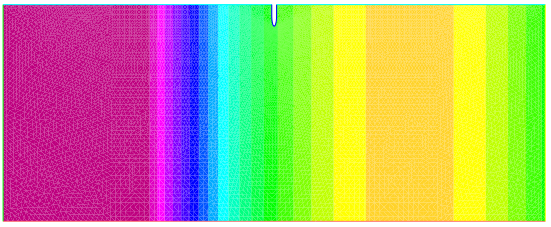

(b) α_f distribution with needle close to acupoint.

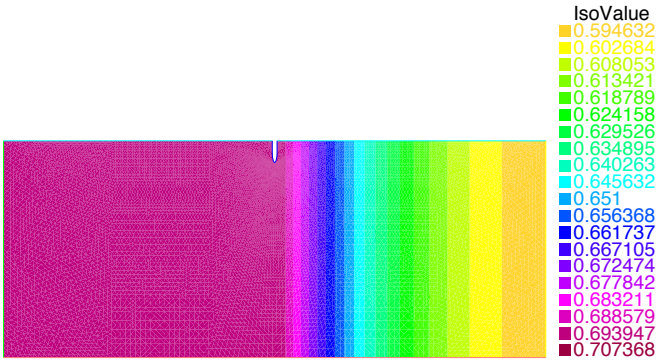

(c) α_f distribution with needle far from acupoint.

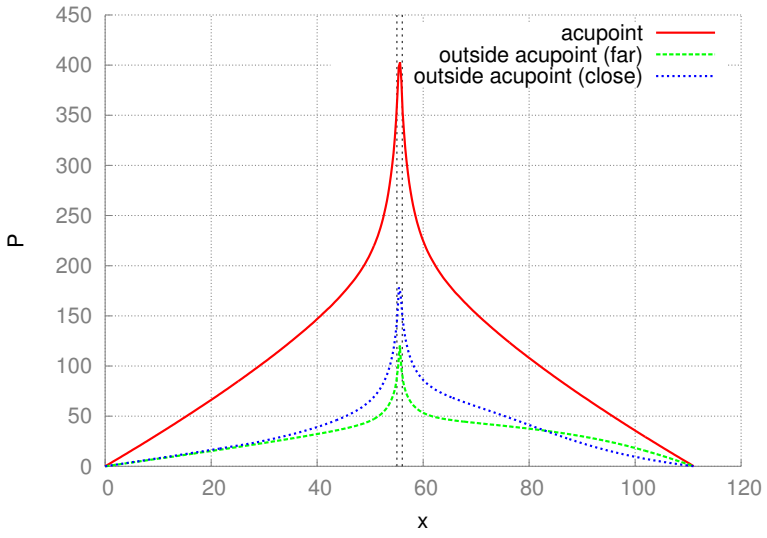

(d) Pressure p resulting from the motion of the needle at different locations.

Figure 3.8: The α_f profiles given (a) at the acupoint, (b) close to the acupoint, and (c) far from the acupoint. For each numerical experiment, the needle is inserted at the same coordinate while the α_f distribution is shifted. (d) The corresponding simulated pressure profiles. High interstitial pressure is only expected to occur when the needle, displayed by the dot lines, is inserted at acupoint.

around the cell surface of the maximum shear stress and pressure value. This shows that the entire cell surface could be stimulated.

Mastocytes have been shown to respond to fluid shear stress [53]. These local mechanical forces participate in the activation of mechanoresponsive proteins on the cell surface [6] so that Ca^{++} is allowed to enter the cytosol via pressure and shear stress gated ion channels.

3.6 Concluding remarks

This chapter has shown that the numerical prediction of the interstitial pressure and shear stress is an essential tool to gain a better understanding of the mechanism involved in acupuncture needling. In the present study, the deformation of the extracellular matrix is neglected and only the effect of interstitial flow is considered, which leads to the following general remarks.

The proposed model for the interstitial flow is able to describe the shear stress on a given mastocyte and the interstitial pressure from the macroscopic point of view. The simulation results suggest that the needling is most effective when needles are accurately inserted and manipulated. High local fluid pressure and shear stress on cells are most likely to appear near the needling region. Fluidic stimuli can then contribute to the mastocyte activation via sensory transduction that is immediately followed by granule exocytosis.

The numerical results shown in this chapter seem to be sensitive to the fractional fluid volume and Darcy permeability. These two parameters describe the macroscopic property of the fiber matrix. The choice for the value of these parameters is a limitation of the model due to the lack of biological data. Thus, it is not possible to build a quantitative model for the acupoint.

The proposed method does not allow the rotation of the needle to be taken into account. When considering the rotation of the needle, a large deformation of the tissue is observed with the twisting of the fibers around the needle, that in turn makes the corresponding change in interstitial flow. A 3D fluid/structure model taking into account the mechanics of the fibers should then be considered.

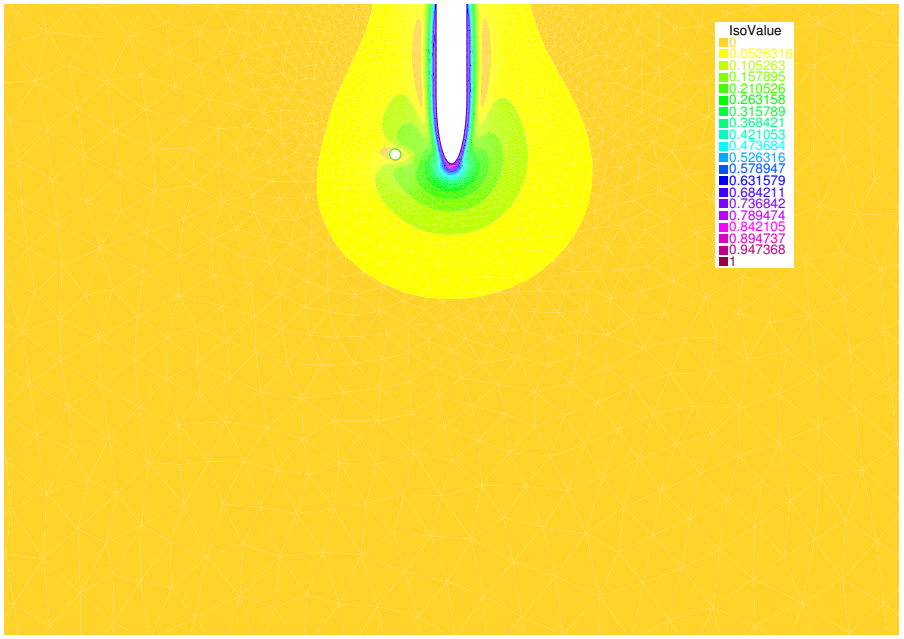

(a)

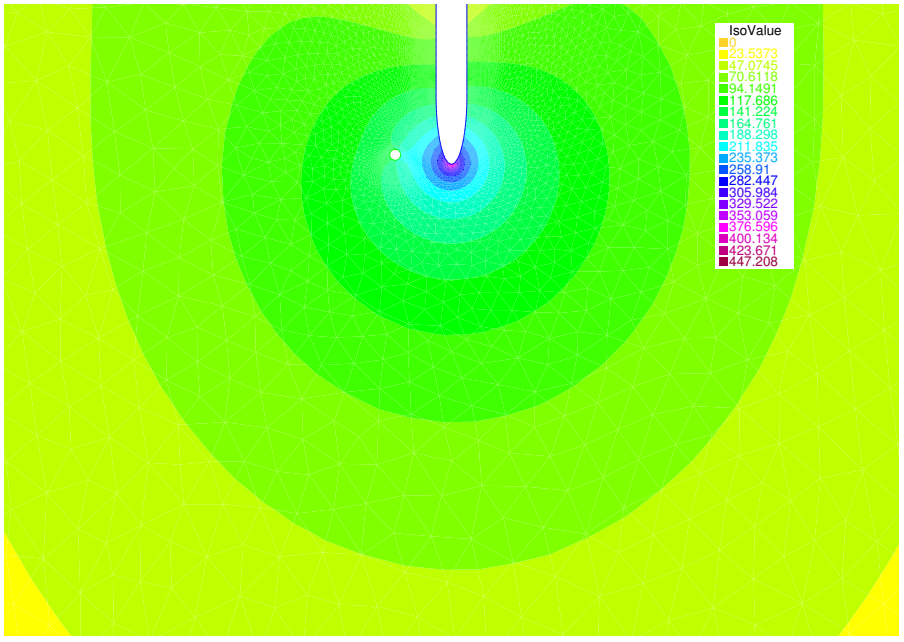

(b)

Figure 3.9: The simulated (a) velocity and (b) pressure profiles with an interstitial cell

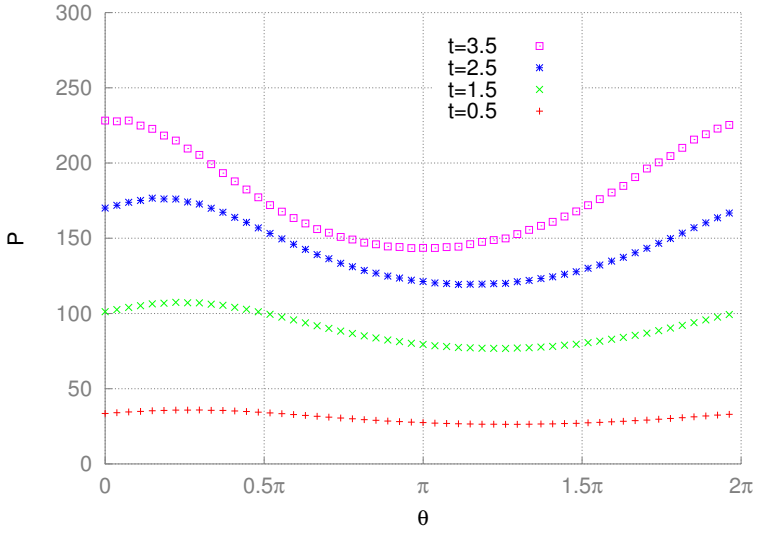

(a)

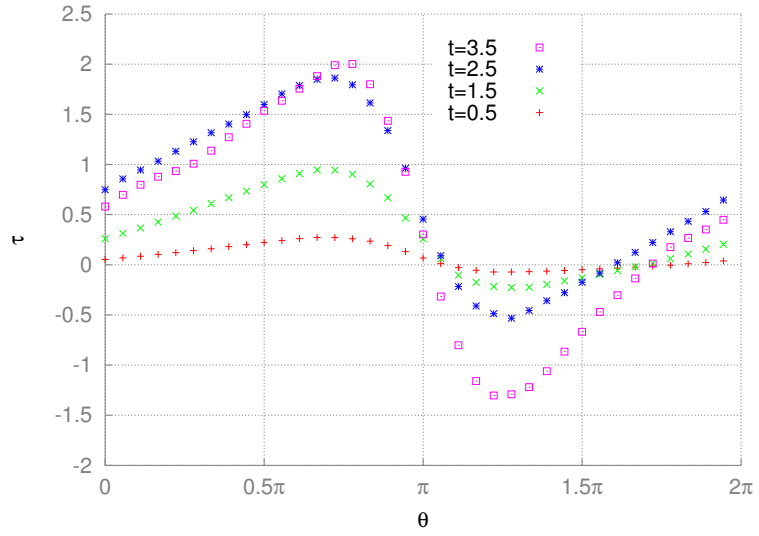

(b)

Figure 3.10: Evolution of (a) the pressure and (b) the shear stress distributions along the cell surface. The cell is mapped to the trigonometric unit circle where θ, in radian, is the angle defined in figure 3.1.

Chapter 4

Mastocyte response to acupuncture

Contents

4.1 Introduction 96
4.2 Mathematical model of mastocyte response to acupuncture treatment 98
4.3 Blow-up and existence conditions in the Keller-Segel system 100
4.4 Blow-up condition in a simplified system with mass conservation . . 104
4.5 Blow-up condition in the case of a sole state for mastocytes 108
4.6 Existence condition in the case of a sole state for mastocytes 112
4.7 Scaling and numerical method 113
4.7.1 Scaling 113
4.7.2 Finite element method 114
4.8 Computational model 121
4.8.1 Acupoints 121
4.8.2 Stress function Φ 122
4.9 Numerical results 124
4.10 Concluding remarks 124

The work presented in this chapter has association with the following publications.

- Y. Deleuze, "A mathematical model of mastocyte response to acupuncture needling," *Comptes Rendus Mathematique* 351, 101–105 (2013).
- M. Thiriet. "Conclusion," in *Intracellular Signaling Mediators in the Circulatory and Ventilatory Systems*, 911–918. Biomathematical and Biomechanical Modeling of the Circulatory and Ventilatory Systems 4. Springer New York, 2013.
- M. Thiriet, Y. Deleuze, T.W.H. Sheu. "A Biological Model of Acupuncture and its Derived Mathematical Modeling and Simulations" (forthcoming).

Parameter	Definition	Dimension
$n_\cdot$	mastocyte number density	m^{-3}
c	chemoattractant concentration	$\mathrm{mol.\,m}^{-3}$
$s_\cdot$	stimulant concentration	$\mathrm{mol.\,m}^{-3}$
S	chemotactic sensitivity of mastocytes	$\mathrm{m}^5.\,\mathrm{s}^{-1}.\,\mathrm{mol}^{-1}$
A	activation rate of mastocytes	s^{-1}
k_r	regeneration rate	s^{-1}
$\mathcal{D}_\cdot$	diffusion coefficient	$\mathrm{m}^2.\,\mathrm{s}^{-1}$
$\delta_\cdot$	degradation rate	s^{-1}
$\kappa_\cdot$	release quantity coefficient	mol
Φ	physical stress function	
ℓ	distance range of the applied stress	m
t	time	s
x	spatial coordinate	m
Subscripts		
$\cdot_m$	mastocyte	
$\cdot_c$	chemoattractant	
$\cdot_{s_n}$	nerve stimulant	
$\cdot_{s_e}$	endocrine stimulant	

Table 4.1: Nomenclature and parameter dimensions

Abstract

A new mathematical model, related to the Keller-Segel system for chemotaxis, is proposed to describe chemotaxis of mastocytes in response to physical stimuli. First, a biological model is developed, based on stimulation in a given domain around a mastocyte population. A simple mathematical model is studied analytically and demonstrates the conditions filled by a mastocyte population to operate efficiently. A theorem gives the blow-up condition. Blow-up of the solution is interpreted as a hyper reactivity at the acupoint where a large quantity of mastocytes is suddenly found. Conversely, if the forcing term times the initial condition is not large, the solution to the coupled nonlinear partial differential equations exists. Chemotaxis and continuous recruitment of mastocytes provide long-standing signaling. Therefore, the density and distribution of mastocytes are crucial factors for efficient acupuncture treatments.

4.1 Introduction

Mathematical modeling of chemotaxis was developed by Patlak Patlak [112] and Keller and Segel Keller and Segel [113]. The Keller-Segel model, also called Keller-Segel-Patlak model, describes the collective motion of cells that are attracted by chemical stimuli and are able to emit it.

Chemotaxis refers to several mechanisms through which small organisms can move in response to a chemical signal. These small organisms possess several biological mechanisms that allow them to move. Some organisms such as the bacterium Escherichia coli are propelled by flagella. Other organisms such as the Amebae Dictyostelium discoïdeum can crawl using internal arms. Another example is the so-called mesenchymal migration characterized by the formation of adhesive interactions with the extracellular matrix, like in the case of fibroblasts [114].

The migration of cells occurs in many physiological and pathophysiological processes. For example, in cancer development, cancerous cells move to the vasculature then penetrate the vasculature to create metastases. Angiogenesis refers to the motion of endothelial cells to form new blood vessels from preexisting vessels so as to locally supply oxygen. During tumor growth, tumor cells secrete a set of substances to attract endothelial cells [115, 116].

In chemotaxis models, the signal that attracts the other cells is produced by the cells and in angiogenesis models, the signal is exogenous and consumed by the cells. Chapter chapter 5 deals with another application of cell chemotaxis that can be classified as an "angiogenesis" type of model.

The time derivative of the cell density depends on cell diffusion flux, cell chemotactic flux, cell proliferation, and cell death rate. The chemotactic flux is a function of the chemotactic sensitivity to a chemoattractant concentration, the available cell number, and the chemoattractant concentration gradient. The time derivative of the chemoattractant concentration depends on the production and destruction rates as well as on the chemoattractant diffusion flux. A general form of the chemotaxis system of PDEs in two dimensional domain reads

$$\begin{aligned}
\frac{\partial n}{\partial t} - \nabla^2 \mathsf{d}(n) + \nabla \cdot (\mathsf{s}(n,c) n \nabla c) &= \mathsf{g}(n,c) \qquad && t \geq 0, x \in \Omega \\
\varepsilon \frac{\partial c}{\partial t} - \mathsf{d} \nabla^2 c &= \mathsf{p}(u)\, n - \tau^{-1} c && t \geq 0, x \in \Omega \\
n_{|_{t=0}}(x) &= n_0(x) \geq 0 \\
c_{|_{t=0}}(x) &= c_0(x) \geq 0
\end{aligned} \tag{4.1}$$

where $n(x,t)$ denotes the cell density number and $c(x,t)$ is the chemoattractant concentration. The first equation expresses the evolution of the cell density number subject to the random or nonlinear diffusion and growth ($\mathsf{g}(.)$) with a bias directed by the chemoattractant sensitivity $\mathsf{s}(.)$ of the cells. $\mathsf{p}(.)$ and $\mathsf{d}(.)$, and τ^{-1} describe the production, diffusion,

and degradation of the cells, respectively.

Because the number of cells is expected to be constant in time, the above system is endowed with homogeneous Neumann boundary condition

$$\mathbf{n} \cdot \nabla n = 0, \quad \mathbf{n} \cdot \nabla c = 0 \quad \text{on } \partial\Omega, \tag{4.2}$$

or zero total flux boundary condition

$$\mathbf{n} \cdot (\nabla n - \mathsf{s}(c)\nabla c) = 0, \quad \mathbf{n} \cdot \nabla c = 0 \quad \text{on } \partial\Omega, \tag{4.3}$$

where $\mathbf{n}$ denotes the outward unit normal on the boundary $\partial\Omega$.

The Keller-Segel system proposed by Patlak [112] and Keller and Segel [113], which is the minimal model of chemotaxis, in it's dimensionless form, reads

$$\begin{aligned} \frac{\partial n}{\partial t} - \nabla^2 n + \nabla \cdot (\mathsf{S} n \nabla c) = 0, \qquad & t \geq 0, x \in \Omega, \\ \varepsilon \frac{\partial c}{\partial t} - \nabla^2 c = n - \tau^{-1} c, \quad & t \geq 0, x \in \Omega, \\ n_{|_{t=0}}(x) = n_0(x) \geq 0, & \\ c_{|_{t=0}}(x) = c_0(x) \geq 0. & \end{aligned} \tag{4.4}$$

The previous system can be obtained from the general model (4.1) by choosing the following coefficients:

$$\mathsf{D}(n) = n, \quad \mathsf{s}(n, c) = \mathsf{S}, \quad \mathsf{g}(n, c) = 0, \quad \mathsf{p}(c) = 1, \quad \mathsf{d}(n) = 1.$$

Mathematical analysis mainly focuses on pattern formation and blow-up phenomena in finite time. Existence and boundedness of the solution of the Neumann problem for the Keller-Segel system (4.1) has been studied under the assumption that $\mathsf{s}(n, c) = \mathsf{s}(n)$, $\mathsf{g}(n, c) = 0$ and $\frac{\mathsf{s}(n,c)\, n}{\mathsf{D}'(n)}$ is small enough [117, 118]. On the other hand, for $\frac{\mathsf{s}(n,c)\, n}{\mathsf{D}'(n)}$ large enough, smooth solutions blow-up in finite or infinite time [119]. For the case of degenerate diffusion ($\mathsf{D}'(n) = 0$), the reader can refer to [120]. When considering g and D to be Lipschitz continuous, local existence of weak solutions to (4.1) is proven in [121]. In the case of non-Lipschitz function g, the reader can refer to [122].

Key contributions on chemotactic collapse of the solution of the Keller-Segel system (4.5) have been brought in [123–128].. Especially, for a small initial mass it has been proven [123] that the system is well-posed globally in time. But there is blow-up, i.e. the solution does not remain bounded in a finite time, for a large initial mass. This result is presented in theorem 4.3.1 for $\varepsilon, \tau^1 \to 0$ and $\mathsf{S} > 0$, i.e., c is a chemoattractant ($\mathsf{S} < 0$ results in c being chemorepulsive). Conversely, in angiogenesis models, chemotactic collapse was not observed due to distribution along a path rather than accumulation at one point [129, 130].

The Keller-Segel system, in the full space $\mathbb{R}^2$, reads

$$\begin{aligned} \frac{\partial n}{\partial t} - \nabla^2 n + \nabla \cdot (\mathsf{S} n \nabla c) = 0, \qquad & t \geq 0, x \in \mathbb{R}^2, \\ -\nabla^2 c = n, \qquad & t \geq 0, x \in \mathbb{R}^2, \\ n_{|_{t=0}}(x) = n_0(x) \geq 0 & \\ t \geq 0, x \in \mathbb{R}^2 & \end{aligned} \tag{4.5}$$

The system (4.5) presents two main properties. First, if $n_0 \in L^\infty \cap L^1_+$, the system (4.5) has non-negative solutions for cell density and chemical concentrations

$$n(t,x) \geq 0, \qquad c(t,x) \geq 0. \tag{4.6}$$

The second property is the conservation of mass, i.e. the conservation of the total number of cells

$$m := \int_{\mathbb{R}^2} n_0(x) dx = \int_{\mathbb{R}^2} n(t,x) dx. \tag{4.7}$$

Solutions of the system (4.5) may blow-up in finite time. This corresponds to a limiting case of aggregation of cells at one or multiple points. In the latter, the effectiveness of acupuncture treatments is associated with the blow-up of the solution at the acupoint.

4.2 Mathematical model of mastocyte response to acupuncture treatment

The present mathematical model that describes the response of mastocytes to external physical stimuli is formulated. Whatever form of acupuncture treatment is employed (needle, electro acupuncture, laser acupuncture), a physical stress field is created and sensed by the mastocytes. In turn, activated mastocytes release their granule content leading to further effects of acupuncture.

Following chemotaxis from regional pools and blood, newly arrived mastocytes at acupoints experience a degranulation triggered by the stress field when they enter a subdomain close to the needle ($|x| < \ell$) where physical constraint magnitude is high enough. Two mastocyte states indeed exist: granulated and degranulated. The model (4.8) differs from another chemotaxis model since the chemoattractant is only emitted close to the needle where the mastocytes are excited.

The release of chemical mediators relies on mechanotransduction processes activated by a rapid and copious calcium entry in the mastocyte cytosol. Unlike the quasi-instantaneous liberation of chemical messengers, the regeneration of granule content inside the mastocyte is delayed and slow (O(1 h)).

The resulting self-sustained process enables a local elevation of vascular permeability and vasodilation, an increase in blood flow, and endocrine signaling to central nervous

system. In this way, the neurons located in a brain region characterized by hyperemia can receive sets of action potentials during a long period. Then, the continuous flux of activators ensures a delayed and permanent response.

The mathematical model of acupuncture can be represented by the set of equations that incorporates two equations related to the populations of granulated and degranulated mastocytes. $n_g(t,x)$ and $n_d(t,x)$ denote the density of granulated and degranulated mastocytes, respectively. Three equations describe the temporal evolution of the concentrations of chemoattractant $c(t,x)$, nerve stimulant, $s_n(t,x)$, and endocrine activator, $s_e(t,x)$ (of some sites of the central nervous system). The convection (i.e., Stokes flow of extracellular water) of chemical mediators is considered negligibly small in the extracellular matrix. The interaction of chemotaxis with an incompressible fluid is investigated in chapter 5.

The mathematical model to describe the mastocyte response to acupuncture treatment reads

$$\begin{aligned}
\frac{\partial n_g}{\partial t} - \mathcal{D}_m \nabla^2 n_g + \nabla.\left(\mathsf{S}\, n_g \nabla c\right) &= -\mathsf{A}\Phi n_g + k_r n_d, \quad t>0, x\in\Omega \\
\frac{\partial c}{\partial t} - \mathcal{D}_c \nabla^2 c &= \kappa_c \mathsf{A}\Phi n_g - \delta_c c, \\
\frac{\partial n_d}{\partial t} - \mathcal{D}_m \nabla^2 n_d &= \mathsf{A}\Phi n_g - k_r n_d, \\
\frac{\partial s_n}{\partial t} - \mathcal{D}_{s_n} \nabla^2 s_n &= \kappa_n \mathsf{A}\Phi n_g - \delta_{s_n} s_n, \\
\frac{\partial s_e}{\partial t} - \mathcal{D}_{s_e} \nabla^2 s_e &= \kappa_e \mathsf{A}\Phi n_g - \delta_{s_e} s_e.
\end{aligned} \tag{4.8}$$

The above system is endowed with the following prescribed initial conditions

$$n_g|_{t=0} = n_g^0, \quad n_d|_{t=0} = n_d^0, \quad c|_{t=0} = c^0, \quad s_n|_{t=0} = s_n^0, \quad s_e|_{t=0} = s_e^0. \tag{4.9}$$

In a closed domain Ω, the above system is endowed with the boundary conditions, homogeneous Neumann boundary condition given by

$$\mathbf{n}\cdot\nabla n_d = 0, \quad \mathbf{n}\cdot\nabla n_g = 0, \quad \mathbf{n}\cdot\nabla c = 0, \quad \mathbf{n}\cdot\nabla s_n = 0, \quad \mathbf{n}\cdot\nabla s_e = 0, \tag{4.10}$$

or the zero total flux boundary conditions given by

$$\mathbf{n}\cdot(\nabla n_g - \mathsf{S}\nabla c) = 0, \quad \mathbf{n}\cdot\nabla n_d = 0, \quad \mathbf{n}\cdot\nabla c = 0, \quad \mathbf{n}\cdot\nabla s_n = 0, \quad \mathbf{n}\cdot\nabla s_e = 0, \tag{4.11}$$

where $\mathbf{n}$ denotes the outward unit normal on the boundary $\partial\Omega$.

All the parameters are constants. $\mathsf{S} > 0$ is the chemotactic sensitivity of the mastocytes to the chemoattractant. A is the activation rate i.e., the rate of mastocytes subjected to the mechanical stress Φ that will degranulate. $\mathcal{D}_m$, $\mathcal{D}_c$, $\mathcal{D}_{s_n}$ and $\mathcal{D}_{s_e}$ are the diffusion coefficients. δ_c, δ_{s_n} and δ_{s_e} are the degradation rate. κ_c, κ_n and κ_e are the release quantity coefficients of chemoattractant and stimulants. k_r is the regeneration coefficient of degranulated mastocytes. The dimension of the parameters is given in table 4.

Whatever the acupuncture treatment (needling, moxibustion, electroacupuncture, laser-acupuncture), the function Φ describes the dimensionless magnitude of the physical stress created in the extracellular matrix. The function Φ is defined as a C^∞ and compactly supported function from $\mathbb{R}^2$ to $[0,1]$ with the following properties:

$$\begin{aligned} &\forall (x,y) \in \mathbb{R}^2, |\Phi(x) - \Phi(y)| \leq k_\Phi |x-y| \\ &\Phi(x) \leq 1, \forall x \in \mathbb{R}^2, \\ &\Phi(x) = 0, \forall x \in \mathbb{R}^2, |x| \geq \ell. \end{aligned} \tag{4.12}$$

These properties are essential for the theoretical results given in the following sections. An example of function Φ is plotted in figure 4.1.

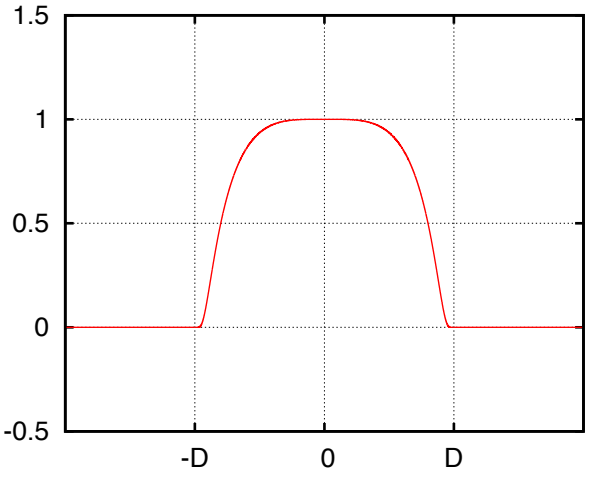

Figure 4.1: Stress function Φ in 1D. Here $\Phi(x) = e^{-\frac{1}{1-x^4}} e^1$ that reaches its maximum $\Phi(O) = 1$ at $O = (0,0)$.

4.3 Blow-up and existence conditions in the Keller-Segel system

The main result on the blow-up solution in finite time of the system (4.5) in two dimensions, as it is found in [127, 128], can be presented in the following theorem.

Theorem 4.3.1. *In $\mathbb{R}^2$, if $\int_{\mathbb{R}^2} |x|^2 n_0(x) dx < \infty$*

(i) when $m > \frac{8\pi}{S}$, then the Keller-Segel system blows-up in finite time

(ii) when $m < \frac{8\pi}{S}$ *and* $\int_{\mathbb{R}^2} n_0(x)|\log(n_0(x))|dx < \infty$*, then there exist weak solutions to (4.5) satisfying the a priori estimates*

$$\begin{gathered}\int_{\mathbb{R}^2} n(x)\left(|\log n(x)| + |x|^2\right) dx \geq C(t),\\ ||n(t)||_{L^p(\mathbb{R}^2)} \geq C(p,t,n_0) \quad \textit{for} \quad ||n_0(t)||_{L^p(\mathbb{R}^2)} < \infty, \quad 1 < p < \infty\end{gathered}$$

The proof of theorem 4.3.1 given in [127, 128] is recalled. On the one hand, the blow-up solution of the Keller-Segel system (4.5) in finite time results from a large enough initial number of cells for a given chemotaxis sensitivity of the cells. On the other hand, the existence of weak solutions is the consequence of a small enough initial number of cells.

4.3.0.1 Blow-up condition

The key steps of the formal proof of the blow-up are presented in this paragraph. The detailed proof is presented in Lemma 3 in [127].

Proof. Let the second moment be defined by

$$m^*(t) := \int_{\mathbb{R}^2} \frac{|x|^2}{2} n(t,x)\, dx. \tag{4.13}$$

The time derivative of (4.5) is given by

$$\frac{d}{dt}m^*(t) = \int_{\mathbb{R}^2} \frac{|x|^2}{2}\left[\Delta n(t,x) - \nabla.\left(\mathsf{S}\nabla c(t,x)\cdot n(t,x)\right)\right] dx \tag{4.14}$$

and integration by parts yields

$$\begin{aligned}\frac{d}{dt}m^*(t) &= \int_{\mathbb{R}^2} \Delta\left(\frac{|x|^2}{2}\right) n(t,x)dx + \int_{\mathbb{R}^2} \mathsf{S}x\nabla c(t,x)n(t,x)\, dx,\\ &= \int_{\mathbb{R}^2} 2n(t,x)dx + \int_{\mathbb{R}^2} \mathsf{S}x\nabla c(t,x)n(t,x)\, dx.\end{aligned} \tag{4.15}$$

The second equation (4.5) gives the following result

$$\nabla c(t,x) = -\frac{1}{2\pi}\int_{\mathbb{R}^2} \frac{x-y}{|x-y|^2} n(t,y)\, dy. \tag{4.16}$$

Introducing (4.16) back to the equation (4.15) yields

$$\begin{aligned}\frac{d}{dt}m^*(t) &= \int_{\mathbb{R}^2} 2n(t,x)\, dx - \frac{1}{2\pi}\mathsf{S}\int_{\mathbb{R}^2}\int_{\mathbb{R}^2} x\frac{x-y}{|x-y|^2} n(t,y)n(t,x)\, dydx,\\ &= \int_{\mathbb{R}^2} 2n(t,x)\, dx - \frac{1}{2\pi}\mathsf{S}\frac{1}{2}\int_{\mathbb{R}^2}\int_{\mathbb{R}^2} (x-y)\frac{x-y}{|x-y|^2} n(t,y)n(t,x)\, dydx,\\ &= \int_{\mathbb{R}^2} 2n(t,x)\, dx - \frac{1}{4\pi}\mathsf{S}\int_{\mathbb{R}^2}\int_{\mathbb{R}^2} n(t,y)n(t,x)\, dydx,\\ &= \int_{\mathbb{R}^2} 2n(t,x)\, dx - \frac{1}{4\pi}\mathsf{S}\left(\int_{\mathbb{R}^2} n(t,x)\, dx\right)^2.\end{aligned} \tag{4.17}$$

In the light of the conservation of the total mass property (4.7), it results in

$$\frac{d}{dt}m^*(t) \;=\; 2m\left(1-\frac{\mathsf{S}}{8\pi}m\right). \tag{4.18}$$

Therefore, if $m > \frac{8\pi}{\mathsf{S}}$, m^* is known to become negative in finite time which contradicts that n is non negative. This means that the solution n cannot be smooth until that time is reached. □

4.3.0.2 Existence condition

The key steps of the proof of the existence using the moment method are presented below in this paragraph. The detailed proof is given in [127].

Proof. Let the free energy, as it is defined in [127], be

$$E(t) = \int_{\mathbb{R}^2} n(t,x)\log(n(t,x))dx - \frac{\mathsf{S}}{2}\int_{\mathbb{R}^2} n(t,x)c(t,x)dxdy \tag{4.19}$$

One can show that the energy $E(t)$ is bounded. Time derivation of (4.19) yields

$$\frac{d}{dt}E(t) = \frac{d}{dt}\int_{\mathbb{R}^2} n(t,x)\log(n(t,x))\,dx - \frac{\mathsf{S}}{2}\frac{d}{dt}\int_{\mathbb{R}^2} n(t,x)c(t,x)\,dxdy. \tag{4.20}$$

First, the first term of the right hand side shown above can be rewritten as

$$\frac{d}{dt}\int_{\mathbb{R}^2} n(t,x)\log(n(t,x))dx = \int_{\mathbb{R}^2}\left(\frac{d}{dt}n(t,x)\log(n(t,x)) + \frac{d}{dt}n(t,x)\right)dx \tag{4.21}$$

and, using (4.5) and integrating by parts, it results in

$$\frac{d}{dt}\int_{\mathbb{R}^2} n(t,x)\log(n(t,x))dx = \int_{\mathbb{R}^2}\nabla\log(n(t,x))\left[-\nabla n(t,x) + \mathsf{S}n(t,x)\nabla c(t,x)\right]dx. \tag{4.22}$$

Then, the second term of the right hand side of (4.20) can be rewritten as

$$\frac{\mathsf{S}}{2}\frac{d}{dt}\int_{\mathbb{R}^2} n(t,x)c(t,x)dx = \frac{\mathsf{S}}{2}\int_{\mathbb{R}^2}\left(\frac{d}{dt}n(t,x)c(t,x) + n(t,x)\frac{d}{dt}c(t,x)\right)dxdy \tag{4.23}$$

and using (4.5) and integrating by parts yields twice yields

$$\frac{\mathsf{S}}{2}\frac{d}{dt}\int_{\mathbb{R}^2} n(t,x)c(t,x)dx \;= \mathsf{S}\int_{\mathbb{R}^2}\nabla c(t,x)\left[-\nabla n(t,x) + \mathsf{S}n(t,x)\nabla c(t,x)\right]dx. \tag{4.24}$$

Moreover,

$$-\nabla n + \mathsf{S}n\nabla c = n\left[-\frac{\nabla n}{n} + \mathsf{S}\nabla c\right] = n\left[-\nabla\log(n) + \mathsf{S}\nabla c\right]. \tag{4.25}$$

Therefore, substituting (4.22) and (4.24) in (4.20), the following inequation can be derived

$$\frac{d}{dt}E(t) = -\int_{\mathbb{R}^2} n(t,x)\left[\nabla \log(n(t,x)) - \mathsf{S}\nabla c(t,x)\right]^2 \, dx \leq 0. \tag{4.26}$$

It results that

$$E(t) \leq E^0 \tag{4.27}$$

.

The Hardy-Littlewood-Sobolev inequality (see [128]) is recalled.

Lemma 4.3.2 (Hardy-Littlewood-Sobolev inequality)**.** *For any function $f \geq 0$ in $L^1(\mathbb{R}^2)$ with $m := \int_{\mathbb{R}^2} f$ such that $\int_{\mathbb{R}^2} f|\log(f)| < \infty$ and $\int_{\mathbb{R}^2} f|\log(1+|x^2|)| < \infty$, then*

$$\frac{m}{2}\int_{\mathbb{R}^2} f\log(f)\,dx + \int\int_{\mathbb{R}^2\times\mathbb{R}^2} f(x)f(y)\log|x-y|\,dxdy \geq C(m) \tag{4.28}$$

Recall that the solution of the Poisson equation in (4.5) is given by

$$c(x,t) = -\frac{1}{2\pi}\int_{\mathbb{R}^2} \log|x-y| n(t,y)\,dy. \tag{4.29}$$

Then, from the equations (4.27) and (4.29), the following equation on the free energy (4.19) can be derived

$$\int_{\mathbb{R}^2} n\log(n) \leq E^0 - \frac{\mathsf{S}}{4\pi}\int\int_{\mathbb{R}^2\times\mathbb{R}^2} n(t,x)n(t,y)\log|x-y|\,dxdy. \tag{4.30}$$

Then, the Hardy-Littlewood-Sobolev inequality yields

$$\int_{\mathbb{R}^2} n\log(n) \leq E^0 - \frac{\mathsf{S}}{4\pi}C(m_0) + m_0\frac{\mathsf{S}}{8\pi}\int_{\mathbb{R}^2} n(t,x)\log n(t,x)\,dx \tag{4.31}$$

and thus

$$\left(\int_{\mathbb{R}^2} n\log(n)\right)\left(1 - m_0\frac{\mathsf{S}}{8\pi}\right) \leq E^0 - \frac{\mathsf{S}}{4\pi}C(m_0) \tag{4.32}$$

If $m_0 > \frac{8\pi}{\mathsf{S}}$, then the following a priori bound is derived

$$\int_{\mathbb{R}^2} n\log(n) \;\leq\; C_1 := \left(\frac{1}{m_0\frac{\mathsf{S}}{8\pi}}\right)\left(E^0 - \frac{\mathsf{S}}{4\pi}C(m_0)\right). \tag{4.33}$$

In addition, from (4.18) the second moment bound is deduced

$$\int_{\mathbb{R}^2} |x|^2 n(t,x)dx \leq C_2(T), \qquad\qquad \forall t \leq T. \tag{4.34}$$

The a priori upper bound on $\int_{\mathbb{R}^2} n\log(n)$ in (4.33) combined with the second moment bound (4.34) gives the final estimate for $\int_{\mathbb{R}^2} |n\log(n)|$ (details in Lemma 8 of [127]). Let $\overline{n} := n\mathbb{1}_{n\leq 1}$ and $\overline{m} := \int_{\mathbb{R}^2}\overline{n} \leq M$, then

$$\int_{\mathbb{R}^2} \overline{n}\left(\log\overline{n} + \frac{1}{2}|x|^2\right)dx \quad = \quad \int_{\mathbb{R}^2} U\log U d\mu$$

where $U = \frac{\overline{n}}{\mu}$, $d\mu(x) = \mu(x)dx$ and $\mu = e^{-\frac{|x|^2}{2}}$. By Jensen's inequality, one can have

$$\int_{\mathbb{R}^2} U\log U d\mu \quad \geq \quad \left(\int_{\mathbb{R}^2} U d\mu\right)\log\left(\int_{\mathbb{R}^2} U d\mu\right) = \overline{m}\log\overline{m}.$$

Then

$$\int_{\mathbb{R}^2}\overline{n}\log\overline{n} \geq \overline{m}\log\overline{m} - \frac{1}{2}\int_{\mathbb{R}^2}\overline{n}|x|^2dx \geq -\frac{1}{e} - \frac{1}{2}\int_{\mathbb{R}^2}\overline{n}|x|^2dx$$

and using the fact that

$$\int_{\mathbb{R}^2}|n\log n| = \int_{\mathbb{R}^2} n\log n - 2\int_{\mathbb{R}^2}\overline{n}\log\overline{n},$$

one can conclude, combining (4.33) and (4.34), that

$$\int_{\mathbb{R}^2}|n\log(n)| \leq C_3(T) \tag{4.35}$$

From (4.35), it is possible to prove the existence of weak solutions. This result is completely detailed in section 2.4 of [127]

Then L^p estimates must be derived with the Gagliardo-Nirenberg-Sobolev inequality (see (6.34) in [131]). □

4.4 Blow-up condition in a simplified system with mass conservation

The first result of the action of compact support stress function Φ on the production of chemoattractant is presented. Until now, blow-up is shown to occur when the initial number of mastocytes is large enough. The aim of this section is to show that with the local action of the stress function Φ, blow-up only occurs when a large pool of mastocytes is present in the vicinity of the acupoint. Blow-up corresponds to the significant recruitment of mastocytes close to the treated acupoint, and thus to the effectiveness of acupuncture manipulation.

This section deals with the case where only the density of the granulated mastocytes and the chemoattractant concentration are considered. Mastocytes are assumed to infinitely degranulate so that the total number of mastocytes remains the same. This is done

by removing the local stress Φ from the right hand side of the first equation in (4.8). Presuming that the diffusion of the chemoattractant is instantaneous, the previous hypothesis leads to the system of equations

$$\begin{aligned} \frac{\partial n_g}{\partial t} - \mathcal{D}_m \nabla^2 n_g + \nabla.\left(\mathsf{S}\, n_g \nabla c\right) = 0, \qquad & t > 0, x \in \Omega = \mathbb{R}^2, \\ -\mathcal{D}_c \nabla^2 c = \kappa_c\, \mathsf{A}\, \Phi\, n_g, & \\ n_g|_{t=0} = n_g^0 & \end{aligned} \tag{4.36}$$

In this scenario, the chemoattractant is only released by the mastocytes in the vicinity of the acupoint ($|x| < \ell$) and not in the whole domain such as in the Keller-Segel model (4.5). Blow-up is thus expected to be more difficult to achieve.

First, if $n_g^0 \in L^\infty \cap L^1_+(\Omega)$, the system (4.5)) has non-negative solutions

$$n_g(t,x) \geq 0, \qquad c(t,x) \geq 0. \tag{4.37}$$

To quantify the spatial distribution of the cells, let the total cell number (0th moment) and the second moment be defined as follows

$$m_0(t) := \textstyle\int_{\mathbb{R}^2} n_g(t,x)dx \qquad\qquad m_2(t) := \textstyle\int_{\mathbb{R}^2} \frac{|x|^2}{2} n_g(t,x)dx. \tag{4.38}$$

***Remark* 1.** *The second (central) moment measures the spatial distribution of the cell population. A small second moment indicates that the cells are gathered in the vicinity of the center of the domain (as defined in (def:moments)), i.e., in this work, the acupoint.*

In the differential system (4.36), one can easily state that the total mass is conserved, i.e. the total number of cells remains a constant with time

$$m_0 := m_0(0). \tag{4.39}$$

Theorem 4.4.1. *In $\mathbb{R}^2$, let $n_0 \in L^1_+(\mathbb{R}^2, (1+|x|^2)dx)$. Let n be a non-negative smooth solution of (4.36) and let $[0, T^*)$ be the maximal interval of existence. Then, if the initial mass $m_0(0)$ is large enough and the second momentum $m_2(0)$ is small enough (to be given in the proof), the solution blows-up as $t \to T^*$.*

Proof. Using (4.36) one can get

$$\frac{d}{dt} m_2(t) \;=\; \int_{\mathbb{R}^2} \frac{|x|^2}{2} \left[\Delta n_g(t,x) - \nabla.\left(\mathsf{S}\nabla c(t,x) \cdot n_g(t,x)\right)\right] dx.$$

Integration by parts leads to

$$\begin{aligned} \frac{d}{dt} m_2(t) \;&=\; \int_{\mathbb{R}^2} \Delta\left(\frac{|x|^2}{2}\right) n_g(t,x)dx + \int_{\mathbb{R}^2} \mathsf{S} x \nabla c(t,x) n_g(t,x)dx \\ &=\; \int_{\mathbb{R}^2} 2 n_g(t,x)dx + \int_{\mathbb{R}^2} S x \nabla c(t,x) n_g(t,x)dx. \end{aligned}$$

Moreover, the second equation in (4.36) yields

$$\nabla c(t,x) = -\frac{\mathsf{A}}{2\pi}\int_{\mathbb{R}^2}\frac{x-y}{|x-y|^2}\Phi(y)n_g(t,y)dy,$$

so that the following equation can be derived

$$\begin{aligned}\frac{d}{dt}m_2(t) &= \int_{\mathbb{R}^2}2n_g(t,x)dx - \frac{1}{2\pi}\mathsf{AS}\int_{\mathbb{R}^2}\int_{\mathbb{R}^2}x\frac{x-y}{|x-y|^2}\Phi(y)n_g(t,y)n_g(t,x)dydx\\ &= 2m_0\left(1-\frac{\mathsf{AS}}{8\pi}m_0\right)+\frac{1}{2\pi}\mathsf{AS}\int_{\mathbb{R}^2}\int_{\mathbb{R}^2}x\frac{x-y}{|x-y|^2}\left(1-\Phi(y)\right)n_g(t,y)n_g(t,x)dydx.\end{aligned}$$

In the previous result, let the second term on the right hand side be defined as

$$\begin{aligned}I(t) &= \frac{1}{2\pi}\mathsf{AS}\int_{\mathbb{R}^2}\int_{\mathbb{R}^2}x\frac{x-y}{|x-y|^2}\left(1-\Phi(y)\right)n_g(t,y)n_g(t,x)dydx\\ &= \frac{1}{2\pi}\mathsf{AS}\int_{|x|\le\frac{\Delta\ell}{2}}\int_{|y|>\Delta\ell}x\frac{x-y}{|x-y|^2}\left(1-\Phi(y)\right)n_g(t,y)n_g(t,x)dydx\\ &\quad+\frac{1}{2\pi}\mathsf{AS}\int_{|x|\ge\frac{\Delta\ell}{2}}\int_{|y|>\Delta\ell}x\frac{x-y}{|x-y|^2}\left(1-\Phi(y)\right)n_g(t,y)n_g(t,x)dydx\end{aligned}$$

Let I_1 and I_2 be the first term and second term of I, respectively. If $|x|\le\frac{\Delta\ell}{2}$ and $|y|>\Delta\ell$, then $|x-y|\ge\frac{\Delta\ell}{2}$ i.e. $\frac{1}{|x-y|}\le\frac{2}{\Delta\ell}$.Moreover, $(1-\Phi(y))$ is bounded from above by 1, thus

$$\begin{aligned}|I_1(t)| &= \frac{1}{2\pi}\mathsf{AS}\int_{|x|\le\frac{\Delta\ell}{2}}\int_{|y|>\Delta\ell}|x|\frac{|x-y|}{|x-y|^2}\left(1-\Phi(y)\right)n_g(t,y)n_g(t,x)dydx\\ &= \frac{1}{2\pi}\mathsf{AS}\int_{|x|\le\frac{\Delta\ell}{2}}\int_{|y|>\Delta\ell}|x|\frac{1}{|x-y|}\left(1-\Phi(y)\right)n_g(t,y)n_g(t,x)dydx\\ &\le \frac{1}{2\pi}\mathsf{AS}\int_{|x|\le\frac{\Delta\ell}{2}}\int_{|y|>\Delta\ell}|x|\frac{2}{\Delta\ell}n_g(t,y)n_g(t,x)dydx\\ &\le \frac{1}{2\pi}\frac{2\sqrt{2}}{\Delta\ell}\mathsf{AS}\left(\int_{|x|\le\frac{\Delta\ell}{2}}\frac{|x|^2}{2}n_g(t,x)dx\right)^{\frac{1}{2}}\left(\int_{|x|\le\frac{\Delta\ell}{2}}n_g(t,x)xdx\right)^{\frac{1}{2}}\left(\int_{|y|>\Delta\ell}n_g(t,y)dy\right)\\ &\le \frac{\sqrt{2}}{\pi}\frac{\mathsf{AS}}{\Delta\ell}(m_2(t))^{\frac{1}{2}}(m_0)^{\frac{3}{2}}.\end{aligned}$$

For the second term I_2, because $(1-\Phi(y))=0$ for $\frac{\Delta\ell}{2}\leq|y|\leq\Delta\ell$, then

$$\begin{aligned}
I_2(t) &= \frac{1}{2\pi}\mathsf{AS}\int_{|x|\geq\frac{\Delta\ell}{2}}\int_{|y|>\Delta\ell} x\frac{x-y}{|x-y|^2}\left(1-\Phi(y)\right)n_g(t,y)n_g(t,x)dydx\\
&= \frac{1}{2\pi}\mathsf{AS}\int_{|x|\geq\frac{\Delta\ell}{2}}\int_{|y|\geq\frac{\Delta\ell}{2}} x\frac{x-y}{|x-y|^2}\left(1-\Phi(y)\right)n_g(t,y)n_g(t,x)dydx\\
&= \frac{1}{4\pi}\mathsf{AS}\int_{|x|\geq\frac{\Delta\ell}{2}}\int_{|y|\geq\frac{\Delta\ell}{2}} \frac{x-y}{|x-y|^2}\left[x(1-\Phi(y))-y(1-\Phi(x))\right]n_g(t,y)n_g(t,x)dydx\\
&= \frac{1}{4\pi}\mathsf{AS}\int_{|x|\geq\frac{\Delta\ell}{2}}\int_{|y|\geq\frac{\Delta\ell}{2}} \frac{x-y}{|x-y|^2}\left[(x-y)(1-\Phi(y))+y(\Phi(x)-\Phi(y))\right]n_g(t,y)n_g(t,x)dydx
\end{aligned}$$

with

$$\begin{aligned}
|I_{2a}(t)| &= \frac{1}{4\pi}\mathsf{AS}\int_{|x|\geq\frac{\Delta\ell}{2}}\int_{|y|\geq\frac{\Delta\ell}{2}} \frac{|x-y|}{|x-y|^2}\left[|x-y|(1-\Phi(y))\right]n_g(t,y)n_g(t,x)dydx\\
&= \frac{1}{4\pi}\mathsf{AS}\int_{|x|\geq\frac{\Delta\ell}{2}}\int_{|y|\geq\frac{\Delta\ell}{2}} (1-\Phi(y))n_g(t,y)n_g(t,x)dydx\\
&\leq \frac{1}{4\pi}\mathsf{AS}\int_{|x|\geq\frac{\Delta\ell}{2}}\int_{|y|\geq\frac{\Delta\ell}{2}} \frac{2|x|}{\Delta\ell}n_g(t,y)n_g(t,x)dydx\\
&\leq \frac{\sqrt{2}}{2\pi}\frac{\mathsf{AS}}{\Delta\ell}\left(\int_{|x|\geq\frac{\Delta\ell}{2}}\frac{|x|^2}{2}n_g(t,x)dx\right)^{\frac{1}{2}}\left(\int_{|x|\geq\frac{\Delta\ell}{2}}n_g(t,x)xdx\right)^{\frac{1}{2}}\left(\int_{|y|\geq\frac{\Delta\ell}{2}}n_g(t,y)dy\right)\\
&\leq \frac{\sqrt{2}}{2\pi}\frac{\mathsf{AS}}{\Delta\ell}(m_2(t))^{\frac{1}{2}}(m_0)^{\frac{3}{2}}
\end{aligned}$$

and

$$\begin{aligned}
|I_{2b}|(t) &= \frac{1}{4\pi}\mathsf{AS}\int_{|x|\geq\frac{\Delta\ell}{2}}\int_{|y|\geq\frac{\Delta\ell}{2}} \frac{|x-y|}{|x-y|^2}|y||\Phi(x)-\Phi(y)|n_g(t,y)n_g(t,x)dydx\\
&\leq \frac{1}{4\pi}\mathsf{AS}\int_{|x|\geq\frac{\Delta\ell}{2}}\int_{|y|\geq\frac{\Delta\ell}{2}} k_\Phi\frac{2|y|^2}{\Delta\ell}n_g(t,y)n_g(t,x)dydx\\
&\leq \frac{k_\Phi}{\Delta\ell\pi}\mathsf{AS}\int_{|x|\geq\frac{\Delta\ell}{2}}n_g(t,x)dx\int_{|y|\geq\frac{\Delta\ell}{2}}\frac{|y|^2}{2}n_g(t,y)dy\\
&\leq \frac{k_\Phi}{\Delta\ell\pi}\mathsf{AS}m_2(t)m_0.
\end{aligned}$$

Finally, the following equation is obtained

$$\frac{d}{dt}m_2(t) \leq 2m_0\left(1-\frac{\mathsf{AS}}{8\pi}m_0\right)+\frac{3\sqrt{2}}{2\pi}\frac{\mathsf{AS}}{\Delta\ell}(m_2(t))^{\frac{1}{2}}(m_0)^{\frac{3}{2}}+\frac{1}{\pi}\frac{\mathsf{AS}}{\Delta\ell}k_\Phi m_2(t)m_0.$$

Moreover, following the arguments from [132], one can get

$$m_2(t)\leq m_2(0)+\int_0^t f(m_2(s))ds, \tag{4.40}$$

where $f(\xi) = 2m_0\left(1 - \frac{\mathsf{AS}}{8\pi}m_0\right) + \frac{3\sqrt{2}}{2\pi}\frac{\mathsf{AS}}{\Delta\ell}\xi^{\frac{1}{2}}(m_0)^{\frac{3}{2}} + \frac{1}{\pi}\frac{\mathsf{AS}}{\Delta\ell}k_\Phi m_0\xi$ is a strictly increasing function. If

$$m_0 > \frac{8\pi}{\mathsf{AS}}, \tag{4.41}$$

then a unique ξ^* exists such that $f(\xi^*) = 0$, namely

$$\xi^* = \frac{(b^2 - 2ac) - b\sqrt{4ac + b^2}}{2c^2}, \tag{4.42}$$

where

$$a = 2m_0\left(1 - \frac{\mathsf{AS}}{8\pi}m_0\right), \quad b = \frac{3\sqrt{2}}{2\pi}\frac{\mathsf{AS}}{\Delta\ell}(m_0)^{\frac{3}{2}} \text{ and } \quad c = \frac{1}{\pi}\frac{\mathsf{AS}}{\Delta\ell}k_\Phi m_0.$$

In conclusion, if $m_2(0) < \xi^*$, then $f(m_2(0)) < 0$. Therefore, $\int_0^t f(m_2(s))ds < 0$ provided that (4.48) holds true and $m_2(t) \leq m_2(0) + tf(m_2(0))$ as long as (4.48) is valid. The second moment becomes non-positive for $t \geq -\frac{m_2(0)}{f(m_2(0))}$ which is impossible since n is non-negative (4.37). Therefore, a singularity appears before that time and the density of cells n becomes infinitely large at the singularity point before a finite time T^*. The reason is that the manipulations in the proof hold true for the correctly defined L^1 solutions (see [133]). □

4.5 Blow-up condition in the case of a sole state for mastocytes

The second result of the action of compact supported stress function Φ is presented. The granulated mastocytes liberate their stored granules once they have reached a region with significant stress. Then, blow-up of the solution in finite time occurs when a large initial pool of mastocytes is present in the vicinity of the acupoint. In this work, the prime interest is the blow-up of the solution that characterizes the agglomeration of regional and remote (present in the blood) mastocytes at the acupoint. The migration of mastocytes toward the acupoint may create a self-sustained process in response to the acupuncture treatment.

This section considers a simple situation dominated by two of the components from (4.8), the evolution of the granulated mastocyte density n_g and the instantaneous diffusion of the chemoattractant c. In order to avoid the effects of boundary conditions, the system (4.43) is considered in the full space $\mathbb{R}^2$. Let the stress function Φ be equally distributed in a region close to the needle, in other words, for $|x| \leq \lambda$, $\Phi(x) = 1$. These assumptions lead to the following system

$$\begin{aligned} \partial_t n_g - \mathcal{D}_m\nabla^2 n_g + \nabla.\left(\mathsf{S}\, n_g\nabla c\right) &= -\mathsf{A}\Phi(x)n_g, \quad t > 0, x \in \Omega = \mathbb{R}^2, \\ -\nabla^2 c &= \kappa_c\mathsf{A}\Phi(x)n_g, \\ n_g|_{t=0} &= n_0 \geq 0. \end{aligned} \tag{4.43}$$

Since the initial condition n_0 is non-negative, the parabolic equation for n in (4.43) gives a non-negative solution.

***Remark* 2.** *The local stress $\Phi(x)$ is reintroduced in the first equation. In the system (4.43), the equation for mastocyte density doesn't have the property of mass conservation. Granulated mastocytes release their granule content once when they are activated by the local stress Φ but are not reintroduced in the system.*

Theorem 4.5.1. *In $\mathbb{R}^2$, let $n_0 \in L^1_+(\mathbb{R}^2, (1+|x|^2)dx)$. Let n be a non-negative smooth solution of (4.43) and let $[0, T^*)$ be the maximal interval of existence. Then, if the initial mass $m_0(0)$ is large enough and the second momentum $m_2(0)$ is small enough (to be precised in the proof), the solution blows-up as $t \to T^*$.*

Proof. The proof follows the argument previously introduced by Nagai and Senba [125], and used in [133] and [127] as presented in section 4.3.0.2.

First step: total mass. Taking the time derivative on the zeroth moment in (4.38) and taking (4.43) into consideration, one can get

$$\begin{aligned} \frac{d}{dt}m_0(t) &= \int_{\mathbb{R}^2} \nabla^2 n(t,x) - \nabla.\left(\mathsf{S}n(t,x)\nabla c(t,x)\right) - \mathsf{A}\Phi(x)n(t,x)dx \\ &= \int_{\mathbb{R}^2} -\mathsf{A}\Phi(x)n(t,x)dx \geq -\mathsf{A}m_0(t). \end{aligned} \tag{4.44}$$

Then, $\forall t \leq \mathsf{T}^*$

$$m_0(0) \quad \geq m_0(t) \geq \quad m_0(0)\exp^{-\mathsf{A}\mathsf{T}^*} \tag{4.45}$$

Second step: second moment. Taking the time derivative on the second moment in (4.38) into account and using (4.43), one can derive

$$\frac{d}{dt}m_2(t) \quad = \quad \int_{\mathbb{R}^2} \frac{|x|^2}{2}\left[\nabla^2 n(t,x) - \nabla.\left(\mathsf{S}n(t,x)\nabla c(t,x)\right) - \mathsf{A}\Phi(x)n(t,x)\right]dx.$$

Integration by parts yields

$$\begin{aligned} \frac{d}{dt}m_2(t) &= \int_{\mathbb{R}^2} \nabla^2\left(\frac{|x|^2}{2}\right) n(t,x)dx + \int_{\mathbb{R}^2} \mathsf{S}x\nabla c(t,x)n(t,x)dx \\ &\quad - \int_{\mathbb{R}^2} \mathsf{A}\frac{|x|^2}{2}\Phi(x)n(t,x)dx \\ &= \int_{\mathbb{R}^2} 2n(t,x)dx + \int_{\mathbb{R}^2} \mathsf{S}x\nabla c(t,x)n(t,x)dx \\ &\quad - \int_{\mathbb{R}^2} \mathsf{A}\frac{|x|^2}{2}\Phi(x)n(t,x)dx. \end{aligned} \tag{4.46}$$

Moreover, the second equation in (4.43) yields

$$\nabla c(t,x) = -\frac{\mathsf{A}\kappa_c}{2\pi}\int_{\mathbb{R}^2}\frac{x-y}{|x-y|^2}\Phi(y)n(t,y)dy. \tag{4.47}$$

By substituting the gradient of c into (4.46), the following equation is derived

$$\begin{aligned}\frac{d}{dt}m_2(t) =& 2\int_{\mathbb{R}^2} n(t,x)dx - \frac{1}{2\pi}\mathsf{AS}\kappa_c\int_{\mathbb{R}^2}\int_{\mathbb{R}^2} x\frac{x-y}{|x-y|^2}\Phi(y)n(t,y)n(t,x)dydx\\ &-\int_{\mathbb{R}^2}\mathsf{A}\frac{|x|^2}{2}\Phi(x)n(t,x)dx\\ =&2m_0(t)\left(1-\frac{\mathsf{AS}\kappa_c}{8\pi}m_0(t)\right)-\int_{\mathbb{R}^2}\mathsf{A}\frac{|x|^2}{2}\Phi(x)n(t,x)dx\\ &+\frac{\mathsf{AS}\kappa_c}{2\pi}\int_{\mathbb{R}^2}\int_{\mathbb{R}^2} x\frac{x-y}{|x-y|^2}\left(1-\Phi(y)\right)n(t,y)n(t,x)dydx.\end{aligned}$$

Let $I(t)$, the last term in the previous equation, be defined by

$$\begin{aligned}I(t) &= \frac{1}{2\pi}\mathsf{AS}\kappa_c\int_{\mathbb{R}^2}\int_{\mathbb{R}^2} x\frac{x-y}{|x-y|^2}\left(1-\Phi(y)\right)n(t,y)n(t,x)dydx\\ &= \frac{1}{2\pi}\mathsf{AS}\kappa_c\int_{|x|\le\frac{\lambda}{2}}\int_{|y|>\lambda} x\frac{x-y}{|x-y|^2}\left(1-\Phi(y)\right)n(t,y)n(t,x)dydx\\ &\quad+\frac{1}{2\pi}\mathsf{AS}\kappa_c\int_{|x|\ge\frac{\lambda}{2}}\int_{|y|>\lambda} x\frac{x-y}{|x-y|^2}\left(1-\Phi(y)\right)n(t,y)n(t,x)dydx\end{aligned}$$

Let I_1 and I_2 be the first term and second term of I, respectively. If $|x|\le\frac{\lambda}{2}$ and $|y|>\lambda$, then $|x-y|\ge\frac{\lambda}{2}$ i.e. $\frac{1}{|x-y|}\le\frac{2}{\lambda}$. Moreover, $(1-\Phi(y))$ is bounded from above by 1 so that

$$\begin{aligned}|I_1(t)| &= \frac{1}{2\pi}\mathsf{AS}\kappa_c\int_{|x|\le\frac{\lambda}{2}}\int_{|y|>\lambda}|x|\frac{|x-y|}{|x-y|^2}\left(1-\Phi(y)\right)n(t,y)n(t,x)dydx\\ &= \frac{1}{2\pi}\mathsf{AS}\kappa_c\int_{|x|\le\frac{\lambda}{2}}\int_{|y|>\lambda}|x|\frac{1}{|x-y|}\left(1-\Phi(y)\right)n(t,y)n(t,x)dydx\\ &\le \frac{1}{2\pi}\mathsf{AS}\kappa_c\int_{|x|\le\frac{\lambda}{2}}\int_{|y|>\lambda}|x|\frac{2}{\lambda}n(t,y)n(t,x)dydx\\ &\le \frac{1}{2\pi}\frac{2\sqrt{2}}{\lambda}\mathsf{AS}\kappa_c\left(\int_{|x|\le\frac{\lambda}{2}}\frac{|x|^2}{2}n(t,x)dx\right)^{\frac{1}{2}}\left(\int_{|x|\le\frac{\lambda}{2}}n(t,x)xdx\right)^{\frac{1}{2}}\left(\int_{|y|>\lambda}n(t,y)dy\right)\\ &\le \frac{\sqrt{2}}{\pi}\frac{\mathsf{AS}\kappa_c}{\lambda}(m_2(t))^{\frac{1}{2}}(m_0)^{\frac{3}{2}}.\end{aligned}$$

For the second term I_2, because Φ is a k_Φ-Lipchitz function and $(1-\Phi(y))=0$ for $\frac{\lambda}{2}\leq|y|\leq\lambda$, one can derive

$$\begin{aligned}
I_2(t) &= \frac{1}{2\pi}\mathsf{AS}\kappa_c\int_{|x|\geq\frac{\lambda}{2}}\int_{|y|>\lambda} x\frac{x-y}{|x-y|^2}\left(1-\Phi(y)\right)n(t,y)n(t,x)dydx\\
&= \frac{1}{2\pi}\mathsf{AS}\kappa_c\int_{|x|\geq\frac{\lambda}{2}}\int_{|y|\geq\frac{\lambda}{2}} x\frac{x-y}{|x-y|^2}\left(1-\Phi(y)\right)n(t,y)n(t,x)dydx\\
&= \frac{1}{4\pi}\mathsf{AS}\kappa_c\int_{|x|\geq\frac{\lambda}{2}}\int_{|y|\geq\frac{\lambda}{2}} \frac{x-y}{|x-y|^2}\left[x(1-\Phi(y))-y(1-\Phi(x))\right]n(t,y)n(t,x)dydx\\
&= \frac{1}{4\pi}\mathsf{AS}\kappa_c\int_{|x|\geq\frac{\lambda}{2}}\int_{|y|\geq\frac{\lambda}{2}} \frac{x-y}{|x-y|^2}\left[(x-y)(1-\Phi(y))+y(\Phi(x)-\Phi(y))\right]n(t,y)n(t,x)dydx
\end{aligned}$$

with

$$\begin{aligned}
|I_{2a}(t)| &= \frac{1}{4\pi}\mathsf{AS}\kappa_c\int_{|x|\geq\frac{\lambda}{2}}\int_{|y|\geq\frac{\lambda}{2}} \frac{|x-y|}{|x-y|^2}\left[|x-y|(1-\Phi(y))\right]n(t,y)n(t,x)dydx\\
&= \frac{1}{4\pi}\mathsf{AS}\kappa_c\int_{|x|\geq\frac{\lambda}{2}}\int_{|y|\geq\frac{\lambda}{2}} (1-\Phi(y))n(t,y)n(t,x)dydx\\
&\leq \frac{1}{4\pi}\mathsf{AS}\kappa_c\int_{|x|\geq\frac{\lambda}{2}}\int_{|y|\geq\frac{\lambda}{2}} \frac{2|x|}{\lambda}n(t,y)n(t,x)dydx\\
&\leq \frac{\sqrt{2}}{2\pi}\frac{\mathsf{AS}\kappa_c}{\lambda}\left(\int_{|x|\geq\frac{\lambda}{2}}\frac{|x|^2}{2}n(t,x)dx\right)^{\frac{1}{2}}\left(\int_{|x|\geq\frac{\lambda}{2}}n(t,x)xdx\right)^{\frac{1}{2}}\left(\int_{|y|\geq\frac{\lambda}{2}}n(t,y)dy\right)\\
&\leq \frac{\sqrt{2}}{2\pi}\frac{\mathsf{AS}\kappa_c}{\lambda}(m_2(t))^{\frac{1}{2}}(m_0)^{\frac{3}{2}},
\end{aligned}$$

and

$$\begin{aligned}
|I_{2b}|(t) &= \frac{1}{4\pi}\mathsf{AS}\kappa_c\int_{|x|\geq\frac{\lambda}{2}}\int_{|y|\geq\frac{\lambda}{2}} \frac{|x-y|}{|x-y|^2}|y||\Phi(x)-\Phi(y)|n(t,y)n(t,x)dydx\\
&\leq \frac{1}{4\pi}\mathsf{AS}\kappa_c\int_{|x|\geq\frac{\lambda}{2}}\int_{|y|\geq\frac{\lambda}{2}} k_\Phi\frac{2|y|^2}{\lambda}n(t,y)n(t,x)dydx\\
&\leq \frac{k_\Phi}{\lambda\pi}\mathsf{AS}\kappa_c\int_{|x|\geq\frac{\lambda}{2}} n(t,x)dx\int_{|y|\geq\frac{\lambda}{2}}\frac{|y|^2}{2}n(t,y)dy\\
&\leq \frac{k_\Phi}{\lambda\pi}\mathsf{AS}\kappa_c m_2(t)m_0.
\end{aligned}$$

Thus, from the previous estimates, $\forall t\leq T^*$, the following inequality results

$$\begin{aligned}
\frac{d}{dt}m_2(t) &\leq 2m_0(0)\left(1-\frac{\mathsf{AS}\kappa_c}{8\pi}m_0(0)\exp^{-LT^*}\right)+\frac{3\sqrt{2}}{2\pi}\frac{\mathsf{AS}\kappa_c}{\lambda}(m_2(t))^{\frac{1}{2}}(m_0(0))^{\frac{3}{2}}\\
&\quad+\frac{1}{\pi}\frac{\mathsf{AS}\kappa_c}{\lambda}k_\Phi m_2(t)m_0(0).
\end{aligned}$$

Finally, following the arguments from Calvez and Corrias [132], the following estimate can be derived

$$m_2(t) \leq m_2(0) + \int_0^t f(m_2(s))ds, \tag{4.48}$$

where $f(\xi) = 2m_0(0)\left(1 - \frac{\mathsf{AS}\kappa_c}{8\pi} m_0(0)\exp^{-LT^*}\right) + \frac{3\sqrt{2}}{2\pi}\frac{\mathsf{AS}\kappa_c}{\lambda}\xi^{\frac{1}{2}} m_0(0)^{\frac{3}{2}} + \frac{1}{\pi}\frac{\mathsf{AS}\kappa_c}{\lambda} k_\Phi m_0(0)\xi$. f is a strictly increasing function and if

$$m_0(0) > \frac{8\pi}{\mathsf{AS}\kappa_c}\exp^{\mathsf{AT}^*}, \tag{4.49}$$

a unique ξ^* exists such that $f(\xi^*) = 0$, namely

$$\xi^* = \frac{(b^2 - 2ac) - b\sqrt{4ac + b^2}}{2c^2}, \tag{4.50}$$

where

$$a = 2m_0(0)\left(1 - \frac{\mathsf{AS}\kappa_c}{8\pi} m_0(0)\exp^{-LT^*}\right), \quad b = \frac{3\sqrt{2}}{2\pi}\frac{\mathsf{AS}\kappa_c}{\lambda} m_0(0)^{\frac{3}{2}} \text{ and } \quad c = \frac{1}{\pi}\frac{\mathsf{AS}\kappa_c}{\lambda} k_\phi m_0(0).$$

So, if $m_2(0) < \xi^*$, then $f(m_2(0)) < 0$. Therefore, $\int_0^t f(m_2(s))ds < 0$ and $m_2(t) \leq m_2(0) + tf(m_2(0))$ provided that (4.48) holds true. The second moment becomes non-positive for $T^* \geq -\frac{m_2(0)}{f(m_2(0))}$ which is impossible since n is non-negative. Therefore, a singularity appears before the time T^* and the solution n blows-up at the singularity point. This behavior indicates the appearance of a singular measure because the manipulation in the proof hold true for the correctly defined L^1 solutions (see [133]). □

4.6 Existence condition in the case of a sole state for mastocytes

In this section, the existence of a weak solution of the system (4.43) when the initial number of mastocytes is small enough is proven. Acupoints are characterized by the presence of large pools of mastocytes. Hence, this result shows that when the acupuncture treatment is applied at a non-acupoint, then the response of the mastocyte is not large enough to trigger a sufficient recruitment of mastocytes. Considering the simplified model (4.43), the following L^p a priori estimate will be proven.

In this section, the existence of weak solution of the system (4.43) when the initial number of mastocyte is small enough is proven. Acupoint are characterized by the presence of large pools of mastocytes. Hence, this result shows that when the acupuncture treatment is applied at a non-acupoint, then the response of the mastocyte is not large enough to trigger a sufficient recruitment of mastocytes. Considering the simplified model (4.43), the following L^p a priori estimate will be proven.

Theorem 4.6.1. *In $\mathbb{R}^2$, let $p > 1$ and assume that $n_0 \in L^1_+(\mathbb{R}^2, (1+|x|^2)dx)$. There exists a constant α such that when the initial data satisfies $m_0(0) < \frac{4\alpha}{p\,\mathsf{A}\,\mathsf{S}\,\kappa_c}$, there exists a weak solution to (4.43) in $L^p(\mathbb{R}^2, dx)$ at all times.*

Proof. The estimates are derived based on the Sobolev inequalities following the argument by Jager and Luckhaus [123].

Multiplying (4.43) by n^{p-1} and integrating, one can get

$$\frac{1}{p}\int_{\mathbb{R}^2}\frac{dn^p}{dt} = -\int_{\mathbb{R}^2}\frac{4(p-1)}{p^2}|\nabla n^{p/2}|^2 + \frac{p-1}{p}\int_{\mathbb{R}^2}\mathsf{A}\,\mathsf{S}\,\kappa_c\Phi(x)n^{p+1} - \int_{\mathbb{R}^2}\mathsf{A}\Phi(x)n^p.$$

To estimate the integral with power $p+1$, the following Gagliardo-Nirenberg-Sobolev inequality is employed

$$\int_{\mathbb{R}^2}|n|^{p+1} \le C_{GNS}\int_{\mathbb{R}^2}|n|\int_{\mathbb{R}^2}|\nabla n^{p/2}|^2. \tag{4.51}$$

Recalling that $\Phi(x) \le 1$ and $m_0(t) \le m_0(0)$,

$$\frac{1}{p}\int_{\mathbb{R}^2}\frac{dn^p}{dt} \le \frac{p-1}{p}\left(-\frac{4}{p} + C_{GNS}\,\mathsf{A}\,\mathsf{S}\,\kappa_c m_0(0)\right)\int_{\mathbb{R}^2}|\nabla n^{p/2}|^2 - \int_{\mathbb{R}^2}\mathsf{A}\Phi(x)n^p. \tag{4.52}$$

Then, if $m_0(0) < \frac{4}{pC_{GNS}\mathsf{A}\,\mathsf{S}\,\kappa_c}$, $\int_{\mathbb{R}^2} n^p dx$ decays in time. From this a priori estimate, one may conclude the existence as done in [127]. □

4.7 Scaling and numerical method

The present section and the following section deal with the numerical study of the model (4.8). This section presents the dimensionless form of the model and the finite element method employed to discretize the differential equations in (4.8). All computations presented are realized by means of the FreeFem++ code presented in chapter 2.

4.7.1 Scaling

The dimensionless variables $n_g{}'$, $n_d{}'$, c', $s_n{}'$, $s_e{}'$, x', and t' are defined by

$$\begin{array}{lll} n_g{}' = n^{ref} n_g, & n_d{}' = n^{ref} n_d, & c' = c^{ref} c, \quad s_n{}' = s_n^{ref} s_n, \\ s_e{}' = s_e^{ref} s_e, & x' = \frac{1}{\ell} x, & t' = \frac{\mathcal{D}_m}{\ell^2} t. \end{array} \tag{4.53}$$

Thus, introducing (4.53) in (4.8) and removing the prime of the dimensionless variables, the dimensionless system given below can be derived

$$\begin{aligned}
\frac{\partial n_g}{\partial t} - \nabla^2 n_g + \Pi_{\mathsf{S}} \nabla.\,(n_g \nabla c) &= -\Pi_{\mathsf{A}} \Phi n_g + \Pi_{k_r} n_d, \quad t > 0, x \in \Omega \\
\frac{\partial c}{\partial t} - \Pi_{\mathcal{D}_c} \nabla^2 c &= \Pi_{\kappa_c} \Phi n_g - \Pi_{\delta_c} c, \\
\frac{\partial n_d}{\partial t} - \nabla^2 n_d &= \Pi_{\mathsf{A}} \Phi n_g - \Pi_{k_r} n_d, \\
\frac{\partial s_n}{\partial t} - \Pi_{\mathcal{D}_{s_n}} \nabla^2 s_n &= \Pi_{\kappa_n} \Phi n_g - \Pi_{\delta_{s_n}} s_n, \\
\frac{\partial s_e}{\partial t} - \Pi_{\mathcal{D}_{s_e}} \nabla^2 s_e &= \Pi_{\kappa_e} \Phi n_g - \Pi_{\delta_{s_e}} s_e.
\end{aligned} \tag{4.54}$$

where

$$\begin{aligned}
\Pi_{\mathsf{S}} &= \frac{S\, c^{ref}}{\mathcal{D}_m}, \qquad \Pi_{\mathsf{A}} = \frac{\ell^2\, \mathsf{A}}{\mathcal{D}_m}, \qquad \Pi_{k_r} = \frac{\ell^2\, k_r}{\mathcal{D}_m}, \\
\Pi_{\mathcal{D}_c} &= \frac{\mathcal{D}_c}{\mathcal{D}_m}, \quad \Pi_{\kappa_c} = \frac{\kappa_c\, \mathsf{A}\, \ell^2\, n^r ef}{\mathcal{D}_m\, c^{ref}}, \quad \Pi_{\delta_c} = \frac{\ell^2\, \delta_c}{\mathcal{D}_m}, \\
\Pi_{\mathcal{D}_{sn}} &= \frac{\mathcal{D}_{s_n}}{\mathcal{D}_m}, \quad \Pi_{\kappa_n} = \frac{\kappa_n\, \mathsf{A}\, \ell^2\, n^r ef}{\mathcal{D}_m\, s_n^{ref}}, \quad \Pi_{\delta_{sn}} = \frac{\ell^2\, \delta_{s_n}}{\mathcal{D}_m}, \\
\Pi_{\mathcal{D}_{se}} &= \frac{\mathcal{D}_{s_e}}{\mathcal{D}_m}, \quad \Pi_{\kappa_e} = \frac{\kappa_e\, \mathsf{A}\, \ell^2\, n^r ef}{\mathcal{D}_m\, s_e^{ref}}, \quad \Pi_{\delta_{se}} = \frac{\ell^2\, \delta_{s_e}}{\mathcal{D}_m}.
\end{aligned}$$

The reference quantities are chosen as

n^{ref} = initial concentration of granulated mastocytes,

c^{ref} = concentration of the stored chemoattractant before degranulation,

s_n^{ref} = concentration of the stored nerve stimulant before degranulation,

s_e^{ref} = concentration of the stored endocrine stimulant before degranulation.

4.7.2 Finite element method

For the sake of clarity, let us simplify the notation by changing the previous dimensionless parameters Π_{i} into i. Then, the chemotaxis system is solved in the domain Ω in a

time interval $(0, T)$

$$\begin{aligned}
\frac{\partial n_g}{\partial t} - \nabla^2 n_g + \mathsf{S}\nabla \cdot (n_g \nabla c) &= -\mathsf{A}\Phi n_g + k_r n_d, \quad \text{in } \Omega \times (0,T), \\
\frac{\partial c}{\partial t} - \mathcal{D}_c \nabla^2 c &= \kappa_c \Phi n_g - \delta_c c, \\
\frac{\partial n_d}{\partial t} - \nabla^2 n_d &= \mathsf{A}\Phi n_g - k_r n_d, \\
\frac{\partial s_n}{\partial t} - \mathcal{D}_{s_n} \nabla^2 s_n &= \kappa_n \Phi n_g - \delta_{s_n} s_n, \\
\frac{\partial s_e}{\partial t} - \mathcal{D}_{s_e} \nabla^2 s_e &= \kappa_e \Phi n_g - \delta_{s_e} s_e.
\end{aligned} \tag{4.55}$$

The above system is endowed with the prescribed initial conditions in (4.9) and the homogeneous Neumann boundary condition (4.10) or the zero total flux boundary conditions (4.11).

4.7.2.1 Weak formulation

Let the solution (n_g, n_d, c, s_n, s_e) of (4.55) be regular enough, for example in $(H^2(\Omega))^5$. The equations in (4.55) are multiplied by a test function w_i in $(H^1(\Omega))^5$ $(i = g, d, c, n, e)$ and are integrated over Ω. Applying the Green formula and taking into account the homogeneous Neumann boundary condition (4.10) yield the weak formulation of the problem in the subspace $H^1(\Omega)$ that reads as follows. Find $(n_g, n_d, c, s_n, s_e) \in (H^1(\Omega))^5$ such as

$$\begin{aligned}
\int_\Omega \frac{\partial n_g}{\partial t} w_g + \int_\Omega \nabla n_g \cdot \nabla w_g - \int_\Omega \mathsf{S}\, n_g \nabla c \cdot \nabla w_g + \int_\Omega \mathsf{A}\Phi n_g w_g &= \int_\Omega k_r n_d w_g, \\
\int_\Omega \frac{\partial c}{\partial t} w_c + \int_\Omega \mathcal{D}_c \nabla c \nabla w_c + \int_\Omega \delta_c c w_c &= \int_\Omega \kappa_c \Phi n_g w_c, \\
\int_\Omega \frac{\partial n_d}{\partial t} w_d + \int_\Omega \nabla n_d \cdot \nabla w_d + \int_\Omega k_r n_d w_d &= \int_\Omega \mathsf{A}\Phi n_g w_d, \\
\int_\Omega \frac{\partial s_n}{\partial t} w_n + \int_\Omega \mathcal{D}_{s_n} \nabla s_n \cdot \nabla w_n + \int_\Omega \delta_{s_n} s_n w_n &= \int_\Omega \kappa_n \Phi n_g w_n, \\
\int_\Omega \frac{\partial s_e}{\partial t} w_e + \int_\Omega \mathcal{D}_{s_e} \nabla s_e \cdot \nabla w_e + \int_\Omega \delta_{s_e} s_e w_e &= \int_\Omega \kappa_e \Phi n_g w_e,
\end{aligned} \tag{4.56}$$

$\forall w_g, w_d, w_c, w_n, w_e \in H^1(\Omega)$.

4.7.2.2 Decoupled method

The term $n_g \nabla c$ is not easy to treat because of its nonlinear nature when considering a monolithic method. It is convenient to decouple the system using the previously computed solutions. For the temporal discretization scheme, the θ - scheme given in (**??**) is employed.

A semi-discretization in time gives the following scheme.

1. Solve the semi-linear scheme in c^{m+1} using n_g^m

$$\frac{c^{m+1}-c^m}{\Delta t} - \mathcal{D}_c \nabla^2 c^{m+1} = \kappa_c \Phi n_g^m - \delta_c c^{m+1}. \tag{4.57}$$

   The solution c^{m+1} serves to compute the mastocyte density.

2. Solve the semi-linear scheme in n_d^{m+1} using n_g^m

$$\frac{n_d^{m+1}-n_d^n}{\Delta t} - \nabla^2 n_d^{m+1} = \mathsf{A}\Phi n_g^m - k_r n_d^{m+1}. \tag{4.58}$$

   The solution n_d^{m+1} serves to compute the mastocyte density.

3. Solve the semi-linear scheme in n_g^{m+1} using c^{m+1}, n_d^{m+1}

$$\frac{n_g^{m+1}-n_g^m}{\Delta t} - \nabla^2 n_g^{m+1} + \mathsf{S}\nabla\cdot\left(n_g^{m+1}\nabla c^{m+1}\right) = -\mathsf{A}\Phi n_g^{m+1} + k_r n_d^{m+1}. \tag{4.59}$$

4. Solve the semi-linear scheme in s_n^{m+1} using n_g^{m+1}

$$\frac{s_n^{m+1}-s_n^m}{\Delta t} - \mathcal{D}_{s_n} \nabla^2 s_n^{m+1} = \kappa_n \Phi n_g^{m+1} - \delta_{s_n} s_n^{m+1}. \tag{4.60}$$

5. Solve the semi-linear scheme in s_e^{m+1} using n_g^{m+1}

$$\frac{s_e^{m+1}-s_e^m}{\Delta t} - \mathcal{D}_{s_e} \nabla^2 s_e^{m+1} = \kappa_e \Phi n_g^{m+1} - \delta_{s_e} s_e^{m+1}. \tag{4.61}$$

4.7.2.3 Full discretization

The full discretization of the problem (4.56) corresponds to the finite element space discretization of the semi-discretized scheme represented by (4.57)-(4.61). The scheme for the model (4.8)-(4.9)-(4.10) is summarized as follows

1. Find $c^{m+1} \in V_c^h$ such that

$$\int_\Omega \frac{c^{m+1}-c^m}{\Delta t} w_c^h + \int_\Omega \mathcal{D}_c \nabla c^{m+1} \nabla w_c^h + \int_\Omega \delta_c c^{m+1} w_c^h = \int_\Omega \kappa_c \Phi n_g^m w_c^h, \quad \forall w_c^h \in V_c^h. \tag{4.62}$$

2. Find $n_d^{m+1} \in V_d^h$ such that

$$\int_\Omega \frac{n_d^{m+1}-n_d^n}{\Delta t} w_d^h + \int_\Omega \nabla n_d^{m+1} \cdot \nabla w_d^h + \int_\Omega k_r n_d^{m+1} w_d^h = \int_\Omega \mathsf{A}\Phi n_g^m w_d^h, \quad \forall w_d^h \in V_d^h. \tag{4.63}$$

3. Find $n_g^{m+1} \in V_g^h$ such that

$$\int_\Omega \frac{n_g^{m+1}-n_g^n}{\Delta t} w_g + \int_\Omega \nabla n_g^{m+1} \cdot \nabla w_g^h - \int_\Omega \mathsf{S}\, n_g^{m+1} \nabla c^{m+1} \cdot \nabla w_g^h + \int_\Omega \mathsf{A}\Phi n_g^{m+1} w_g^h$$
$$= \int_\Omega k_r n_d^{m+1} w_g^h,\ \forall w_g^h \in V_g^h. \tag{4.64}$$

4. Find $s_n^{m+1} \in V_n^h$ such that

$$\int_\Omega \frac{s_n^{m+1}-s_n^m}{\Delta t} w_n^h + \int_\Omega \mathcal{D}_{s_n} \nabla s_n^{m+1} \cdot \nabla w_n^h + \int_\Omega \delta_{s_n} s_n^{m+1} w_n^h = \int_\Omega \kappa_n \Phi n_g^{m+1} w_n^h, \quad \forall w_n^h \in V_n^h. \tag{4.65}$$

5. Find $s_e^{m+1} \in V_e^h$ such that

$$\int_\Omega \frac{s_e^{m+1}-s_e^m}{\Delta t} w_e^h + \int_\Omega \mathcal{D}_{s_e} \nabla s_e^{m+1} \cdot \nabla w_e^h + \int_\Omega \delta_{s_e} s_e^{m+1} w_e^h = \int_\Omega \kappa_e \Phi n_g^{m+1} w_e^h, \quad \forall w_e^h \in V_e^h. \tag{4.66}$$

***Remark* 3.** *To complete the numerical method, one needs to choose the finite element spaces. The choice of the classical P^1 finite element space for n_g^{m+1}, n_d^{m+1}, s_n^{m+1}, and s_e^{m+1} is reasonable. However, for c^{n+1} the classical P^2 finite element space is required. Indeed, if c^{m+1} is piecewise $\mathbb{P}_2$, then the chemotactic vector field $\mathsf{S}\nabla c^{m+1}$ is piecewise $\mathbb{P}_1$.*

The scheme can be applied to the models (4.36)-(4.9)-(4.10) and (4.43)-(4.9)-(4.10) by skipping the steps corresponding to the omitted equations.

One of the advantages of the artificial decoupling is the quasi-linearity of the equations. This reduces the computational cost and thus the efficiency of the method is improved. Nevertheless, the quality of the solutions depends on the chemotactic sensitivity S, the activation rate A, and the release coefficient κ_c. To enhance the quality of the computation (and to reduce the computation cost), mesh adaptation (a subroutine of FreeFem++) fits the initial condition, i.e., a given cell distribution within the domain of interest, as the solution evolves locally.

4.7.2.4 Code validation

Verification of the traditional Keller-Segel equation To quantify the convergence behavior with respect to the mesh size, several meshes are considered on the domain Ω and the errors are evaluated on the density n_g and the concentration c with respect to the $L^2(\Omega)$ and $H^1(\Omega)$ norms. The related convergence are plotted in figures 4.2, 4.3, and 4.4 in logarithmic scales. For the $\mathbb{P}_1$-$\mathbb{P}_2$ finite elements, the slope for n_g in the $L^2(\Omega)$ norm is evaluated to be 2.50, in the $L^\infty(\Omega)$ norm evaluated to be 2.11 and in the $H^1(\Omega)$ norm

evaluated to be 1.01. The slope for c in the $L^2(\Omega)$ norm is evaluated to be 2.11, in the $L^\infty(\Omega)$ norm evaluated to be 2.10 and in the $H^1(\Omega)$ norm evaluated to be 2.08. For the $\mathbb{P}_2$-$\mathbb{P}_2$ finite elements, the slope for n_g in the $L^2(\Omega)$ norm is evaluated to be 2.57, in the $L^\infty(\Omega)$ norm evaluated to be 2.70 and in the $H^1(\Omega)$ norm evaluated to be 2.37. The slope in c in the $L^2(\Omega)$ norm is evaluated to be 2.06, in the $L^\infty(\Omega)$ norm evaluated to be 2.07 and in the $H^1(\Omega)$ norm evaluated to be 2.07. The rate of convergence for n_g in the $H^1(\Omega)$ norm is considerably improved. For the $\mathbb{P}_2$-$\mathbb{P}_3$ finite elements, the slope for n_g and c are close to the previous one. Thus for the $\mathbb{P}_2$-$\mathbb{P}_3$ finite elements, the rates of convergence for n_g and c are not improved. From the computed convergence rates the choice of $\mathbb{P}_2$-$\mathbb{P}_2$ finite elements drastically improves the quality of the solution. Therefore, from now on, numerical simulations will be carried out using $\mathbb{P}_2$-$\mathbb{P}_2$ finite elements

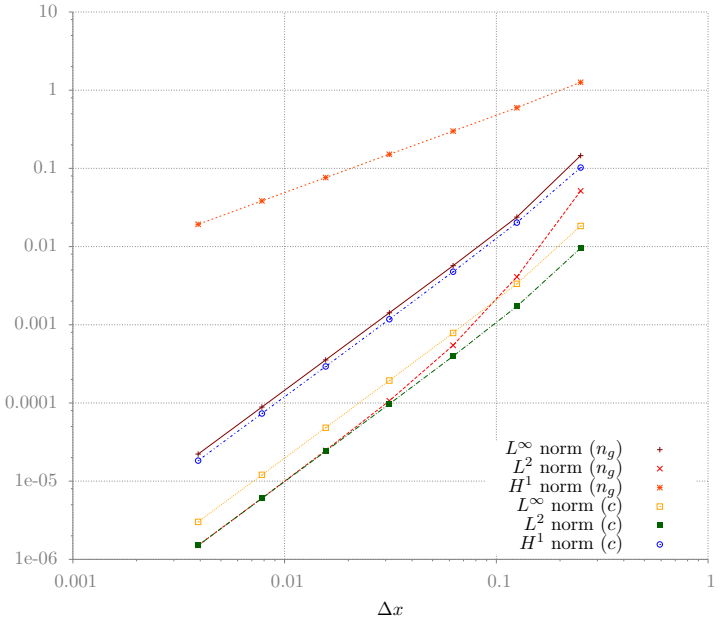

Figure 4.2: Convergence rates for the $\mathbb{P}_1$-$\mathbb{P}_2$ finite elements

Sensitivity to the chemotactic sensitivity The next issue is to check the sensitivity of the computation to the chemotactic sensitivity parameter S. Numerical simulations are carried out with a fixed mesh where the chemotactic sensitivity parameter S varies in the interval $[1, 100]$. The error curves are then plotted against S for different meshes. Figures 4.5, 4.6, and 4.7 show the curves for mesh sizes $\Delta x = 1/16$, $\Delta x = 1/64$, and $\Delta x = 1/256$, respectively. The important observation is that the chemotactic sensitivity parameter affects strongly the results of n_g. However, the chemotactic sensitivity parameter seems to affect very slightly the results of c. This shows the necessity to refine the mesh to improve the quality of the results. Mesh adaptation can be used to refine the mesh locally according to the weight of the chemotaxis term $\mathsf{S}\nabla \cdot (n_g \nabla c)$.

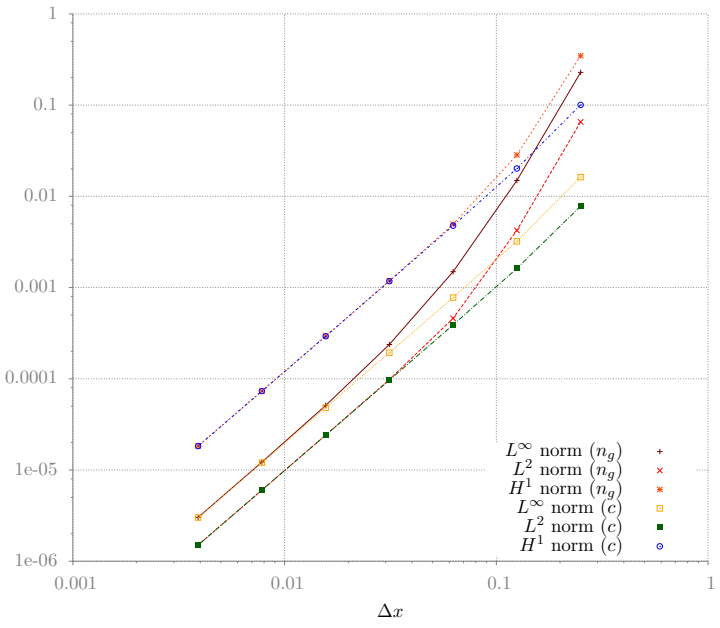

Figure 4.3: Convergence rates for the $\mathbb{P}_2$-$\mathbb{P}_2$ finite elements

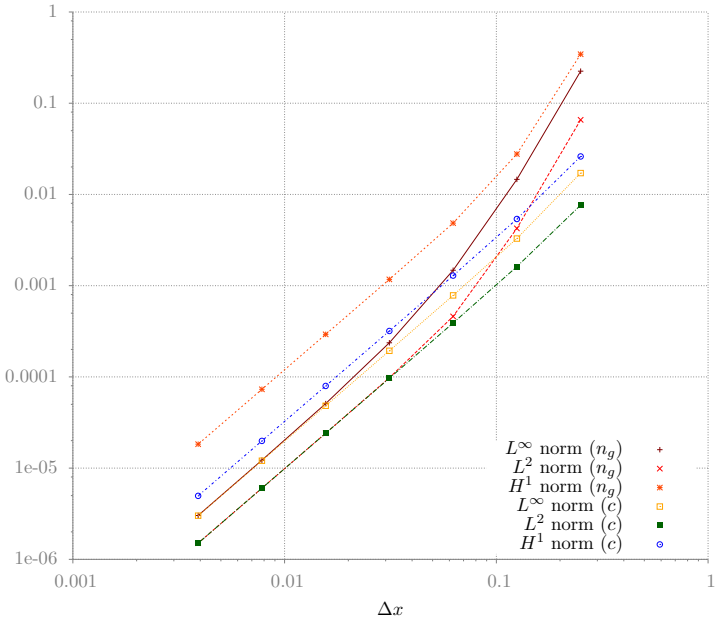

Figure 4.4: Convergence rates for the $\mathbb{P}_2$-$\mathbb{P}_3$ finite elements

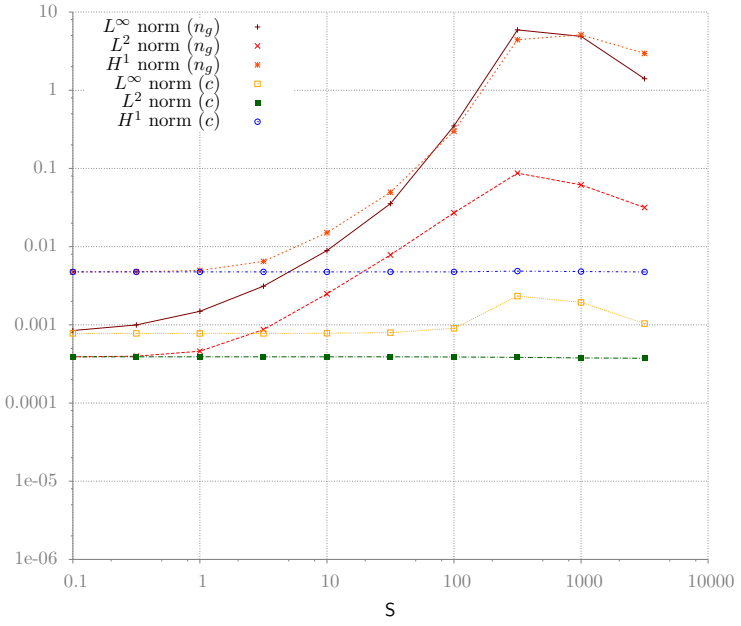

Figure 4.5: Influence of the chemotactic sensitivity parameter S with a mesh size $\Delta x = 1/16$.

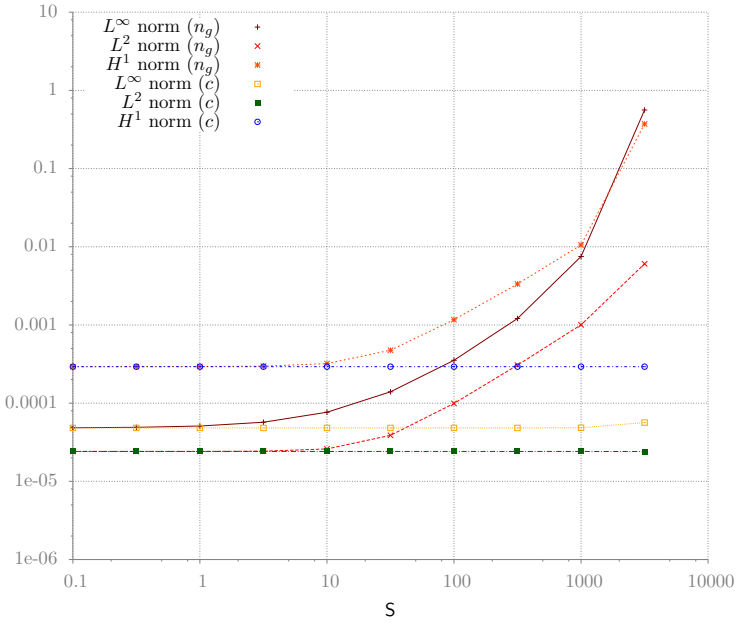

Figure 4.6: Influence of the chemotactic sensitivity parameter S with a mesh size $\Delta x = 1/64$.

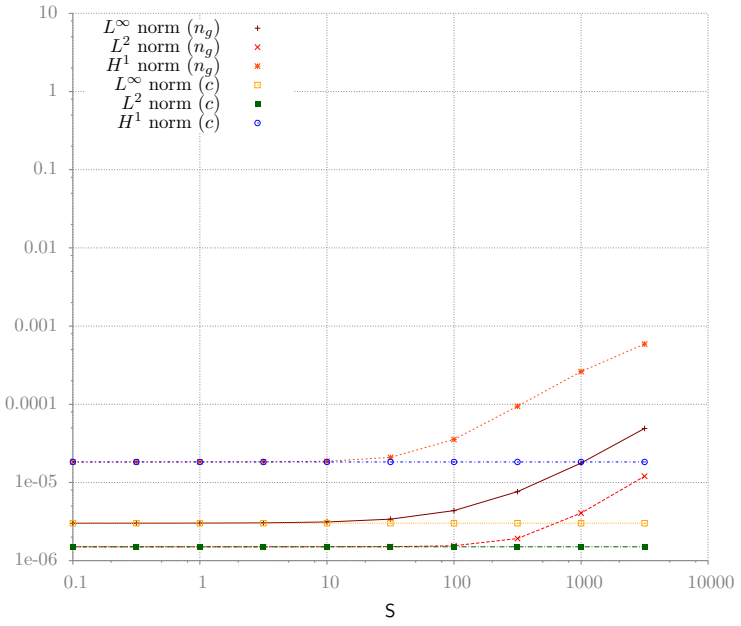

Figure 4.7: Influence of the chemotactic sensitivity parameter S with a mesh size $\Delta x = 1/256$.

4.8 Computational model

4.8.1 Acupoints

Acupoints feature a higher mastocyte density than its neighboring regions. The initial mastocyte distribution can be modeled by one Gaussian distribution given below

$$n(x, y, t = 0) = a_n \exp\left(-\left(\frac{(x - x_{n_0})^2}{2\sigma_{n_x}^2} + \frac{(y - y_{n_0})^2}{2\sigma_{n_y}^2}\right)\right) + b_n, \quad (x, y) \in \mathbb{R}^2. \quad (4.67)$$

In the above, a_n is the amplitude of the Gaussian distribution, b_n the minimal mastocyte density in the tissue, $\sigma_{n_x}$the dispersion in the x-direction, σ_{n_y} the dispersion in the y-direction, and (x_{n_0}, y_{n_0}) the coordinates of maximum mastocyte density.

In the full space $\mathbb{R}^2$, if $b_n = 0$, $\sigma_{n_x} = \sigma_{n_y} = \sigma$, and $x_{n_0} = y_{n_0} = 0$, the number of mastocyte is given by

$$m_{|_{\mathbb{R}^2}} = \int_{-\infty}^{-\infty} \int_{-\infty}^{-\infty} n(x, y, t = 0) dx dy = 2\pi a_n \sigma^2. \quad (4.68)$$

On the disc centered at $(0,0)$ with radius R, the number of mastocyte is given by

$$\begin{aligned} m_{|_{D(0,R)}} &= \int\int_{D(0,R)} n(x,y,t=0)dxdy \\ &= \int_0^{2\pi}\int_0^R a_n R \exp\left(-\left(\frac{R^2}{2\sigma^2}\right)\right)drd\theta \\ &= 2\pi a_n \sigma^2 (1 - e^{-\frac{R^2}{2\sigma^2}}). \end{aligned} \tag{4.69}$$

By choosing accordingly the parameter a_n, σ_{n_x} and σ_{n_y}, the quantity of mastocytes and their dispersion can be controlled (see figure 4.8.1 and table 4.2) in the initial distribution. Acupointa are represented by a large quantity and the concentrated distribution of mastocytes, whereas non-acupoints are characterized by a dispersed distribution of mastocytes (see figure 4.10).

Table 4.2: Repartition of the mass in a Gaussian distribution in the full domain $\mathbb{R}$ and $\mathbb{R}^2$

1D		2D	
$R=$	$m_{\|_{[-R,R]}} =$	$R=$	$m_{\|_{D(0,R)}} =$
σ	$0.683 m_{\|_{\mathbb{R}}}$	σ	$0.393 m_{\|_{\mathbb{R}^2}}$
2σ	$0.955 m_{\|_{\mathbb{R}}}$	2σ	$0.632 m_{\|_{\mathbb{R}^2}}$
3σ	$0.997 m_{\|_{\mathbb{R}}}$	3σ	$0.776 m_{\|_{\mathbb{R}^2}}$
		4σ	$0.865 m_{\|_{\mathbb{R}^2}}$
		5σ	$0.918 m_{\|_{\mathbb{R}^2}}$
		6σ	$0.950 m_{\|_{\mathbb{R}^2}}$
		7σ	$0.970 m_{\|_{\mathbb{R}^2}}$
		8σ	$0.982 m_{\|_{\mathbb{R}^2}}$
		9σ	$0.989 m_{\|_{\mathbb{R}^2}}$
		10σ	$0.993 m_{\|_{\mathbb{R}^2}}$
		14σ	$0.999 m_{\|_{\mathbb{R}^2}}$

4.8.2 Stress function Φ

The stress function Φ is smooth and compactly supported as defined in (4.12). In the numerical simulations, the so-called bump function defined below is employed

$$\Phi_B(x,y) = \begin{cases} \alpha \exp\left(-\frac{\beta}{\ell^2 - x^2 - y^2}\right), \text{ if } x^2 + y^2 < \ell^2, \\ 0, \text{ elsewhere.} \end{cases} \tag{4.70}$$

In the above, ℓ is the distance range of the applied stress. α and β are the two positive parameters that control the amplitude and the shape of the function Φ (see figure 4.9)

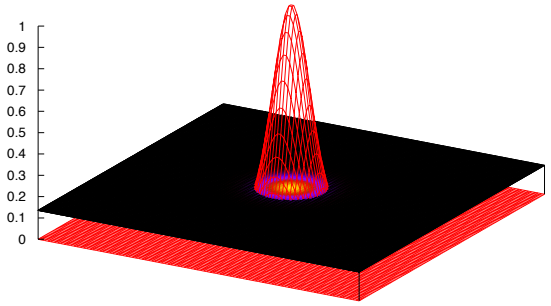

Figure 4.8: Gaussian spatial distribution of mastocytes in a bounded domain Ω. If $b_n = 0$ and $\sigma_{n_x} = \sigma_{n_y} = \sigma = \frac{R}{2}$, then approximately 86.5% of the total initial mastocytes is in the disc $D((x_{n_0}, y_{n_0}), 2\sigma)$.

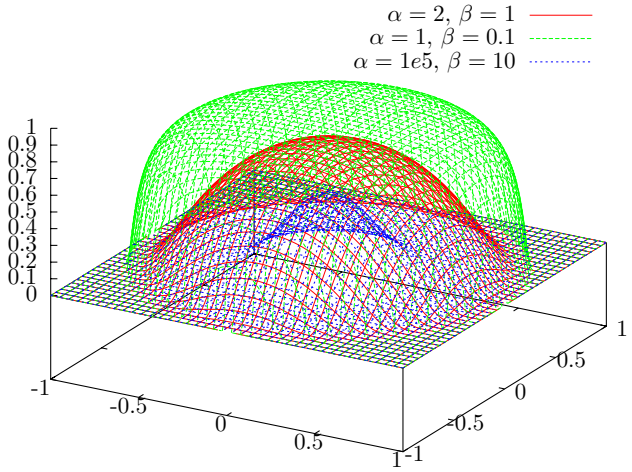

Figure 4.9: Stress function Φ defined as the bump function (4.70)

4.9 Numerical results

Any acupoint is characterized by the distribution of mastocytes, the major biological constituent assumed to be involved in acupuncture. A small second moment of the mastocyte distribution at acupoint correspond to a mastocyte density high enough to trigger effectively the acupuncture mechanism. According to the initial distribution of the mastocytes on the one hand and to the needle position with respect to the location of the peak cell density on the other hand, i.e., whether the practician is an expert or not, the expected blow-up solution can be obtained (see figure 4.10). Acupuncture is successful when the needle is implanted in the acupoint and not in a nearby pool of mastocytes that can have the same cell number (see figure 4.11).

Strong aggregation of mastocytes indicates the expertise of the practician and efficiency of the stimulation of selected acupoints. Numerical results are presented for three initial mastocyte Gaussian distributions with the identical cell number (see figure 4.12): (i) acupoint (large density; concentrated distribution; $m^0 = 50.00$, $m_2^0 = 11.12$), (ii) non-acupoint (large density; dispersed distribution; $m^0 = 50.00$, $m_2^0 = 165.19$), and (iii) non-acupoint (small density; $m^0 = 10.00$). Successful acupuncture targets a subcutaneous region where mastocytes densely aggregate. Conversely, acupuncture fails when the needle is implanted in a zone poor in mastocytes or enriched in mastocytes, but where cells spread over too large a volume.

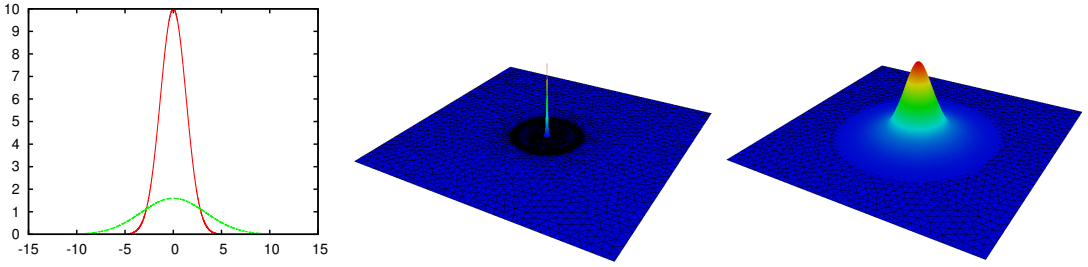

Figure 4.10: Initial (**left**) and final distributions of mastocytes at the acupoint (**middle**) and non-acupoint (**right**). The blow-up solution is expected only at acupoint.

4.10 Concluding remarks

This chapter has shown that the mathematical analysis of the proposed model can help gain a better understanding of the role of chemotactic recruitment of mastocytes in response to physical stimuli. The lack of experimental data to validate the model raises the following remarks.

The mathematical analysis of the proposed simplified model has shown a mechanism for blow-up in the chemotactic mechanism during acupuncture. A small second moment of the density of mastocytes conveys the idea that the cells are concentrated at the

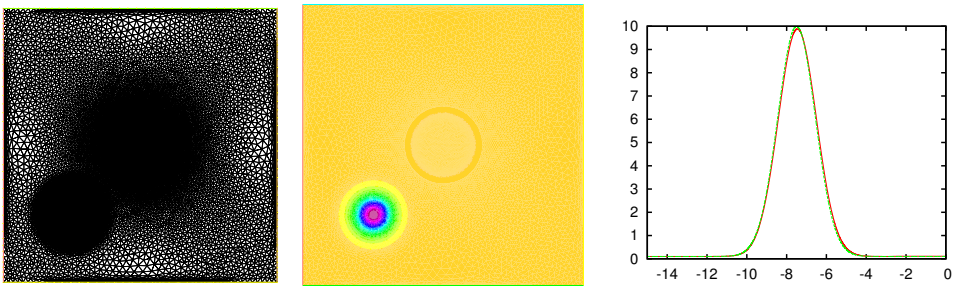

Figure 4.11: Needling outside an acupoint. Refined mesh in the needle region (center) and mastocyte pool region (left bottom corner). Absence of a significant change in the cell population distribution.

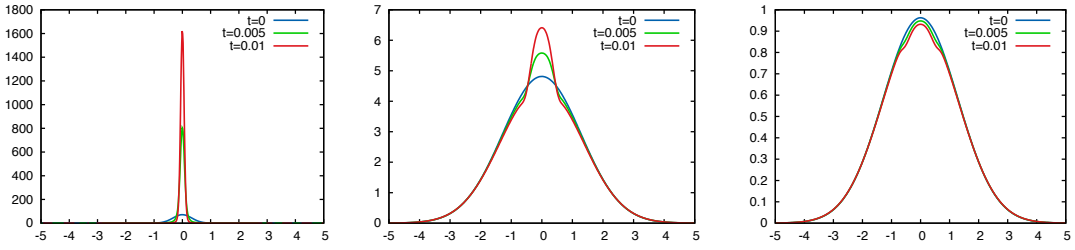

Figure 4.12: Granulated mastocyte density dynamics. (**left**) Acupoint : $m^0 = 50.00$, $m_2^0 = 11.12$; (**middle**) Non-acupoints : $m^0 = 50.00$, $m_2^0 = 165.19$; (**right**) Non-Acupoint : $m^0 = 10.00$.

acupuncture points. Blow-up will occur when the initial number of mastocytes is high enough and when they are sufficiently concentrated around the acupuncture points. A blow-up solution means that incoming mastocytes converge toward the needle, the expected behavior.

The blow-up solution shows the limitation of the proposed model that corresponds to an over-simplification of the biology. A blow-up solution is defined as a solution that becomes unbounded in either finite or infinite time. Following the definition of Horstmann [134], a model describes aggregation of cells if the solution remains bounded and the L^∞ norm of the solution is larger than the L^∞ norm of the initial data. However, a blow-up solution can still be considered as a limiting case of aggregation where the cell distribution is a Dirac function.

The numerical treatment of the proposed model is able to support the expected behavior. The expected blow-up solution is obtained depending on the initial mastocyte distribution that corresponds to an acupoint or a non-acupoint, and on the needle position with respect to the location of the maximum of the mastocyte distribution.

The present work is aimed at investigating the local effect of acupuncture at a single acupoint and does not allow to describe neither the effect on the brain and its response to a given target organ, nor at multiple acupoints. Hence, little focus is put on nerve and endocrine messenger concentrations.

Chapter 5

Chemotaxis–diffusion–convection coupling system

Contents

5.1 Introduction 128

5.2 Mathematical model 131

5.3 Computational model 133

5.3.1 Scaling and setting for numerical simulations 133

5.3.2 Numerical methods 134

5.3.3 Code validation for the coupled Navier-Stokes and Keller-Segel equations 135

5.4 Numerical results and discussion 136

5.4.1 Descending plumes 136

5.4.2 Stabilizing effect of chemotaxis 141

5.4.3 Distribution and number of plumes and initial conditions 144

5.4.4 Comparison with other buoyancy-driven convections 151

5.5 Concluding remarks 155

The work presented in this chapter has association with the following publication.

- Y. Deleuze, C.Y. Chiang, M. Thiriet, T.W.H. Sheu. "Numerical study of plume patterns in the chemotaxis–diffusion–convection coupling system" (forthcoming).

Abstract

A chemotaxis–diffusion–convection coupling system for describing a form of buoyant convection in which the fluid develops convection cells and plume patterns will be investigated numerically in this study. Based on the two-dimensional convective chemotaxis-fluid model proposed in the literature, an upwind finite element model for investigating the pattern formation and the hydrodynamical stability of the system is developed. The numerical simulations illustrate different predicted physical regimes in the system. In the convective regime, the predicted plumes resemble Bénard instabilities. Numerical results show how structured layers of bacteria are formed before bacterium rich plumes fall in the fluid. The plumes have a well defined spectrum of wavelengths and have an exponential growth rate, yet their position can only be predicted in very simple examples. In the chemotactic and diffusive regimes, the effects of chemotaxis are investigated. Numerical results also indicate that the chemotaxis can stabilize the overall system when the chemotaxis head and sensitivity is large. Finally, a qualitative comparison of the differential systems of chemotaxis–diffusion–convection, double diffusive convection, and Rayleigh-Bénard convection is made to clarify the close relationship between the three systems. The physical mechanisms of the three differential system are different, the differential systems expressed in their dimensionless form are, however, very similar to each other.

5.1 Introduction

The phenomenon that couples chemotaxis, diffusion, and convection has been illustrated by experiments on suspensions of bacteria in a container filled with water [135, 136]. In particular, aerotaxis is related to the movement toward a gradient of increasing oxygen concentration. Oxygen diffuses in the container from the surface. As bacteria consume oxygen, oxygen concentration falls everywhere except at the surface, hence creating a vertical concentration difference. Bacteria move up to higher concentration of oxygen and quickly get densely packed below the surface in a relatively thin layer. Subsequently, Rayleigh–Bénard-like instability appears near the surface. These dynamical instabilities exhibit complex convection patterns with plumes of bacteria falling in the fluid.

Chemotaxis–diffusion–convection is a particular case of the so-called bioconvection. Bioconvection is a more general term for suspensions of swimming microorganisms which are denser than the solvent fluid. Bioconvection and the different mechanisms of upswimming have been reviewed [137].

In this study, the model equations (5.1) are used to describe chemotactic response of bacterium suspensions. The unstable agglomeration of bacterium cells at the surface leads to the formation of plume patterns. Formation and stability of plumes result from

Parameter	Definition	Dimension
c	concentration of oxygen	mol
c_{air}	concentration of oxygen in air	mol
D	diffusivity	$\mathrm{m}^2.\,\mathrm{s}^{-1}$
h	container height	m
H	chemotaxis head	
$\mathbf{j}$	vertical unit vector upwards	
ℓ	dimensionless container width	
Le	Lewis number	
n	number density of bacteria	m^{-3}
$\mathbf{n}$	unit outward normal vector	
n_0	initial number density of bacteria	m^{-3}
$\overline{n_0}$	initial average number density of bacteria	m^{-3}
p	pressure	$\mathrm{kg.\,m.\,s}^{-2}$
Pr	Prandtl number	
Ra	Rayleigh number	
S	dimensionless chemotaxis sensitivity	
S_{dim}	dimensional chemotaxis sensitivity	$\mathrm{m}^5.\,\mathrm{s}^{-1}.\,\mathrm{mol}^{-1}$
t	time	s
T	time scale of bacterium transport	s
$\mathbf{u}$	velocity vector	$\mathrm{m.\,s}^{-1}$
V_b	volume of a bacterium	m^3
$\mathbf{x} = (x, y)$	coordinate axes	m
Greek symbols		
κ	bacterium oxygen consumption rate	s^{-1}
μ	dynamic viscosity	$\mathrm{kg.\,m}^{-1}.\,\mathrm{s}^{-1}$
ν	kinematic viscosity	$\mathrm{m}^2.\,\mathrm{s}^{-1}$
ρ	fluid density	$\mathrm{kg.\,m}^{-3}$
ρ_b	bacterium volumetric mass density	$\mathrm{kg.\,m}^{-3}$
Subscripts		
$\cdot_b$	bacterium	
$\cdot_c$	critical	
$\cdot_{\mathrm{conv}}$	convection	
$\cdot_{\mathrm{diff}}$	diffusion	
$\cdot_m$	mass	
$\cdot_O$	oxygen	
$\cdot_s$	solute	
$\cdot_\tau$	taxis	

Table 5.1: Nomenclature and parameter dimensions

	DDC	**CDC**	**RBC**
Rayleigh number	$\mathrm{Ra}_T = \dfrac{g\,\beta_T\,\Delta T\,\mathsf{L}^3}{\mathsf{D}_T\,\nu}$ $\mathrm{Ra}_m = \dfrac{g\,\beta_s\,\Delta s\,\mathsf{L}^3}{\mathsf{D}_s\,\nu}$	$\mathrm{Ra}_\tau = \dfrac{g\,V_b\overline{n_0}(\rho_b-\rho)\mathsf{L}^3}{\mathsf{D}_b\,\mu}$	$\mathrm{Ra}_T = \dfrac{g\,\beta_T\,\Delta T\,\mathsf{L}^3}{\mathsf{D}_T\,\mu}$
Prandtl number	$\mathrm{Pr}_T = \dfrac{\nu}{\mathsf{D}_T}$	$\mathrm{Pr}_\tau = \dfrac{\nu}{\mathsf{D}_b}$	$\mathrm{Pr}_T = \dfrac{\nu}{\mathsf{D}_T}$
Lewis number	$\mathrm{Le}_T = \dfrac{\mathsf{D}_T}{\mathsf{D}_s}$	$\mathrm{Le}_\tau = \dfrac{D_O}{D_b}$	
Chemotaxis sensitivity		$\mathsf{S} = \dfrac{\mathsf{S}_{dim}\,c_{\mathrm{air}}}{\mathsf{D}_b}$	
Chemotaxis head		$\mathsf{H} = \dfrac{\kappa\,\overline{n_0}\,\mathsf{L}^2}{c_{\mathrm{air}}\,D_b}$	

Table 5.2: Representative dimensionless numbers involved in the double diffusive convection (DDC), chemotaxis–diffusion–convection (CDC), and Rayleigh-Bénard convection (RBC). Subscripts $\cdot_m$, $\cdot_T$, $\cdot_\tau$, $\cdot_s$, $\cdot_O$, $\cdot_b$ stand for mass, thermal, taxis, solute, oxygen, and bacterium, respectively; g is the acceleration due to gravity; β_T and β_s are the coefficients for thermal and solute expansion, respectively; ν is the kinematic viscosity.

the balance between chemotaxis, diffusion, and convection of bacteria. The particular impact of each mechanism still needs to be understood.

The linear stability analysis of the chemotaxis-diffusion-convection system [135] showed that a condition for linear instability depends on the taxis Rayleigh number Ra_τ . The taxis Rayleigh number is defined as the ratio of buoyancy and viscosity forces times the ratio of momentum and cell diffusivity. The dimensionless parameters introduced in previous papers were renamed for better readability (see table 5.2). Below a critical value ($\mathrm{Ra}_\tau < \mathrm{Ra}_c$), then the process remains stable. From experiments, several stages were observed starting from the upward bacterium accumulation and leading to hydrodynamic formation of plumes. A weakly nonlinear stability analysis was conducted to investigate the stability of hexagon and roll patterns formed by the system of equations (5.1) [138]. The hydrodynamic vortices formed by convection strengthen circulation of fluid and enhance the intake of oxygen into the solvent [139]. Global existence for the chemotaxis–Stokes system under small initial bacterium population density was proven in [140]. Then, global existence for the chemotaxis–Navier-Stokes system for a large initial bacterium population density as well as global existence of 3D weak solutions for the chemotaxis-Stokes equations were proven in [141].

A detailed numerical study of the plume formation and merging that was related to the convergence of Rayleigh-Bénard-type patterns was carried out in [142]. The shape and number of plumes can be controlled by initial bacterium population density. However, the

sites of plumes have not been predicted. The convergence toward numerically stable and stationary plumes for low and high initial density of cells is revealed in [142].

In this chapter, a computational model based on the finite element method is proposed aiming at investigating the behavior of the two-dimensional chemotaxis–diffusion–convection system.

5.2 Mathematical model

The mathematical model for the chemotaxis–diffusion–convection is proposed in [136] and reads as follows:

$$\begin{aligned} \rho\left(\frac{\partial \mathbf{u}}{\partial t} + \mathbf{u}\cdot\boldsymbol{\nabla}\mathbf{u}\right) + \boldsymbol{\nabla}p - \mu\nabla^2\mathbf{u} &= -n\,V_b g(\rho_b-\rho)\mathbf{j}, \\ \boldsymbol{\nabla}\cdot\mathbf{u} &= 0, \\ \frac{\partial n}{\partial t} + \boldsymbol{\nabla}\cdot[\mathbf{u}n - D_b\boldsymbol{\nabla}n + \mathsf{S}_{dim}r(c)n\boldsymbol{\nabla}c] &= 0, \\ \frac{\partial c}{\partial t} + \boldsymbol{\nabla}\cdot(\mathbf{u}c - D_{\mathrm{O}}\boldsymbol{\nabla}c) &= -n\,\kappa r(c), \end{aligned} \tag{5.1}$$

where $\mathbf{u} = (u, v)$ denotes the velocity field of water (solvent), p the pressure, ρ and μ the water density and viscosity, n the areal number density of bacteria (i.e., number of bacteria per unit area in a 2D space), V_b and ρ_b the volume and volumetric mass density of a bacterium, c the concentration of oxygen, $V_b g(\rho_b - \rho)\mathbf{j}$ the buoyancy force exerted by a bacterium on the fluid in the vertical direction (unit vector $\mathbf{j}$), S_{dim} the dimensional chemotaxis sensitivity, D_b and D_{O} the bacterium and oxygen diffusivities, κ the bacterium oxygen consumption rate, and $r(c)$ the dimensionless cut-off function for oxygen concentration. The cut-off function $r(c)$ is defined by the step function

$$r(c) = \begin{cases} 1 & \text{if } c > c^*, \\ 0 & \text{if } c \le c^*, \end{cases} \tag{5.2}$$

where $c^* = 0.3$.

Bacteria are slightly denser than water and are diluted in the solvent, so that $(\rho_b - \rho)/\rho \ll 1$ and $n\,V_b \ll 1$, respectively. The consumption of oxygen is proportional to the bacterium population density n. Both n and c are advected by the fluid. When the oxygen concentration is lower than a threshold, the bacteria become quiescent [136], that is, they neither consume oxygen nor swim toward sites of higher oxygen concentrations. The dynamics of space filling, intercellular signaling, and quorum sensing are also neglected.

The system of equations (5.1) with the boundary conditions introduced in the previous papers (e.g. [135, 139, 142]) is solved in a two-dimensional rectangular container (Ω). The top boundary (Γ_{top}) represents the interface between liquid and air. On the free surface the concentration of oxygen is equal to the air concentration of oxygen (c_{air}) and

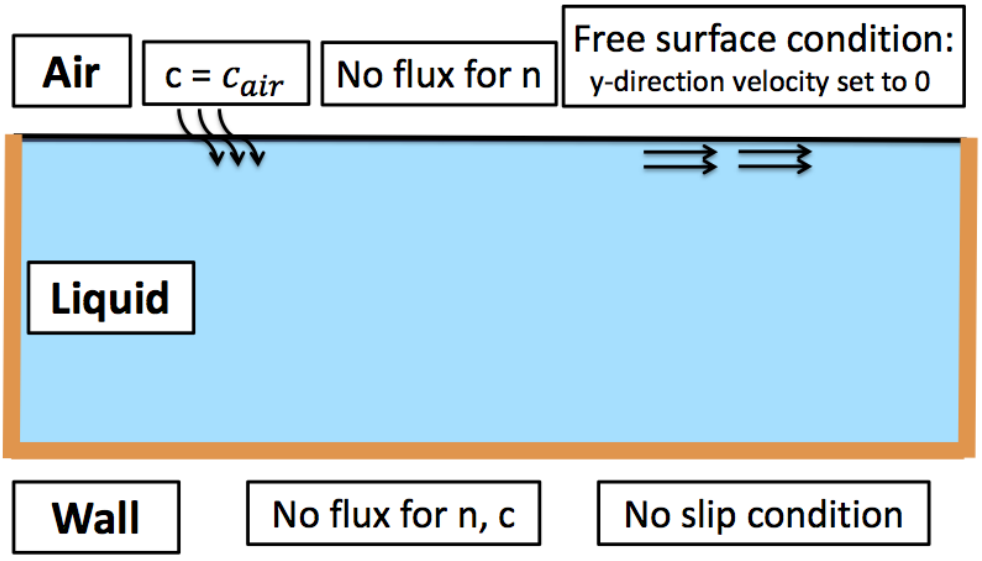

Figure 5.1: Boundary conditions for the the chemotaxis–diffusion–convection system (5.1). The air–water interface, where the oxygen concentration is equal to that of air, is not crossed by bacteria; the fluid vertical velocity component equals zero and the fluid is assumed to be free of tangential stress. The container walls are impermeable to bacteria and oxygen; a no-slip condition is imposed.

the free tangential stress condition as well as the absence of bacterium flux are prescribed (figure 5.1). It is therefore rational to prescribe the following boundary conditions

$$\begin{aligned} &\frac{\partial u}{\partial y} = 0,\ v = 0,\ c = c_{\text{air}}, \\ &\mathsf{S}_{dim}\, n\, r(c)\, \boldsymbol{\nabla} c \cdot \mathbf{n} - D_b\, \boldsymbol{\nabla} n \cdot \mathbf{n} = 0 \ \text{ on } \Gamma_{top}, \end{aligned} \tag{5.3}$$

where $\mathbf{n}$ is the unit outward normal vector. On the container walls (Γ_w), a no-slip boundary condition is prescribed and the fluxes of bacteria and oxygen are equal to zero:

$$u = 0,\ v = 0,\ \boldsymbol{\nabla} n \cdot \mathbf{n} = 0,\ \boldsymbol{\nabla} c \cdot \mathbf{n} = 0 \ \text{ on } \Gamma_w. \tag{5.4}$$

A no-slip condition at the air–water interface would enable the formation of hydrodynamic instabilities. The effect of a moving boundary due to the advection caused by an incompressible fluid flow is to be explored.

5.3 Computational model

5.3.1 Scaling and setting for numerical simulations

The characteristic length is defined by the container height h and the characteristic bacterium density by the average of the initial bacterium population density defined as

$$\overline{n_0} := \frac{1}{|\Omega|} \int_\Omega n_0(x,t)\, dx. \tag{5.5}$$

This particular choice of the characteristic bacterium density gives an easy measure of the total number of bacteria in each simulation for different initial distributions of bacteria.

Dimensionless variables are defined as

$$\begin{aligned} &\mathbf{x}' = \frac{\mathbf{x}}{h},\ t' = \frac{t}{h^2/D_b},\ n' = \frac{n}{\overline{n_0}}, \\ &c' = \frac{c}{c_{\text{air}}},\ p' = \frac{p}{\mu D_b/h^2},\ \mathbf{u}' = \frac{\mathbf{u}}{D_b/h}. \end{aligned} \tag{5.6}$$

Five dimensionless parameters given below characterize the hydrodynamic and chemotaxis transport equations:

$$\begin{aligned} &\mathrm{Pr}_\tau = \frac{\nu}{D_b},\ \mathrm{Ra}_\tau = \frac{g\, V_b \overline{n_0} (\rho_b - \rho) \mathsf{L}^3}{\mathsf{D}_b\, \mu},\ \mathsf{S} = \frac{\mathsf{S}_{dim} c_{\text{air}}}{D_b}, \\ &\mathsf{H} = \frac{\kappa\, \overline{n_0}\, \mathsf{L}^2}{c_{\text{air}}\, D_b},\ \mathrm{Le}_\tau = \frac{D_{\mathrm{O}}}{D_b} \end{aligned} \tag{5.7}$$

where Pr_τ is the taxis Prandtl number, Ra_τ the taxis Rayleigh number (buoyancy-driven flow), Le_τ the taxis Lewis number, S the dimensionless chemotaxis sensitivity, and H the

chemotaxis head. The taxis Prandtl, Rayleigh, and Lewis numbers are analogous to the respective heat and mass Prandtl, Rayleigh, and Lewis numbers in heat and mass transfer (table 5.2). The chemotaxis sensitivity (S) and head (H) characterize the chemotaxis system. Only Ra_τ and H depend on the characteristic length L and characteristic bacterium density $\overline{n_0}$.

After removing the prime in dimensionless quantities, the set of dimensionless equations becomes

$$\begin{aligned} \frac{\partial \mathbf{u}}{\partial t} + \mathbf{u}\cdot\boldsymbol{\nabla}\mathbf{u} - \mathrm{Pr}_\tau\nabla^2\mathbf{u} + \mathrm{Pr}_\tau\boldsymbol{\nabla}p &= -\mathrm{Ra}_\tau\,\mathrm{Pr}_\tau\,n\,\mathbf{j}, \\ \boldsymbol{\nabla}\cdot\mathbf{u} &= 0, \\ \frac{\partial n}{\partial t} + \mathbf{u}\cdot\boldsymbol{\nabla}n - \nabla^2 n + \mathsf{S}\,\boldsymbol{\nabla}\cdot(r(c)n\boldsymbol{\nabla}c) &= 0, \\ \frac{\partial c}{\partial t} + \mathbf{u}\cdot\boldsymbol{\nabla}c - \mathrm{Le}_\tau\nabla^2 c &= \mathsf{H}\,n\,r(c). \end{aligned} \tag{5.8}$$

The system (5.15) is solved in a rectangular domain $\Omega = [-\ell, \ell] \times [0, 1]$ with the initial conditions:

$$\mathbf{u}(\mathbf{x}, 0) = \mathbf{u}_0(\mathbf{x}),\ n(\mathbf{x}, 0) = n_0(\mathbf{x}),\ c(\mathbf{x}, 0) = c_0(\mathbf{x}). \tag{5.9}$$

On the top of the domain Ω, the dimensionless boundary conditions are prescribed as

$$\frac{\partial u}{\partial y} = 0,\ v = 0,\ \mathsf{S}\,r(c)\,n\,\boldsymbol{\nabla}c\cdot\mathbf{n} - D_b\,\boldsymbol{\nabla}n\cdot\mathbf{n} = 0,\ c = 1, \tag{5.10}$$

while on the other boundaries, the dimensionless boundary conditions are imposed as follows

$$u = 0,\ v = 0,\ \boldsymbol{\nabla}n\cdot\mathbf{n} = 0,\ \boldsymbol{\nabla}c\cdot\mathbf{n} = 0. \tag{5.11}$$

In the following sections, the hydrodynamic system will refer to the first two equations in (5.15) and the chemotaxis system to the last two equations in (5.15).

5.3.2 Numerical methods

The governing equations in (5.15) are solved using the finite element method. The biquadratic quadrilateral elements for the primitive variables $\mathbf{u}$ and the bilinear quadrilateral elements for the primitive variables p are adopted to satisfy the LBB stability condition [84–87]. There are nine nodes in one biquadratic quadrilateral element and four nodes in one bilinear quadrilateral element. In each element, the function ϕ can be written as $\phi = \Sigma_i N^i \phi_i$, where ϕ_i are the nodal unknowns.

To avoid the convective instability while solving the convection dominated flow equations, a streamline upwind/Petrov-Galerkin (SUPG) method [143] is employed. The inconsistent Petrov-Galerkin weighted residual model developed in [144] yields the follow-

ing weak formulation

$$\begin{aligned}\int_\Omega [N\frac{\partial \phi}{\partial t} + W(u\frac{\partial \phi}{\partial x} + v\frac{\partial \phi}{\partial y}) + k(\frac{\partial N}{\partial x}\frac{\partial \phi}{\partial x} + \frac{\partial N}{\partial y}\frac{\partial \phi}{\partial y})]d\Omega \\ = \int_\Omega f d\Omega + k(N\frac{\partial \phi}{\partial x}\Big|_{x_1}^{x_2} + N\frac{\partial \phi}{\partial y}\Big|_{y_1}^{y_2}).\end{aligned} \tag{5.12}$$

In the previous inconsistent formulation, the test function W is only applied to the convective term so as to add a numerical stabilizing term. The main purpose of employing a SUPG model is to add an amount of streamline artificial viscosity. The test function W is therefore rewritten in two parts $W = N + B$. B is called the biased part. On each node i, the biased part is $B_j^i = \tau u_j \frac{\partial N^i}{\partial x_j}$ where $j \in \{1, 2\}$ corresponds to the Cartesian coordinates and $(u_1, u_2) = (u, v)$.

From the exact solution of the convection–diffusion equation in one dimension, following the derivation in [144], the constant τ is determined as

$$\tau = \frac{\delta(\gamma_1)\, u\, h_1 + \delta(\gamma_2)\, v\, h_2}{2(u^2 + v^2)}, \tag{5.13}$$

where $\gamma_j = \frac{u_j\, h_j}{2\, k}$ with $(h_1, h_2) = (\Delta x, \Delta y)$ being denoted as the grid sizes. Finally, the derived expression for $\delta(\gamma)$ is given below

$$\delta(\gamma) = \begin{cases} \frac{2 - \cosh(\gamma) - \frac{4}{\gamma}\ \tanh(\frac{\gamma}{2}) + \frac{1}{\gamma}\ \sinh(\gamma)}{4\ \tanh(\frac{\gamma}{2}) - \sinh(\gamma) - \frac{6}{\gamma}\ \sinh(\gamma)\ \tanh(\frac{\gamma}{2})}, & \text{at end-nodes,} \\ \frac{1}{2}\coth(\frac{\gamma}{2}) - \frac{1}{\gamma}, & \text{at center-nodes.} \end{cases} \tag{5.14}$$

For comparison purpose in section 5.4.4, the double diffusion system (5.23) and the Rayleigh–Bénard system (5.24) are solved using the software Freefem++ [1]. The code uses a finite element method based on the weak formulation of the problem. Taylor-Hood $\mathbb{P}_2$–$\mathbb{P}_1$ elements are chosen in FreeFem++. These elements are used together with a characteristic/Galerkin formulation to stabilize the convection terms.

5.3.3 Code validation for the coupled Navier-Stokes and Keller-Segel equations

In this validation study, the following dimensionless differential equations accounting for the coupled Keller-Segel and incompressible viscous hydrodynamic equations are solved

$$\begin{aligned}
\frac{\partial \mathbf{u}}{\partial t} + \mathbf{u}\cdot\boldsymbol{\nabla}\mathbf{u} - \mathrm{Pr}_\tau\nabla^2\mathbf{u} + \mathrm{Pr}_\tau\boldsymbol{\nabla}p &= -\mathrm{Ra}_\tau\,\mathrm{Pr}_\tau\, n\,\mathbf{j} + \mathbf{f}_\mathbf{u},\\
\boldsymbol{\nabla}\cdot\mathbf{u} &= 0,\\
\frac{\partial n}{\partial t} + \mathbf{u}\cdot\boldsymbol{\nabla}n - \nabla^2 n + \mathsf{S}\,\boldsymbol{\nabla}\cdot(r(c)n\boldsymbol{\nabla}c) &= f_n,\\
\frac{\partial c}{\partial t} + \mathbf{u}\cdot\boldsymbol{\nabla}c - \mathrm{Le}_\tau\nabla^2 c &= \mathsf{H}\,n\,r(c) + f_c \text{ in } \Omega.
\end{aligned} \tag{5.15}$$

The physical properties are set at the constant values of $\mathrm{Pr}_\tau = \mathrm{Ra}_\tau = \mathsf{S} = r(c) = \mathrm{Le}_\tau = \mathsf{H} = 1$ in $\Omega = [0,1]\times[0,1]$. Equations in (5.15) are solved at $\Delta t = 0.0001$ in the continuously refined four meshes with $\Delta x = \Delta y = 0.125, 0.1, 0.0625, 0.05$. The predicted errors between the simulated and exact solutions, which are $u_{exact} = -\cos(\pi x)\sin(\pi y)e^{-2\pi^2 t}$, $v_{exact} = \sin(\pi x)\cos(\pi y)e^{-2\pi^2 t}$, $p = c_1 - 0.25(\cos(2\pi x) + \cos(2\pi y))e^{-4\pi^2 t}$, $n_{exact} = \cos(\pi x)\cos(\pi y)e^{-2\pi^2 t}$ and $c_{exact} = \cos(\pi x)\cos(\pi y)e^{-2\pi^2 t}$, are cast in their $L_2 - norms$. The source terms $\mathbf{f}_\mathbf{u}$, f_n, and f_c are derived from the previous exact solutions. From the predicted error norms, the spatial rates of convergence are plotted in Fig. 5.2.

The good agreement between the exact and simulated results and rates of convergence demonstrate the applicability of the proposed SUPG scheme and the flow solver described in section 5.3.2 to investigate the chemotactic phenomena in hydrodynamic environment.

5.4 Numerical results and discussion

The linear stability analysis of the system (5.15) showed that the steady state becomes unstable for a range of physical parameters [135]. For sufficiently large characteristic bacterium density $\overline{n_0}$ and Rayleigh number Ra_τ, hydrodynamic instabilities appear in the region near the surface at which the bacterium density is high. This instability may be related to the Rayleigh-Bénard instability occurring in thermal convection [136, 138]. This instability develops into a descending family of bacterium-rich plumes and leads possibly to the formation of convection cells (figure 5.3 (a)).

When $\overline{n_0}$ is small, small perturbations of the velocity field are damped due to stabilizing effects of viscous friction and chemotaxis and therefore convective motion is negligible. It is shown that for low initial bacterium cell density $\overline{n_0}$ the system (5.15) evolves to a steady and homogeneous state in the horizontal direction governed by the chemotaxis system [136, 142]. Like in the Keller-Segel or angiogenesis system, the random diffusion of cells in this case is balanced by the chemotaxis sensitivity of cells.

5.4.1 Descending plumes

In the present numerical simulations, the descending plumes can be described using three phases. In the first phase (figure 5.4 (a)-(c)), chemotaxis is a dominant mecha-

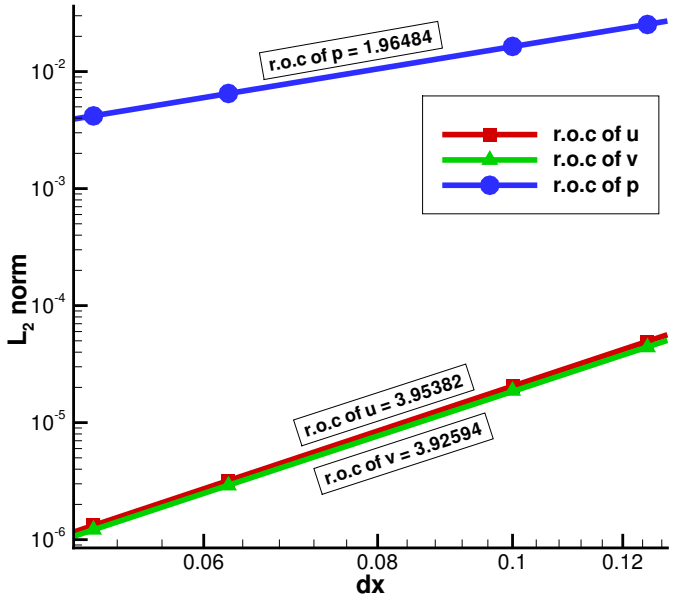

(a)

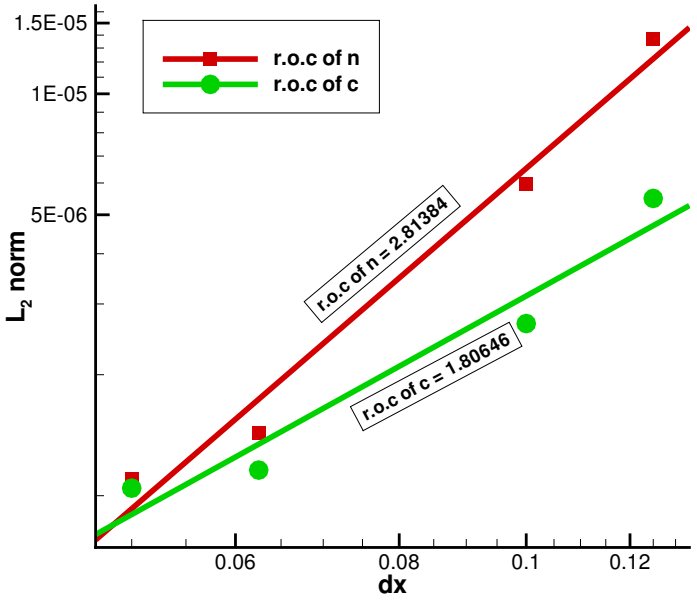

(b)

Figure 5.2: The computed rates of convergence (roc) for the coupled set of Navier-Stokes and Keller-Segel equations. (a) roc= 3.95382 for u, roc= 3.92594 for v, roc= 1.96484 for p; (b) roc= 2.81384 for n, roc= 1.80646 for c.

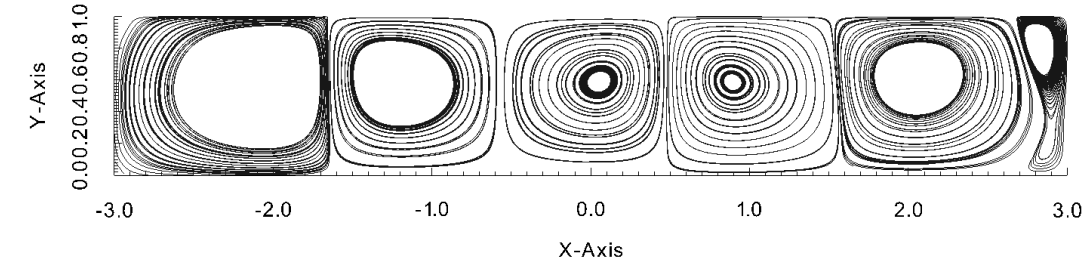

(a) CDC

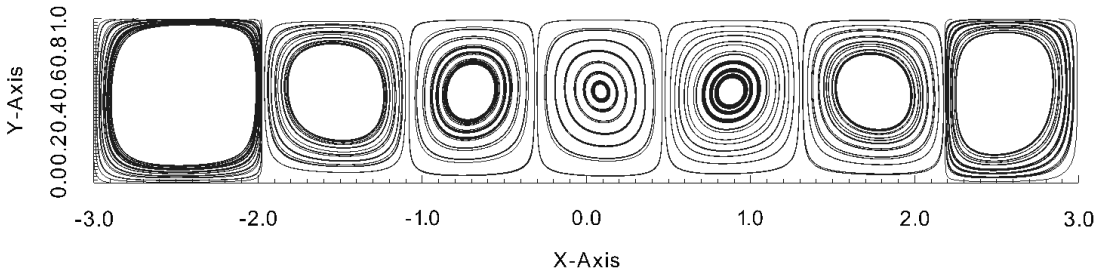

(b) RBC

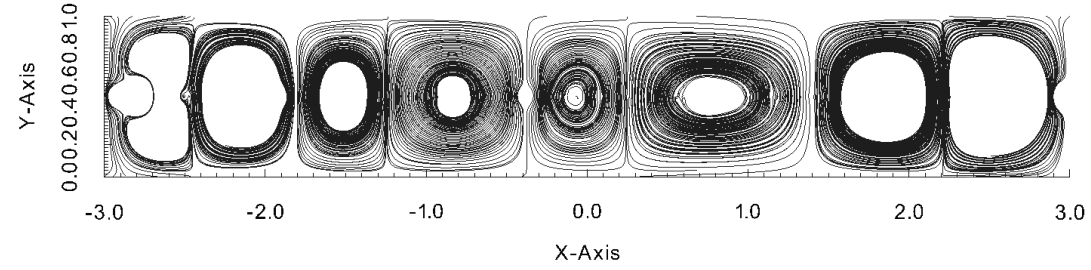

(c) DDC

Figure 5.3: Examples of convection cells for the chemotaxis–diffusion–convection (CDC), Rayleigh-Bénard convection (RBC), and double diffusive convection (DDC)

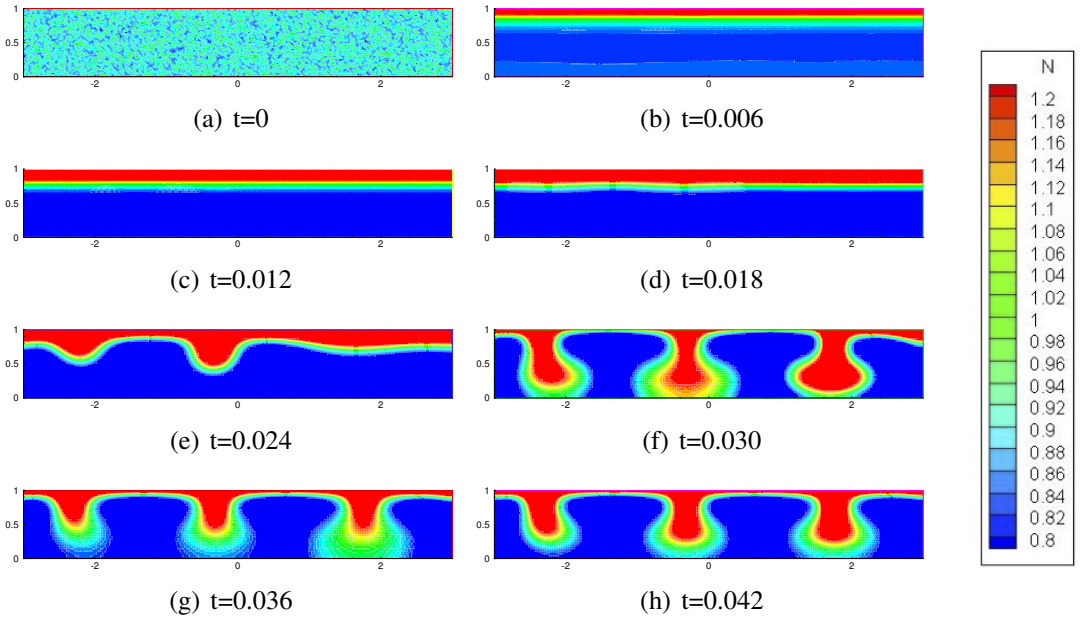

(a) t=0 (b) t=0.006

(c) t=0.012 (d) t=0.018

(e) t=0.024 (f) t=0.030

(g) t=0.036 (h) t=0.042

Figure 5.4: Time evolution of the cell density n. Descending plumes of bacteria develop from an initial randomly distributed bacterium population.

nism. As bacteria consume oxygen, an oxygen concentration gradient is created that in turn provokes a bacterium motion toward the open surface where the oxygen is abundant. Bacterium chemotaxis causes the fluid to set in a motion and engenders counter rotating vortices to form (figure 5.3 (a)). Quickly, the bacterium density n becomes quasi-homogeneous in the horizontal direction and is structured in layers in the vertical direction. A three-layer configuration is induced. A layer of higher concentration of bacteria forms below the air surface: the *stack layer*. When bacteria have migrated in the stack layer, a *depletion layer* is generated. At the container bottom, some bacteria are inactive, because the oxygen concentration decreases below a certain threshold. An *inactive layer* is established.

The second phase (figures 5.4 (d)-(e)) exhibits high bacterium density on the surface. As bacteria swim toward air-supply region, the bacterium density in the stack layer increases. Consequently, advection from the counter rotating vortices becomes significant and brings in perturbations to the stack layer (figure 5.5). Therefore, advection causes instabilities to occur in the bacterium density distribution in the stack layer that sets the fluid in motion. At the same time, the oxygen concentration falls to its minimum at the bottom.

In the third phase (figures 5.4 (f)-(h)), in fluid regions with a greater bacterium density in the stack layer, buoyancy force constrains bacteria to descend in the fluid. As a result, descending plumes of bacteria develop at these particular locations. This mechanism is analogous to the Rayleigh-Bénard instability in heat transfer problems where the fluid

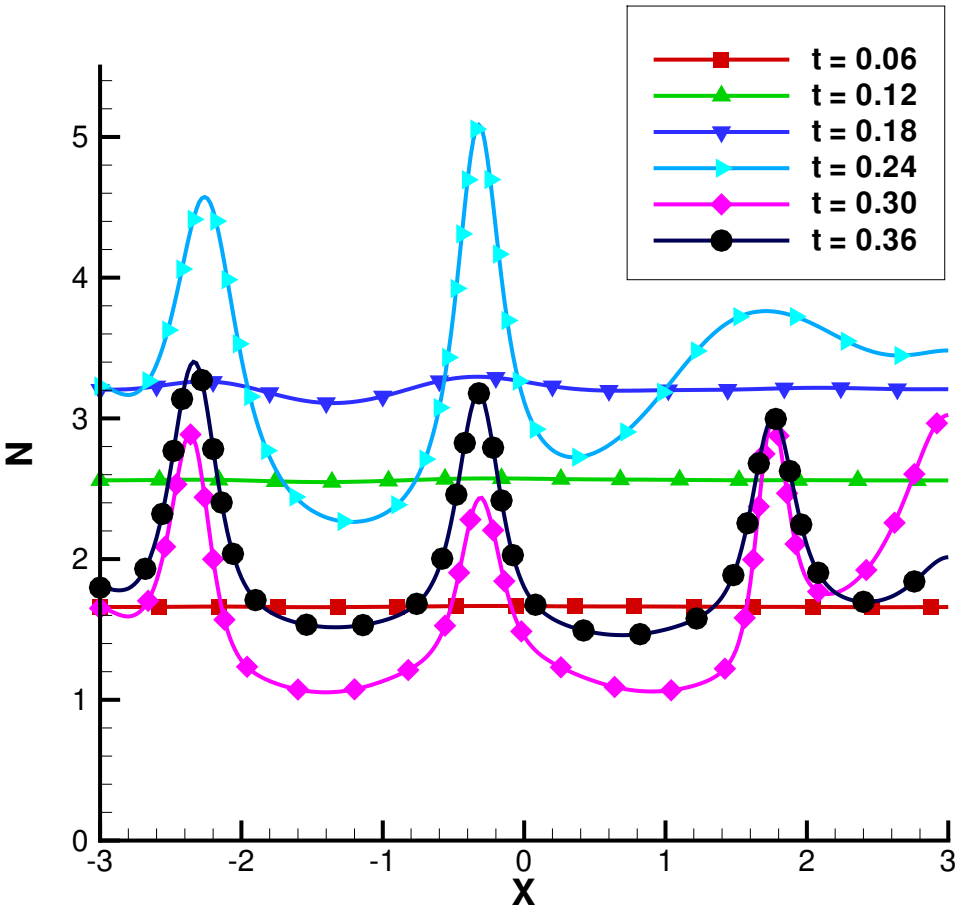

Figure 5.5: Time evolution of the cell density number n at the surface. In the initial stage of the chemotaxis–diffusion–convection, n is homogeneous in the horizontal direction. As the cell density n increases, hydrodynamic instability arises and the bacterium density becomes higher at some particular points.

with a higher temperature and thus a lighter density than that above it rises to develop plumes of hot fluid.

5.4.2 Stabilizing effect of chemotaxis

When the average initial cell density $\overline{n_0}$ is large, hydrodynamic instabilities appear in the system (5.15). This section is aimed at estimating $\overline{n_0}$ and dimensionless governing parameters for hydrodynamic instabilities to appear as well as at analyzing the time scales for each of the three competitive physical mechanisms: (1) chemotaxis, (2) diffusion, and (3) convection of bacteria.

Convection is determined by the properties of the hydrodynamic system as well as the container height and $\overline{n_0}$ via the taxis Rayleigh number Ra_τ. When the Rayleigh number is below the critical value for the hydrodynamic system of interest, motion of bacteria is primarily governed by diffusion and chemotaxis; when the Rayleigh number exceeds a critical value, bacterium taxis is primarily governed by convection [135].

Buoyancy force enables a fluid volume with a low bacterium density to ascend and a fluid volume with a high bacterium density to descend. Nevertheless, bacterium chemotaxis and friction dampen altogether the displacement.

The time scale for bacterium diffusion over the length scale h is given by

$$\mathrm{T}_{\mathrm{diff}} := \frac{h^2}{D_b}. \tag{5.16}$$

The buoyancy force is balanced by friction in the fluid. Therefore, the time scale for the convective displacement of bacteria over the length scale h can be defined by

$$\mathrm{T}_{\mathrm{conv}} := \frac{\mu}{g\, h\, \overline{n_0}\, V_b\, (\rho_b - \rho)}. \tag{5.17}$$

The chemotaxis system is controlled by a competition between diffusion and chemotaxis of bacteria. Therefore, the chemotaxis time scale is expressed as

$$\mathrm{T}_\tau := \frac{D_b}{\mathsf{S}_{dim}\, \kappa\, \overline{n_0}}. \tag{5.18}$$

In a convection-dominant process, the convection time scale is smaller than the diffusion and chemotaxis time scales (table 5.3). Hence:

$$\frac{g\, h^3\, \overline{n_0}\, V_b\, (\rho_b - \rho)}{D_b\, \mu} \equiv \mathrm{Ra}_\tau > 1. \tag{5.19}$$

In particular, $\mathrm{Ra}_\tau > \mathrm{Ra}_c$. The value of the critical Rayleigh number associated with the convection Ra_c given by [135] in their linear stability analysis is described by the solution

Dominant convection	Dominant diffusion	Dominant aerotaxis
$\mathrm{T_{conv}} < \mathrm{T_{diff}}$ and $\mathrm{T_{conv}} < \mathrm{T}_\tau$; i.e., $\mathrm{Ra}_\tau > 1$ and $\mathrm{Ra}_\tau/\mathsf{SH} > 1$	$\mathrm{T_{diff}} < \mathrm{T}_\tau$ $\mathsf{SH} < 1$	$\mathrm{T}_\tau < \mathrm{T_{diff}}$ $\mathsf{SH} > 1$

Table 5.3: Phenomenological analysis based on time scales of the three competitive mechanisms: chemotaxis, diffusion, and convection of bacteria. Both oxygen and bacterium diffusion favor fluid homogenization.

of an ordinary differential system. The second condition on the time scales leads to the following inequality

$$\frac{g\,h\,D_b\,V_b\,(\rho_b-\rho)}{\mathsf{S}_{dim}\,\kappa\,\mu} \equiv \frac{\mathrm{Ra}_\tau}{\mathsf{S}\,\mathsf{H}} > 1. \tag{5.20}$$

Similarly to the critical Rayleigh number (Ra_c), a critical number $(\mathsf{SH})_c$ can be introduced.

On the other hand, the chemotactic motion is predominant when the chemotaxis time scale is smaller than the diffusive time scale and convection is negligible:

$$\frac{\mathsf{S}_{dim}\,\kappa\,\overline{n_0}\,h^2}{{D_b}^2} \equiv \mathsf{S}\,\mathsf{H} > 1. \tag{5.21}$$

The effects of Ra_c and the product $\mathsf{S}\,\mathsf{H}$ were tested subject to a random initial condition. The results are shown in figure 5.6 for $\mathrm{Pr}_\tau = 500$ and $\mathrm{Le}_\tau = 5$. Our numerical results agree with the linear stability analysis carried out in [135]. Ra_c at first falls as $\mathsf{S}\,\mathsf{H}$ increases to reach its minimum value and then rises again. A sufficient decrease or increase of $\mathsf{S}\,\mathsf{H}$ may promote stabilization as both taxis and diffusion operate as the fluid-homogeneization factors, either directly ($\mathsf{S}\,\mathsf{H} < 1$) or indirectly ($\mathsf{S}\,\mathsf{H} > 1$). When $\mathsf{S}\,\mathsf{H}$ is small, stabilizing effect is due to bacterium diffusion and the solution is of the diffusive type. When $\mathsf{S}\,\mathsf{H}$ is large, stabilizing effect results from the bacterium taxis and the solution is of the chemotactic type.

The taxis Rayleigh number (Ra_τ) that characterizes the competition between diffusion and convection plays the same role as the Rayleigh number plays in classical convection. When the Rayleigh number increases, the gravitational force becomes predominant. When $\mathsf{S}\,\mathsf{H}$ rises, competition between chemotaxis and convection of bacteria becomes stronger. The condition (5.20) suggests that Ra_c increases linearly with respect to $\mathsf{S}\,\mathsf{H}$, as illustrated in figure 5.6. As a result, chemotaxis has a stabilizing effect on the differential system of current interest.

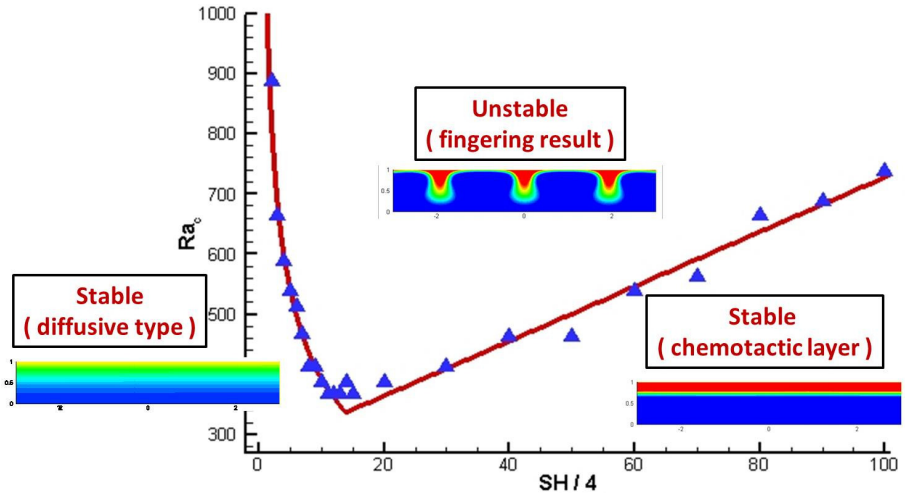

Figure 5.6: The stable and unstable regions of the dimensionless chemotaxis–diffusion–convection coupling system (5.15) plotted with respect to the critical taxis Rayleigh number Ra_c and the product of the dimensionless chemotaxis sensitivity and chemotaxis head SH. The points correspond to the predicted values of Ra_c. The red line corresponds to a fit of data in two parts: on the left side it is fitted by a power function and on the right side by a linear function. In the unstable region, the predicted solution n is of the convective type (b). In the stable region the predicted solution n can be of the diffusive type (a) or the chemotactic type (c).

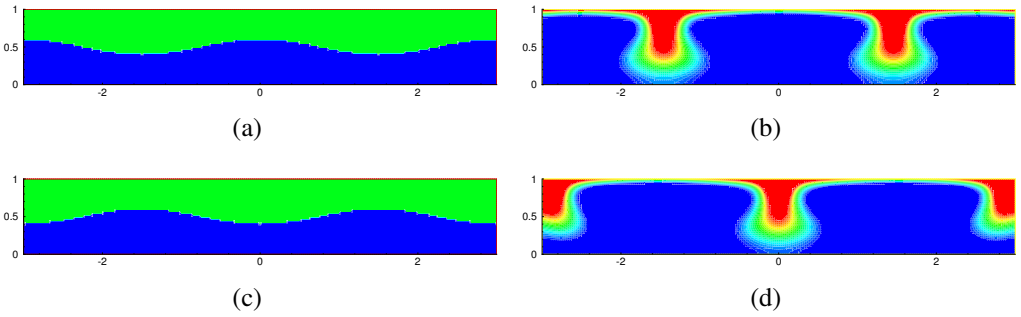

Figure 5.7: Numerical results for n with respect to the deterministic initial conditions. At the initial time, bacterium density is higher in the upper layer. (a) initial condition is $n_0 = \begin{bmatrix} 1, & y \geq 0.5+0.1\cos(2\pi x/3) \\ 0.5, & y<0.5+0.1\cos(2\pi x/3) \end{bmatrix}$; (b) simulation result at $t = 1.2$ for the initial condition given in (a) ; (c) initial condition is $n_0 = \begin{bmatrix} 1, & y \geq 0.5-0.1\cos(2\pi x/3) \\ 0.5, & y<0.5-0.1\cos(2\pi x/3) \end{bmatrix}$; (d) simulation result at $t = 1.2$ for the initial condition given in (c).

5.4.3 Distribution and number of plumes and initial conditions

5.4.3.1 Position and spacing of plumes

The exact localization of plume generation was investigated. Under the random initial condition introduced in [142], the location is hard to be predicted. Deterministic initial conditions are considered to investigate the formation and location of descending plumes. Many initial conditions among the set of tested distribution of bacterium settings are able to trigger convective patterns.

All numerical results are computed at $\mathrm{Le}_\tau = 5$, $\mathrm{Pr}_\tau = 500$, $\mathrm{Ra}_\tau = 2000$, $\mathsf{S} = 10$, and $\mathsf{H} = 4$ to ensure the formation of bacterium rich plumes. Firstly, a profile given by the form of wave function $\cos(2\pi x/3)$ is considered to determine the two initial layers of bacteria. Simulation results and initial conditions are shown in figure 5.7. The upper layer has a higher bacterium density than the lower layer. The plumes form at the initial location of the crest of the wave function where there is a larger number of bacteria. By reversing the initial conditions with a denser inferior layer (figure 5.8), the plumes also form at the same location. We can observe that distinct initial conditions can lead to the formation of a very similar pattern (figures 5.7-5.8).

We vary the profile of the curve between the upper and lower layers in the initial condition with different wave functions $\cos(3\pi x/2)$, $\cos(5\pi x/2)$, and $\cos(2\pi x)$. The wavenumber is defined as the spatial frequency of waves per unit distance. The wavelength is defined as the domain horizontal length divided by the wavenumber. Increasing the wavenumber of the initial wave function causes the formation of additional plumes to occur (figures 5.9 and 5.10). In all simulations, the locations of the plumes correspond to sites of initially greater local bacterium density.

When the wavenumber in the initial profile is large enough, the number of plumes is

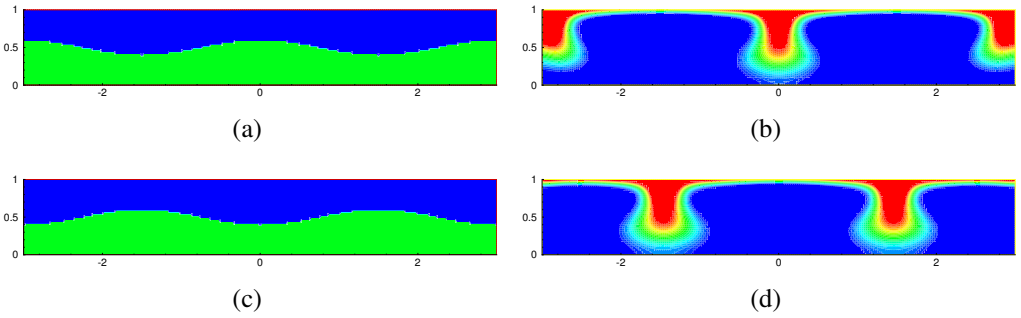

Figure 5.8: Numerical results for n with respect to the deterministic initial conditions. At the initial time, bacterium density is higher in the upper layer. (a) initial condition is $n_0 = \begin{bmatrix} 0.5, & y \geq 0.5+0.1\cos(2\pi x/3) \\ 1, & y<0.5+0.1\cos(2\pi x/3) \end{bmatrix}$; (b) simulation result at $t = 1.2$ for the initial condition given in (a) ; (c) initial condition is $n_0 = \begin{bmatrix} 0.5, & y \geq 0.5-0.1\cos(2\pi x/3) \\ 1, & y<0.5-0.1\cos(2\pi x/3) \end{bmatrix}$; (d) simulation result at $t = 1.2$ for the initial condition given in (c).

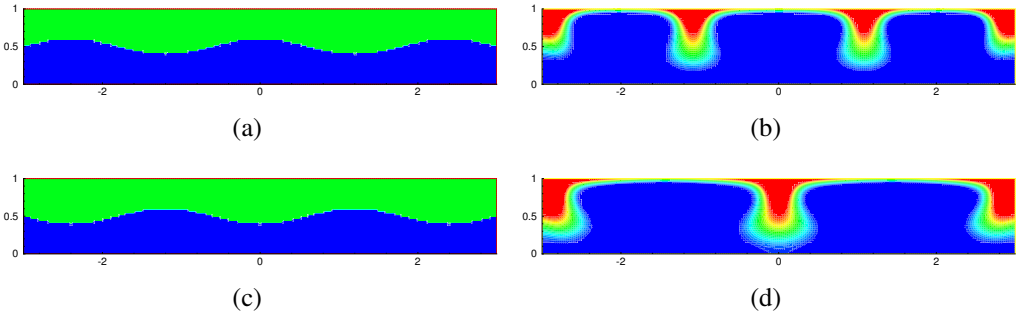

Figure 5.9: Numerical results for n with respect to the deterministic initial conditions. At the initial time, bacterium density is higher in the upper layer. (a) initial condition is $n_0 = \begin{bmatrix} 1, & y \geq 0.5+0.1\cos(5\pi x/2) \\ 0.5, & y<0.5+0.1\cos(5\pi x/2) \end{bmatrix}$; (b) simulation result at $t = 1.2$ for the initial condition given in (a) ; (c) initial condition is $n_0 = \begin{bmatrix} 1, & y \geq 0.5-0.1\cos(5\pi x/2) \\ 0.5, & y<0.5-0.1\cos(5\pi x/2) \end{bmatrix}$; (d) simulation result at $t = 1.2$ for the initial condition given in (c).

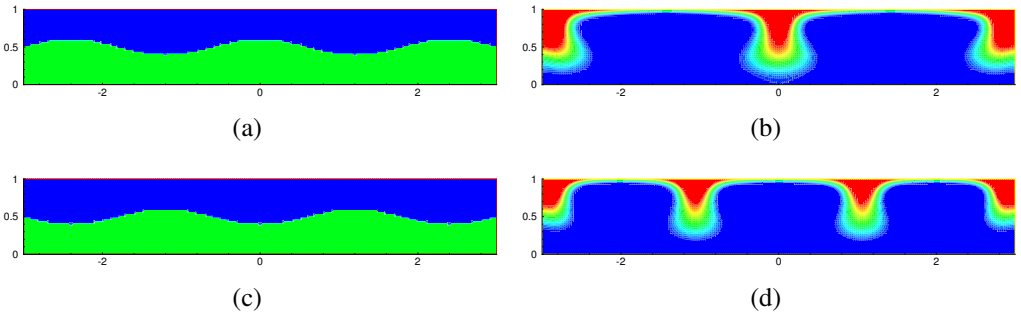

Figure 5.10: Numerical results for n with respect to the deterministic initial conditions. At the initial time, bacterium density is higher in the lower layer. (a) initial condition is $n_0 = \begin{bmatrix} 0.5, & y \geq 0.5+0.1\cos(5\pi x/2) \\ 1, & y < 0.5+0.1\cos(5\pi x/2) \end{bmatrix}$; (b) simulation result at $t = 1.2$ for the initial condition given in (a) ; (c) initial condition is $n_0 = \begin{bmatrix} 0.5, & y \geq 0.5-0.1\cos(5\pi x/2) \\ 1, & y < 0.5-0.1\cos(5\pi x/2) \end{bmatrix}$; (d) simulation result at $t = 1.2$ for the initial condition given in (c).

not equal to the wavenumber fixed by the initial condition. Three plumes, at most, form (figures 5.11 to 5.14). Nonetheless, more than three plumes can form, but they merge later (figure 5.13). Plume merging was previously observed in [142]. The plume merging mechanism is analogous to that of the Rayleigh-Bénard flow. Spacing between plumes seems to be intrinsic to the system and the position can only be predicted in very specific cases such as the examples given above.

The randomly perturbed bacterium density is defined as follows [142]:

$$n(\mathrm{x}) = 0.8 + 0.2\varepsilon(\mathrm{x}), \tag{5.22}$$

with ε being a random number with a uniform probability distribution over $[0, 1]$. Simulation results with the randomly perturbed initial condition are given in figure 5.15. The plume-to-plume spacing is not fixed but the number of plumes in the solution remains the same as that with the solution obtained subject to the deterministic initial condition illustrated in figures 5.11 to 5.14.

In figures 5.7–5.15, plumes form at the border of the domain. These border plumes seem to be caused by the no-slip boundary condition on the velocity depending on the arrangement of the convection cells. Bacteria first agglomerate at the surface near the wall. Because the fluid velocity is equal to zero at the wall boundary, a large amount of bacteria remains close to the wall. At a location away from the wall, the velocity is non-zero, thus bacteria descend into the fluid and form a plume at the border.

The location of the plumes may only be predicted in very simple tests for which the wavelengths of initial conditions are lower than the wavelength of the process. Despite the difficulty to predict the site of plume formation, the system presents a dominant wavelength of the fingering instability. The wavelength and wavenumber are redefined such as those given in [145]. The wavelength is the length of the domain divided by the number of plumes and the wavenumber 2π divided by the wavelength. The wavelength and

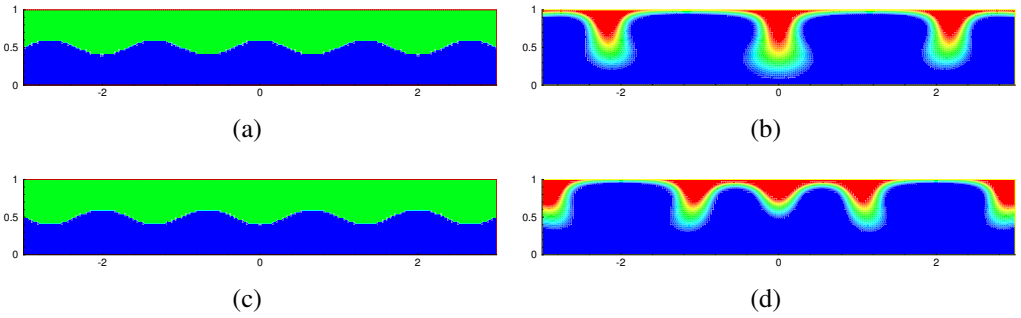

Figure 5.11: Numerical results for n with respect to the deterministic initial conditions. At the initial time, bacterium density is higher in the upper layer. (a) initial condition is $n_0 = \begin{bmatrix} 1, & y \geq 0.5+0.1\cos(3\pi x/2) \\ 0.5, & y<0.5+0.1\cos(3\pi x/2) \end{bmatrix}$; (b) simulation result at $t = 1.2$ for the initial condition given in (a) ; (c) initial condition is $n_0 = \begin{bmatrix} 1, & y \geq 0.5-0.1\cos(3\pi x/2) \\ 0.5, & y<0.5-0.1\cos(3\pi x/2) \end{bmatrix}$; (d) simulation result at $t = 1.2$ for the initial condition given in (c).

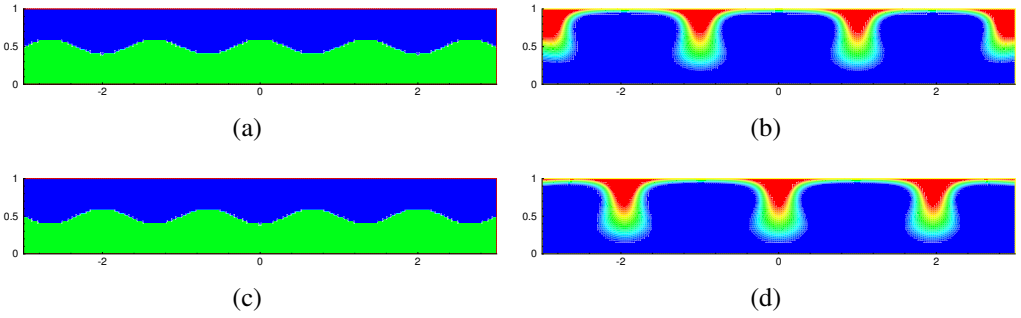

Figure 5.12: Numerical results for n with respect to the deterministic initial conditions. At the initial time, bacterium density is higher in the lower layer. (a) initial condition is $n_0 = \begin{bmatrix} 0.5, & y \geq 0.5+0.1\cos(3\pi x/2) \\ 1, & y<0.5+0.1\cos(3\pi x/2) \end{bmatrix}$; (b) simulation result at $t = 1.2$ for the initial condition given in (a) ; (c) initial condition is $n_0 = \begin{bmatrix} 0.5, & y \geq 0.5-0.1\cos(3\pi x/2) \\ 1, & y<0.5-0.1\cos(3\pi x/2) \end{bmatrix}$; (d) simulation result at $t = 1.2$ for the initial condition given in (c).

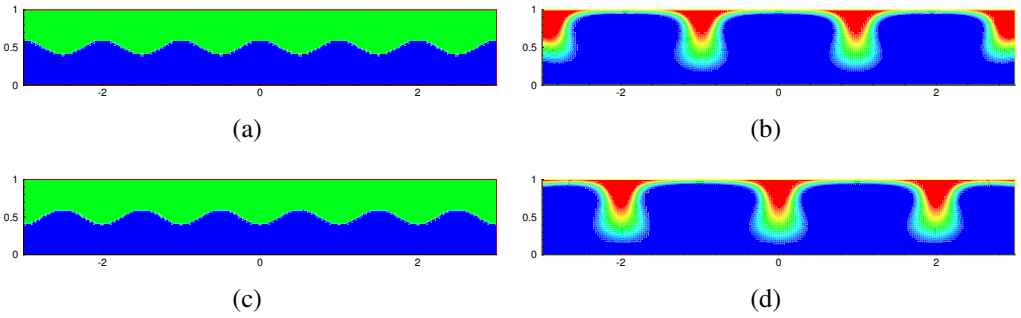

(a) (b)

(c) (d)

Figure 5.13: Numerical results for n with respect to the deterministic initial conditions. At the initial time, bacterium density is higher in the upper layer. (a) initial condition is $n_0 = \begin{bmatrix} 1, & y \geq 0.5+0.1\cos(2\pi x) \\ 0.5, & y < 0.5+0.1\cos(2\pi x) \end{bmatrix}$; (b) simulation result at $t = 1.2$ for the initial condition given in (a) ; (c) initial condition is $n_0 = \begin{bmatrix} 1, & y \geq 0.5-0.1\cos(2\pi x) \\ 0.5, & y < 0.5-0.1\cos(2\pi x) \end{bmatrix}$; (d) simulation result at $t = 1.2$ for the initial condition given in (c).

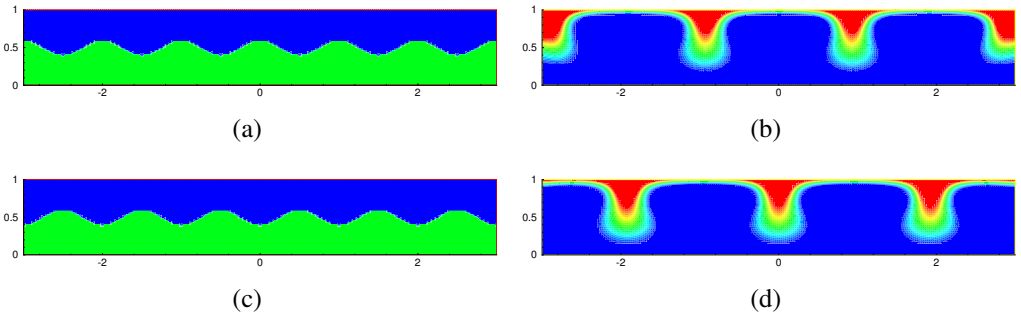

(a) (b)

(c) (d)

Figure 5.14: Numerical results for n with respect to the deterministic initial conditions. At the initial time, bacterium density is higher in the lower layer. (a) initial condition is $n_0 = \begin{bmatrix} 0.5, & y \geq 0.5+0.1\cos(2\pi x) \\ 1, & y < 0.5+0.1\cos(2\pi x) \end{bmatrix}$; (b) simulation result at $t = 1.2$ for the initial condition given in (a) ; (c) initial condition is $n_0 = \begin{bmatrix} 0.5, & y \geq 0.5-0.1\cos(2\pi x) \\ 1, & y < 0.5-0.1\cos(2\pi x) \end{bmatrix}$; (d) simulation result at $t = 1.2$ for the initial condition given in (c).

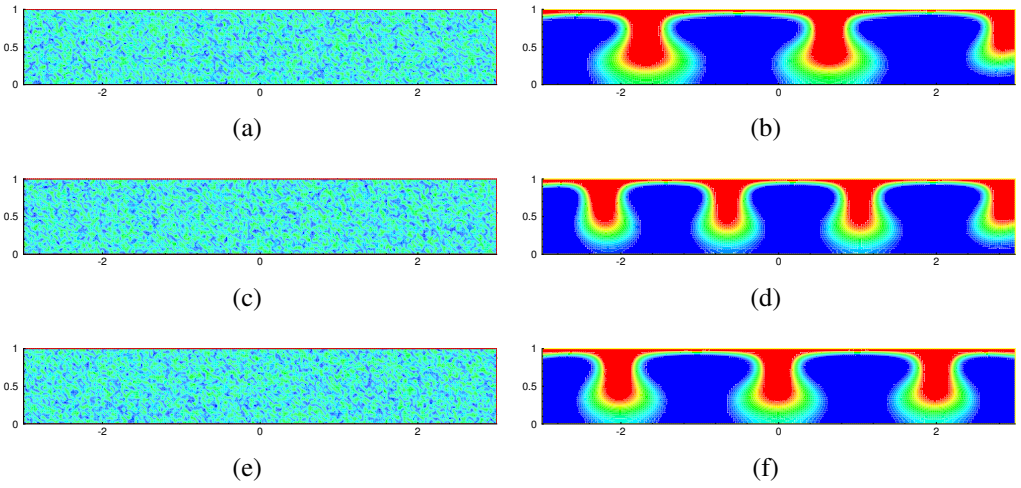

Figure 5.15: Initial random condition given in (5.22) (left) and the corresponding numerical results for n at $t = 1.2$ (right).

number of plumes	wavelength	wavenumber
2	2	3.14
2	2	3.14
2	2	3.14
2	2	3.14

Table 5.4: The predicted number of plumes, wavenumber and wavelength for $\ell = 2$. Each row corresponds to a different simulation result subject to the randomly perturbed initial condition given in (5.22).

wavenumber are similar for all simulation tests whatever the length of the domain is (tables 5.4 to 5.7).

5.4.3.2 Growth of plumes

We now arbitrarily define the plumes by the isoline $n = 1$. This choice allows us to track the stack layer and the plumes being formed. The layer where $n > 1$ represents the layer with a high bacterium density from which plumes form and descend in the fluid. On the other hand, the layer with $n < 1$ corresponds to the depletion layer, from which bacteria have migrated to the stack layer.

We define the growth rate of the plume amplitudes by $\mathsf{G} = (A_t - A_{t-1})/\Delta t$. The plume amplitude A_t is computed by measuring the distance from the surface to the tip of the plume at time t (table 5.8) and Δt is the time increment. Data obtained can be interpolated by the exponential function $g(t) = \exp\{\alpha t + \beta\}$ as the amplitudes of the descending plumes grow exponentially (figure 5.16). The exponential growth is well understood in the conventional Rayleigh-Taylor convection. Subsequent to the exponential

number of plumes	wavelength	wavenumber
3	2	3.14
3	2	3.14
4	1.5	4.19
3	2	3.14

Table 5.5: The predicted number of plumes, wavenumber and wavelength for $\ell = 3$. Each simulation result is subject to the random initial condition given in (5.22).

number of plumes	wavelength	wavenumber
5	1.6	3.93
5	1.6	3.93
5	1.6	3.93
5	1.6	3.93

Table 5.6: The predicted number of plumes, wavenumber and wavelength for $\ell = 4$. Each simulation result is subject to the random initial condition given in (5.22).

Table 5.7: The predicted number of plumes, wavenumber and wavelength for $\ell = 5$. Each simulation result is subject to the random initial condition given in (5.22).

number of plumes	wavelength	wavenumber
5	2	3.14
6	1.67	3.77
5	2	3.14
5	2	3.14

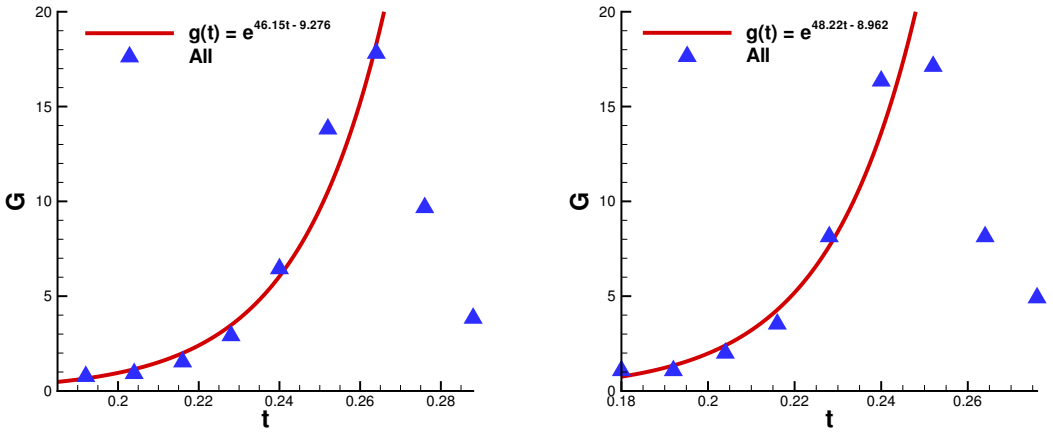

(a) (b)

Figure 5.16: Growth rate G of plume amplitude (dots) corresponding to the data in table 5.8. The growth rate is interpolated by the exponential function $g(t) = e^{\alpha t+\beta}$ (line).

growth phase, the growth rate of amplitude decreases, as plumes get closer to the bottom of the container.

5.4.4 Comparison with other buoyancy-driven convections

The chemotaxis–diffusion–convection system has many features similar to other well known buoyancy-driven flows, such as the double diffusive and Rayleigh Bénard convection.

Double diffusive convection occurs in a fluid containing at least two components with different diffusivities. A destabilizing component diffuses faster than the stabilizing one [146]. The distinct diffusivities yield a density difference capable of driving the motion of fluid [147].

Comparison with a classical example of double diffusive phenomenon in oceanography can be carried out by considering two superposed fluid layers with a specific combination of the temperature (T) and the solute concentration (s), namely the salinity. The system of dimensionless equations of the double diffuse problem is the following:

$$\begin{aligned} \frac{\partial \mathbf{u}}{\partial t}+(\mathbf{u}\cdot\boldsymbol{\nabla})\mathbf{u}-\mathrm{Pr}_T\nabla^2\mathbf{u}+\mathrm{Pr}_T\boldsymbol{\nabla}p &= -\mathrm{Pr}_T\left(\mathrm{Ra}_m\, s-\mathrm{Ra}_T T\right)\mathbf{j}, \\ \boldsymbol{\nabla}\cdot\mathbf{u} &= 0, \\ \frac{\partial T}{\partial t}+\mathbf{u}\cdot\boldsymbol{\nabla}T-\nabla^2 T &= 0, \\ \frac{\partial s}{\partial t}+\mathbf{u}\cdot\boldsymbol{\nabla}s-\mathrm{Le}_T\,\nabla^2 s &= 0, \end{aligned} \tag{5.23}$$

(a)			(b)		
A_t	t	G	A_t	t	G
0.18	0.16		0.18	0.16	
0.19	0.18	0.46	0.20	0.18	1.07
0.20	0.19	0.76	0.21	0.19	1.07
0.21	0.20	0.92	0.23	0.20	1.99
0.23	0.21	1.53	0.28	0.21	3.53
0.26	0.22	2.91	0.37	0.22	8.13
0.34	0.24	6.44	0.57	0.24	16.34
0.51	0.25	13.81	0.78	0.25	17.12
0.72	0.26	17.81	0.87	0.26	8.13
0.83	0.27	9.67	0.93	0.27	4.91

Table 5.8: The predicted growth rate G of the plume amplitudes A_t for two simulations subject to the random initial condition (5.22).

where Ra_T and Ra_m are the thermal and mass Rayleigh number, respectively, Pr_T the Prandtl number, and Le_T the Lewis number (table 5.2).

The stability of the system that exhibits a diffusive and a finger regime depends on both Rayleigh number types. In the finger regime, a small perturbation at the interface between the layers develops into a pattern of descending fingers, for instance salt fingers.

Another buoyancy-driven convection is the Rayleigh-Bénard convection that arises by fluid in a reservoir heated from below. Convection results from thermal gradient. The set of equations is as follows:

$$\begin{aligned} \frac{\partial \mathbf{u}}{\partial t} + (\mathbf{u}\cdot\boldsymbol{\nabla})\mathbf{u} - \mathrm{Pr}_T\,\nabla^2\mathbf{u} + \mathrm{Pr}_T\,\boldsymbol{\nabla} p &= -\mathrm{Pr}_T\,\mathrm{Ra}_T\,T\,\mathbf{j}, \\ \boldsymbol{\nabla}\cdot\mathbf{u} &= 0, \\ \frac{\partial T}{\partial t} + \mathbf{u}\cdot\boldsymbol{\nabla} T - \nabla^2 T &= 0, \\ T = 1 \text{ at bottom}, \quad T = 0 \text{ at top}. & \end{aligned} \tag{5.24}$$

Ra_T and Pr_T are the Rayleigh and Prandtl number, respectively. The balance between the gravitational and viscous forces is expressed by the Rayleigh number Ra_T. When Ra_T is larger than a critical value that can be obtained analytically, convective patterns appear [148].

The double diffusive convection equations in (5.23) and the Rayleigh-Bénard convection equations in (5.24) are solved (figures 5.17 and 5.18). Plumes formed in the Rayleigh-Bénard convection process are similar in shape to plumes of the chemotaxis–diffusion–convection. However, double diffusive and Rayleigh-Bénard convections exhibit both ascending and descending plumes, whereas chemotaxis–diffusion–convection is only characterized by descending plumes.

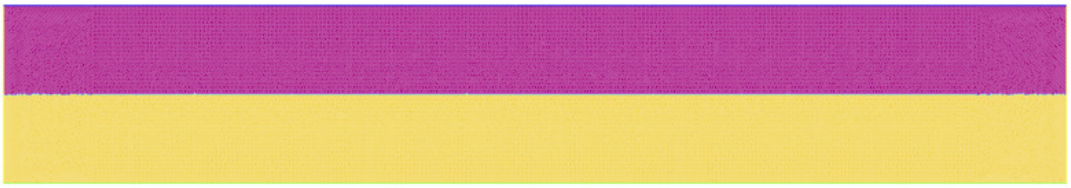

(a)

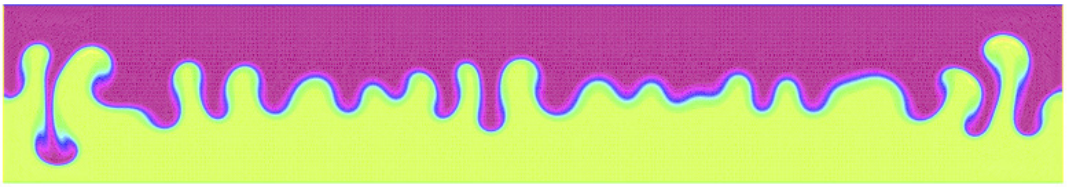

(b)

Figure 5.17: Numerical solution s of the double diffusive system (5.23). Red area designates the region rich in s, while yellow area is poor in s. Descending plumes rich in s and ascending plumes poor in s form at the interface of two layers of fluid. The green color designates a region where the concentration of s is slightly higher than that in the yellow area due to diffusion. (a) Initial condition: $s(x, y, t = 0) = 2/7$, if $y < 0.5$, and $s(x, y) = 1.0$, if $y \geq 0.5$. (b) s at time t=0.1 for $\mathrm{Ra}_T = 8000$, $\mathrm{Ra}_m = \mathrm{Ra}_T/6.2$, $\mathrm{Pr}_T = 7$ and $\mathrm{Le}_T = 0.01$.

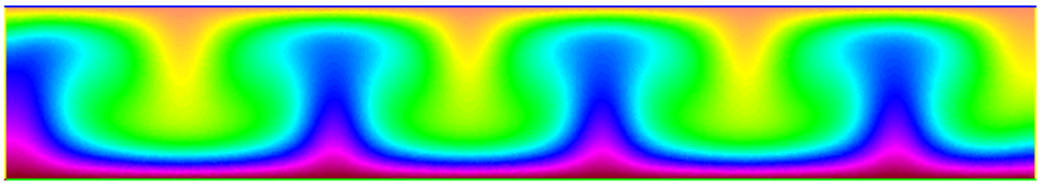

Figure 5.18: Numerical solution T of the Rayleigh-Bénard system (5.24). Descending plumes of lower temperature and ascending plumes of higher temperature form in the fluid. $\mathrm{Ra}_T = 6000$, $\mathrm{Pr}_T = 50$.

	DDC	CDC	RBC
Hydrodynamics buoyancy $(\rho V g)$	$\boldsymbol{\nabla}\cdot u=0$ $\frac{\mathrm{D}\mathbf{u}}{\mathrm{D}t}=\mathrm{Pr}_T\nabla^2\mathbf{u}-\mathrm{Pr}_T\boldsymbol{\nabla}p$ $-\mathrm{Pr}_T\,(\mathrm{Ra}_m\,s-\mathrm{Ra}_T T)\mathbf{j}$	$\boldsymbol{\nabla}\cdot u=0$ $\frac{\mathrm{D}\mathbf{u}}{\mathrm{D}t}=\mathrm{Pr}_\tau\nabla^2\mathbf{u}-\mathrm{Pr}_\tau\boldsymbol{\nabla}p$ $-\mathrm{Ra}_\tau\,\mathrm{Pr}_\tau\,n\,\mathbf{j}$	$\boldsymbol{\nabla}\cdot u=0$ $\frac{\mathrm{D}\mathbf{u}}{\mathrm{D}t}=\mathrm{Pr}_T\,\nabla^2\mathbf{u}-\mathrm{Pr}_T\,\boldsymbol{\nabla}p$ $-\mathrm{Pr}_T\,\mathrm{Ra}_T\,\mathbf{j}$
Diffusion	$\frac{\mathrm{D}T}{\mathrm{D}t}=\nabla^2 T$ $\frac{\mathrm{D}s}{\mathrm{D}t}=\mathrm{Le}_T\nabla^2 s$	$\frac{\mathrm{D}n}{\mathrm{D}t}=\nabla^2 n$	$\frac{\mathrm{D}T}{\mathrm{D}t}=\nabla^2 T$
Chemotaxis	Ω	$\frac{\mathrm{D}n}{\mathrm{D}t}=-\mathsf{S}\boldsymbol{\nabla}\cdot(n\,\boldsymbol{\nabla}c)$ $\frac{\mathrm{D}c}{\mathrm{D}t}=\mathrm{Le}_\tau\nabla^2 c-\mathsf{H}n$	Ω
Convection	$\frac{\mathrm{D}T}{\mathrm{D}t}=\mathbf{u}\cdot\boldsymbol{\nabla}T$ $\frac{\mathrm{D}s}{\mathrm{D}t}=\mathbf{u}\cdot\boldsymbol{\nabla}s$	$\frac{\mathrm{D}n}{\mathrm{D}t}=\mathbf{u}\cdot\boldsymbol{\nabla}n$	$\frac{\mathrm{D}n}{\mathrm{D}t}=\mathbf{u}\cdot\boldsymbol{\nabla}n$
I.C. for fingers	Layers	Any	Layers
B.C. for mass	Neumann	Neumann	Dirichlet
Physical regime	Diffusive & convective	Diffusive, convective & chemotactic	Diffusive & convective

Table 5.9: Recapitulative of the physical mechanisms involved in the double diffusive convection (DDC), chemotaxis–diffusion–convection (CDC), and the Rayleigh-Bénard convection (RBC)

In each problem, the effective Rayleigh numbers depend on the temperature difference between the opposite fluid domain surfaces, the gradients of temperature and salinity between the fluid layers, and the difference of density between the bacteria and solvent, for the Rayleigh-Bénard, double diffusive, and chemotaxis–diffusion–convection systems, respectively. All of the three diffusion–convection processes have similar and distinct features (table 5.9). The involved dimensionless parameters are listed in table 5.2.

Figure 5.3 shows that the arrangement of the convection cell structure can be the same for the three systems mentioned above. A particular position of the domain will be in a clockwise cell in some simulations and counter-clockwise cell in others. This behavior is also observed in Rayleigh-Bénard convection simulations.

In the chemotaxis–diffusion–convection system, chemotaxis plays an essential role in the early stage, as it organizes the fluid domain. In a rectangular domain, starting from a given initial condition, aerotaxis of bacteria builds quasi-homogeneous layers in the hori-

zontal direction, similarly to the double diffusive [147]. The multi-layered fluid creates a density gradient between the top of the stack layer and the bottom of the depletion layer that is similar to the temperature gradient set by the Dirichlet boundary condition imposed in the Rayleigh-Bénard case. The chemotaxis–diffusion–convection system evolves itself to a proper condition that leads to instabilities. Chemotaxis, that is not present in the other systems, brings flexibility in the choice of initial as well as boundary conditions.

5.5 Concluding remarks

In this chapter, the chemotaxis–diffusion–convection system was investigated with the focus on the differential system rather than on the experimental settings. Several simulations of the the coupled convective chemotaxis-fluid equations exhibit physically different spatially organized convection patterns.

The model for the chemotaxis–diffusion–convection system interstitial flow is able to describe three physical regimes. The convective regime exhibits the formation of plume patterns. The diffusive and chemotactic regimes are characterized by the stabilizing effect of the chemotaxis system on the fluid. The chemotaxis/fluid coupling gives a method to prevent blow-up of the solution of the chemotaxis. Incorporation of the mastocytes – interstitial fluid interaction in the model proposed in chapter 4 could give more realistic results.

The proposed comparison of buoyancy-driven flows (chemotaxis–diffusion, double diffusive, and Rayleigh-Bénard convection) shows that the dimensionless differential systems and the convection patterns are similar. This analogies between these types of convection should launch a further analytical study of the chemotaxis–diffusion–convection problem to gain a better understanding of the role of the chemotaxis in the convection system.

Conclusion and future work

The selected major involved biological, physical, and chemical mechanisms in acupuncture have led to the conception of a novel mathematical model of mastocyte response to external stimuli.

The first main contribution of this work is the study of the needle motion in the interstitial flow approximation through fibrous matrix using a convective Brinkman model. This approach has shed light on the physical nature of the mechanical stress field induced by pistoning the needle that affects the interstitial flow and in turn the cell activity. The numerical results presented have also helped to define a stress function to model the external stimuli of acupuncture.

The second main contribution is the development of the model for the mastocyte response to external stimuli. The extension of the Keller-Segel model with a forcing term allows us to take into account the stress field previously mentioned. A theoretical study on the chemotaxis model suggests that the recruitment of mastocytes through chemotaxis plays an essential role in the sustainability of the biochemical and cellular responses to acupuncture. A theorem gives the conditions for the effectiveness of the response. The numerical simulations carried out confirm the behavior of the system.

The main limitation of this study is the lack of experimental data. However, our goal was not to establish quantitative models but rather to establish multiscale models that incorporate the major biochemical processes, the cell responses, and mass transfer.

The model developed in this work hopes to be a first step toward the set up of a larger acupuncture framework. The external stimuli trigger a biochemical reaction cascade that leads to the effects of mastocytes. The acupuncture framework includes the external stimulation, the signal development at the acupoint region, the signal transmission to the central nervous system, and the signal processing targeting peripheral organs.

The work presented above focuses on the external stimulation and the local signal development. The correlated works in progress include the transport of calcium ions Ca^{2+} in ion channels (Poisson-Nernst-Planck/Navier-Stokes model), mastocyte degranulation (granule exocytosis model). The signal transmission has yet to be studied. Future work in this matter should focus on the modeling of mass transport across the blood-brain barrier. The blood-brain barrier is a highly selective permeable barrier that separates the circulating blood from the brain's extracellular fluid in the central nervous system. It

provides a suitable environment for neuronal signaling. Endocrine messengers liberated at the acupoint conveyed in the blood can modulate neuron activity.

The preliminary results can be expanded with the extension of the mathematical models, the further development of numerical methods, and the inclusion of experimental measurements.

On the theoretical point of view, additional work will be required to extend the analysis to the full parabolic chemotaxis model. Also, it would be interesting to extend the fluid/chemotaxis model presented in this work to the acupuncture study. Fluid/chemotaxis interaction may prevent blow-up of the solution of the chemotaxis model.

The study of a model that takes into account the fiber mechanics could allow extension of the needle pistoning case to the needle rotation case. A first step towards the study of the effects of the needle rotation worth considering is to extend the present numerical study to 3D. The 3D model may lead to a deeper understanding of the stress field.

Last but not least, it is crucial to validate the theoretical findings with experimental results. To our knowledge, the evolution of the spatial distribution and motion of mastocytes has not yet been fully studied experimentally. Future experimental work could help in the development of the proposed mathematical models.

Bibliography

[1] F. Hecht. New development in FreeFem++. *Journal of Numerical Mathematics*, 20(3-4):251, 2013. 22, 48, 81, 135

[2] X. Cheng. *Chinese Acupuncture and Moxibustion*. Foreign Language Press, Beijing, 1st ed. edition, 1987. 23, 25, 26, 27

[3] D. Pearl and E. Schrollinger. Acupuncture: its use in medicine. *Western Journal of Medicine*, 171(3):176–180, 1999. 24

[4] J. Reston. Now, about my operation in peking. *New York Times*, 1971. 24

[5] K. VanderPloeg and X. Yi. Acupuncture in modern society. *Journal of Acupuncture and Meridian Studies*, 2(1):26–33, 2009. 25

[6] M. Thiriet. *Intracellular Signaling Mediators in the Circulatory and Ventilatory Systems*, volume 4 of *Biomathematical and Biomechanical Modeling of the Circulatory and Ventilatory Systems*. Springer New York, New York, NY, 2013. 25, 41, 91

[7] V. Napadow, A. Ahn, J. Longhurst, L. Lao, E. Stener-Victorin, R. Harris, and H. M. Langevin. The status and future of acupuncture mechanism research. *Journal of Alternative and Complementary Medicine*, 14(7):861–869, 2008. 28

[8] H. M. Langevin, D. L. Churchill, J. Wu, G. J. Badger, J. A. Yandow, J. R. Fox, and M. H. Krag. Evidence of connective tissue involvement in acupuncture. *The FASEB Journal: Official Publication of the Federation of American Societies for Experimental Biology*, 16(8):872–874, 2002. 28, 38

[9] D. Zhang, G. Ding, X. Shen, W. Yao, Z. Zhang, Y. Zhang, J. Lin, and Q. Gu. Role of mast cells in acupuncture effect: a pilot study. *Explore (New York, N.Y.)*, 4(3): 170–177, 2008. 28, 36, 38, 39

[10] L. Fei, H. Cheng, D. Cai, S. Yang, J. Xu, E. Chen, R. Dang, G. Ding, X. Shen, Y. Tang, and W. Yao. Experimental exploration and research prospect of physical bases and functional characteristics of meridians. *Chinese Science Bulletin*, 43(15): 1233–1252, 1998. 29

[11] M. P. Brenner, L. S. Levitov, and E. O. Budrene. Physical mechanisms for chemotactic pattern formation by bacteria. *Biophysical Journal*, 74(4):1677–1693, 1998. 29

[12] M. Thiriet. *Biology and mechanics of blood flows: Part I: Biology*. CRM Series in Mathematical Physics. Springer, NY, 2008. 34, 35, 36, 37, 44

[13] M. Thiriet. Cells and tissues. In *Cell and Tissue Organization in the Circulatory and Ventilatory Systems*, number 1 in Biomathematical and Biomechanical Modeling of the Circulatory and Ventilatory Systems, pages 11–67. Springer New York, 2011. 34

[14] J. C. Iatridis, J. Wu, J. A. Yandow, and H. M. Langevin. Subcutaneous tissue mechanical behavior is linear and viscoelastic under uniaxial tension. *Connective Tissue Research*, 44(5):208–217, 2003. 34

[15] B. Alberts. *Molecular biology of the cell*. Garland Science, New York, 5th ed. edition, 2007. 34

[16] A. Delalleau. *Analyse du comportement mecanique de la peau in vivo*. PhD thesis, University Jean Monnet de Saint-Etienne, 2007. 34, 35

[17] S. Kawamata, J. Ozawa, M. Hashimoto, T. Kurose, and H. Shinohara. Structure of the rat subcutaneous connective tissue in relation to its sliding mechanism. *Archives of Histology and Cytology*, 66(3):273–279, 2003. 34

[18] M. Thiriet. *Cell and Tissue Organization in the Circulatory and Ventilatory Systems*, volume 1 of *Biomathematical and Biomechanical Modeling of the Circulatory and Ventilatory Systems*. Springer New York, New York, NY, 2011. 34, 78

[19] D. Fawcett. *Bloom and Fawcett, a textbook of histology*. Chapman & Hall, New York, 12th ed. edition, 1993. 34

[20] C. Jacquemoud. *Caracterisation mecanique et modelisation du comportement jusqu'a rupture de membranes biologiques fibreuses : application à la peau humaine*. PhD thesis, INSA Lyon, 2007. 35

[21] H. F. Helander and G. D. Bloom. Quantitative analysis of mast cell structure. *Journal of Microscopy*, 100(3):315–321, 1974. 35

[22] H. M. Langevin, N. A. Bouffard, J. R. Fox, B. M. Palmer, J. Wu, J. C. Iatridis, W. D. Barnes, G. J. Badger, and A. K. Howe. Fibroblast cytoskeletal remodeling contributes to connective tissue tension. *Journal of Cellular Physiology*, 226(5): 1166–1175, 2011. 35

[23] D. D. Metcalfe, D. Baram, and Y. A. Mekori. Mast cells. *Physiological Reviews*, 77(4):1033–1079, 1997. 36, 37

[24] G. Nilsson, M. Johnell, C. H. Hammer, H. L. Tiffany, K. Nilsson, D. D. Metcalfe, A. Siegbahn, and P. M. Murphy. C3a and c5a are chemotaxins for human mast cells and act through distinct receptors via a pertussis toxin-sensitive signal transduction pathway. *The Journal of Immunology*, 157(4):1693–1698, 1996. 36

[25] M. Urb and D. C. Sheppard. The role of mast cells in the defence against pathogens. *PLoS Pathog*, 8(4):e1002619, 2012. 36

[26] M. Thiriet. Intracellular transport. In *Cell and Tissue Organization in the Circulatory and Ventilatory Systems*, number 1 in Biomathematical and Biomechanical Modeling of the Circulatory and Ventilatory Systems, pages 521–601. Springer New York, 2011. 36

[27] S.-H. Hsiao and L.-J. Tsai. A neurovascular transmission model for acupuncture-induced nitric oxide. *Journal of Acupuncture and Meridian Studies*, 1(1):42–50, 2008. 36, 41

[28] H. Hsiu, W.-C. Hsu, C.-L. Hsu, and S.-M. Huang. Assessing the effects of acupuncture by comparing needling the hegu acupoint and needling nearby nonacupoints by spectral analysis of microcirculatory laser doppler signals. *Evidence-Based Complementary and Alternative Medicine: Ecam*, 2011:Article ID 435928, 2011. 36, 41

[29] T. Kuo, Y. Chen, H. Kuo, and C. Chan. Blood flow effect of acupuncture on the human meridian. *Medical Acupuncture*, 22(1):33–40, 2010. 36, 41

[30] M. Grossmann, M. J. Jamieson, and W. Kirch. Histamine response and local cooling in the human skin: involvement of h1- and h2-receptors. *British Journal of Clinical Pharmacology*, 48(2):216–222, 1999. 37

[31] G. F. Clough. Role of nitric oxide in the regulation of microvascular perfusion in human skin in vivo. *The Journal of Physiology*, 516(2):549–557, 1999. 37

[32] M. Thiriet. *Biology and mechanics of blood flows: Part II: Mechanics and medical aspects*. Biology and Mechanics of Blood Flows. Springer, New York (N.Y.), 2008. 37

[33] C. Weidner, M. Klede, R. Rukwied, G. Lischetzki, U. Neisius, P. S. Skov, L. J. Petersen, and M. Schmelz. Acute effects of substance p and calcitonin gene-related peptide in human skin – a microdialysis study. *Journal of Investigative Dermatology*, 115(6):1015–1020, 2000. 37

[34] J. Raud, S.-E. Dahlén, A. Sydbom, L. Lindbom, and P. Hedqvist. Prostaglandin modulation of mast cell-dependent inflammation. *Agents and Actions*, 26(1-2): 42–44, 1989. 37

[35] T. Williams. Prostaglandin e2, prostaglandin i2 and the vascular changes of inflammation. *British Journal of Pharmacology*, 65(3):517–524, 1979. 37

[36] R. K. Shepherd and B. R. Duling. Inosine-induced vasoconstriction is mediated by histamine and thromboxane derived from mast cells. *American Journal of Physiology - Heart and Circulatory Physiology*, 270(2):H560–H566, 1996. 37

[37] A. S. Thakor and D. A. Giussani. Role of nitric oxide in mediating in vivo vascular responses to calcitonin gene-related peptide in essential and peripheral circulations in the fetus. *Circulation*, 112(16):2510–2516, 2005. 37

[38] S. D. Brain. Vascular actions of calcitonin gene-related peptide and adrenomedullin. *Physiological Reviews*, 84(3):903–934, 2004. 37

[39] N. Paolocci, T. Katori, H. C. Champion, M. E. S. John, K. M. Miranda, J. M. Fukuto, D. A. Wink, and D. A. Kass. Positive inotropic and lusitropic effects of HNO/NO− in failing hearts: Independence from β-adrenergic signaling. *Proceedings of the National Academy of Sciences*, 100(9):5537–5542, 2003. 37

[40] A. Misiak-Tloczek and E. Brzezinska-BlAszczyk. IL-6, but not IL-4, stimulates chemokinesis and TNF stimulates chemotaxis of tissue mast cells: involvement of both mitogen-activated protein kinases and phosphatidylinositol 3-kinase signalling pathways. *APMIS*, 117(8):558–567, 2009. 38

[41] E. Brzezinska-Blaszczyk, A. Pietrzak, and A. H. Misiak-Tloczek. Tumor necrosis factor (TNF) is a potent rat mast cell chemoattractant. *Journal of Interferon & Cytokine Research*, 27(11):911–920, 2007. 38

[42] S. He, M. D. A. Gaça, and A. F. Walls. A role for tryptase in the activation of human mast cells: Modulation of histamine release by tryptase and inhibitors of tryptase. *Journal of Pharmacology and Experimental Therapeutics*, 286(1):289–297, 1998. 38

[43] J. Sawada, A. Itakura, A. Tanaka, T. Furusaka, and H. Matsuda. Nerve growth factor functions as a chemoattractant for mast cells through both mitogen-activated protein kinase and phosphatidylinositol 3-kinase signaling pathways. *Blood*, 95(6): 2052–2058, 2000. 38

[44] J. Foreman. Substance p and calcitonin gene-related peptide: Effects on mast cells and in human skin. *International Archives of Allergy and Immunology*, 82(3-4): 366–371, 1987. 38

[45] N. Schwenger, M. Dux, R. d. Col, R. Carr, and K. Messlinger. Interaction of calcitonin gene-related peptide, nitric oxide and histamine release in neurogenic blood flow and afferent activation in the rat cranial dura mater. *Cephalalgia*, 27(6): 481–491, 2007. 38

[46] P. Fung. Probing the mystery of chinese medicine meridian channels with special emphasis on the connective tissue interstitial fluid system, mechanotransduction, cells durotaxis and mast cell degranulation. *Chinese Medicine*, 4(1):10, 2009. 38

[47] Z.-J. Zhang, X.-M. Wang, and G. M. McAlonan. Neural acupuncture unit: A new concept for interpreting effects and mechanisms of acupuncture. *Evidence-Based Complementary and Alternative Medicine*, 2012. 38

[48] X. Yu, G. Ding, H. Huang, J. Lin, W. Yao, and R. Zhan. Role of collagen fibers in acupuncture analgesia therapy on rats. *Connective Tissue Research*, 50(2):110–120, 2009. 38, 39

[49] A. Comunetti, S. Laage, N. Schiessl, and A. Kistler. Characterisation of human skin conductance at acupuncture points. *Experientia*, 51(4):328–331, 1995. 38

[50] A. P. Colbert, J. Yun, A. Larsen, T. Edinger, W. L. Gregory, and T. Thong. Skin impedance measurements for acupuncture research: Development of a continuous recording system. *Evidence-Based Complementary and Alternative Medicine*, 5 (4):443–450, 2008. 38

[51] F. Zhou, D. Huang, and YingXia. Neuroanatomic basis of acupuncture points. In P. Y. Xia, P. X. Cao, P. G. Wu, and P. J. Cheng, editors, *Acupuncture Therapy for Neurological Diseases*, pages 32–80. Springer Berlin Heidelberg, 2010. 38

[52] H. M. Langevin, D. L. Churchill, and M. J. Cipolla. Mechanical signaling through connective tissue: a mechanism for the therapeutic effect of acupuncture. *The FASEB Journal: Official Publication of the Federation of American Societies for Experimental Biology*, 15(12):2275–2282, 2001. 38, 39

[53] F. Wei, X. Shi, J. Chen, and L. Zhou. Fluid shear stress-induced cytosolic calcium signaling and degranulation dynamics in mast cells. *Cell Biology International Reports*, 2012. 38, 45, 46, 91

[54] Y. Shi, L. Qi, J. Wang, M.-S. Xu, D. Zhang, L.-Y. Wu, and H.-G. Wu. Moxibustion activates mast cell degranulation at the ST25 in rats with colitis. *World Journal of Gastroenterology*, 17(32):3733–3738, 2011. 38

[55] X. Shi, Y. Zheng, Z. Liu, and W. Yang. A model of calcium signaling and degranulation dynamics induced by laser irradiation in mast cells. *Chinese Science Bulletin*, 53(15):2315–2325, 2008. 38, 45

[56] G. A. Ulett, S. Han, and J.-s. Han. Electroacupuncture: mechanisms and clinical application. *Biological Psychiatry*, 44(2):129–138, 1998. 39

[57] P. Whittaker. Laser acupuncture: past, present, and future. *Lasers in Medical Science*, 19(2):69–80, 2004. 39

[58] J. Liang and Y. Xia. Acupuncture modulation of neural transmitters/modulators. In Y. Xia, G. Ding, and G.-C. Wu, editors, *Current Research in Acupuncture*, pages 1–36. Springer New York, 2013. 41

[59] M. Tsuchiya, E. F. Sato, M. Inoue, and A. Asada. Acupuncture enhances generation of nitric oxide and increases local circulation:. *Anesthesia & Analgesia*, 104(2): 301–307, 2007. 41

[60] V. C. Huang and T. W. H. Sheu. On a dynamical view on the meridian transmission. *Journal of Accord Integrative Medicine*, 4(2), 2008. 43, 44

[61] V. C. Huang and T. W. H. Sheu. Heat transfer involved in a warm (moxa-heated) needle treatment. *Acupuncture & Electro-Therapeutics Research*, 33(3-4):169–178, 2008.

[62] V. C. Huang and T. W. H. Sheu. Tissue fluids in microchannel subjected to an externally applied electric potential. *International Journal of Numerical Methods for Heat & Fluid Flow*, 19(1):64–77, 2009. 44

[63] C. Huang and T. W. H. Sheu. Study of the heat transfer effect in moxibustion practice. In M. A. Dos Santos Bernardes, editor, *Developments in Heat Transfer*. InTech, 2011. 46

[64] C. Huang and T. W. Sheu. Study of the effect of moxibustion on the blood flow. *International Journal of Heat and Mass Transfer*, 63:141–149, 2013. 43

[65] M. A. Swartz and M. E. Fleury. Interstitial flow and its effects in soft tissues. *Annual Review of Biomedical Engineering*, 9(1):229–256, 2007. 44, 84

[66] H. C. Brinkman. A calculation of the viscous force exerted by a flowing fluid on a dense swarm of particles. *Applied Scientific Research*, 1(1):27–34, 1949. 44

[67] W. Yao and G. H. Ding. Interstitial fluid flow: simulation of mechanical environment of cells in the interosseous membrane. *Acta Mechanica Sinica*, 27(4): 602–610, 2011. 44, 46

[68] W. Yao, Y. Li, and G. Ding. Interstitial fluid flow: The mechanical environment of cells and foundation of meridians. *Evidence-Based Complementary and Alternative Medicine*, 2012:1–9, 2012. 44, 46

[69] T. F. Wiesner, B. C. Berk, and R. M. Nerem. A mathematical model of the cytosolic-free calcium response in endothelial cells to fluid shear stress. *Proceedings of the National Academy of Sciences*, 94(8):3726–3731, 1997. 45

[70] W. Yao, H. Yang, and G. Ding. Mechanisms of qi-blood circulation and qi deficiency syndrome in view of blood and interstitial fluid circulation. *Journal of Traditional Chinese Medicine*, 33(4):538–544, 2013. 46

[71] W. Yao, H. Yang, N. Yin, and G. Ding. Mast cell-nerve cell interaction at acupoint: Modeling mechanotransduction pathway induced by acupuncture. *International Journal of Biological Sciences*, 10(5):511–519, 2014. 46

[72] L. Mingfu, D. Xiaotong, S. Xiaojing, J. Jin, Z. Jinling, and H. Ying. Study on the dynamic compound structure composed of mast cells, blood vessels, and nerves in rat acupoint. *Evidence-Based Complementary and Alternative Medicine*, 2013, 2013. 46

[73] C. Geuzaine and J.-F. Remacle. Gmsh: A 3-d finite element mesh generator with built-in pre- and post-processing facilities. *International Journal for Numerical Methods in Engineering*, 79(11):1309–1331, 2009. 50

[74] H. Si. Tetgen user's manual: A quality tetrahedral mesh generator and 3d delaunay triangulator, 2013. 50

[75] P. Frey. MEDIT : An interactive mesh visualization software. report, 2001. 54

[76] T. E. Tezduyar, M. Behr, S. Mittal, and J. Liou. A new strategy for finite element computations involving moving boundaries and interfaces – the deforming-spatial-domain/space-time procedure: II. computation of free-surface flows, two-liquid flows, and flows with drifting cylinders. *Computer Methods in Applied Mechanics and Engineering*, 94(3):353–371, 1992. 63

[77] O. Pironneau, J. Liou, and T. Tezduyar. Characteristic-galerkin and galerkin/least-squares space-time formulations for the advection-diffusion equation with time-dependent domains. *Computer Methods in Applied Mechanics and Engineering*, 100(1):117–141, 1992.

[78] T. E. Tezduyar. Computation of moving boundaries and interfaces and stabilization parameters. *International Journal for Numerical Methods in Fluids*, 43(5):555–575, 2003. 70

[79] K. Takizawa and T. E. Tezduyar. Multiscale space–time fluid–structure interaction techniques. *Computational Mechanics*, 48(3):247–267, 2011. 63, 70

[80] O. Pironneau. On the transport-diffusion algorithm and its applications to the navier-stokes equations. *Numerische Mathematik*, 38(3):309–332, 1982. 65

[81] A. J. Chorin. A numerical method for solving incompressible viscous flow problems. *Journal of Computational Physics*, 2(1):12–26, 1967. 66, 82

[82] R. Témam. Une méthode d'approximation de la solution des équations de navier-stokes. *Bulletin de la Société Mathématique de France*, 96:115–152, 1968. 66, 82

[83] M. Bercovier. Perturbation of mixed variational problems. application to mixed finite element methods. *ESAIM: Mathematical Modelling and Numerical Analysis-Modélisation Mathématique et Analyse Numérique*, 12(3):211–236, 1978. 67

[84] O. A. Ladyženskaja. *The mathematical theory of viscous incompressible flow*. Gordon and Breach Science, New York, 1969. 67, 83, 134

[85] P. I. Babuška. Error-bounds for finite element method. *Numerische Mathematik*, 16(4):322–333, 1971.

[86] F. Brezzi. On the existence, uniqueness and approximation of saddle-point problems arising from lagrangian multipliers. *ESAIM: Mathematical Modelling and Numerical Analysis - Modélisation Mathématique et Analyse Numérique*, 8(R2): 129–151, 1974.

[87] P.-A. Raviart and J.-M. Thomas. *Introduction à l'analyse numérique des équations aux dérivées partielles*. Masson, 1983. 67, 83, 134

[88] C. S. Peskin. Numerical analysis of blood flow in the heart. *Journal of Computational Physics*, 25(3):220–252, 1977. 68

[89] R. Glowinski, T.-W. Pan, and J. Periaux. A fictitious domain method for dirichlet problem and applications. *Computer Methods in Applied Mechanics and Engineering*, 111(3–4):283–303, 1994. 68

[90] R. Glowinski, T.-W. Pan, and J. Periaux. A fictitious domain method for external incompressible viscous flow modeled by navier-stokes equations. *Computer Methods in Applied Mechanics and Engineering*, 112(1–4):133–148, 1994.

[91] R. Glowinski, T. W. Pan, T. I. Hesla, D. D. Joseph, and J. Périaux. A fictitious domain approach to the direct numerical simulation of incompressible viscous flow past moving rigid bodies: Application to particulate flow. *Journal of Computational Physics*, 169(2):363–426, 2001. 68

[92] J. Janela, A. Lefebvre, and B. Maury. A penalty method for the simulation of fluid-rigid body interaction. In *ESAIM: Proceedings*, volume 14, pages 115–123. EDP Sciences, 2005. 68

[93] A. Lefebvre. Fluid-particle simulations with freefem++. In *ESAIM: Proceedings*, volume 18, pages 120–132. EDP Sciences, 2007. 68

[94] B. Maury. Characteristics ALE method for the unsteady 3d navier-stokes equations with a free surface. *International Journal of Computational Fluid Dynamics*, 6(3): 175–188, 1996. 70

[95] Decoene A. and Maury B. Moving meshes with freefem++. *Journal of Numerical Mathematics*, 20:195, 2013. 70, 71

[96] M. A. Fernández, L. Formaggia, J.-F. Gerbeau, and A. Quarteroni. The derivation of the equations for fluids and structure. In L. Formaggia, A. Quarteroni, and A. Veneziani, editors, *Cardiovascular Mathematics*, number 1 in MS&A, pages 77–121. Springer Milan, 2009. 70

[97] C.-C. Liao, Y.-W. Chang, C.-A. Lin, and J. M. McDonough. Simulating flows with moving rigid boundary using immersed-boundary method. *Computers & Fluids*, 39(1):152–167, 2010. 73

[98] H. Dütsch, F. Durst, S. Becker, and H. Lienhart. Low-reynolds-number flow around an oscillating circular cylinder at low keulegan–carpenter numbers. *Journal of Fluid Mechanics*, 360:249–271, 1998. 73

[99] J. A. Pedersen, F. Boschetti, and M. A. Swartz. Effects of extracellular fiber architecture on cell membrane shear stress in a 3d fibrous matrix. *Journal of Biomechanics*, 40(7):1484–1492, 2007. 78

[100] A. Blasselle. *Modélisation mathématique de la peau*. Thèse de doctorat, Université Pierre et Marie Curie, Paris, France, 2011. 78

[101] M. A. Biot. General theory of three–dimensional consolidation. *Journal of Applied Physics*, 12(2):155–164, 1941. 78

[102] M. A. Biot. Theory of elasticity and consolidation for a porous anisotropic solid. *Journal of Applied Physics*, 26(2):182–185, 1955.

[103] M. A. Biot. Mechanics of deformation and acoustic propagation in porous media. *Journal of Applied Physics*, 33(4):1482–1498, 1962.

[104] M. Biot. Theory of finite deformations of porous solids. *Indiana University Mathematics Journal*, 21(7):597–620, 1972. 79

[105] J. Y. Park, S. J. Yoo, L. Patel, S. H. Lee, and S.-H. Lee. Cell morphological response to low shear stress in a two-dimensional culture microsystem with magnitudes comparable to interstitial shear stress. *Biorheology*, 47(3):165–178, 2010. 79

[106] P. Forchheimer. Wasserbewegung durch boden. *Z. Ver. Deutsch. Ing*, 45(1782): 1788, 1901. 79

[107] C. T. Hsu and P. Cheng. Thermal dispersion in a porous medium. *International Journal of Heat and Mass Transfer*, 33(8):1587–1597, 1990. 79

[108] P. Nithiarasu, K. N. Seetharamu, and T. Sundararajan. Natural convective heat transfer in a fluid saturated variable porosity medium. *International Journal of Heat and Mass Transfer*, 40(16):3955–3967, 1997.

[109] K. Vafai and C. L. Tien. Boundary and inertia effects on flow and heat transfer in porous media. *International Journal of Heat and Mass Transfer*, 24(2):195–203, 1981. 79

[110] J. R. Levick. Flow through interstitium and other fibrous matrices. *Experimental Physiology*, 72(4):409–437, 1987. 84

[111] J. Happel. Viscous flow relative to arrays of cylinders. *AIChE Journal*, 5(2):174–177, 1959. 84

[112] C. S. Patlak. Random walk with persistence and external bias. *The Bulletin of Mathematical Biophysics*, 15(3):311–338, 1953. 96, 97

[113] E. F. Keller and L. A. Segel. Model for chemotaxis. *Journal of Theoretical Biology*, 30(2):225–234, 1971. 96, 97

[114] P. Friedl and K. Wolf. Tumour-cell invasion and migration: diversity and escape mechanisms. *Nature Reviews Cancer*, 3(5):362–374, 2003. 96

[115] M. Chaplain, S. McDougall, and A. Anderson. Mathematical modeling of tumor-induced angiogenesis. *Annual Review of Biomedical Engineering*, 8(1):233–257, 2006. 96

[116] N. V. Mantzaris, S. Webb, and H. G. Othmer. Mathematical modeling of tumor-induced angiogenesis. *Journal of Mathematical Biology*, 49(2):111–187, 2004. 96

[117] Y. Tao and M. Winkler. Boundedness in a quasilinear parabolic–parabolic keller-segel system with subcritical sensitivity. *Journal of Differential Equations*, 252(1): 692–715, 2012. 97

[118] S. Ishida, K. Seki, and T. Yokota. Boundedness in quasilinear keller-segel systems of parabolic-parabolic type on non-convex bounded domains. *Journal of Differential Equations*, 256(8):2993–3010, 2014. 97

[119] M. Winkler. Does a 'volume-filling effect' always prevent chemotactic collapse? *Mathematical Methods in the Applied Sciences*, 33(1):12–24, 2010. 97

[120] S. Ishida and T. Yokota. Global existence of weak solutions to quasilinear degenerate keller–segel systems of parabolic–parabolic type. *Journal of Differential Equations*, 252(2):1421–1440, 2012. 97

[121] G. Marinoschi. Well-posedness for chemotaxis dynamics with nonlinear cell diffusion. *Journal of Mathematical Analysis and Applications*, 402(2):415–439, 2013. 97

[122] T. Yokota and N. Yoshino. Existence of solutions to chemotaxis dynamics with lipschitz diffusion and superlinear growth. *Journal of Mathematical Analysis and Applications*, 419(2):756–774, 2014. 97

[123] W. Jager and S. Luckhaus. On explosions of solutions to a system of partial differential equations modelling chemotaxis. *Transactions of the American Mathematical Society*, 329(2):819–824, 1992. 97, 113

[124] M. A. Herrero and J. J. L. Velázquez. Singularity patterns in a chemotaxis model. *Mathematische Annalen*, 306(1):583–623, 1996.

[125] T. Nagai and T. Senba. Global existence and blow-up of radial solutions to a parabolic-elliptic system of chemotaxis. *Advances in Mathematical Sciences and Applications*, 8:145–156, 1998. 109

[126] J. J. L. Velázquez. Point dynamics in a singular limit of the keller–segel model 2: Formation of the concentration regions. *SIAM Journal on Applied Mathematics*, 64(4):1224–1248, 2004.

[127] A. Blanchet, J. Dolbeault, and B. Perthame. Two-dimensional keller-segel model: optimal critical mass and qualitative properties of the solutions. *Electronic Journal of Differential Equations*, 44:1–33, 2006. 100, 101, 102, 104, 109, 113

[128] B. Perthame. Cell motion and chemotaxis. In *Transport Equations in Biology*, pages 111–149. Birkhauser, Basel, 2007. 97, 100, 101, 103

[129] L. Corrias, B. Perthame, and H. Zaag. A chemotaxis model motivated by angiogenesis. *Comptes Rendus Mathematique*, 336(2):141–146, 2003. 97

[130] L. Corrias, B. Perthame, and H. Zaag. Global solutions of some chemotaxis and angiogenesis systems in high space dimensions. *Milan Journal of Mathematics*, 72 (1):1–28, 2004. 97

[131] B. Perthame. General mathematical tools. In *Transport Equations in Biology*, Frontiers in Mathematics, pages 151–178. Birkhäuser Basel, 2007. 104

[132] V. Calvez and L. Corrias. The parabolic-parabolic keller-segel model in r2. *Communications in Mathematical Sciences*, 6(2):417–447, 2008. 107, 112

[133] B. Perthame. *Transport Equations in Biology*. Birkhauser, 2007. 108, 109, 112

[134] D. Horstmann. From 1970 until present: the keller-segel model in chemotaxis and its consequences. 2003. 126

[135] A. J. Hillesdon and T. J. Pedley. Bioconvection in suspensions of oxytactic bacteria: linear theory. *Journal of Fluid Mechanics*, 324(10):223–259, 1996. 128, 130, 131, 136, 141, 142

[136] A. J. Hillesdon, T. J. Pedley, and J. O. Kessler. The development of concentration gradients in a suspension of chemotactic bacteria. *Bulletin of Mathematical Biology*, 57(2):299–344, 1995. 128, 131, 136

[137] N. Hill and T. Pedley. Bioconvection. *Fluid Dynamics Research*, 37(1–2):1–20, 2005. 128

[138] A. Metcalfe and T. Pedley. Bacterial bioconvection: weakly nonlinear theory for pattern selection. *Journal of Fluid Mechanics*, 370:249–270, 1998. 130, 136

[139] I. Tuval, L. Cisneros, C. Dombrowski, C. W. Wolgemuth, J. O. Kessler, and R. E. Goldstein. Bacterial swimming and oxygen transport near contact lines. *Proceedings of the National Academy of Sciences of the United States of America*, 102(7): 2277–2282, 2005. 130, 131

[140] R. Duan, A. Lorz, and P. Markowich. Global solutions to the coupled chemotaxis-fluid equations. *Communications in Partial Differential Equations*, 35(9):1635–1673, 2010. 130

[141] J.-G. Liu and A. Lorz. A coupled chemotaxis-fluid model: Global existence. *Annales de l'Institut Henri Poincare (C) Non Linear Analysis*, 28(5):643–652, 2011. 130

[142] A. Chertock, K. Fellner, A. Kurganov, A. Lorz, and P. A. Markowich. Sinking, merging and stationary plumes in a coupled chemotaxis-fluid model: A high-resolution numerical approach. *Journal of Fluid Mechanics*, 694:155–190, 2012. 130, 131, 136, 144, 146

[143] A. N. Brooks and T. J. Hughes. Streamline upwind/petrov-galerkin formulations for convection dominated flows with particular emphasis on the incompressible navier-stokes equations. *Computer Methods in Applied Mechanics and Engineering*, 32(1–3):199–259, 1982. 134

[144] M.-T. Wang. *Development of finite element method for incompressible Navier-Stokes equations*. PhD thesis, National Taiwan University, 1996. 134, 135

[145] T. W. Pan, D. D. Joseph, and R. Glowinski. Modelling rayleigh–taylor instability of a sedimenting suspension of several thousand circular particles in a direct numerical simulation. *Journal of Fluid Mechanics*, 434:23–37, 2001. 146

[146] L. Lemaigre, M. A. Budroni, L. A. Riolfo, P. Grosfils, and A. D. Wit. Asymmetric rayleigh-taylor and double-diffusive fingers in reactive systems. *Physics of Fluids*, 25(1):014103, 2013. 151

[147] J. S. Turner. Double-diffusive phenomena. *Annual Review of Fluid Mechanics*, 6 (1):37–54, 1974. 151, 155

[148] E. Bodenschatz, W. Pesch, and G. Ahlers. Recent developments in rayleigh-bénard convection. *Annual Review of Fluid Mechanics*, 32(1):709–778, 2000. 152